Exploring the Reactivity of Bio-inspired Manganese Complexes with Dioxygen and its Derivatives

By

Joshua D. Parham

Submitted to the graduate degree program in Chemistry and the Graduate Faculty of the University of Kansas in partial fulfillment of the requirements for the degree of Doctor of Philosophy.

_____

Chairperson: Dr. Timothy A. Jackson

_____

Dr. Mikhail V. Barybin

_____

Dr. James D. Blakemore

_____

Dr. Jon A. Tunge

_____

Dr. Juan Bravo-Suarez

Date Defended: July 19, 2019

The Dissertation Committee for Joshua D. Parham

certifies that this is the approved version of the following dissertation:

Exploring the Reactivity of Bio-inspired Manganese Complexes with Dioxygen and its Derivatives

_____

Chairperson: Dr. Timothy A. Jackson

Date approved:

07/23/2019

Abstract

The reactivity of manganese centers with dioxygen and its derivatives is well known in nature, but the exact nature of the intermediates involved is often unclear. Synthetic manganese complexes have been developed to serve as models of some of these enzymatic systems and aid in our understanding of what factors control these important pathways. The work presented herein focuses on the reactivity of Mn complexes supported by pentacoordinate amide-containing ligands with O_2, alkylhydrogenperoxide, and H_2O_2. These studies have resulted in the formation and characterization of many new intermediates, adding to the general knowledge base regarding this kind of reactivity.

The dioxygen activation pathways of mononuclear Mn^{II} complexes supported by pentacoordinate amide-containing ligands, $[Mn^{II}(dpaq)](OTf)$ and the sterically modified $[Mn^{II}(dpaq^{2Me})](OTf)$, are investigated. Through titration experiments and isotopic-labeling studies, a change of mechanism is observed as a result of the steric modification of $[Mn^{II}(dpaq^{2Me})](OTf)$. This highlights the use of steric effects as a means to control which intermediates form along dioxygen activation pathways.

The formation and properties of two new Mn^{III}-alkylperoxo complexes, $[Mn^{III}(OO^tBu)(dpaq)]^+$ and $[Mn^{III}(OO^tBu)(dpaq^{2Me})]^+$, are described. These complexes were generated by reacting the corresponding Mn^{II} precursors with a large excess of ^{t}BuOOH at -15 °C in MeCN. These unstable Mn^{III}-alkylperoxo complexes were spectroscopically characterized, and complementary density functional theory (DFT) calculations were also performed to gain insight into their bonding and structural properties.

Additionally, the development of a new derivative of the dpaq ligand with steric functionalization is reported herein. The Mn^{II} and Mn^{III}-hydroxo complexes of this ligand have

been both spectroscopically and structurally characterized, revealing elongated equatorial Mn-N bonds as a result of the steric functionalization. These new complexes react with ^{t}BuOOH at room temperature to generate the first room temperature-stable Mn^{III}-alkylperoxo species. Based on the ability to form Mn^{III}-alkylperoxo species from the reaction between Mn^{III}-hydroxo species and alkylhydrogenperoxides, the reactivity of Mn^{III}-hydroxo complexes with H_2O_2 has been investigated as a possible means to form rare Mn^{III}-hydroperoxo species.

Acknowledgements

First of all, I would like to thank my research advisor, Professor Tim Jackson. You've been a great professor, teaching us the ins and outs of spectroscopy and bioinorganic chemistry and keeping the material accessible. You've been a great research mentor, always available to talk about the latest result with invaluable insight. You've pushed my boundaries as a chemist, and been extremely patient and understanding as I've grown over the past few years. You've also been a great mentor in regards to teaching, and I value all that I learned as your CHEM 195 teaching assistant. Your lectures will always hold influence as I go on teach my own students in the years to come.

I also would like to thank my research committee members. Professor Misha Barybin, you were one of the first professors that I interacted with at KU, and straight away you were a great mentor. Throughout the remainder of my career, you always maintained an interest in me and my research, helping KU to feel like home. Professor James Blakemore, I have appreciated and enjoyed conversations with you about science, and I'm excited to see where the future takes your research. Professor Jon Tunge, I have greatly appreciated the role you have played in my career at KU, both on my orals committee and now on my final dissertation defense committee. Professor Juan Bravo-Suarez, thank you so much for agreeing to serve on my final dissertation committee.

I would also like to thank Dr. Justin Douglas and Sarah Neuenswander for all of the help with EPR and NMR over the years. Thanks to Victor Day for providing insight into growing crystals and solving our crystal structures. I'd like to thank Larry Seib and Dr. Todd Williams in the mass spectrometry lab for their assistance.

The support of the past and present members of the Jackson group has proven priceless during my studies. To Gayan, you made my first semester in the group incredibly enjoyable and memorable. I treasure the strong friendship we've maintained since then. To Hannah, you were always a constant force of encouragement and support, for which I am so very grateful. To Derek, our long conversations about music or politics were probably more distracting than either of us ever needed, but I value those times and look forward to picking them back up some day. To Allyssa, you were the best office neighbor I could ask for, and I appreciate the laughs we shared as well as your encouragement. Melissa, thank you so much for listening and talking and being there through all five years of this endeavor. Yuri, you are an incredible scientist and lab member, and you're going to do great things in your future! Abraham, I enjoyed showing you the ropes when you first joined our group and look forward to many years of friendship. Liz, your sense of perseverance is awesome, and I'm glad you joined our group. Jaycee, I've enjoyed teaching with you and working with you over the past couple of years. Sam, it's been a pleasure to share a hood the past few months, and I'm glad I could impart some

knowledge to you before I left. Keep the trivia team going strong! Priya, we did not work together much, but I could always count on you as a positive force in the group and have really enjoyed getting to know you. Javier, good luck in your studies and with your research! Shannon, I've enjoyed becoming friends with you and talking about music and books over the years. Ellie, your passion for learning is inspiring and will lead you far.

I have to thank my friends outside of the group for helping me stay sane. Nate, I can always count on you as an understanding ear and a good pal to help me unwind in the hard times. You were great to play music with, and I hope we can all do that again soon. Tal, I'm going to miss board game nights, movie nights, and our long chats. Chris, our road trips to Colorado will remain fond memories of mine, and I'm hoping for another to come visit you in Chicago soon. To Jess, Mason, and Tom – I absolutely loved spending my Sundays with you guys playing DnD. To James and Josh, you guys made visiting Arkansas something to look forward to, and I will always enjoy talking science and philosophy with you guys

To my family – Mom and Dad, thank you for always being there and encouraging me. To my sister, Audre, you've become such an awesome person. You've grown so much in the past five years, and I'm so proud of how you've taken charge of your destiny. Thanks for visiting me the last two summers and always coming through with a good laugh just when I need it.

Finally, I must thank Amy. I can honestly say that I would not have made it through without you there, holding me up. Thank you for making every day bright. Thank you for your understanding and your patience. Thank you for listening while I just rattled off endless words about whatever problem I was facing at the time, even if you never had the chance to give your input. Thank you for taking care of me when I was sick. Thank you for reminding me to eat during the late nights. Thank you for making me take breaks. Thank you for all of the memories over the past years. I can't wait to see what memories we'll make in the future.

Table of Contents

Chapter 1

An Overview of the Reactivity of Mn Complexes with O_2 and its Derivatives

1.1 Introduction. The reactions of transition metal complexes with O_2 or its derivatives have been an area of interest in regard to both biological pathways and synthetic applications.[1-10] While a majority of studies regarding this kind of reactivity have focused on Fe- and Cu-containing enzymes or model complexes,[1-3, 10] there are also cases of Mn-containing enzymes and model complexes that participate in O_2 activation.[4, 5] Mn-dependent enzymes react with O_2 and its derivatives to perform a variety of reactions, including the detoxification of reactive oxygen species,[6-8] peroxidation of fatty acids,[11-15] the biosynthesis of dexyribonucleotides,[16] and the oxidation of water to dioxygen.[17-22] The active sites of these enzymes typically consist of one or more Mn centers bound to histidine and carboxylate ligands and solvent (Figure 1.1). Synthetic systems also react with dioxygen and its derivatives, forming various intermediates capable of a wide range of reactions, including olefin epoxidation and the oxidation of alcohols.[4, 5, 23-36]

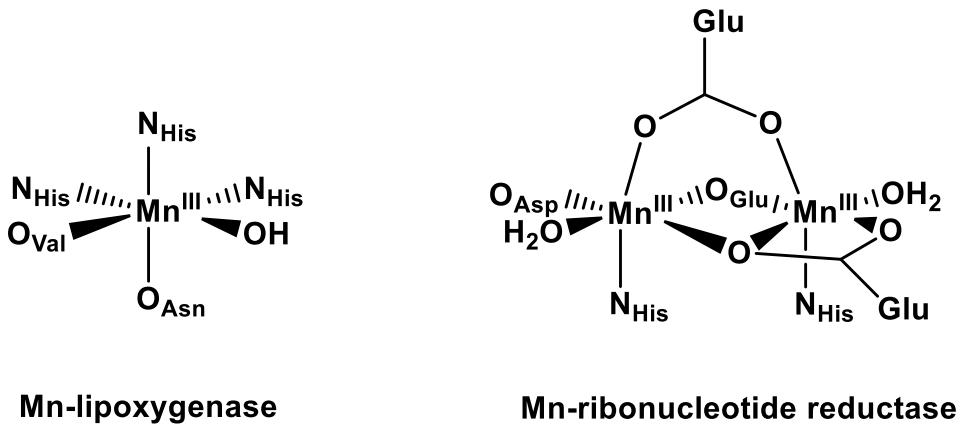

Figure 1.1. Active site structures of two Mn-dependent enzymes. Left: Mn-LOX.[12] Right: Mn-RNR.[37]

1.2 Reactivity of manganese-dependent enzymes with O_2. Important examples of manganese-dependent enzymes that employ O_2 include oxalate oxidase and oxalate decarboxylase, which serve to degrade toxic oxalate.[38] Many fungal species produce oxalate to serve a variety of

functions, including pathogenesis on plant hosts and control of nutrients in the environment.[39, 40] Oxalate decarboxylase is expressed in these fungal species as a means to control oxalate concentration, using dioxygen to break down oxalate into formate and CO_2.[40] Oxalate oxidase is found in plants and serves the purpose of defending against the chemical attack of the oxalate-forming fungi.[41] The products of oxalate degradation by oxalate oxidase are CO_2 and H_2O_2, the latter of which the plant uses for cross-linking within the cell wall and for tissue remodeling.[41, 42]

In addition to the oxalate degrading enzymes, there are two other Mn-dependent enzymes that utilize O_2 for substrate oxidation, Mn-dependent dioxygenases (MndD) in soil bacteria and Mn-lipoxygenases (Mn-LOX) in certain fungi, for which complete mechanisms have been proposed.[4, 5, 11-15, 43-46] The Mn-dependent dioxygenases serve to break down aromatic catechol substrates through a ring-opening mechanism involving the insertion of two oxygen atoms from O_2.[43, 47] An EPR study from Hendrich et al., in which samples were prepared at different time points of the reaction between enzyme and O_2, resulted in the observation of several intermediates along the MndD pathway.[43] The treatment of a substrate-bound Mn^{II} center (Scheme 1.1, **I**) with dioxygen resulted in the initial observation of an EPR signal consistent with an S=5/2 system that was attributed to the coupling of a Mn^{III} ion to a radical center, presumably a superoxo adduct (Scheme 1.1, **II**).[43] The EPR spectrum obtained proceeding the formation of this intermediate was consistent with the formation of an S=5/2 Mn^{II} center with significant geometric distortions.[43] This signal was attributed to a Mn^{II}-alkylperoxo intermediate formed through the reaction of the Mn^{III}-superoxo species with the bound substrate molecule (Scheme 1.1, **III**).[43] The formation of this intermediate is proposed to be followed by a Criegee rearrangement involving O-O bond cleavage to yield the ring-opened dioxygenated product (Scheme 1.1).[43]

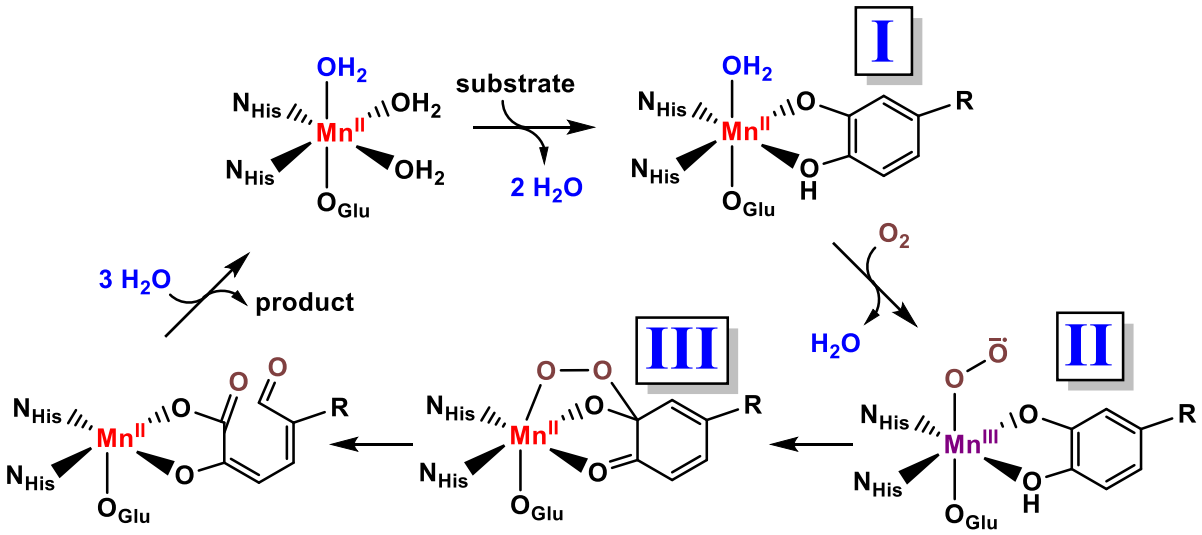

Scheme 1.1. Proposed catalytic cycle of Mn-dependent extradiol catechol dioxygenase.

Mn-lipoxygenase is responsible for the hydroperoxidation of fatty acids with *cis*,*cis*-1,4-diene motifs. The resultant peroxides serve as precursors in the biosynthesis of a class of signaling molecules known as eicosanoids.[4, 46] The catalytic cycle is initiated by the rate-limiting abstraction of a hydrogen atom from a fatty acid substrate by an active-site Mn^{III}-hydroxo adduct (Scheme 1.2, **I**), resulting in the formation of a Mn^{II}-aqua species and an organic radical (**II**).[11, 13, 45] The resultant organic radical reacts with dioxygen to form an alkylperoxyl radical. The final alkylhydroperoxide product (**III**) can be formed by one of two proposed pathways that diverge at the Mn^{II}-aqua intermediate (Scheme 1.2, A or B). One possibility is that the substrate radical could displace the aqua ligand and oxidize the Mn^{II} center, forming an Mn^{III}-alkylperoxo adduct (Scheme 2B).[4] Indirect support for this mechanism comes from the X-ray crystal structure of an iron-containing soybean lipoxygenase which shows the alkylperoxyl radical bound to the metal center.[46] A subsequent ligand substitution reaction with water would generate the product and the Mn^{III}-hydroxo resting state.[4] Alternatively, proton-coupled electron transfer from the bound water

molecule to the alkylperoxyl radical could yield the organic product and regenerate the Mn^{III}-hydroxo oxidant (Scheme 1.2A).[48]

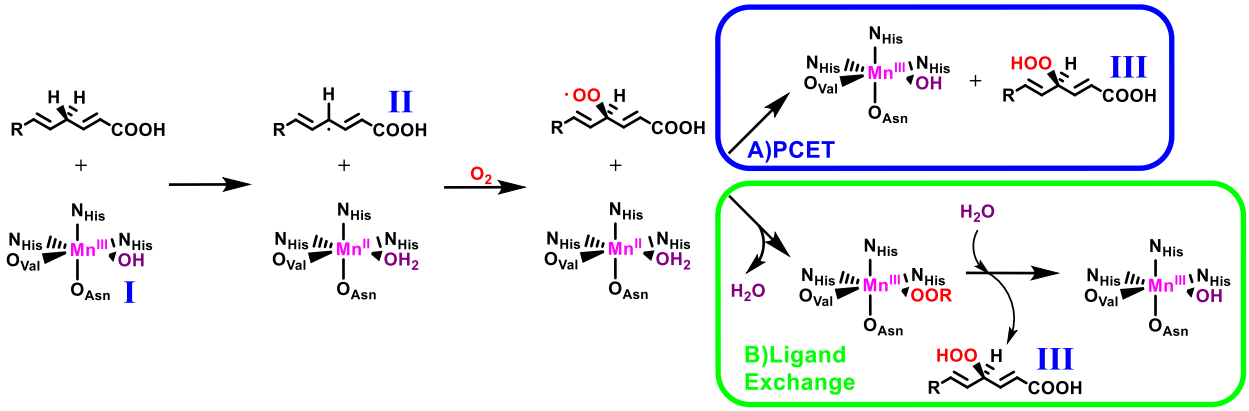

Scheme 1.2. Proposed mechanisms for fatty acid oxidation by manganese lipoxygenase. Reproduced with permission from *Inorg. Chem.* **2018**, *575*, 2489-2502. Copyright 2018 American Chemical Society.

1.3 Mn^{III}-peroxo intermediates in Mn-superoxide dismutase. There are also examples of manganese-dependent enzymes in nature that are known to react with the reduced derivatives of O_2, such as superoxide and hydrogen peroxide.[6, 7] One such class of enzymes, the manganese superoxide dismutases (Mn-SOD), are found in both prokaryotic and eukaryotic cells, including the mitochondria of humans.[7, 8] These enzymes catalyze both the oxidation of superoxide to O_2 and the reduction of superoxide to H_2O_2 through separate reactions in which the Mn center alternates between reactive Mn^{III} and Mn^{II} states.[7] Under normal conditions, the reduction of superoxide occurs through a prompt protonation pathway (Scheme 1.3). However, under high concentrations of superoxide, Mn-SOD forms a product-inhibited complex (Scheme 1.3).[49-51] The product-inhibited complex slowly re-enters the catalytic cycle through an inner-sphere pathway (Scheme 1.3).[7, 50]

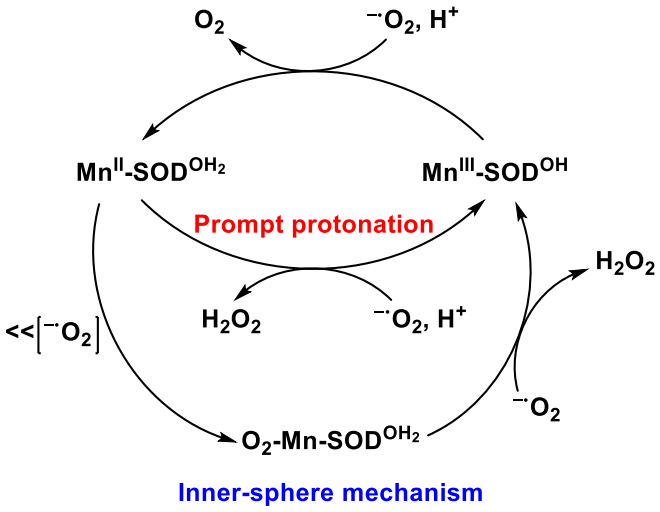

Scheme 1.3. Catalytic cycle of Mn-SOD including both the prompt protonation and inner-sphere mechanisms of the reduction of superoxide to H_2O_2.[7, 9, 49, 50, 52]

The product-inhibited complex is proposed to be a Mn^{III}-peroxo adduct based on spectroscopic characterization.[50, 51] However, the exact nature of this intermediate is a matter of contention. Computational studies have proposed both end-on hydroperoxo and side-on peroxo adducts (Figure 1.2, A and B).[53-55] Regardless of protonation state, these studies all show the peroxo moiety bound to the metal center in between the two equatorial hisitidine residues. In contrast to this, a crystal-structure obtained from a H_2O_2 treated crystal of *Escherichia coli* Mn-SOD included a side-on peroxo adduct bound to the metal center in the axial site (Figure 1.2, C).[56]

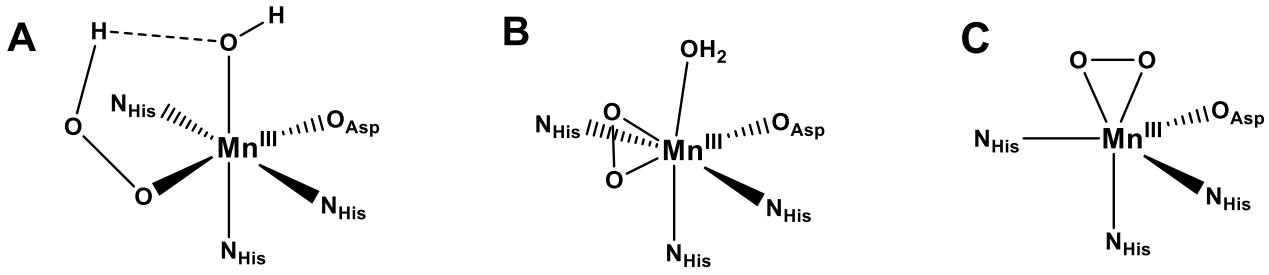

Figure 1.2. Possible structures of the product-inhibited complex in Mn-SOD. A) End-on Mn^{III}-hydroperoxo adduct. B) Side-on Mn^{III}-peroxo adduct geometry from computational studies. C) Side-on Mn^{III}-peroxo adduct geometry from crystal structure of Mn-SOD from *E. coli*.[9, 54-57]

1.4 Reactivity of Mn-containing model complexes with O_2. The possibility of pairing an earth-abundant metal like Mn with an oxidant as benign and ubiquitous as O_2 is attractive, especially as industrial O_2 activation often employs expensive precious-metal catalysts.[58] However, examples of Mn^{II} complexes that can activate dioxygen to give isolable products are relatively uncommon. This lack of reactivity towards O_2 is due in part to the high reduction potential of the $Mn^{III/II}$ redox couple (1.5 V vs. NHE in H_2O).[59] To circumvent this shortcoming, electron-rich ligands have been used to modulate the redox potential of the Mn^{II} center and therefore facilitate O_2 activation.[60] Mn^{II} systems employing these electron-rich ligand scaffolds perform catalytic dioxygen reduction and organic substrate oxidation using O_2.[61-69] The mechanistic details of many of these catalysts remain unclear, due in part to the fleeting nature of the intermediates along these reaction pathways.[60, 64, 67, 68]

An early example of O_2 as an oxidant for Mn-catalyzed substrate oxidation was reported by Fontecave and coworkers and utilized the Mn(TPP) system (TPP = tetraphenylporphyrin).[64] In the presence of O_2, 1-methylimidazole as a co-catalyst, and acetic acid as a proton source, the [Mn^{II}(TPP)] catalysts performed epoxidation of cyclooctene, 2-methylhept-2-ene, cyclohexene, and non-1-ene, with up to 75 turnovers.[64] Although impressive in coupling O_2 activation with substrate oxidation, the mechanistic details of this system are not well understood.

Much of the founding work in this area focused on Schiff-base ligands as a means to control the electronic and steric properties of the metal complexes (Figure 1.3).[70] The reaction of Mn Schiff-base complexes with dioxygen resulted in a complex mixtures of products, possibly consisting of both monomeric and dimeric species. Consequently, the exact nature of all of the

products and the mechanistic details of O_2 activation by Mn Schiff-base complexes remain unclear.[70]

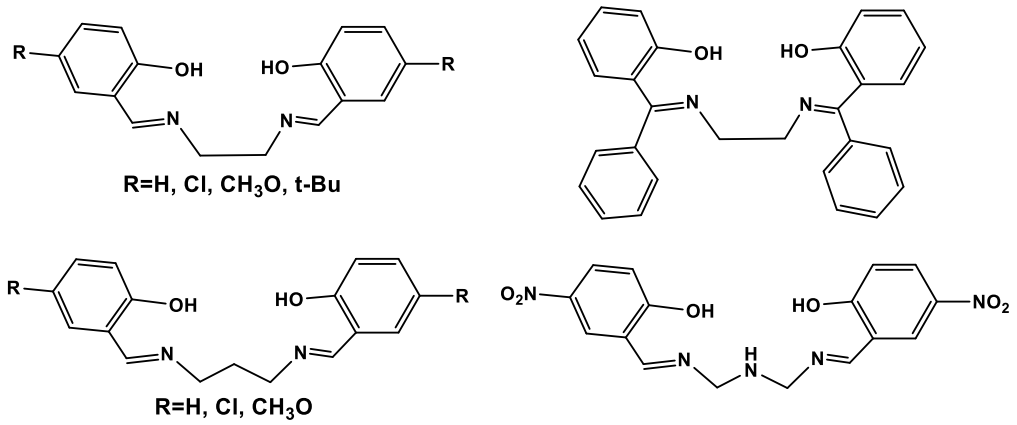

Figure 1.3. Schiff base ligands used to support Mn complexes capable of O_2 activation.[70]

In one of the first reports to propose a mechanism of O_2 activation by a Mn Schiff-base complex, Horwitz described electrocatalytic epoxidation of cyclootene, *trans*-2-octene, and cyclohexene using the $[Mn^{II}(salen)]$ complex, which was generated electrochemically via reduction of $[Mn^{III}(salen)]^+$ (salen = N,N′-bis(salicylidene)ethylenediamine).[65] On the basis of cyclic voltammetry, the Mn^{II} species was proposed to bind dioxygen and, with the electrochemical transfer of a second electron, yield a peroxomanganese(III) complex (Scheme 1.4, **I**). The putative $[Mn^{III}(O_2)(salen)]^-$ species was proposed to react with benzoic anhydride to form a high-valent Mn^{V}-oxo adduct (**II**) that performed olefin epoxidation or allylic hydroxylation (Scheme 1.4).[65] The $[Mn^{III}(salen)]^+$ complex is capable of catalytic turnover under electrochemical conditions, but has a short lifetime due to the formation of inactive dimer species.[65, 70, 71]

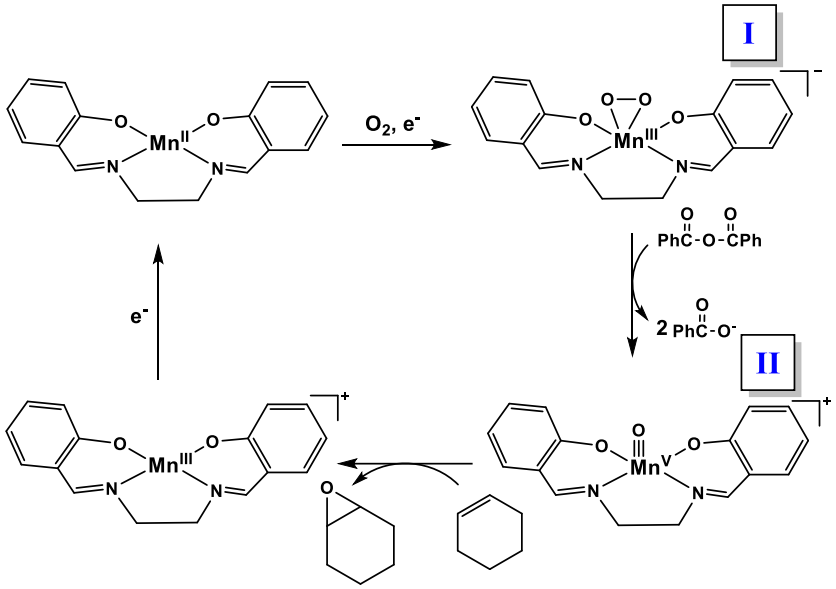

Scheme 1.4. Proposed mechanism of the electrochemical epoxidation of olefins by $[Mn^{III}(salen)]^{+}$.[65]

While the systems discussed above have primarily been studied in regards to the catalytic ability of dioxygen-activating Mn complexes in substrate oxidation, there have also been a small number of Mn^{II} complexes for which mechanistic studies of O_2-activation have been performed (Scheme 3).[11, 72-79] Borovik and co-workers described a Mn^{II} complex with trianionic N4 ligation that reacts with O_2 to form a monomeric Mn^{III}-hydroxo complex, with a Mn:O_2 stoichiometry of 2:1.[72] Isotopic labeling experiments with $^{18}O_2$ confirmed that the O atoms in the Mn^{III}-hydroxo product came solely from dioxygen. When this reaction was carried out in the presence of 1 equivalent of PPh_3, the oxygen atom transfer (OAT) product $Ph_3P{=}O$ was observed in 33% yield. Additionally, reactions in deuterated solvent yielded only the Mn^{III}–OD complex. These observations support a mechanism involving the initial formation of a peroxodimanganese(III) species from two equivalents of the Mn^{II} complex and O_2. This dimer was proposed to undergo

homolytic O–O bond cleavage to yield a Mn^{IV}-oxo complex that abstracts hydrogen atoms from solvent to generate the observed Mn^{III}-hydroxo product (Scheme 1.5A).[72]

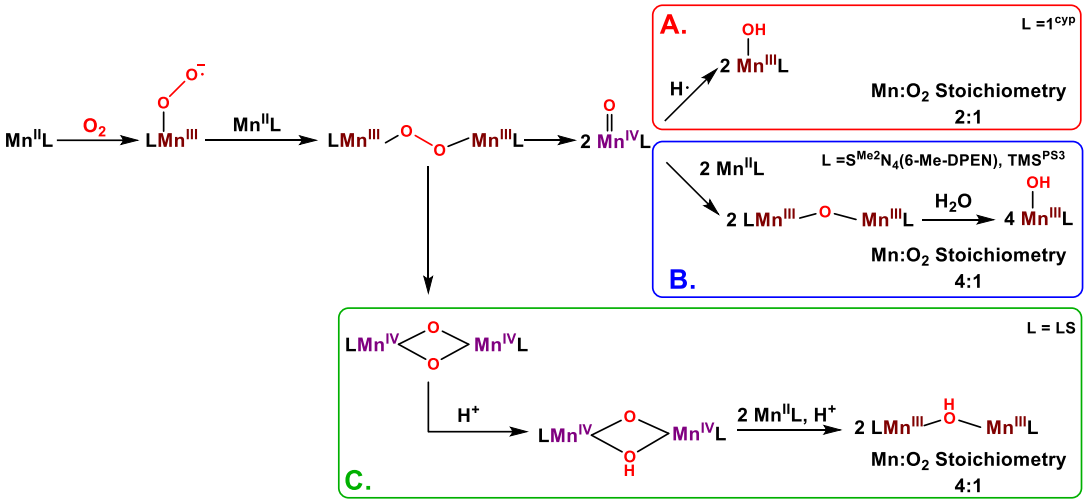

Scheme 1.5. Proposed mechanisms for the reaction of Mn^{II} complexes with O_2 to generate Mn^{III}-hydroxo species. Ligand abbreviations are as follows: 1^{cyp} = tris(N-cyclopentylcarbamoylmethyl)amine; $S^{Me2}N_4$(6-Me-DPEN) = (E)-3-((2-(bis((6-methylpyridin-2-yl)methyl)amino)ethyl)imino)-2-methylbutane-2-thiolate); TMS^{PS3} = (2,2′,2″-trimercapto-3,3′,3″-tris(trimethylsilyl)triphenylphosphine); LS = 2,2′-(2,2′-bipyridine-6,6′-diyl)bis(1,1′-diphenylethanethiolate).[62, 72-75, 77, 78]

More recently, Kovacs et al. reported a series of Mn^{II} complexes featuring N_4S^- ligation that also reacted with O_2 to give the corresponding mononuclear Mn^{III}-hydroxo complexes.[22] However, these systems operate with a Mn:O_2 stoichiometry of 4:1, differing from that of the Borovik system (2:1). An X-ray diffraction structure of $[Mn^{III}Mn^{III}(\mu\text{-}\eta^1\text{:}\eta^1\text{-}O_2)(S^{Me2}N_4(6\text{-Me-DPEN}))_2]^{2+}$ confirmed the initial formation of a peroxodimanganese(III, III) species from the reaction of two equivalents of the five-coordinate $[Mn^{II}(S^{Me2}N_4(6\text{-Me-DPEN}))]^+$ complex with O_2 ($S^{Me2}N_4$(6-Me-DPEN)) = (E)-3-((2-(bis((6-methylpyridin-2-yl)methyl)amino)ethyl)imino)-2-methylbutane-2-thiolate). The decay of $[Mn^{III}Mn^{III}(\mu\text{-}\eta^1\text{:}\eta^1\text{-}O_2)(S^{Me2}N_4(6\text{-Me-DPEN}))_2]^{2+}$ yielded the (μ-oxo)dimanganese(III, III) species $[Mn^{III}Mn^{III}(\mu\text{-O})(S^{Me2}N_4(6\text{-Me-DPEN}))_2]^{2+}$,[20] which can undergo hydrolysis to generate the Mn^{III}-hydroxo complex (Scheme 1.5B).[62, 73, 75] The formation

of the (μ-oxo)dimanganese(III, III) species, which was also characterized by X-ray diffraction, suggests a mechanism where a Mn^{IV}-oxo adduct is intercepted by unreacted Mn^{II} complex, rather than abstracting a hydrogen atom from solvent.[78]

A similar mechanism was invoked by Lee et al. for O_2 activation by the $[Mn(^{TMS}PS3)(DABCO)]^-$ system ($^{TMS}PS3$ = (2,2′,2″-trimercapto-3,3′,3″-tris(trimethylsilyl)triphenylphosphine) and DABCO = 1,4- diazabicyclo[2.2.2]octane).[77] In this work, a crystallographically characterized monomeric side-on Mn^{IV}-peroxo species is formed from the reaction of $[Mn(^{TMS}PS3)(DABCO)]^-$ with O_2. This species is able to dimerize with additional $[Mn(^{TMS}PS3)(DABCO)]^-$, leading to the formation of a putative peroxodimanganese(III, III) species that is proposed to decay and form either a terminal Mn^{IV}-oxo or a bis(μ-oxo)dimanganese(IV, IV) intermediate. This intermediate undergoes a subsequent comproportionation with residual Mn^{II} complex in solution to form a (μ-oxo)dimanganese(III, III) species.[77, 79]

A subtly different mechanism of O_2 activation, by a dimercapto-bridged Mn^{II} dimer, was recently proposed by Duboc et al.[74, 76] In this system, O_2 activation resulted in the production of a (μ-hydroxo)dimanganese(III, III) complex, which was characterized crystallographically. The initial formation of a peroxodimanganese(III, III) intermediate was proposed from the reaction of the Mn^{II} dimer with O_2. However, instead of yielding terminal Mn^{IV}-oxo species upon homolytic O−O bond cleavage, the peroxo-bridged dimer was proposed to convert to a bis(μ-oxo)dimanganese(IV, IV) intermediate, which was crystallographically characterized.[21] The bis(μ-oxo)dimanganese(IV, IV) complex then decayed by an intramolecular proton transfer between the supporting ligand and one of the bridging oxo atoms to give yields a (μ-oxo)(μ-hydroxo)dimanganese(IV) species. Finally, the (μ-oxo)(μ-hydroxo)dimanganese(IV) species was

proposed to comproportionate with residual Mn^{II} dimer to give the final (μ-hydroxo)dimanganese(III) product (Scheme 1.5C).[74, 76]

Collectively, these reports highlight some central features in O_2 activation by Mn^{II} centers. In all cases, a μ-peroxodimanganese(III, III) species is invoked as an early intermediate, and this species decays by O–O homolysis to give either mononuclear Mn^{IV}-oxo or dinuclear bis(μ-oxo)dimanganese(IV, IV) intermediates. At this point, the paths diverge (Scheme 1.5), but isolable Mn^{III} complexes are the products of all pathways, and trapping of high-valent Mn^{IV} species by reaction with the Mn^{II} starting complex is common. Importantly, in no pathway is the starting Mn^{II} complex regenerated.

1.5 Dioxygen activation by a series of Mn^{II} complexes supported by amide-containing pentadentate ligands. As part of the on-going efforts to mimic the chemistry of Mn-dependent enzymes,[23, 9] the Jackson group has reported a pair of Mn^{II} complexes supported by amide-containing N_5 ligands, $[Mn^{II}(dpaq)](OTf)$ and $[Mn^{II}(dpaq^{2Me})](OTf)$, that react with O_2 to yield the corresponding Mn^{III}-hydroxo adducts, $[Mn^{III}(OH)(dpaq)]^+$ and $[Mn^{III}(OH)(dpaq^{2Me})]^+$, in 98% yield (Scheme 1.6, dpaq = 2-[bis(pyridin-2-ylmethyl)]amino-N-quinolin-8-yl-acetamidate and $dpaq^{2Me}$ = 2-[bis(pyridin-2-ylmethyl)]amino-N-2-methyl-quinolin-8-yl-acetamidate). These Mn^{III}-hydroxide complexes can oxidize 2,2′-6,6′-tetramethylpiperidine-1-ol (TEMPOH), phenols, and xanthene through a hydrogen-atom transfer (HAT) mechanism, mimicking the reactivity of Mn-LOX (Scheme 1.7).[63, 80, 81]

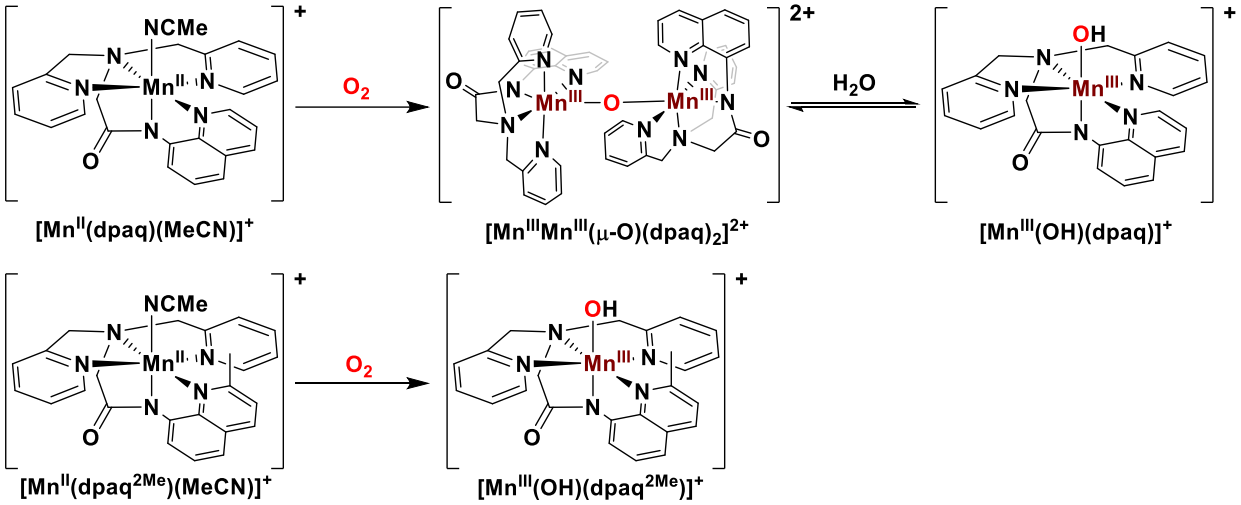

Scheme 1.6. $[Mn^{II}(dpaq)(MeCN)]^+$ reacts with O_2 to produce a (μ-oxo)dimanganese(III, III) complex that is in equilibrium with monomeric $[Mn^{III}(OH)(dpaq)]^+$ (top). $[Mn^{II}(dpaq^{2Me})(MeCN)]^+$ does not show formation of a (μ-oxo)dimanganese(III, III) complex in the reaction with O_2, instead only forming $[Mn^{III}(OH)(dpaq^{2Me})]^+$ (bottom).

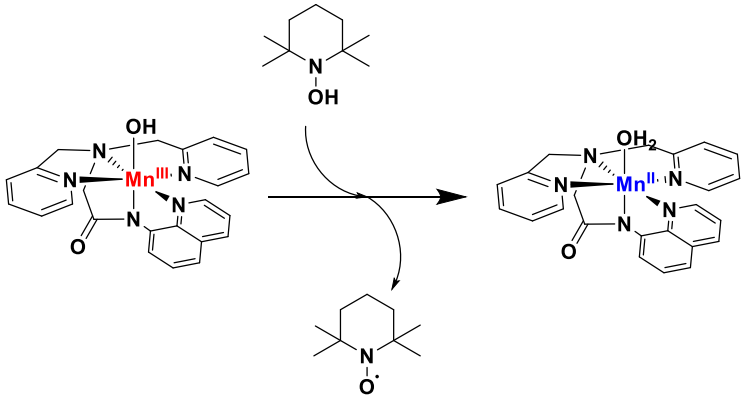

Scheme 1.7. $[Mn^{III}(OH)(dpaq)]^+$ reacts with the weak O–H bond of TEMPOH to yield a Mn^{II}-aqua complex and TEMPO radical.

The pathway by which $[Mn^{II}(dpaq)](OTf)$ and $[Mn^{II}(dpaq^{2Me})](OTf)$ react with dioxygen has not been explored. A recent report has shown that, upon dissolution of the $[Mn^{III}(OH)(dpaq)](OTf)$ salt in MeCN solution, the mononuclear Mn^{III}-hydroxo adduct exists in a water-dependent equilibrium with a (μ-oxo)dimanganese(III, III) species (Scheme 1.6).[81] Using

^{1}H-NMR and electronic absorption spectroscopies, it was demonstrated that the addition of a small amount of water (440 equivalents per Mn^{III}) to an equilibrium mixture of $[Mn^{III}(OH)(dpaq)]^+$ and $[Mn^{III}Mn^{III}(\mu\text{-oxo})(dpaq)_2]^{2+}$ shifts the equilibrium to favor the mononuclear Mn^{III}-hydroxo species.[81] This equilibrium has also been observed for complexes featuring different substituents in the 5-quinolinyl position of the dpaq ligand ($[Mn^{III}(OH)(dpaq^{5Cl})_2](OTf)$, $[Mn^{III}(OH)(dpaq^{5OMe})_2](OTf)$, and $[Mn^{III}(OH)(dpaq^{5NO2})_2](OTf)$), and XRD structures of each of the respective $[Mn^{III}Mn^{III}(\mu\text{-O})(dpaq^{5R})_2](OTf)_2$ complexes have been obtained (R = Cl, OMe, and NO_2).[82] The observation of the (μ-oxo)dimanganese(III, III) complexes could be taken to suggest that the $[Mn^{II}(dpaq^{5R})](OTf)$ complexes carry out O_2 activation in a manner similar to that observed for the $[Mn^{II}(S^{Me2}N_4(6\text{-Me-DPEN}))]^+$ complex of Kovacs and co-workers (Scheme 4B).[22] Intriguingly, complementary ^{1}H-NMR investigations studies of $[Mn^{II}(dpaq^{2Me})](OTf)$ provided no evidence for a (μ-oxo)dimanganese(III, III) species (Scheme 1.6, bottom).[81] Presumably, the steric bulk of the 2-Me-appended quinoline moiety in $dpaq^{2Me}$ disfavors the formation of an oxo-bridged dimer.

1.6 Reactivity of Mn-containing model complexes with reduced dioxygen derivatives.

In addition to modeling the O_2 reactivity of metalloenzymes, synthetic complexes have also been used to investigate the reactivity of Mn^{II} centers with reduced dioxygen derivatives. There are several reports of Mn^{II} complexes that react with H_2O_2 or superoxide to yield side-on Mn^{III}-peroxo species.[83-102] The reaction between the Mn^{II} center and superoxide presumably proceeds through the one-electron oxidation of the metal center, much like the reactivity proposed for Mn-SOD under high superoxide concentration.[7] The mechanism through which Mn^{II} reacts with H_2O_2 to form Mn^{III}-peroxo complexes is currently unknown, and understanding this kind of reactivity is complicated by the fact that a base is sometimes, but not always, required for Mn^{III}-peroxo

formation through the reaction with H_2O_2.[9] Mn^{III}-peroxo complexes have been supported by both heme and non-heme ligand platforms, and crystal structures have been reported for several Mn^{III}-peroxo complexes.[83-90] Mn^{III}-peroxo complexes have been supported by a wide variety of ligands (Figure 1.4). These include tetradentate ligands, and ligands that are normally pentadentate coordinating in a tetradentate fashion (Figure 1.4).[9] Additionally, both neutral and anionic ligands have been reported to support Mn^{III}-peroxo adducts, leading to a wide range of structural and electronic properties and obscuring a general understanding of the reactivity of this class of complexes.[9] Several of the reported Mn^{III}-peroxo complexes are capable of performing nucleophilic aldehyde deformylation reactions.[61, 88-92, 101-104]

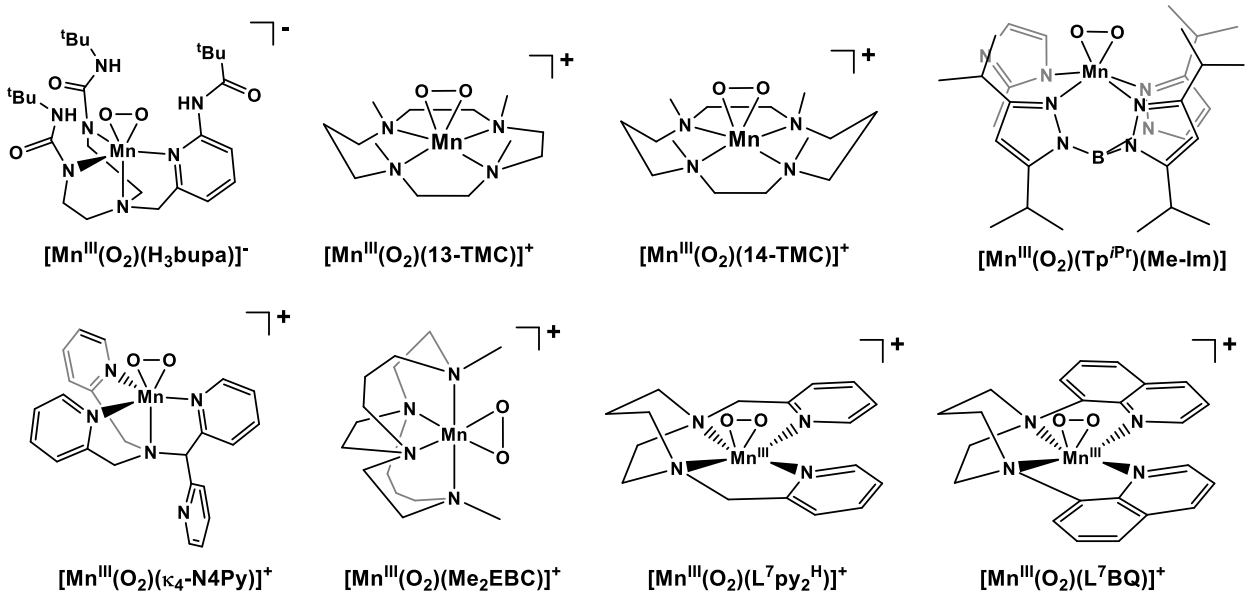

Figure 1.4. Molecular structures of select side-on Mn^{III}-peroxo species.[85, 88, 90-92, 95, 99, 103, 105]

O–O bond activation of Mn^{III}-peroxo complexes leads to the formation of various intermediates, including $(\mu\text{-O})_2Mn^{III}Mn^{IV}$ dimers, high valent Mn^{IV}-oxo complexes, or Mn^{III}-hydroxo species. Reports in which Mn^{II} complexes react with H_2O_2 to yield $(\mu\text{-O})_2Mn^{III}Mn^{IV}$ species, presumably through a Mn^{III}-peroxo intermediate, are numerous.[6, 31, 106-110] The putative

Mn^{III}-peroxo species is proposed to react with residual Mn^{II} complex in solution to form a peroxodimanganese(II,III) intermediate that can isomerize to form the final $(\mu\text{-}O)_2Mn^{III}Mn^{IV}$ dimer product. In support of this pathway, the O–O bonds of select Mn^{III}-peroxo complexes have shown to be cleaved through reactions with Mn^{II} complexes, generating $(\mu\text{-}O)_2Mn^{III}Mn^{IV}$ species.[105, 111] The addition of $[Mn^{II}(N4Py)(OTf)](OTf)$ to a solution of the Mn^{III}-peroxo complex $[Mn^{III}(O_2)(\kappa^4\text{-}N4Py)]^+$ in MeCN results in the formation of a species with electronic absorption features at 710 nm and 550 nm and an EPR spectrum consisting of a sixteen-line signal similar to that observed for previously reported $(\mu\text{-}O)_2Mn^{III}Mn^{IV}$ complexes (N4Py = *N*,*N*-bis(2-pyridylmethyl)-*N*-bis(2-pyridyl)methylamine).[105] An X-ray crystal structure confirmed the formulation of the species as $[Mn^{III}Mn^{IV}(\mu\text{-}O)_2(\kappa^4\text{-}N4Py)_2]^{3+}$ (Scheme 1.8).[105] The $(\mu\text{-}O)_2Mn^{III}Mn^{IV}$ complex can also be formed directly through the reaction of $[Mn^{II}(N4Py)(OTf)]^+$ with H_2O_2 in the presence of Et_3N (Scheme 1.8).[105] Similar reactivity was observed for $[Mn^{II}(^{DMM}N4Py)]^{2+}$ (^{DMM}N4Py = *N*,*N*-bis(4-methoxy-3,5-dimethyl-2-pyridylmethyl)-*N*-bis(2-pyridyl)methylamine).[111]

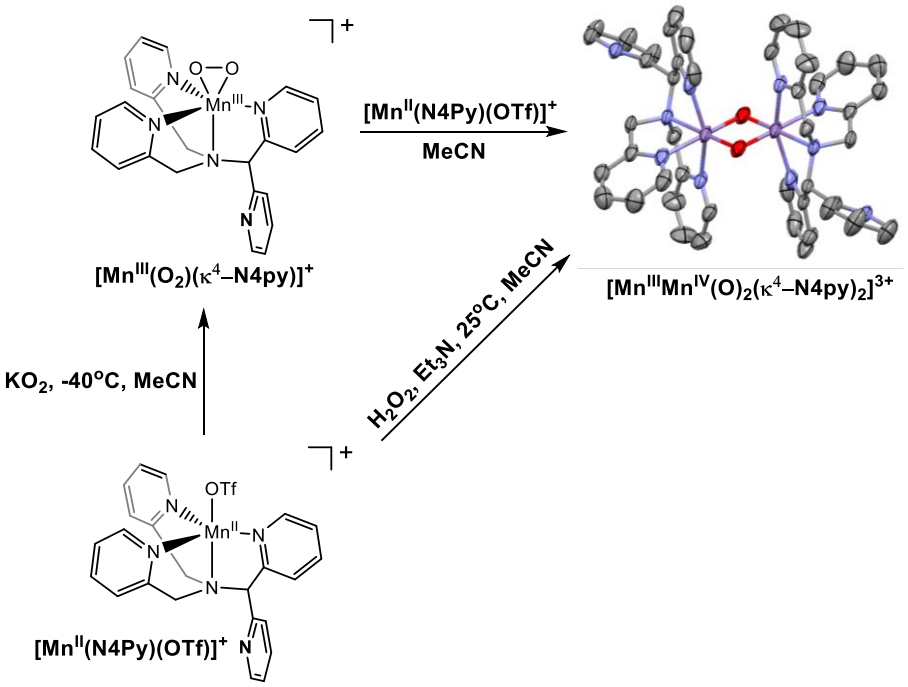

Scheme 1.8. The different formation pathways of $[Mn^{III}Mn^{IV}(\mu\text{-}O)_2(\kappa^4\text{-}N4Py)_2]^{3+}$.[105] ORTEP diagram of $[Mn^{III}Mn^{IV}(\mu\text{-}O)_2(\kappa^4\text{-}N4Py)_2]$ $(OTf)_{2.8}(PF_6)_{0.2}$ shown with thermal ellipsoids at the 50% probability level with hydrogen atoms, solvent molecules, and counterions omitted for clarity.

Cleavage of Mn^{III}-peroxo O–O bonds has also been reported to yield other products besides $(\mu\text{-}O)_2Mn^{III}Mn^{IV}$ species.[99, 112] The $[Mn^{III}(O_2)(Me_2EBC)]^+$ complex was formed in 60% yield from the reaction of $[Mn^{II}(Me_2EBC)(Cl)_2]$ with 4 equivalents of KO_2.[99] Under these conditions, the Mn^{III}-peroxo complex thermally decays to result in the formation of a solution composed of a mixture of products. Through EPR analysis, this complex mixture was determined to be composed of a Mn^{IV}-oxo complex, a Mn^{III}-hydroxo complex, and an unidentified Mn^{II} species.[99] Based on these decay products, it was proposed that the thermal decay involved the reaction of residual Mn^{II} complex in solution with $[Mn^{III}(O_2)(Me_2EBC)]^+$ to form an unobserved peroxodimanganese(II,III) species. This proposed peroxo-bridged dimer would then undergo O–O bond homolysis to generate monomeric Mn^{IV}-oxo and Mn^{III}-hydroxo species, foregoing the formation of a (μ-

$O)_2Mn^{III}Mn^{IV}$ complex due to the steric effect of the methyl substituents (Scheme 1.9).[99] The Mn^{IV}-oxo subsequently decayed to form the Mn^{III}-hydroxo complex.

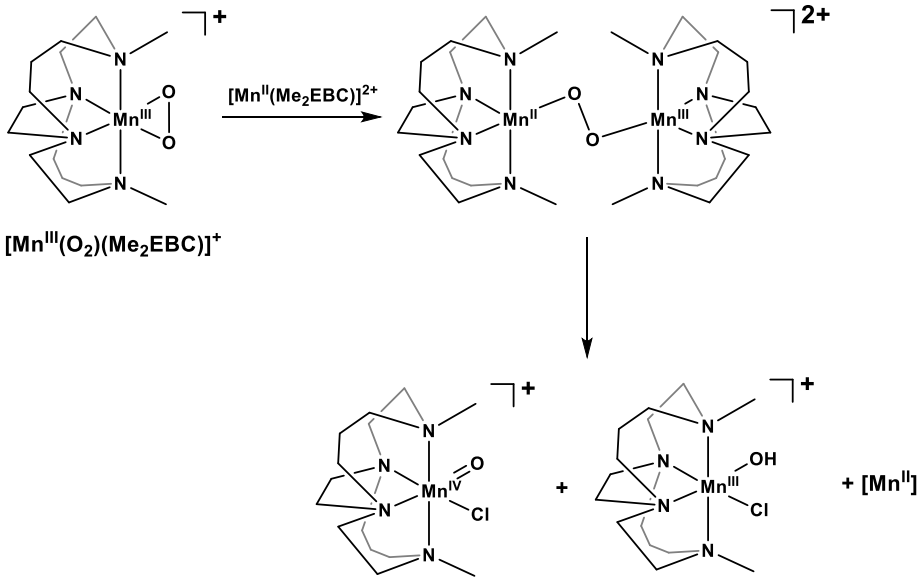

Scheme 1.9. Proposed decay pathway of $[Mn^{III}(O_2)(Me_2EBC)]^+$ to yield a mixture of products that include a Mn^{IV}-oxo species and a Mn^{III}-hydroxo complex.[99]

Adding to this, different products are also seen upon the addition of acid to Mn^{III}-peroxo complexes. A solution of the $[Mn^{III}(O_2)(N_4O)]$ complex in dimethylformamide (DMF) decayed electrochemically in the presence of a weak acid (such as water) to generate a bis-hydroxomanganese(III) species (Scheme 1.10).[112] This report also showed that the addition of a strong acid like $HClO_4$ pulled the reaction away from O–O bond activation, generating H_2O_2 as a product instead (Scheme 1.10).[112]

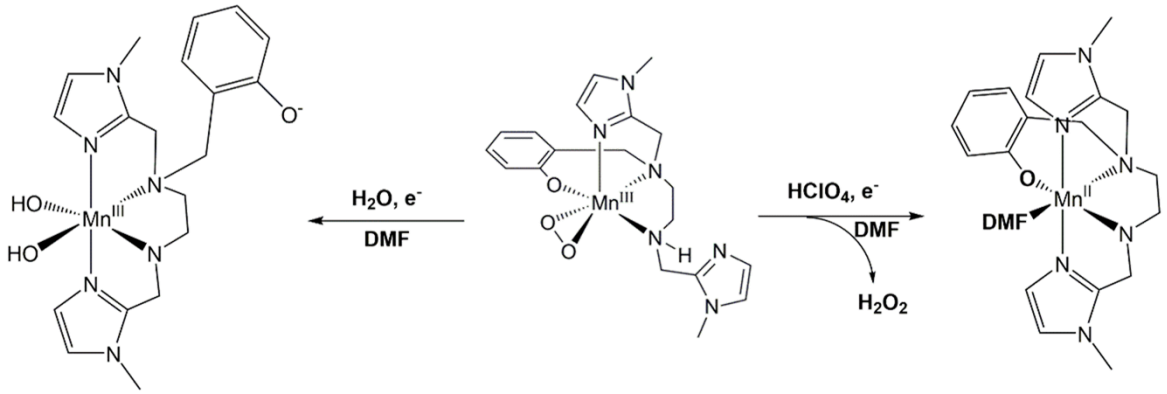

Scheme 1.10. The effect of acid strength on the reduction of $[Mn^{III}(O_2)(N_4O)]$.[112]

A report from Groves and coworkers in which an aqueous solution of $[Mn^{III}(TDMImP)]Cl$ is treated with H_2O_2 at 25°C to form high-valent Mn^{IV}- or Mn^{V}-oxo complexes proposes an end-on Mn^{III}-hydroperoxo species as an intermediate (TDMImP = 5,10,15,20-tetrakis-(1,3-dimethylimidazolium-2-yl)porphyrin).[113] The nature of the ligand trans to the hydroperoxo ligand was proposed to direct whether the O–O bond of the hydroperoxo ligand decayed via homolytic or heterolytic cleavage.[113] The formation of the end-on Mn^{III}-hydroperoxo complex $[Mn^{III}(OOH)(TMC)]^{2+}$ has also been reported to occur through the reaction of a side-on Mn^{III}-peroxo species with $HClO_4$ in MeCN at -40°C (Scheme 1.11). This spectroscopically characterized species is capable of performing both nucleophilic aldehyde deformylation and electrophilic oxygen atom- or hydrogen atom-transfer reactions.[114, 115]

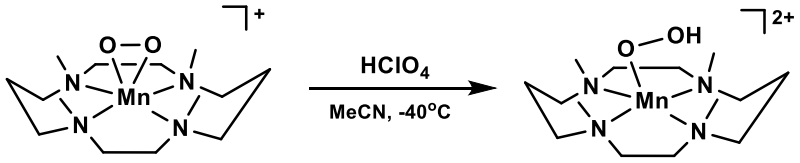

Scheme 1.11. The protonation of $[Mn^{III}(O_2)(TMC)]^{+}$ to yield $[Mn^{III}(OOH)(TMC)]^{2+}$.[114, 115]

1.7 Reactivity of Fe- and Mn-containing model complexes with alkylhydroperoxides.

The properties of Mn-alkyperoxo complexes have also been studied over the last 8 years, both for the relevance to enzymatic pathways and as analogues to end-on Mn^{III}-hydroperoxo complexes.[116-118] However, our understanding of these complexes remains very limited. The first synthetically isolated Mn-alkylperoxo complex was a Mn^{II}-alkylperoxo complex reported by Komatsuzaki and coworkers (Figure 1.5).[116] This species was generated through the addition of cumenylhydroperoxide (CmOOH) to a solution of [Mn^{II}(OH)($Tp^{tBu,iPr}$)] ($Tp^{tBu,iPr}$ = hydrotris(3-tert-butyl-5-iso-propyl-1-pyrazolyl)borate). Though the Mn^{II}-alkylperoxo complex was unstable at room temperature, a crystal structure was obtained for this Mn^{II}-alkylperoxo complex. The [Mn^{II}(OOCm)($Tp^{tBu,iPr}$)] complex was unreactive towards organic substrates.[116]

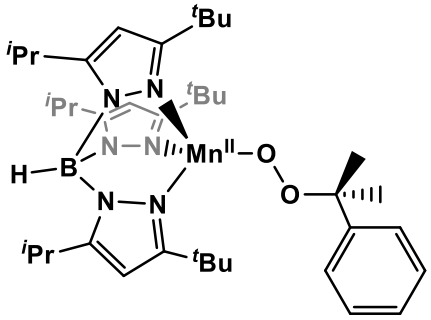

$Mn^{II}(OOCMe_2Ph)(Tp^{tBu,iPr})$

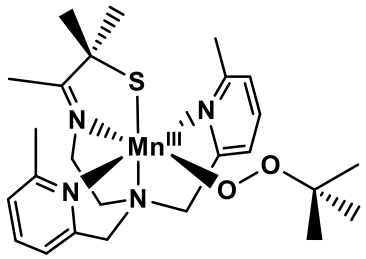

$[Mn^{III}(OO^tBu)(S^{Me2}N_4(6\text{-}MeDPEN))]^+$

Figure 1.5. Molecular structures of representative Mn^{II} and Mn^{III}-alkylperoxo complexes.

Kovacs and co-workers have used a series of N_4S^- ligands to generate an array of Mn^{III}-alkylperoxo complexes generated through the reaction of Mn^{II} complexes with 1.5 equivalents of either *tert*-butylhydroperoxide (^{t}BuOOH) or CmOOH in the presence of 2 equivalents of Et_3N (Figure 1.5).[117, 118] The Mn^{III}-alkylperoxo complexes have all been structurally characterized by X-ray crystallography, and feature a donating thiolate ligand *cis* to the η^1-alkylperoxo ligand, as well as two elongated Mn-N bonds *cis* to the alkylperoxo moiety (average distance of 2.46 Å).[117,

[118] Decreasing length of the elongated Mn-N bond correlated with increasing O–O bond length, consistent with electron donation from ligands giving rise to more activated O–O bonds.[118] An analysis of the organic decay products of two Mn^{III}-cumenylperoxo complexes provided strong evidence for O–O bond homolysis.[118] Further evidence for decay by O–O bond cleavage was provided by variable-temperature kinetic studies of the decay process. Both the enthalpy ($\Delta H^{\ddagger}$) and entropy ($\Delta S^{\ddagger}$) of activation for the decay process decreased with increasing O–O distance, while there was no trend between the activation parameters of decay and Mn–O bond length.[118] The Mn-based decay products could not be identified, although a black precipitate was observed and attributed to formation of a manganese oxide.

While our understanding of Mn-alkylperoxo complexes remains limited, the analogous Fe systems have been thoroughly investigated.[4, 10, 119-133] These complexes are thermally unstable, and have only been characterized spectroscopically. The pathway that these complexes decay through is dependent on spin state. In computational studies of $[Fe(TPA)(OH_x)(OO^tBu)]^{x+}$ (TPA = tris(2-pyridylmethyl)amine, x = 1 or 2), homolytic cleavage of the O–O bond in high-spin Fe^{III}-alkylperoxo complexes was calculated to be thermodynamically unfavorable, suggesting that Fe–O cleavage is a viable pathway for high-spin Fe^{III}-alkylperoxo complexes.[121] Likewise, Fe–O bond cleavage was found to be thermodynamically unfavorable for low-spin Fe^{III}-alkylperoxo complexes.[121] These computational findings were supported by resonance Raman studies of the Fe–O and O–O vibrations of both low-spin and high-spin complexes.[120, 121] The low-spin Fe^{III}-alklyperoxo complexes were found to generally have higher energy Fe–O vibrations and lower energy O–O vibrations than their high-spin analogues.[120, 121] Limited structural information has come from EXAFS analysis, but the available data also supports the difference in decay

mechanism between spin state.[129, 131] A high-spin Fe^{III}-alkylperoxo complex has been reported to have an Fe–O bond length of 1.88Å, while low-spin Fe^{III}-alkylperoxo species exhibit Fe–O bond lengths around 1.76-1.78 Å.[10, 120, 129, 131] Additional studies on Fe^{III}-alkylperoxo complexes have shown that the nature of the ligands *cis* to the alkylperoxo moiety have an effect on the spin state of the complex.[134] It was observed that methylation of the amine ligands *cis* to the alkylperoxo ligand, thereby weakening electron donation, results in a change in the spin state from a low-spin to a high-spin Fe^{III}-alkylperoxo complex.[134] Additionally, modification of the ligand *trans* to the alkylperoxo moiety was observed to have an effect on the Fe–O bond strength of low-spin Fe^{III}-alkylperoxo complexes.[123] Complexes featuring strongly donating thiol ligands *trans* to the alkylperoxo ligand exhibited weak Fe–O bonds in comparison to other low-spin Fe^{III}-alkylperoxo complexes.[123] The strength of the O–O bond was not affected.

Although there has been much work regarding the reactivity of Mn-containing enzymes and model complexes with O_2 and its derivatives, there remains a gap in our understanding of the mechanisms through which these important reactions occur. The few mechanisms that have been proposed often invoke the formation of intermediates that either lack characterization or remain unobserved. The work presented in the following chapters was carried out in an effort to add to the limited knowledge regarding some of these reactive pathways. The reactivity of $[Mn^{II}(dpaq)](OTf)$ and $[Mn^{II}(dpaq^{2Me})](OTf)$ with O_2 is more thoroughly explored, including mechanistic studies and an investigation into the effect of steric bulk on the O_2 activation pathway. Three new Mn^{III}-alkylperoxo complexes are reported, adding to the limited number of examples of this class of compounds. The reactivity of Mn^{III}-hydroxo complexes with H_2O_2 is explored as a possible route to the formation of a rare Mn^{III}-hydroperoxo complex.

1.8 References.

1. A. J. Jasniewski and L. Que, *Chem. Rev.*, 2018, **118**, 2554-2592.
2. E. I. Solomon, D. E. Heppner, E. M. Johnston, J. W. Ginsbach, J. Cirera, M. Qayyum, M. T. Kieber-Emmons, C. H. Kjaergaard, R. G. Hadt and L. Tian, *Chem. Rev.*, 2014, **114**, 3659-3853.
3. X. Huang and J. T. Groves, *Chem. Rev.*, 2018, **118**, 2491-2553.
4. A. Company, J. Lloret-Fillol and M. Costas, Elsevier B.V., 2013, pp. 487-564.
5. A. T. Fiedler and A. A. Fischer, *J. Biol. Inorg. Chem.*, 2017, **22**, 407-424.
6. A. J. Wu, J. E. Penner-Hahn and V. L. Pecoraro, *Chem. Rev.*, 2004, **104**, 903-938.
7. Y. Sheng, I. A. Abreu, D. E. Cabelli, M. J. Maroney, A.-F. Miller, M. Teixeira and J. S. Valentine, *Chem. Rev.*, 2014, **114**, 3854-3918.
8. A.-F. Miller, *Curr. Opin. Chem. Biol.*, 2004, **8**, 162-168.
9. D. F. Leto and T. A. Jackson, *J. Biol. Inorg. Chem.*, 2014, **19**, 1-15.
10. M. Costas, M. P. Mehn, M. P. Jensen and L. Que, *Chem. Rev.*, 2004, **104**, 939-986.
11. A. Wennman, S. Karkehabadi and E. H. Oliw, *Arch. Biochem. Biophys.*, 2014, **555-556**, 9-15.
12. A. Wennman, E. H. Oliw, S. Karkehabadi and Y. Chen, *J. Biol. Chem.*, 2016.
13. C. Su, M. Sahlin and E. H. Oliw, *J. Biol. Chem.*, 2000, **275**, 18830-18835.
14. C. Su and E. H. Oliw, *J. Biol. Chem.*, 1998, **273**, 13072-13079.
15. M. Hamberg, C. Su and E. Oliw, *J. Biol. Chem.*, 1998, **273**, 13080-13088.
16. J. J. A. Cotruvo and J. Stubbe, *Metallomics*, 2012, **4**, 1020-1036.
17. N. Cox, D. A. Pantazis, F. Neese and W. Lubitz, *Acc. Chem. Res.*, 2013, **46**, 1588-1596.
18. J. P. McEvoy and G. W. Brudvig, *Chem. Rev.*, 2006, **106**, 4455-4483.
19. V. K. Yachandra, K. Sauer and M. P. Klein, *Chem. Rev.*, 1996, **96**, 2927-2950.
20. D. J. Vinyard, G. M. Ananyev and G. C. Dismukes, *Annu. Rev. Biochem*, 2013, **82**, 577-606.
21. J. P. McEvoy, J. A. Gascon, V. S. Batista and G. W. Brudvig, *Photochem. Photobio. Sci.*, 2005, **4**, 940-949.
22. K. Sauer, *Acc. Chem. Res.*, 1980, **13**, 249-256.
23. D. B. Rice, A. A. Massie and T. A. Jackson, *Acc. Chem. Res.*, 2017, **50**, 2706-2717.
24. J. A. Kovacs, *Acc. Chem. Res.*, 2015, **48**, 2744-2753.
25. W. Nam, Y.-M. Lee and S. Fukuzumi, *Acc. Chem. Res.*, 2018, **51**, 2014-2022.
26. A. S. Borovik, *Acc. Chem. Res.*, 2005, **38**, 54-61.
27. W. Liu and J. T. Groves, *Acc. Chem. Res.*, 2015, **48**, 1727-1735.
28. C. W. Cady, R. H. Crabtree and G. W. Brudvig, *Coord. Chem. Rev.*, 2008, **252**, 444-455.
29. G. C. Dismukes, R. Brimblecombe, G. A. N. Felton, R. S. Pryadun, J. E. Sheats, L. Spiccia and G. F. Swiegers, *Acc. Chem. Res.*, 2009, **42**, 1935-1943.
30. M. D. Kärkäs, E. V. Johnston, O. Verho and B. Åkermark, *Acc. Chem. Res.*, 2014, **47**, 100-111.
31. C. S. Mullins and V. L. Pecoraro, *Coord. Chem. Rev.*, 2008, **252**, 416-443.
32. K. J. Young, B. J. Brennan, R. Tagore and G. W. Brudvig, *Acc. Chem. Res.*, 2015, **48**, 567-574.
33. D. G. Nocera, *Acc. Chem. Res.*, 2012, **45**, 767-776.
34. R. Hage and A. Lienke, *J. Mol. Catal. A: Chem.*, 2006, **251**, 150-158.

35. R. Hage and A. Lienke, *Angew. Chem. Int. Ed.*, 2006, **45**, 206-222.
36. B. S. Lane and K. Burgess, *Chem. Rev.*, 2003, **103**, 2457-2474.
37. A. K. Boal, J. A. Cotruvo, J. Stubbe and A. C. Rosenzweig, *Science*, 2010, **329**, 1526.
38. D. Svedružic, S. Jónsoon, C. G. Toyota, L. A. Reinhardt, S. Ricagno, Y. Lindqvist and N. G. J. Richards, *Arch. Biochem. Biophys.*, 2005, **433**, 176-192.
39. M. V. Dutton and C. S. Evans, *Can. J. Microbiol.*, 1996, **42**, 881-895.
40. A. Tanner, L. Bowater, S. A. Fairhurst and S. Bornemann, *J. Biol. Chem.*, 2001, **276**, 43627-43634.
41. T. Borowski, A. Bassan, N. G. J. Richards and P. E. M. Siegbahn, *J. Chem. Theory Comp.*, 2005, **1**, 686-693.
42. O. Opaleye, R.-S. Rose, M. M. Whittaker, E.-J. Woo, J. W. Whittaker and R. W. Pickersgill, *J. Biol. Chem.*, 2006, **281**, 6428-6433.
43. W. A. Gunderson, A. I. Zatsman, J. P. Emerson, E. R. Farquhar, L. Que, J. D. Lipscomb and M. P. Hendrich, *J. Am. Chem. Soc.*, 2008, **130**, 14465-14467.
44. J. D. Lipscomb, *Curr. Opin. Struct. Biol.*, 2008, **18**, 644-649.
45. M. H. Glickman and J. P. Klinman, *Biochem.*, 1995, **34**, 14077-14092.
46. E. Skrzypczak-Jankun, R. A. Bross, R. T. Carroll, W. R. Dunham and M. O. Funk, *J. Am. Chem. Soc.*, 2001, **123**, 10814-10820.
47. E. G. Kovaleva, M. B. Neibergall, S. Chakrabarty and J. D. Lipscomb, *Acc. Chem. Res.*, 2007, **40**, 475-483.
48. N. Lehnert and E. I. Solomon, *JBIC Journal of Biological Inorganic Chemistry*, 2003, **8**, 294-305.
49. Y. Sheng, E. Butler Gralla, M. Schumacher, D. Cascio, D. E. Cabelli and J. Selverstone Valentine, *Proc. Natl. Acad. Sci.*, 2012, **109**, 14314.
50. C. Bull, E. C. Niederhoffer, T. Yoshida and J. A. Fee, *J. Am. Chem. Soc.*, 1991, **113**, 4069-4076.
51. A. S. Hearn, C. K. Tu, H. S. Nick and D. N. Silverman, *J. Biol. Chem.*, 1999, **274**, 24457-24460.
52. A. S. Hearn, M. E. Stroupe, D. E. Cabelli, J. R. Lepock, J. A. Tainer, H. S. Nick and D. N. Silverman, *Biochem.*, 2001, **40**, 12051-12058.
53. T. A. Jackson, A. Karapetian, A.-F. Miller and T. C. Brunold, *Biochem.*, 2005, **44**, 1504-1520.
54. I. A. Abreu, J. A. Rodriguez and D. E. Cabelli, *J. Phys. Chem. B*, 2005, **109**, 24502-24509.
55. R. Carrasco, I. Morgenstern-Badarau and J. Cano, *Inorg. Chim. Acta*, 2007, **360**, 91-101.
56. J. Porta, A. Vahedi-Faridi and G. E. O. Borgstahl, *J. Mol. Biol.*, 2010, **399**, 377-384.
57. T. A. Jackson, A. Karapetian, A.-F. Miller and T. C. Brunold, *Biochem.*, 2005, **44**, 1504-1520.
58. P. Saisaha, J. W. d. Boer and W. R. Browne, *Chem. Soc. Rev.*, 2013, **42**, 2059-2074.
59. E. V. Rybak-Akimova, in *Physical Inorganic Chemistry*, ed. A. Bakac, John Wiley and Sons, Inc., Hoboken, NJ, 2010, ch. Mechanisms of Oxygen Binding and Activation at Transition Metal Centers., pp. 109-188.
60. V. L. Pecoraro, M. J. Baldwin and A. Gelasco, *Chem. Rev.*, 1994, **94**, 807-826.
61. R. L. Shook, S. M. Peterson, J. Greaves, C. Moore, A. L. Rheingold and A. S. Borovik, *J. Am. Chem. Soc.*, 2011, **133**, 5810-5817.

62. M. K. Coggins, L. M. Brines and J. M. Kovacs, *Inorg. Chem.*, 2013, **52**, 12383-12393.
63. G. C. Wijeratne, B.; Day, V. W.; Jackson, T. A., *Inorg. Chem.*, 2014, **53**, 7622-7634.
64. P. Battioni, J. F. Bartoli, P. Leduc, M. Fontecave and D. Mansuy, *Chem. Comm.*, 1987, 791-792.
65. C. P. Horwitz, S. E. Creager and R. W. Murray, *Inorg. Chem.*, 1990, **29**, 1006-1011.
66. C. Zhang, Z. Xu, T. Shen, G. Wu, L. Zhang and N. Jiao, *Org. Lett.*, 2012, **14**, 2362-2365.
67. J. Christoffers, *J. Org. Chem.*, 1999, **64**, 7668-7669.
68. Y. Nishida, N. Tanaka, A. Yamazaki, T. Tokii, N. Hashimoto, K. Ide and K. Iwasawa, *Inorg. Chem.*, 1995, **34**, 3616-3620.
69. H. Komatsuzaki, Y. Nagasu, K. Suzuki, T. Shibasaki, M. Satoh, F. Ebina, S. Hikichi, M. Akita and Y. Moro-oka, *J. Chem. Soc., Dalton Trans.*, 1998, 511-512.
70. C. P. Horwitz and G. C. Dailey, *Comments Inorg. Chem.*, 1993, **14**, 283-319.
71. C. P. Horwitz, P. J. Winslow, J. T. Warden and C. A. Lisek, *Inorg. Chem.*, 1993, **32**, 82-88.
72. Z. Shirin, A. S. Borovik and V. G. Young Jr, *Chem. Comm.*, 1997, 1967-1968.
73. M. K. Coggins, X. Sun, Y. Kwak, E. I. Solomon, E. Rybak-Akimova and J. A. Kovacs, *J. Am. Chem. Soc.*, 2013, **135**, 5631-5640.
74. D. C. R. Brazzolotto, Fabian G.; Smith-Jones, Julian; Retegan, Marius; Amidani, Lucia; Faponle, Abayomi S.; Ray, Kallol; Philouze, Christian; de Visser, Sam P.; Gennari, Marcello; Duboc, Carole, *Angew. Chem.*, 2017, **56**, 8211-8215.
75. M. K. Coggins, S. Toledo, E. Shaffer, W. Kaminsky, J. Shearer and J. A. Kovacs, *Inorg. Chem.*, 2012, **51**, 6633-6644.
76. M. Gennari, D. Brazzolotto, J. Pecaut, M. V. Cherrier, C. J. Pollock, S. DeBeer, M. Retegan, D. A. Pantazis, F. Neese, M. Rouzieres, R. Clerac and C. Duboc, *J. Am. Chem. Soc.*, 2015, **137**, 8644-8653.
77. W.-Y. W. Chien-Ming Lee, Ming-Hsi Chiang, D. Scott Bohle, Gene-Hsiang Lee, *Inorg. Chem.*, 2017, **56**, 10559-10569.
78. J. A. Rees, V. Martin-Diaconescu, J. A. Kovacs and S. DeBeer, *Inorg. Chem.*, 2015, **54**, 6410-6422.
79. C.-M. Lee, C.-H. Chuo, C.-H. Chen, C.-C. Hu, M.-H. Chiang, Y.-J. Tseng, C.-H. Hu and G.-H. Lee, *Angew. Chem. Int. Ed.*, 2012, **51**, 5427-5430.
80. D. B. Rice, G. B. Wijeratne, A. D. Burr, J. D. Parham, V. W. Day and T. A. Jackson, *Inorg. Chem.*, 2016, **55**, 8110-8120.
81. D. B. Rice, S. D. Jones, J. T. Douglas and T. A. Jackson, *Inorganic Chemistry*, 2018, DOI: 10.1021/acs.inorgchem.8b00917.
82. D. B. Rice, A. Munasinghe, E. N. Grotemeyer, A. D. Burr, V. W. Day and T. A. Jackson, *Inorg. Chem.*, 2019, **58**, 622-636.
83. R. B. VanAtta, C. E. Strouse, L. K. Hanson and J. S. Valentine, *J. Am. Chem. Soc.*, 1987, **109**, 1425-1434.
84. N. Kitajima, H. Komatsuzaki, S. Hikichi, M. Osawa and Y. Moro-oka, *J. Am. Chem. Soc.*, 1994, **116**, 11596-11597.
85. U. P. Singh, A. K. Sharma, S. Hikichi, H. Komatsuzaki, Y. Moro-oka and M. Akita, *Inorg. Chim. Acta*, 2006, **359**, 4407-4411.
86. H. E. Colmer, R. A. Geiger, D. F. Leto, G. B. Wijeratne, V. W. Day and T. A. Jackson, *Dalton Trans.*, 2014, **43**, 17949-17963.

87. J. Cho, R. Sarangi and W. Nam, *Acc. Chem. Res.*, 2012, **45**, 1321-1330.
88. M. S. Seo, J. Y. Kim, J. Annaraj, Y. Kim, Y.-M. Lee, S.-J. Kim, J. Kim and W. Nam, *Angew. Chem. Int. Ed.*, 2007, **46**, 377-380.
89. H. Kang, J. Cho, K.-B. Cho, T. Nomura, T. Ogura and W. Nam, *Chem. Eur*, 2013, **19**.
90. J. Annaraj, J. Cho, Y.-M. Lee, S. Y. Kim, R. Latifi, S. P. de Visser and W. Nam, *Angew. Chem. Int. Ed.*, 2009, **48**, 4150-4153.
91. R. A. Geiger, D. F. Leto, S. Chattopadhyay, P. Dorlet, E. Anxolabéhère-Mallart and T. A. Jackson, *Inorg. Chem.*, 2011, **50**, 10190-10203.
92. M. C. Denler, G. B. Wijeratne, D. B. Rice, H. E. Colmer, V. W. Day and T. A. Jackson, *Dalton Trans.*, 2018, **47**, 13442-13458.
93. S. Groni, G. Blain, R. Guillot, C. Policar and E. Anxolabéhère-Mallart, *Inorg. Chem.*, 2007, **46**, 1951-1953.
94. S. Groni, P. Dorlet, G. Blain, S. Bourcier, R. Guillot and E. Anxolabéhère-Mallart, *Inorg. Chem.*, 2008, **47**, 3166-3172.
95. R. A. Geiger, S. Chattopadhyay, V. W. Day and T. A. Jackson, *J. Am. Chem. Soc.*, 2010, **132**, 2821-2831.
96. R. A. Geiger, G. Wijeratne, V. W. Day and T. A. Jackson, *Eur. J. Inorg. Chem.*, 2012, 1598-1608.
97. J. Du, C. Miao, C. Xia and W. Sun, *Chin. Chem. Lett.*, 2018, **29**, 1869-1871.
98. J. Du, D. Xu, C. Zhang, C. Xia, Y. Wang and W. Sun, *Dalton Trans.*, 2016, **45**, 10131-10135.
99. H. E. Colmer, A. W. Howcroft and T. A. Jackson, *Inorg. Chem.*, 2016, **55**, 2055-2069.
100. P. Barman, P. Upadhyay, A. S. Faponle, J. Kumar, S. S. Nag, D. Kumar, C. V. Sastri and S. P. de Visser, *Angew. Chem. Int. Ed.*, 2016, **55**, 11091-11095.
101. M. F. Sisemore, M. Selke, J. N. Burstyn and J. S. Valentine, *Inorg. Chem.*, 1997, **36**, 979-984.
102. R. A. Geiger, S. Chattopadhyay, V. W. Day and T. A. Jackson, *Dalton Trans.*, 2011, **40**.
103. R. L. Shook, W. A. Gunderson, J. Greaves, J. W. Ziller, M. P. Hendrich and A. S. Borovik, *J. Am. Chem. Soc.*, 2008, **130**, 8888-8889.
104. R. L. Shook and A. S. Borovik, *Inorg. Chem.*, 2010, **49**, 3646-3660.
105. D. F. Leto, S. Chattopadhyay, V. W. Day and T. A. Jackson, *Dalton Trans.*, 2013, **42**, 13014.
106. S. Mukhopadhyay, S. K. Mandal, S. Bhaduri and W. H. Armstrong, *Chem. Rev.*, 2004, **104**, 3981-4026.
107. H. Chen, R. Tagore, S. Das, C. Incarvito, J. W. Faller, R. H. Crabtree and G. W. Brudvig, *Inorg. Chem.*, 2005, **44**, 7661-7670.
108. L. Dubois, L. Jacquamet, J. Pecaut and J.-M. Latour, *Chem. Comm.*, 2006, DOI: 10.1039/B609072A, 4521-4523.
109. S. Schindler, O. Walter, J. Z. Pedersen and H. Toftlund, *Inorg. Chim. Acta*, 2000, **303**, 215-219.
110. P. A. Goodson, J. Glerup, D. J. Hodgson, K. Michelsen and H. Weihe, *Inorg. Chem.*, 1991, **30**, 4909-4914.
111. Y. Lee and T. A. Jackson, *Chem. Sel.*, 2018, **3**, 13507-13516.
112. H. Y. V. Ching, Anxolabe´he`re-Mallart, H. E. Colmer, C. Constentin, P. Dorlet, T. A. Jackson, C. Policar and M. Robert, *Chem. Sci.*, 2014, **5**.

113. N. Jin, D. E. Lahaye and J. T. Groves, *Inorg. Chem.*, 2010, **49**, 11516-11524.
114. M. Sankaralingam, Y.-M. Lee, S. H. Jeon, M. S. Seo, K.-B. Cho and W. Nam, *Chem. Comm.*, 2018, **54**, 1209-1212.
115. H. So, J.-H. Park, K.-B. Cho, Y.-M. Lee, M. S. Seo, J. Cho, R. Sarangi and W. Nam, *J. Am. Chem. Soc.*, 2014, **136**, 12229−12232.
116. H. Komatsuzaki, N. Sakamoto, M. Satoh, S. Hikichi, M. Akita and Y. Moro-oka, *Inorg. Chem.*, 1998, **37**, 6554-6555.
117. M. K. Coggins and J. A. Kovacs, *J. Am. Chem. Soc.*, 2011, **133**, 12470-12473.
118. M. K. Coggins, V. Martin-Diaconescu, S. DeBeer and J. A. Kovacs, *J. Am. Chem. Soc.*, 2013, **135**.
119. J. Kim, E. Larka, E. C. Wilkinson and L. Que Jr, *Angew. Chem. Int. Ed.*, 1995, **34**, 2048-2051.
120. N. Lehnert, R. Y. N. Ho, L. Que and E. I. Solomon, *J. Am. Chem. Soc.*, 2001, **123**, 8271-8290.
121. N. Lehnert, R. Y. N. Ho, L. Que and E. I. Solomon, *J. Am. Chem. Soc.*, 2001, **123**, 12802-12816.
122. J.-U. Rohde, S. Torelli, X. Shan, M. H. Lim, E. J. Klinker, J. Kaizer, K. Chen, W. Nam and L. Que, Jr., *J. Am. Chem. Soc.*, 2004, **126**, 16750-16761.
123. F. Namuswe, G. D. Kasper, A. A. N. Sarjeant, T. Hayashi, C. M. Krest, M. T. Green, P. Moënne-Loccoz and D. P. Goldberg, *J. Am. Chem. Soc.*, 2008, **130**, 14189-14200.
124. Y. Zang, T. E. Elgren, Y. Dong and L. Que, *J. Am. Chem. Soc.*, 1993, **115**, 811-813.
125. S. Hong, Y.-M. Lee, K.-B. Cho, M. S. Seo, D. Song, J. Yoon, R. Garcia-Serres, M. Clémancey, T. Ogura, W. Shin, J.-M. Latour and W. Nam, *Chem. Sci.*, 2014, **5**, 156-162.
126. M. P. Jensen, A. M. i. Payeras, A. T. Fiedler, M. Costas, J. Kaizer, A. Stubna, E. Münck and L. Que, *Inorg. Chem.*, 2007, **46**, 2398-2408.
127. D. Krishnamurthy, G. D. Kasper, F. Namuswe, W. D. Kerber, A. A. Narducci Sarjeant, P. Moënne-Loccoz and D. P. Goldberg, *J. Am. Chem. Soc.*, 2006, **128**, 14222-14223.
128. T. Ogihara, S. Hikichi, M. Akita, T. Uchida, T. Kitagawa and Y. Moro-oka, *Inorg. Chim. Acta*, 2000, **297**, 162-170.
129. X. Shan, J.-U. Rohde, K. D. Koehntop, Y. Zhou, M. R. Bukowski, M. Costas, K. Fujisawa and L. Que, *Inorg. Chem.*, 2007, **46**, 8410-8417.
130. A. P. Sobolev, D. E. Babushkin and E. P. Talsi, *J. Mol. Catal. A: Chem.*, 2000, **159**, 233-245.
131. J. Stasser, F. Namuswe, G. D. Kasper, Y. Jiang, C. M. Krest, M. T. Green, J. Penner-Hahn and D. P. Goldberg, *Inorg. Chem.*, 2010, **49**, 9178-9190.
132. A. Wada, S. Ogo, Y. Watanabe, M. Mukai, T. Kitagawa, K. Jitsukawa, H. Masuda and H. Einaga, *Inorg. Chem.*, 1999, **38**, 3592-3593.
133. L. R. Widger, Y. Jiang, A. C. McQuilken, T. Yang, M. A. Siegler, H. Matsumura, P. Moënne-Loccoz, D. Kumar, S. P. de Visser and D. P. Goldberg, *Dalton Trans.*, 2014, **43**, 7522-7532.
134. F. Namuswe, T. Hayashi, Y. Jiang, G. D. Kasper, A. A. N. Sarjeant, P. Moënne-Loccoz and D. P. Goldberg, *J. Am. Chem. Soc.*, 2010, **132**, 157-167.

Chapter 2:

Steric Control of Dioxygen Activation Pathways for Mn^{II} Complexes Supported by Pentadentate, Amide-containing Ligands

2.1 Introduction.

Dioxygen activation at metal centers is widespread in biology.[1-4] Mn enzymes that require dioxygen for activity include manganese-dependent homoprotocatechuate 2,3-dioxygenase (HPCD),[5, 6] manganese lipoxygenase,[7-11] and the oxalate-degrading enzymes oxalate oxidase[12, 13] and oxalate decarboxylase.[14, 15] Synthetic transition metal complexes have proven to be a valuable tool for understanding and modeling the reactivity observed for nature's metalloenzymes. Much work has been done regarding O_2 activation by Fe and Cu systems,[16, 17] but examples of Mn^{II} complexes that can activate dioxygen to give isolable products are relatively uncommon. Several of the systems that are capable of dioxygen activation perform catalytic organic substrate oxidation using O_2.[18-26] The mechanistic details of many of these catalysts remain unclear.[21, 24, 25, 27]

There have been a small number of Mn^{II} complexes for which a mechanism of dioxygen activation has been proposed.[11, 28-31] Among these systems, it is commonly proposed that Mn^{II} complexes bind O_2 to initially form a Mn^{III}-superoxo adduct that is trapped by a second Mn^{II} complex to generate a peroxodimanganese(III, III) species (Scheme 1).[28, 29, 32] Each mechanism invokes O−O homolysis of the peroxodimanganese(III, III) intermediate to generate mononuclear Mn^{IV}-oxo adducts (Scheme 1).[28, 31] These high-valent Mn^{IV} complexes serve as the point of divergence between the reported mechanisms.[28-30] The $[Mn^{II}(1^{cyp})]^-$ complex reported by Borovik et al. invokes a hydrogen-atom transfer step, in which the proposed Mn^{IV}-oxo complex abstracts a hydrogen atom from solvent to give the Mn^{III}-hydroxo product.[28] The Kovacs report proposes a comproportionation reaction between the Mn^{IV}-oxo species and residual Mn^{II} complex in solution to yield a (μ-oxo)dimanganese(III, III) product.[29, 30, 32, 33] In the presence of water, the (μ-oxo)dimanganese(III, III) product can be hydrolyzed to give a mononuclear Mn^{III}-hydroxo species.

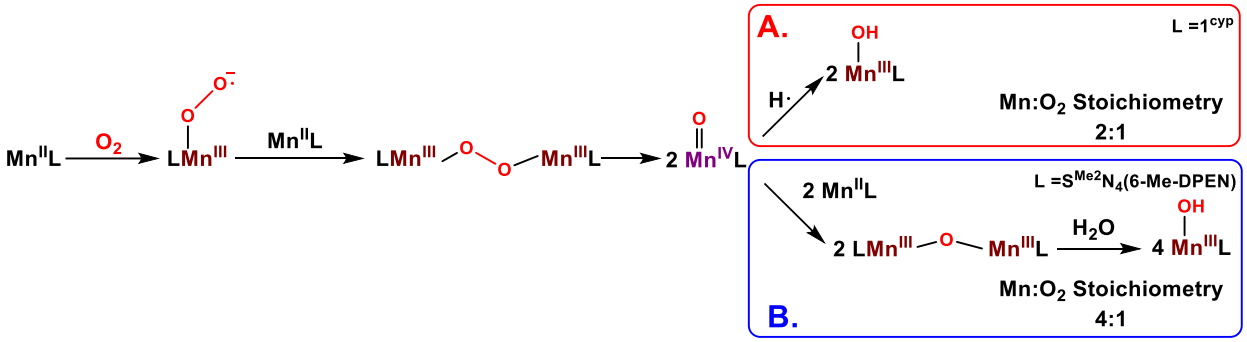

Scheme 1. Proposed mechanisms for the reaction of Mn^{II} complexes with O_2 to generate Mn^{III}-hydroxo species. Ligand abbreviations are as follows: 1^{cyp} = tris(N-cyclopentylcarbamoylmethyl)amine; $S^{Me2}N_4$(6-Me-DPEN) = (E)-3-((2-(bis((6-methylpyridin-2-yl)methyl)amino)ethyl)imino)-2-methylbutane-2-thiolate)

In this study, we have performed O_2 titrations, substrate trapping experiments, and isotopic labeling studies to evaluate the O_2 activation mechanisms of the [Mn^{II}(dpaq)](OTf) and [Mn^{II}(dpaq^{2Me})](OTf) complexes. The O_2 titrations revealed that dioxygen activation by [Mn^{II}(dpaq)](OTf) and [Mn^{II}(dpaq^{2Me})]$^+$ proceeds by different Mn:O_2 stoichiometries. Specifically, [Mn^{II}(dpaq)](OTf) operates according to a Mn:O_2 stoichiometry of 4:1 while [Mn^{II}(dpaq^{2Me})]$^+$ operates with a Mn:O_2 stoichiometry of 2:1. Dioxygen activation experiments for [Mn^{II}(dpaq)](OTf) in deuterated solvent showed complete formation of the unlabeled Mn^{III}–OH product, suggesting that hydrogen-atom abstraction from solvent is not involved in the O_2-activation pathway of this complex. In contrast, when the [Mn^{II}(dpaq^{2Me})](OTf) complex, which features a bulkier supporting ligand, was treated with dioxygen in deuterated solvent, we observed the Mn^{III}–OD product, indicative of an alternative dioxygen-activation pathway involving hydrogen-atom abstraction from solvent. These results demonstrate that subtle changes in the steric properties of the supporting ligand can influence the O_2 activation pathway of Mn^{II} complexes.

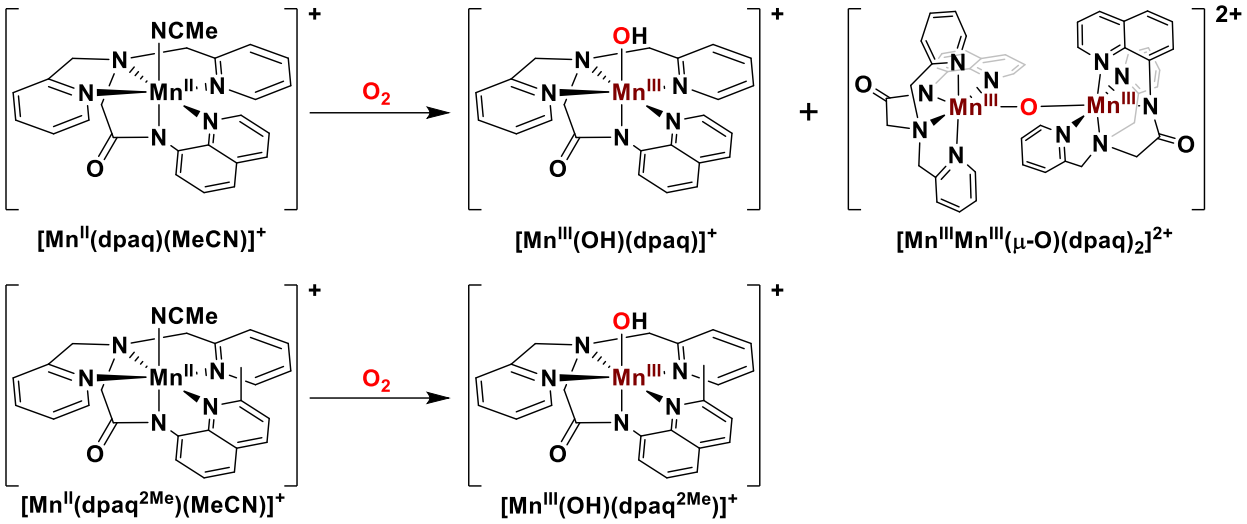

Scheme 2. $[Mn^{II}(dpaq)(MeCN)]^+$ reacts with O_2, presumably to produce a (μ-oxo)dimanganese(III, III) complex that can be hydrolyzed by H_2O and yield the monomeric $[Mn^{III}(OH)(dpaq)]^+$ (top).[34] $[Mn^{II}(dpaq^{2Me})(MeCN)]^+$ does not show formation of a (μ-oxo)dimanganese(III, III) complex in the reaction with O_2, instead only forming $[Mn^{III}(OH)(dpaq^{2Me})]^+$ (bottom).

2.2 Experimental.

Materials and Instrumentation. All chemicals were used as obtained from commercial sources unless noted otherwise. Acetonitrile, diethyl ether, and methanol were dried and degassed using a PureSolv Micro solvent purification system. This drying procedure results in MeCN that, on average, contains 64(8) ppm (or 3.6 mM) H_2O. The O_2 gas used was >99% pure and further purified by passing through a column packed with drierite and 5 Å molecular sieves. $[Mn^{II}(dpaq)](OTf)$ and $[Mn^{II}(dpaq^{2Me})](OTf)$ were synthesized and characterized as reported previously.[20, 35] Electronic absorption experiments were performed using a Varian Cary 50 Bio UV-Visible spectrophotometer. Electrospray ionization-mass spectrometry (ESI-MS) experiments were performed using an LCT Premier MicroMass electrospray time-of-flight instrument. ^1H and ^{31}P NMR spectra were obtained on a Bruker DRX 400 MHz NMR spectrometer. Gas

chromatography-mass spectrometry (GC-MS) experiments were performed with a Quattro Micro GC quadrupole mass analyzer via an Agilent 6890 N gas chromatograph.

Determination of manganese:oxidant stoichiometry in Mn^{III}-hydroxo formation from [Mn^{II}(dpaq)](OTf) or [Mn^{II}($dpaq^{2Me}$)](OTf) and O_2. Solutions of [Mn^{II}(dpaq)](OTf) or [Mn^{II}($dpaq^{2Me}$)](OTf) (6 mM in MeCN) were prepared under an argon atmosphere in a glove box. The solutions were sealed in quartz cuvettes with pierceable septa. In a separate vial, dried MeCN was saturated with O_2 by bubbling the gas through the solvent after running the gas through a 20 cm column packed with drierite and 5 Å molecular sieves. Although the O_2 was passed through drying materials, this procedure did not remove all the H_2O. Karl-Fischer titrations of a 4 mL MeCN solution with a Mettler Toledo DL39 coulometric titrator of a MeCN solution following a 30 minute O_2 purge showed a water content of 2352(4) ppm (or 131 mM), an increase of 368% relative to dried MeCN. This amounts to 0.1 – 1 equivalents of H_2O being introduced to the system in this manner. The concentration of O_2 in saturated MeCN is known to be 8.1 mM at 25˚C.[36] Measured amounts of saturated solvent were added to the solutions of [Mn^{II}(dpaq)](OTf) or [Mn^{II}($dpaq^{2Me}$)](OTf) using gastight syringes to deliver 0.1, 0.18, 0.25, 0.5, or 1 equivalents of O_2 relative to Mn^{II} concentration. This resulted in 0.1 – 1 equivalents of H_2O relative to the Mn concentration being introduced to the system. Additionally, 400 equivalents of H_2O were added to the solutions of [Mn^{II}(dpaq)](OTf) to ensure formation of the monomeric [Mn^{III}(OH)(dpaq)](OTf).[37] The reactions were monitored by electronic absorption spectroscopy at 25˚C until the spectra ceased to change (typically ~4 hours). The percent formation of [Mn^{III}(OH)(dpaq)](OTf) or [Mn^{III}(OH)($dpaq^{2Me}$)](OTf) was determined by exposing the reaction mixtures to additional O_2 (i.e., opening the solutions to atmosphere) until full formation of the

Mn^{III}-hydroxide species was achieved (~18 hours), upon which absorption spectra were obtained and compared to those obtained from the titrations.

Reactions between [Mn^{II}(dpaq)](OTf) or [Mn^{II}($dpaq^{2Me}$)](OTf) and O_2 in deuterated solvent. 6 mM solutions of [Mn^{II}(dpaq)](OTf) or [Mn^{II}($dpaq^{2Me}$)](OTf) in deuterated d_3-MeCN were prepared under an inert atmosphere in a glove box. The solutions were sealed in vials with pierceable septa. 1 equivalent of O_2 was added to the solution via measured amounts of saturated solvent with a gas-tight syringe. The reactions were allowed to stir overnight, and the resulting solutions were analyzed by ESI-MS.

Reactions between [Mn^{II}(dpaq)](OTf) or [Mn^{II}($dpaq^{2Me}$)](OTf) and O_2 in the presence of PPh_3. 6 mM solutions of [Mn^{II}($dpaq^{2Me}$)](OTf) with 50 equivalents of PPh_3 in d_3-MeCN were prepared. Excess O_2 gas was added via syringe, and the reaction was allowed to stir for 3 hours at 25˚C. Following the reaction, the solvent was removed and the organic products were dissolved in diethyl ether. The colorless solution was filtered through a syringe filter. Product analysis was performed by GC-MS and ^{31}P NMR, and signals were compared to authentic samples of PPh_3 and O=PPh_3.

Reactions between [Mn^{II}(dpaq)](OTf) or [Mn^{II}($dpaq^{2Me}$)](OTf) and O_2 in the presence of hydrocarbon substrates. 6 mM solutions of [Mn^{II}(dpaq)](OTf) or [Mn^{II}($dpaq^{2Me}$)](OTf) with 250 equivalents of cyclohexane, *cis*-dimethylcylohexane, cyclooctane, or ethylbenzene in d_3-MeCN were prepared and sealed in vials with pierceable septa. Reactions exploring the oxidation of toluene were carried out in a 1:1 mixture of toluene and d_3-MeCN. Excess O_2 gas was introduced to each solution via syringe, and the reactions were allowed to stir for 3 hours at 25˚C. Following the reaction, the solutions were passed through a silica plug and eluted with 2 mL of d_3-MeCN or deuterated chloroform. Product analysis was performed by ^{1}H-NMR using naphthalene as an internal standard.

The oxidation of 9,10-dihydroanthracene (DHA) was performed in a similar manner by preparing 6 mM solutions of [Mn^{II}(dpaq)](OTf) or [Mn^{II}($dpaq^{2Me}$)](OTf) in d_3-MeCN and adding 100 equivalents of DHA that had been dissolved in the minimal amount of dichloromethane. The vials were sealed with pierceable septa, excess O_2 was added via syringe, and the reactions were allowed to stir for three hours. The reaction mixtures were passed through silica plugs and eluted with dichloromethane. The solvent was removed and product analysis was performed by ^{1}H NMR in $CDCl_3$ with 1,4-benzoquinone as a quantitative reference. ESI-MS experiments were also performed following a reaction between [Mn^{II}(dpaq)](OTf) or [Mn^{II}($dpaq^{2Me}$)](OTf) and DHA in the presence of 1 equivalent of O_2 (delivered via saturated solvent in a gas-tight syringe) in d_3-MeCN.

Reactions between [Mn^{III}(OH)(dpaq)](OTf) or [Mn^{III}(OH)($dpaq^{2Me}$)](OTf) and 9,10-dihydroanthracene in the presence of O_2. 6 mM solutions of [Mn^{II}(dpaq)](OTf) or [Mn^{II}($dpaq^{2Me}$)](OTf) in d_3-MeCN were prepared, and 100 equivalents of DHA that had been dissolved in the minimal amount of dichloromethane was added. The vials were sealed with pierceable septa, excess O_2 was added via syringe, and the reactions were allowed to stir for three hours. The reaction mixtures were passed through silica plugs and eluted with dichloromethane. The solvent was removed and product analysis was performed by ^{1}H NMR in $CDCl_3$ with 1,4-benzoquinone as a quantitative reference.

Reactions between [Mn^{III}(OH)(dpaq)](OTf) or [Mn^{III}(OH)($dpaq^{2Me}$)](OTf) and 9,10-dihydroanthracene in the absence of O_2. 6 mM solutions of [Mn^{II}(dpaq)](OTf) or [Mn^{II}($dpaq^{2Me}$)](OTf) in d_3-MeCN were prepared under inert atmosphere in vials sealed with pierceable septa, and 100 equivalents of DHA that had been dissolved in the minimal amount of dichloromethane was added. The reactions were allowed to stir for three hours. The reaction

mixtures were passed through silica plugs and eluted with dichloromethane. The solvent was removed and product analysis was performed by ^{1}H NMR in $CDCl_3$ with 1,4-benzoquinone as a quantitative reference.

Reactions between [Mn^{II}(dpaq)](OTf) or [Mn^{II}(dpaq^{2Me})](OTf) and excess iodosylbenzene. A 1.5 mM solution of [Mn^{II}(dpaq)](OTf) in MeOH was prepared under an inert atmosphere in a glove box. The solution was transferred to a quartz cuvette and sealed with a pierceable septum. In a separate vial, 20 equivalents of PhIO were dissolved in minimal MeOH, and the vial was sealed with a pierceable septum. The PhIO solution was added to the cuvette at -40˚C, and the reaction monitored by electronic absorption spectroscopy.

Determination of manganese:oxidant stoichiometry in Mn^{III}-methoxy formation from [Mn^{II}(dpaq)](OTf) or [Mn^{II}(dpaq^{2Me})](OTf) and iodosylbenzene. Solutions of [Mn^{II}(dpaq)](OTf) or [Mn^{II}(dpaq^{2Me})](OTf) (2 mM in MeOH) were prepared under an argon atmosphere in a glove box. The solutions were sealed in quartz cuvettes with pierceable septa. In a separate vial, a 9 mM solution of PhIO in MeOH was prepared and sealed with a pierceable septum. Measured amounts of the PhIO solution were added to the solutions of [Mn^{II}(dpaq)](OTf) and [Mn^{II}(dpaq^{2Me})](OTf) using gas tight syringes to deliver 0.1, 0.25, or 0.5 equivalents of PhIO, and the reactions were allowed to stir for 2 hours. After the reactions were complete, absorption spectra were obtained. The percent formations of [Mn^{III}(OMe)(dpaq)]$^+$ and [Mn^{III}(OMe)(dpaq^{2Me})]$^+$ were determined by adding excess PhIO (up to 1 equivalent) to the reaction cuvettes, accounting for dilution, and comparing the absorption spectra to those of the titrations.

Reactions of [Mn^{II}(dpaq)](OTf) and [Mn^{II}(dpaq^{2Me})](OTf) with iodosylbenzene in MeCN. 2 mM solutions of [Mn^{II}(dpaq)](OTf) or [Mn^{II}(dpaq^{2Me})](OTf) in MeCN were prepared under an argon atmosphere in a glove box. The solutions were transferred to quartz cuvettes and sealed with

pierceable septa. In separate vials, 0.5 equivalents of PhIO were suspended in 100 μL of MeCN under an argon atmosphere in a glove box. The vials were subsequently sealed with pierceable septa and sonicated. While monitoring via electronic absorption spectroscopy, the PhIO was transferred to each quartz cuvette containing the solution of $[Mn^{II}(dpaq)](OTf)$ or $[Mn^{II}(dpaq^{2Me})](OTf)$ using a gastight syringe, and the reactions were stirred until the spectra ceased to change. ^{1}H NMR samples were prepared from similar reactions performed in deuterated MeCN. 2 mM solutions of $[Mn^{II}(dpaq)](OTf)$ or $[Mn^{II}(dpaq^{2Me})](OTf)$ in deuterated MeCN were prepared in vials under argon atmosphere in a glove box. Solid PhIO was added to each solution (0.5 equivalents), which were allowed to stir for two hours. An NMR sample was prepared by transferring ~500 μL of the solution following the reaction into an NMR tube and subsequently sealing the tube with a septum.

2.3 Results and Analysis.

Formation of $[Mn^{III}(OH)(dpaq)](OTf)$ from the reaction of $[Mn^{II}(dpaq)](OTf)$ with O_2. Titration experiments were performed to determine the Mn:O_2 stoichiometry for the reaction of $[Mn^{II}(dpaq)](OTf)$ and O_2 to generate the $[Mn^{III}(OH)(dpaq)](OTf)$ complex. A potential complication in these experiments is the equilibrium between $[Mn^{III}(OH)(dpaq)](OTf)$ and $[Mn^{III}Mn^{III}(\mu\text{-}O)(dpaq)_2]^{2+}$ (Scheme 2).[34] We addressed this complication by adding 400 equivalents of N_2-sparged H_2O to each sample, based on previous investigations that demonstrated that the addition of 400 equivalents of water caused the equilibrium to shift such that $[Mn^{III}(OH)(dpaq)](OTf)$ is the only species observed by ^{1}H-NMR spectroscopy.[34]

As the concentration of O_2 in saturated MeCN is known (8.1 mM at 25˚C),[36] the addition of O_2-saturated solvent is a convenient method for accurate O_2 delivery. Aliquots of MeCN solutions containing 0.1, 0.18, 0.25, 0.5, and 1 equivalents of O_2 were added to $[Mn^{II}(dpaq)](OTf)$. The

percent formation of [Mn^{III}(OH)(dpaq)](OTf) from these experiments is shown in Figure 1 and Table 1 (overlay of the electronic absorption spectra collected for each aliquot is shown in Figure A1.1). From these data, it is evident that complete formation of [Mn^{III}(OH)(dpaq)](OTf) is accomplished with ≥ 0.25 equivalents of O_2 (Figure 1, blue markers), giving a 4:1 manganese:dioxygen stoichiometry.

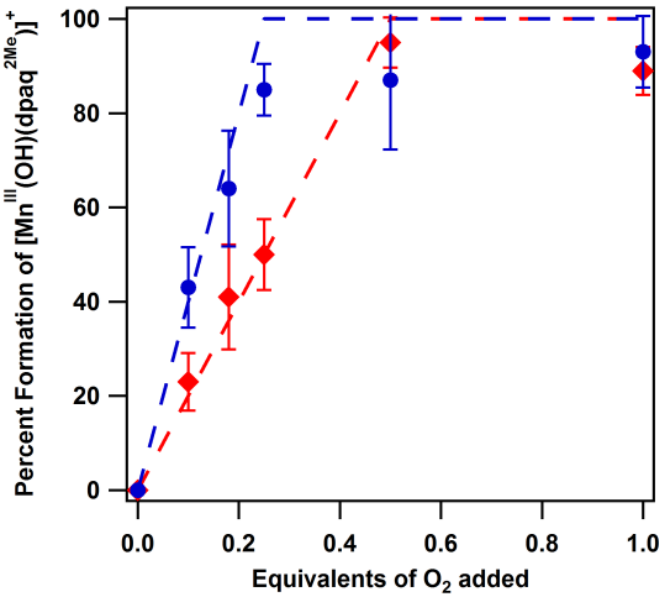

Figure 1. Plot of percent conversion to [Mn^{III}(OH)(dpaq)](OTf) (blue markers) and [Mn^{III}(OH)($dpaq^{2Me}$)](OTf) (red markers) as a function of added O_2. Trend lines for 4:1 (blue dashes) and 2:1 (red dashes) Mn:O_2 stoichiometry are shown for comparison.

Table 1. Percent Conversion to Mn^{III}-hydroxo Adducts [Mn^{III}(OH)(dpaq)](OTf) and [Mn^{III}(OH)($dpaq^{2Me}$)](OTf) Compared to Expected Yields for 4:1 and 2:1 Mn:O_2 Stoichiometry.

Equivalents of O_2 added	Experimental % conversion to [Mn^{III}(OH)(dpaq)](OTf)	Experimental % conversion to [Mn^{III}(OH)($dpaq^{2Me}$)](OTf)	Theoretical yield	
			Mn:O_2 4:1	Mn:O_2 2:1
0	0	0	0	0
0.1	43±9	23±6	40	20
0.18	64±12	41±11	72	36
0.25	85±6	50±8	100	50
0.5	87±15	95±5	100	100
1.0	93±8	89±5	100	100

To assess the involvement of solvent in the formation of [Mn^{III}(OH)(dpaq)](OTf) from the reaction of [Mn^{II}(dpaq)](OTf) with O_2, we carried out the oxygenation reaction in deuterated d_3-MeCN. We observed no change in the apparent rate of formation of [Mn^{III}(OH)(dpaq)](OTf) in d_3-MeCN (Figure A1.2), and an ESI-MS analysis of the solution following the reaction showed only the presence of non-deuterated [Mn^{III}(OH)(dpaq)](OTf) (*m/z* = 454.1086, calculated *m/z* = 454.11, Figure 2A). An additional low-intensity peak around 455.11 *m/z* arises from the natural isotopic splitting of the compound, as illustrated by the mass spectrum of crystalline [Mn^{III}(OH)(dpaq)](OTf) dissolved in d_3-MeCN (Figure 2B). Thus, we observe no evidence that the formation of [Mn^{III}(OH)(dpaq)](OTf) involves a HAT reaction with the solvent as the hydrogen-atom donor.

As the 4:1 manganese:dioxygen stoichiometry in the reaction of [Mn^{II}(dpaq)](OTf) with O_2 could indicate the involvement of a transient Mn^{IV}-oxo species (Scheme 1B), we attempted to trap this putative intermediate by carrying out the oxygenation of [Mn^{II}(dpaq)](OTf) in the presence of PPh_3, a substrate known to react with Mn^{IV}-oxo adducts.[28, 38-40] In a typical reaction, [Mn^{II}(dpaq)](OTf) was treated with an excess of O_2 in the presence of 50 equivalents of PPh_3 in d_3-MeCN. GC-MS experiments showed no evidence for the formation of the expected product of oxygen-atom transfer to PPh_3, triphenylphosphine oxide.

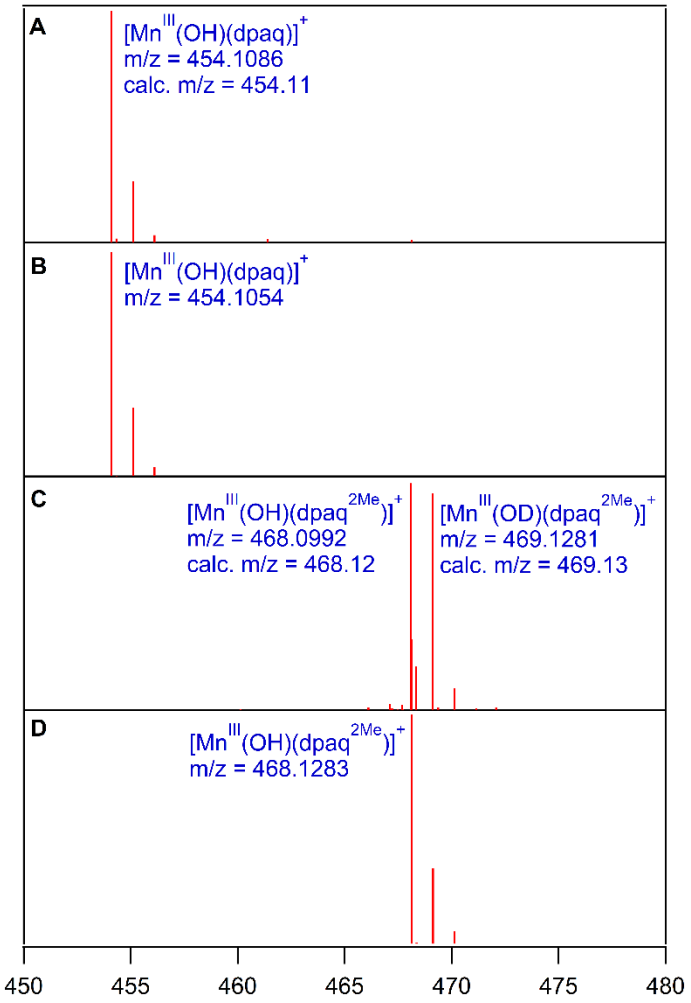

Figure 2. (A) ESI-MS data of $[Mn^{III}(OH)(dpaq)]^+$ from the reaction of $[Mn^{II}(dpaq)](OTf)$ with O_2 in deuterated MeCN. (B) ESI-MS data of $[Mn^{III}(OH)(dpaq)](OTf)$ dissolved in deuterated MeCN. (C) ESI-MS data for $[Mn^{III}(OD)(dpaq^{2Me})]^+$ and $[Mn^{III}(OH)(dpaq^{2Me})]^+$ from the reaction of $[Mn^{II}(dpaq^{2Me})](OTf)$ with O_2 in deuterated MeCN. (D) ESI-MS data for $[Mn^{III}(OH)(dpaq^{2Me})](OTf)$ dissolved in deuterated MeCN.

We also attempted to trap a putative Mn^{IV}-oxo intermediate by performing the oxygenation of $[Mn^{II}(dpaq)](OTf)$ in the presence of various hydrocarbons, which can react with a putative Mn^{IV}-oxo intermediate by a hydrogen-atom transfer mechanism.[39-45] For these experiments, $[Mn^{II}(dpaq)](OTf)$ was incubated with an excess of O_2 in the presence of 250 equivalents of the substrates in deuterated MeCN for 3hours. Oxygenation experiments in the presence of

cyclohexane, *cis*-dimethylcylohexane, cyclooctane, toluene, and ethylbenzene resulted in no detection of oxidized organic products. When 100 equivalents of DHA, which has the weakest C–H bond dissociation free energy of this series, was used as the substrate, the formation of 3 equivalents of anthracene, 13 equivalents of anthrone, 2 equivalents of anthraquinone, and 8 equivalents of 9,10-dihydroanthracen-9-ol was observed by ^{1}H NMR spectroscopy (Figure A1.3). In total, 26 equivalents of DHA were consumed during the oxygenation reaction (Table A1.1). Control experiments in which d_3-MeCN solutions of DHA were stirred with excess O_2 in the absence of Mn^{II} complex did not yield any oxidized products. However, control experiments where $[Mn^{III}(OH)(dpaq)]^+$ was treated with 100 equivalents DHA in d_3-MeCN in the presence of O_2 revealed comparable formation of oxidized products (see Table A1.1), corresponding to the consumption of 30 equivalents of DHA. Accordingly, the DHA oxidation observed upon oxygenation of $[Mn^{II}(dpaq)](OTf)$ does not necessarily provide evidence for the formation of a Mn^{IV}-oxo intermediate. Instead, reaction of DHA with the Mn^{III}-hydroxo product, which can be regenerated by O_2 oxidation of $[Mn^{II}(dpaq)]^+$, could account for the observed DHA oxidation.

Formation of $[Mn^{III}(OH)(dpaq^{2Me})](OTf)$ from the reaction of $[Mn^{II}(dpaq^{2Me})](OTf)$ with O_2. We have previously noted that oxygenation of $[Mn^{II}(dpaq^{2Me})](OTf)$ is substantially slower than that of $[Mn^{II}(dpaq)](OTf)$,[35] and ^{1}H-NMR investigations of $[Mn^{III}(OH)(dpaq^{2Me})](OTf)$ show no signals associated with a (μ-oxo)dimanganese(III, III) species, suggesting that this dimeric species is disfavored due to the bulk of the $dpaq^{2Me}$ ligand.[34] As such, dioxygen titration experiments were performed for solutions of $[Mn^{II}(dpaq^{2Me})](OTf)$ to investigate the effect of the steric bulk imposed by the methyl-quinoline group on this process. Similar to the experiments investigating the dioxygen reactivity of $[Mn^{II}(dpaq)](OTf)$, aliquots of MeCN solutions containing 0.1, 0.18, 0.25, 0.5, and 1 equivalents of O_2 were added to

[Mn^{II}(dpaq^{2Me})](OTf). The percent formation of [Mn^{III}(OH)(dpaq^{2Me})](OTf) from these experiments is shown in Figure 1 and Table 1 (overlay of the electronic absorption spectra collected for each aliquot is shown in Figure A1.4). In contrast to what is observed for [Mn^{II}(dpaq)](OTf), full formation of [Mn^{III}(OH)(dpaq^{2Me})](OTf) requires the addition of 0.5 equivalents of O_2 to a solution of [Mn^{II}(dpaq^{2Me})](OTf), suggesting a different reaction pathway (Figure 1 and Scheme 1A).

To further investigate the difference in mechanism observed for [Mn^{II}(dpaq^{2Me})](OTf), we performed the oxygenation reaction in d_3-MeCN. As is the case for [Mn^{II}(dpaq)](OTf), we observed no change in the apparent rate of formation of [Mn^{III}(OH)(dpaq^{2Me})](OTf) in d_3-MeCN (Figure A1.5). However, an ESI-MS analysis of the product solution revealed signals at *m*/*z* of 468.0992 and 469.1281, corresponding to [Mn^{III}(OH)(dpaq^{2Me})](OTf) and [Mn^{III}(OD)(dpaq^{2Me})](OTf), respectively, of nearly equal intensity (Figure 2C). A control experiment of [Mn^{III}(OH)(dpaq^{2Me})](OTf) dissolved in d_3-MeCN showed no ESI-MS signals associated with [Mn^{III}(OD)(dpaq^{2Me})](OTf) (Figure 2D). The low-intensity peak around 469.13 *m/z* arises from the natural isotopic splitting of the compound. Together, these observations suggest that the deuterium incorporation for [Mn^{III}(OD)(dpaq^{2Me})](OTf) arises from a hydrogen-atom abstraction from d_3-MeCN, although not during the rate determining step of the reaction. The observation of a mixture of [Mn^{III}(OH)(dpaq^{2Me})](OTf) and [Mn^{III}(OD)(dpaq^{2Me})](OTf) could arise from ligand substitution, where a portion of the OD^- ligands in [Mn^{III}(OD)(dpaq^{2Me})](OTf) are substituted by OH^- from adventitious water present in the MeCN solution.

Substrate trapping experiments aimed to probe the formation of a Mn^{IV}-oxo intermediate upon oxygenation of [Mn^{II}(dpaq^{2Me})](OTf) produced similar results to that seen for [Mn^{II}(dpaq)](OTf). Oxygenation of [Mn^{II}(dpaq^{2Me})](OTf) in the presence of 50 equivalents of PPh_3 failed to yield any

observable oxidized products. Oxygenation experiments in the presence of cyclohexane, *cis*-dimethylcylohexane, cyclooctane, toluene, and ethylbenzene likewise resulted in no detection of oxidized organic products. Oxygenation of $[Mn^{II}(dpaq^{2Me})](OTf)$ in the presence of DHA yielded 3 equivalents of anthracene, 11.5 equivalents of anthrone, 7.5 equivalents of 9,10-dihydroanthran-9-ol, and 1.6 equivalents of anthraquinone (Figure A1.6). These amounts correspond to ca. 24 equivalents of DHA consumption during oxygenation (Table A1.1). An ESI-MS examination of a representative solution following the reaction of $[Mn^{II}(dpaq)]^+$ with O_2 in the presence of DHA showed no deuterium incorporation into the Mn^{III}-hydroxo product, indicating that the proton of the hydroxo ligand is not derived from a solvent molecule under these conditions (Figure A1.7). When a control experiment using $[Mn^{III}(OH)(dpaq^{2Me})](OTf)$ was performed, comparable product formation, corresponding to 34 equivalents of DHA consumed, was observed (Table A1.1). Presumably, the reaction between $[Mn^{III}(OH)(dpaq^{2Me})]^+$ and DHA results in the formation of a Mn^{II}-aqua complex that can react with excess O_2 and regenerate the Mn^{III}-hydroxo species.

2.4 Discussion of O_2 reactivity.

Synthetic Mn^{II} systems that are capable of dioxygen activation are relatively rare, and the mechanisms by which these systems operate represent an emerging area of research.[21, 24, 25, 27] Mechanisms of Mn^{II}-based O_2 activation proposed in separate reports are similar in the early steps.[28-30, 32, 33, 46] It is commonly proposed that Mn^{II} complexes bind O_2 to initially form a Mn^{III}-superoxo adduct that is trapped by a second Mn^{II} complex to generate a peroxodimanganese(III, III) species (Scheme 1).[28, 29, 32] Each reported mechanism subsequently invokes O−O homolysis, giving either two mononuclear Mn^{IV}-oxo adducts[28, 31] or a bis(μ-oxo)dimanganese(IV, IV) complex (Scheme 1).[21, 33] These high-valent Mn complexes react further to generate Mn^{III} products.[28-30, 32, 33, 46] The system reported by Borovik *et al.* includes a hydrogen-atom transfer

step, in which the proposed Mn^{IV}-oxo complex abstracts a hydrogen atom from a solvent molecule to give the Mn^{III}-hydroxo product.[28] The Kovacs, Lee, and Duboc reports all propose that the Mn^{IV} species (either a mononuclear Mn^{IV}-oxo adduct or a bis(μ-oxo)dimanganese(IV) complex) react with residual Mn^{II} complex in solution to yield (μ-oxo)dimanganese(III, III) products.[29, 30, 32, 33] In certain cases, and in the presence of a suitable amount of water, the (μ-oxo)dimanganese(III, III) products can be hydrolyzed to give mononuclear Mn^{III}-hydroxo species.[19, 34]

Steric control of O_2 activation pathways. Our titration experiments investigating the oxygenation of $[Mn^{II}(dpaq)](OTf)$ show that this reaction occurs with a $Mn:O_2$ stoichiometry of 4:1. This result supports a mechanism in which a peroxodimanganese(III, III) dimer undergoes homolytic O−O bond cleavage to yield either a monomeric Mn^{IV}-oxo complex or a bis(μ-oxo)dimanganese(IV) dimer. Either of these species can be sequestered by unreacted $[Mn^{II}(dpaq)]^+$ in solution to form $[Mn^{III}Mn^{III}(\mu\text{-}O)(dpaq)_2]^{2+}$. This dinuclear product has been previously observed and characterized by Mn K-edge X-ray absorption spectroscopy (XAS) and ^{1}H NMR spectroscopy.[34] In the presence of sufficient concentrations of H_2O, the $[Mn^{III}Mn^{III}(\mu\text{-}O)(dpaq)_2]^{2+}$ species undergoes hydrolysis to result in monomeric $[Mn^{III}(OH)(dpaq)]^+$ (Scheme 3).[34] This mechanism is further supported by the lack of deuterium incorporation observed during the oxygenation of $[Mn^{II}(dpaq)](OTf)$ in d_3-MeCN.

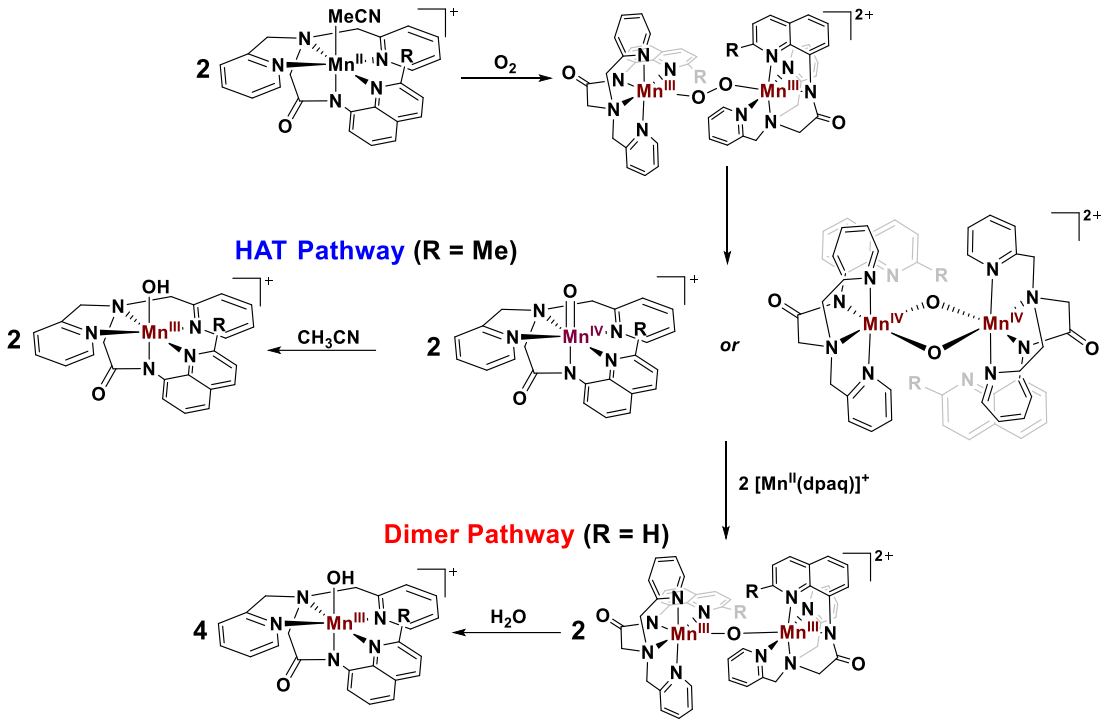

Scheme 3. Proposed pathways for the reactions between [$Mn^{II}dpaq^{R}$](OTf) with O_2 to generate Mn^{III}-hydroxo species.

The pathway proposed for [Mn^{II}(dpaq)](OTf) is very similar to the mechanism proposed by Kovacs and coworkers for N_4S^- bound Mn^{II} complexes.[29, 30] In that work, the (μ-oxo)dimanganese(III, III) species is proposed to form from the reaction of a Mn^{IV}-oxo intermediate with residual Mn^{II} complex in solution (Scheme 1B).[29, 30] Similarly, a mechanism proposed by Duboc and coworkers suggests that a bis(μ-oxo)dimanganese(IV, IV) species undergoes a series of intramolecular proton transfers and a comproportionation with residual Mn^{II} complex in solution to yield a (μ-hydroxo)dimanganese(III, III) species (Scheme 1C).[32, 46] In a system without acidic protons available from the ligand, one can envision a pathway along which the bis(μ-oxo)dimanganese(IV, IV) intermediate reacts with residual Mn^{II} complex in solution to form a (μ-

oxo)dimanganese(III, III) species (Scheme 4). Such a mechanism has been proposed for the reaction of Mn^{II}(SALPRN) with O_2 (SALPRN = l,3-bis(salicylideneamino)propane).[47]

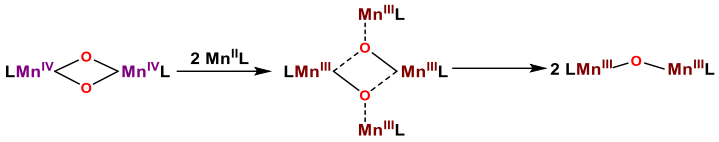

Scheme 4. A bis(μ-oxo)dimanganese(IV, IV) dimer could react with Mn^{II} complex in solution to form a (μ-oxo)dimanganese(III, III) species through a tetranuclear intermediate.

O_2 titration experiments for the bulkier [Mn^{II}($dpaq^{2Me}$)](OTf) complex show that dioxygen activation proceeds with a 2:1 Mn:O_2 stoichiometry, and deuterium incorporation is observed in a deuterated solvent. Compared to [Mn^{II}(dpaq)](OTf), these results suggest a divergent mechanism in which a Mn^{IV}-oxo intermediate (either a terminal oxo or a bis(μ-oxo)dimanganese(IV, IV) species) abstracts a hydrogen-atom from solvent (Scheme 3).

Mononuclear Oxomanganese(IV) versus dinuclear bis(μ-oxo)dimanganese(IV, IV) intermediates. The formation of [Mn^{III}(OD)($dpaq^{2Me}$)]$^+$ from oxygenation of [Mn^{II}($dpaq^{2Me}$)](OTf) in d_3-MeCN is consistent with hydrogen-atom abstraction from solvent by a high-valent oxomanganese(IV) intermediate. Our proposed mechanism for O_2 activation for [Mn^{II}(dpaq)](OTf) also requires the formation of an oxomanganese(IV) intermediate (Scheme 3). In either system, it is unclear whether the proposed high-valent intermediate is a mononuclear Mn^{IV}-oxo adduct or a bis(μ-oxo)dimanganese(IV, IV) species. The formation of a bis(μ-oxo)dimanganese(IV, IV) intermediate would likely require the dissociation of an arm of the $dpaq^R$ ligand to retain hexacoordination at the Mn center (Scheme 3). Thus, in the hypothetical [$Mn^{IV}Mn^{IV}$(μ-oxo)$_2$($dpaq^R$)$_2$]$^{2+}$ species, the $dpaq^R$ ligand would be bound in a tetradentate (κ^4) fashion, rather than the commonly observed pentadentate (κ^5) mode. The κ^4 binding of potentially

pentadentate ligands has been observed in the XRD structures of dimanganese complexes with two bridging oxo ligands. Specifically, the XRD structures of $[Mn^{III}Mn^{IV}(\mu\text{-}O)_2(N4Py)_2]^{3+}$, $[Mn^{IV}Mn^{IV}(\mu\text{-}O)_2(bpmg)_2](ClO_4)_2$, and $[Mn^{IV}Mn^{IV}(\mu\text{-}O)_2(mcbpen)_2](ClO_4)_2$ each show nominally pentadentate ligand bound in a κ^4 mode with non-coordinated pyridine moiety (N4Py = *N*,*N*-bis(2-pyridylmethyl)-*N*-bis(2-pyridyl)methylamine, bpmg = d 2-[[2-[bis(pyridin-2-ylmethyl)amino]-ethyl](methyl)amino]acetic acid, mcbpen = N-methyl-N0 - carboxymethyl-N,N0 - bis(pyridylmethyl)ethane-1,2-diamine).[48, 49] Tetradentate binding of the dpaq ligand has been previously proposed for the $[Mn^{III}Mn^{IV}(\mu\text{-}O)(dpaq)_2]^{3+}$ complex, which was generated from the reaction between $[Mn^{III}(OH)(dpaq)]^+$ and H_2O_2.[50] Although a crystal structure of this bis(μ-oxo)dimanganese(III, IV) complex was not reported, a DFT-optimized structure showed a non-coordinated quinoline moiety.[50] The reaction of $[Mn^{III}Mn^{IV}(\mu\text{-}O)(dpaq)_2]^{3+}$ with phenolic substrates generated the monomeric $[Mn^{III}(OH)(dpaq)]^+$ complex in quantitative yield, where the dpaq ligand is again pentadentate.[50] These results suggest that the dpaq ligand can alternate between pentadentate and tetradentate binding modes without decordinating fully from the Mn center. This flexibility could allow for the formation of bis(μ-oxo)dimanganese(III, IV) intermediate en route to (μ-oxo)dimanganese(III, III) or hydroxomanganese(III) products (Scheme 3).

Alternatively, a terminal Mn^{IV}-oxo adduct could serve as the high-valent intermediate formed during oxygenation of $[Mn^{II}(dpaq)](OTf)$ and $[Mn^{II}(dpaq^{2Me})](OTf)$. A recent report has proposed that iodosylbenzene oxidation of $[Mn^{III}(OH)(dpaq)]^+$ in the presence of the redox-inactive Lewis acid salts (such as $Sc(OTf)_3$) results in the formation of Mn^{IV}-oxo – Lewis acid adducts.[51] EPR experiments provided evidence for the Mn^{IV} oxidation state. The Mn^{IV}-oxo – Lewis acid adducts were capable of reacting with substrates with weak C–H bonds. Oxygenation of

$[Mn^{II}(dpaq^{2Me})](OTf)$ appears to result in the oxidation of the strong C–H of acetonitrile (C–H bond dissociation energy of ~94 kcal mol^{-1}).[52] Given that the coordination of Lewis acids to Mn^{IV}-oxo species can suppress reactivity towards C–H bonds, a $[Mn^{IV}(O)(dpaq^{2Me})]^{+}$ species formed in the absence of Lewis acids could be a strong oxidant. However, when the oxygenation of $[Mn^{II}(dpaq^{2Me})]^{+}$ was performed in the presence of substrates with C–H bonds weaker than that of MeCN (such as ethylbenzene and toluene, which have bond dissociation energies of ~86 and ~92 kcal mol^{-1}, respectively),[53, 54] no substrate oxidation was observed. The reason for the lack of substrate oxidation under these conditions is unclear at present. It could be that the large excess of MeCN relative to substrate favors oxidation of the former. Alternatively, if a bis(μ-oxo)dimanganese(IV, IV) intermediate is responsible for abstracting a hydrogen atom from MeCN, the expected steric bulk of this high-valent species could hinder the approach of substrates more sterically bulky than the relatively small MeCN molecule.

2.5 Reactivity of Mn^{II} complexes with Iodosylbenzene

Formation of $[Mn^{III}(OMe)(dpaq)]^{+}$from the reaction of $[Mn^{II}(dpaq)]^{+}$ with PhIO. The 4:1 Mn:O_2 stoichiometry determined from titration experiments with O_2 is consistent with a pathway in which a Mn^{IV}-oxo species is intercepted by unreacted Mn^{II} complex in solution. Thus, PhIO was explored as a shunt oxidant, as this oxo-atom transfer agent could react with $[Mn^{II}(dpaq)]^{+}$ to afford a Mn^{IV}-oxo species directly. These reactions were carried out in MeOH due to the low solubility of PhIO in MeCN, and the reaction was monitored by electronic absorption spectroscopy at -40˚C. The $[Mn^{II}(dpaq)](OTf)$ complex retains reactivity with O_2 in MeOH, in this case forming the Mn^{III}-methoxy complex $[Mn^{III}(OMe)(dpaq)]^{+}$ in quantitative yield.[55] The reaction of $[Mn^{II}(dpaq)]^{+}$ with an excess of PhIO resulted in the formation of electronic absorption features at 510 and 760 nm (Figure 3). These electronic absorption features are

diagnostic of the Mn^{III}-methoxy complex $[Mn^{III}(OMe)(dpaq)]^+$, which, using published extinction coefficients for this complex, is formed in 90% yield.[55] The electronic absorption data provide no evidence for the formation of any intermediates before the formation of $[Mn^{III}(OMe)(dpaq)]^+$ (Figure 3). The formation of a monomeric Mn^{III} product from the reaction of a Mn^{II} precursor with PhIO was observed previously by Stack and co-workers. In that case, a Mn^{II} complex of the neutral N_5 ligand PY5 (2,6-bis(bis(2-pyridyl)methoxymethane)- pyridine), $[Mn^{II}(PY5)(H_2O)]^{2+}$, reacted with PhIO in MeCN at 25°C to generate the $[Mn^{III}(PY5)(OH)]^{2+}$ complex).[56]

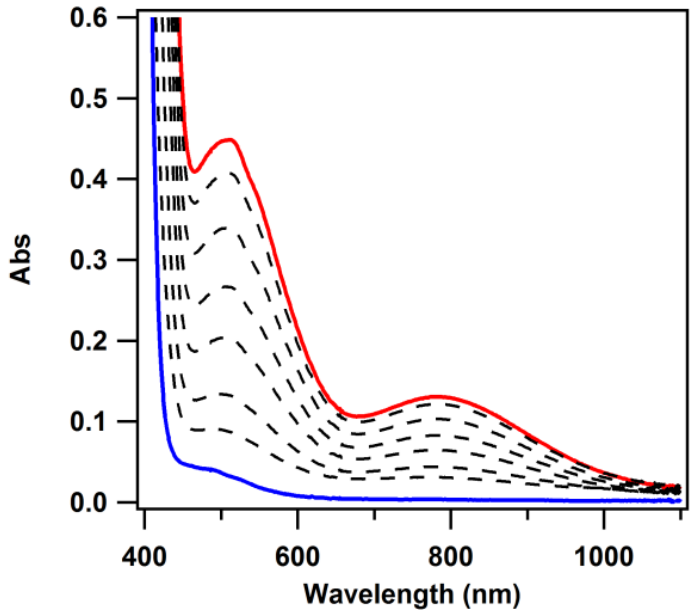

Figure 3. Electronic absorption spectra following the reaction between a 1.5 mM solution of $[Mn^{II}(dpaq)]^+$ (blue trace) and excess PhIO in MeOH at -40˚C to generate $[Mn^{III}(OMe)(dpaq)]^+$ (red trace).

The Mn:PhIO stoichiometry for the formation of $[Mn^{III}(OMe)(dpaq)]^+$ from $[Mn^{II}(dpaq)]^+$ and PhIO was determined by adding various amounts of PhIO and determining the extent of $[Mn^{III}(OMe)(dpaq)]^+$ formation. Under the assumption that $[Mn^{II}(dpaq)]^+$ reacts with PhIO to form an unobserved $[Mn^{IV}(O)(dpaq)]^+$ intermediate, titrations of $[Mn^{II}(dpaq)]^+$ with PhIO could result

in one of two Mn:PhIO stoichiometries. If the Mn^{IV}-oxo is trapped by $[Mn^{II}(dpaq)]^+$, then a 2:1 Mn:PhIO stoichiometry would be observed. Alternatively, if the Mn^{IV}-oxo adduct abstracts an H-atom to give $[Mn^{III}(OH)(dpaq)]^+$, then a 1:1 Mn:PhIO stoichiometry would be observed. These possibilities are summarized in Scheme 3.

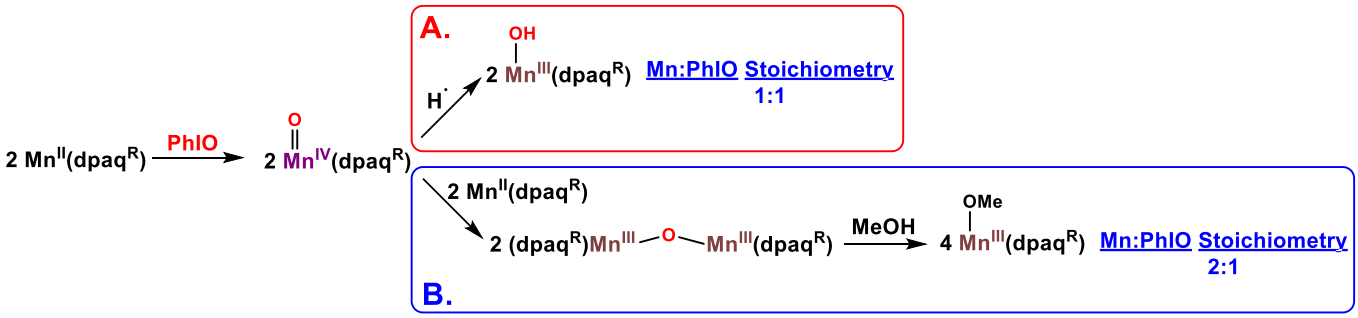

Scheme 3. Possible mechanisms for the reaction between $[Mn^{II}(dpaq^R)]^+$ with PhIO to generate monomeric Mn^{III} species.

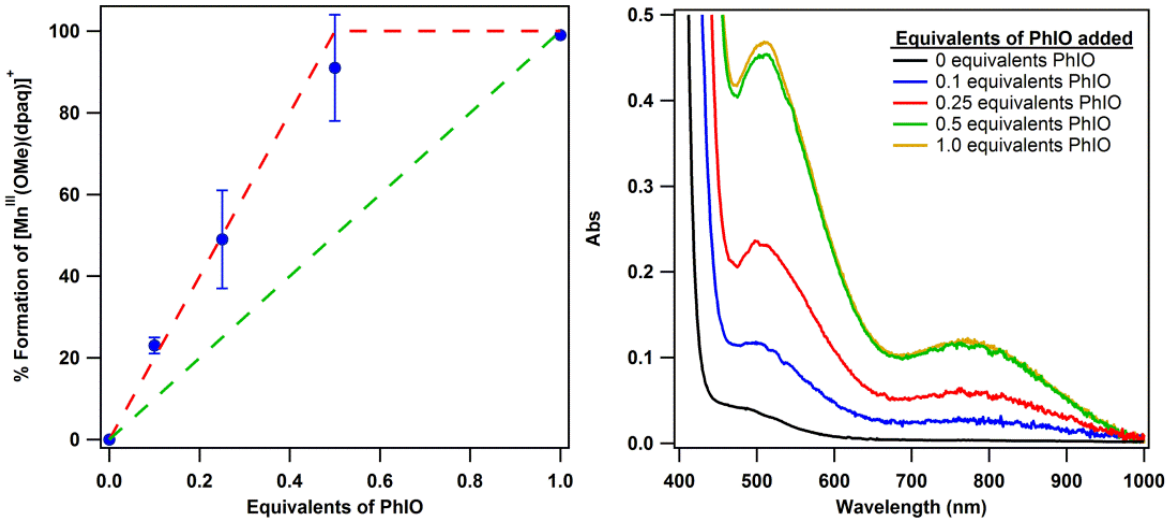

Figure 4. Left: Plot of PhIO titration data (blue) showing percent formation of $[Mn^{III}(OMe)(dpaq)]^+$ as a function of added PhIO. Expected trend lines for 2:1 (red) and 1:1 (green) Mn:PhIO stoichiometry are shown for comparison. Right: Electronic absorption spectra following the addition of sub-stoichiometric amounts of PhIO to solutions of $[Mn^{II}(dpaq)]^+$ in MeOH at 20˚C.

We determined the percent formation of $[Mn^{III}(OMe)(dpaq)]^+$ after each addition of PhIO by comparing the intensity of the feature at 760 nm for the completed reaction and after further addition of PhIO (up to 1 equivalent total). The titration results are summarized in Table 2. Complete formation of $[Mn^{III}(OMe)(dpaq)]^+$ was observed following the addition of at least 0.5 equivalents of PhIO (Figure 4).

Table 2. Percent Formation of Mn^{III}-methoxide Complex, $[Mn^{III}(OMe)(dpaq)]^+$ Compared to Expected Yields for 2:1 and 1:1 Mn:PhIO Stoichiometry.

Equivalents of PhIO added	Experimental % yield of $[Mn^{III}(OMe)(dpaq)]^+$	Experimental % yield of $[Mn^{III}(OMe)(dpaq^{2Me})]^+$	Theoretical yield	
			Mn:Oxidant 2:1	Mn:Oxidant 1:1
0	0	0	0	0
0.1	23±2	26±2	20	10
0.25	49±10	56±6	50	25
0.5	91±12	99±1	100	50

The reaction between $[Mn^{II}(dpaq)]^+$ and PhIO in MeOH was also carried out in MeCN. The electronic absorption spectrum obtained following this reaction is identical to the that observed after the reaction of $[Mn^{II}(dpaq)]^+$ with 0.25 equivalents of O_2 (Figure 5). The ^1H NMR spectrum of the reaction between $[Mn^{II}(dpaq)]^+$ and 0.5 equivalents of PhIO in deuterated MeCN is shown in Figure 6. The spectrum shows 28 signals over the range of -60 to 130 ppm. In the window of -10 to 30 ppm, there are 15 peaks that are at the same chemical shift values as those previously attributed to the antiferromagnetically coupled (μ-oxo)dimanganese(III) species $[Mn^{III}Mn^{III}(\mu\text{-}O)(dpaq)_2]^{2+}$. Three signals at 7.8, 7.4, and 7.2 ppm are assigned to phenyl iodide, the product of O-atom transfer from PhIO. Outside of the window of 0 to 20 ppm, 8 lower intensity signals are observed that were previously assigned to the paramagnetic $[Mn^{III}(OH)(dpaq)]^+$ monomer.[37] Thus, the electronic absorption and ^1H NMR data provide strong evidence that both

PhIO and O_2 oxidation of $[Mn^{II}(dpaq)]^+$ result in a mixture of mononuclear Mn^{III}-hydroxo and (μ-oxo)dimanganese(III,III) species.

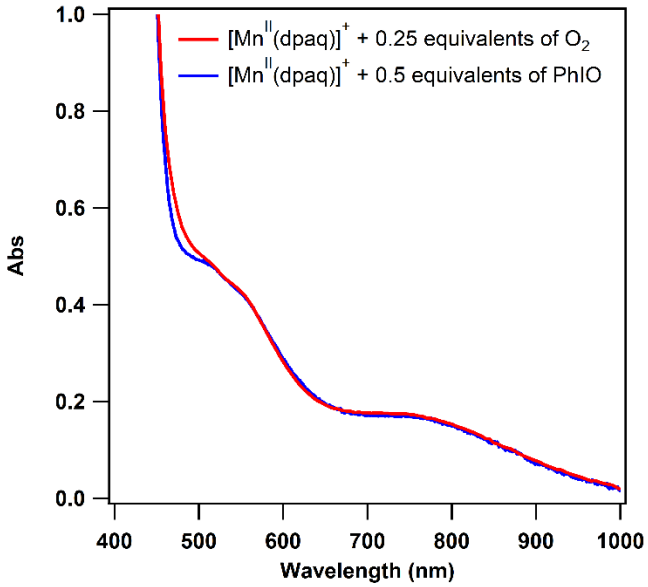

Figure 5. Electronic absorption spectrum of the solution following the reaction of $[Mn^{II}(dpaq)]^+$ with 0.25 equivalents of O_2 in MeCN at 20˚C (red) compared with the spectrum of the solution following the reaction of $[Mn^{II}(dpaq)]^+$ with 0.5equivalents of PhIO in MeCN at 20˚C (blue).

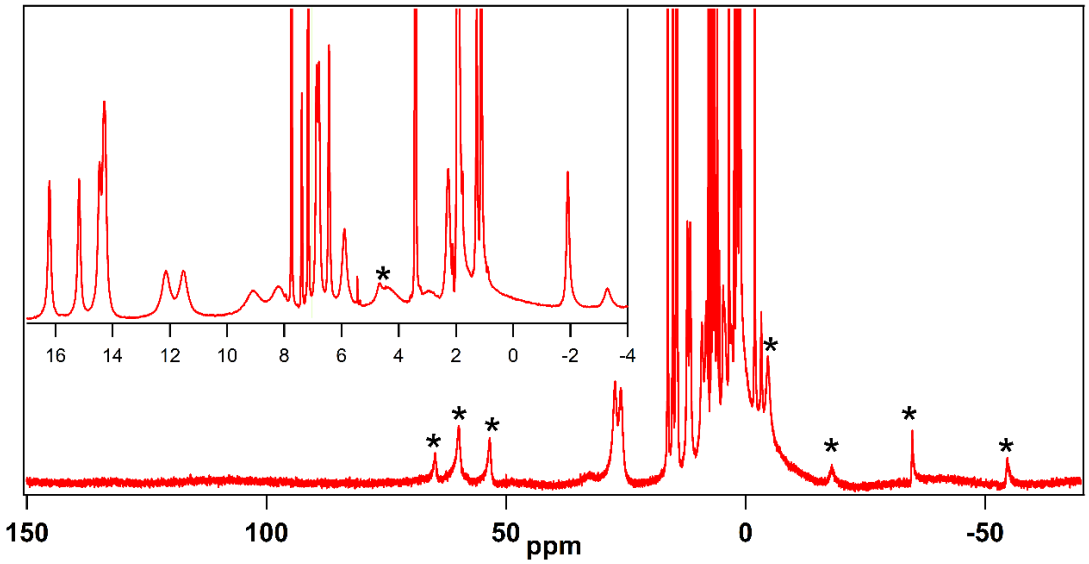

Figure 6. ^1H NMR spectra obtained following the reaction of a 2 mM solution of $[Mn^{II}(dpaq)]^+$ with 0.5 equivalents of PhIO in d_3-MeCN at 25°C. The asterisks mark resonances attributed to $[Mn^{III}(OH)(dpaq)]^+$. Inset: expanded view of the -10 to 30 ppm region of the spectrum.

Reactivity of [Mn^{II}(dpaq^{2Me})](OTf) with PhIO. The reactivity of [Mn^{II}(dpaq^{2Me})]$^{+}$ with PhIO was also investigated. Unexpectedly, titration experiments in MeOH revealed that the formation of [Mn^{III}(OMe)(dpaq^{2Me})]$^{+}$ from [Mn^{II}(dpaq^{2Me})]$^{+}$ only requires 0.5 equivalents of PhIO (Table 2, Figure 7). This stoichiometry is indicative of a mechanism that involves dimerization instead of HAT from a solvent molecule (Scheme 2).

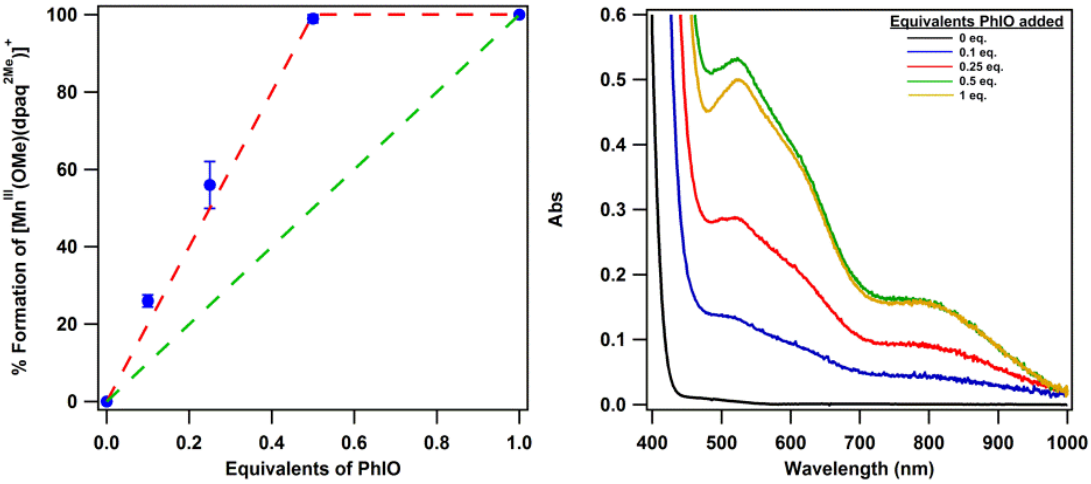

Figure 7. Left: Plot of PhIO titration data (blue) showing percent formation of [Mn^{III}(OMe)(dpaq^{2Me})]$^{+}$ as a function of added PhIO. Expected trend lines for 2:1 (red) and 1:1 (green) Mn:PhIO stoichiometry are shown for comparison. Right: Electronic absorption spectra following the addition of sub-stoichiometric amounts of PhIO to 2 mM solutions of [Mn^{II}(dpaq^{2Me})]$^{+}$ in MeOH at 20˚C.

The reactivity between [Mn^{II}(dpaq^{2Me})]$^{+}$ and PhIO was also investigated in MeCN. When a 2 mM solution of [Mn^{II}(dpaq^{2Me})]$^{+}$ in MeCN was allowed to react with 0.5 equivalents of PhIO at 25˚C, the electronic absorption spectrum of the product solution differed from that of [Mn^{III}(OH)(dpaq^{2Me})]$^{+}$ (Figure 8, blue trace). The electronic absorption spectrum featured broadened peaks that were shifted to higher energy than the corresponding features of [Mn^{III}(OH)(dpaq^{2Me})]$^{+}$ (Figure 8). Similarly broadened spectra have been reported for MeCN

solutions of equilibrium mixtures of monomeric Mn^{III}-hydroxo complexes and dimeric (μ-O)dimanganese(III) species.[34, 57] In those cases, the addition of H_2O to the equilibrium mixtures caused the monomeric Mn^{III}-hydroxo complexes to be favored, resulting in the spectral features becoming more defined.[34, 57] The addition of 250 equivalents of N_2-sparged H_2O to the solution obtained following the reaction between $[Mn^{II}(dpaq^{2Me})]^+$ with 0.5 equivalents of PhIO leads to similar sharpening of the electronic absorption features to give a spectrum consistent with the formation of $[Mn^{III}(OH)(dpaq^{2Me})]^+$ in 90% yield (Figure 8, red trace). These observations support the titration results in suggesting a dimerization pathway for Mn^{II} oxidation by PhIO. However, mass spectral analysis of the Mn^{III} product from the reaction of $[Mn^{II}(dpaq^{2Me})]^+$ with 0.5 equivalents of PhIO in d_3-MeCN without the addition of water revealed a peak at m/z = 469.12, consistent with deuterium incorporation from a solvent molecule to form $[Mn^{III}(OD)(dpaq^{2Me})]^+$ (Figure 9). The observation of deuterium incorporation from solvent stands counter to a dimerization pathway like that supported by the Mn:PhIO stoichiometry determined from titration experiments.

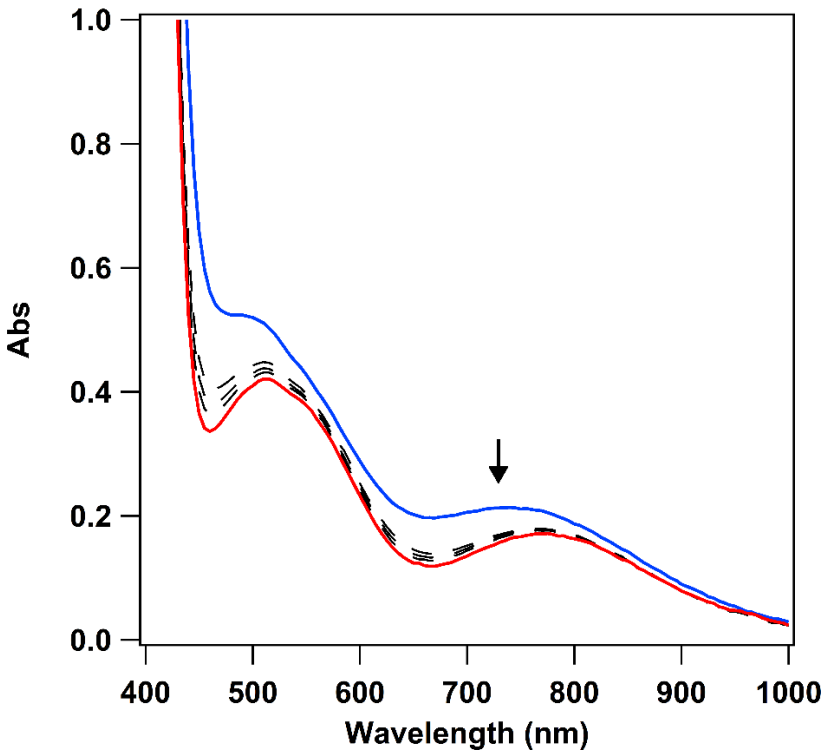

Figure 8. Electronic absorption spectrum following the reaction of a 2 mM solution of $[Mn^{II}(dpaq^{2Me})]^+$ with 0.5 equivalents of PhIO in MeCN at 20˚C (blue). Upon the addition of 250 equivalents of H_2O, formation of $[Mn^{III}(OH)(dpaq^{2Me})]^+$ is observed (red trace).

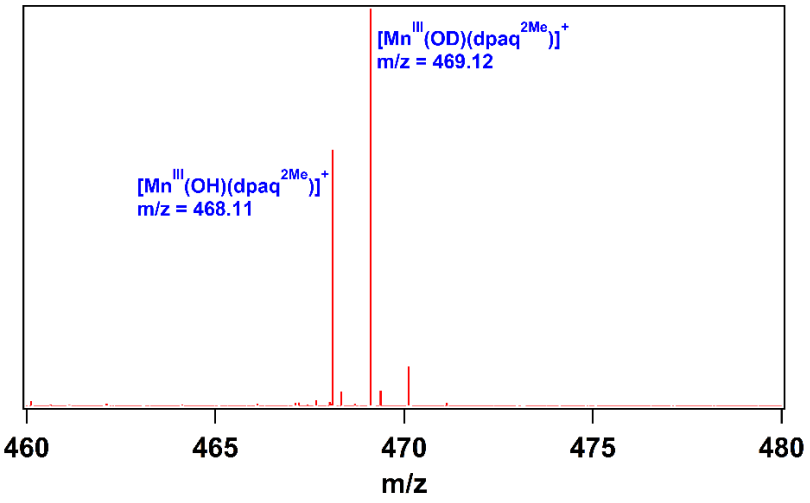

Figure 9. ESI-MS of $[Mn^{III}(OD)(dpaq^{2Me})]^+$ from the reaction between $[Mn^{II}(dpaq^{2Me})]^+$ and PhIO in d_3-MeCN at 25˚C.

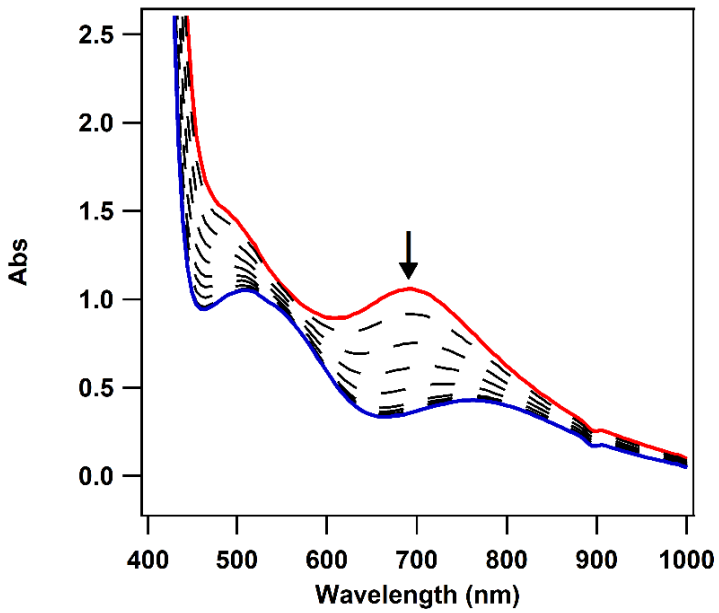

Figure 10. Electronic absorption spectra showing **1** formed through the reaction of a 4 mM solution of $[Mn^{II}(dpaq^{2Me})]^+$ with 0.5 equivalents of PhIO in d_3-MeCN at 25˚C (red trace) and the decay to form $[Mn^{III}(OH)(dpaq^{2Me})]^+$ (blue trace).

A reaction between $[Mn^{II}(dpaq^{2Me})]^+$ and 0.5 equivalents of PhIO was carried out at 4 mM in d_3-MeCN at 25˚C in order to prepare a sample for ^{1}H-NMR analysis. In deuterated solvent, a green intermediate (intermediate **1**) with a defined electronic absorption feature around 700 nm was observed (Figure 10). **1** decayed to form $[Mn^{III}(OH)(dpaq^{2Me})]^+$ in 99% yield over the course of three hours at room temperature (Figure 10).

^{1}H NMR analysis of the solution resulting from the reaction of $[Mn^{II}(dpaq^{2Me})]^+$ with 0.5 equivalents of PhIO in d_3-MeCN shows hyperfine-shifted peaks, as well as several peaks in the range of 0-30 ppm of equal intensity (Figure 11). The observation of peaks corresponding to $[Mn^{III}(OH)(dpaq^{2Me})]^+$ is likely the result of partial decay of **1** within the timeframe of ^{1}H NMR spectrum collection. Another set of lower intensity hyperfine-shifted peaks indicates that the decay of **1** is complicated. The set of peaks in the 0 to 30 ppm range of the spectrum indicate that **1** is an

antiferromagnetically coupled species. It is tempting to assign **1** as a (μ-O)dimanganese(III) species, based on the PhIO titration data and the diamagnetic signals in the ^{1}H NMR spectrum. However, it is important to note that the peaks in the diamagnetic region bear little similarity to those reported for the antiferromagnetically coupled $[Mn^{III}Mn^{III}(\mu\text{-}O)(dpaq)_2]^+$ complex (Figure 11, inset).[34] Additional characterization of this species, including measurement of its magnetic moment and the temperature dependence of its magnetic properties, will aid in the exact formulation of **1**.

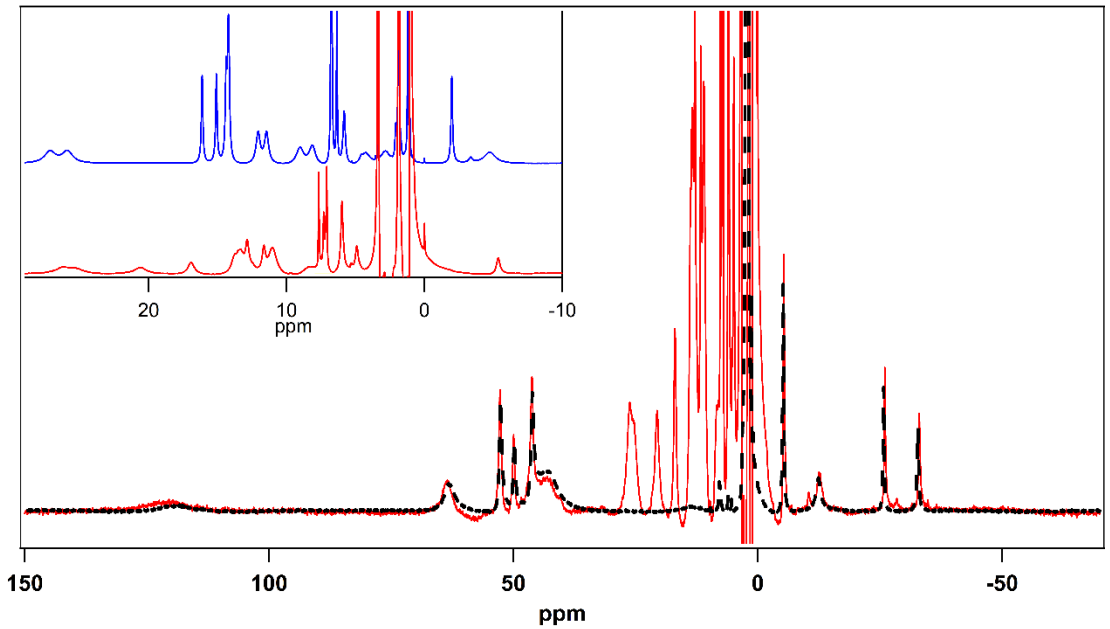

Figure 11. ^{1}H NMR spectra of $[Mn^{III}(OH)(dpaq^{2Me})]^+$ (black dashes) and a 4 mM solution of **1** (red trace) formed by the reaction of a 4 mM solution of $[Mn^{II}(dpaq^{2Me})]^+$ with 0.5 equivalents of PhIO in d_3-MeCN at 25˚C. Inset: expanded view of the -10 to 20 ppm region of the spectra of **1** (red trace) and $[Mn^{III}Mn^{III}(\mu\text{-}O)(dpaq)_2]^{2+}$ (blue trace).

2.6 Conclusion.

Inspired by the dioxygen activating ability of some of Nature's Mn-containing metalloenzymes, there has been interest in developing Mn-based synthetic catalysts that can employ O_2 for the oxidation of organic substrates. However, there are relatively few synthetic Mn^{II}

complexes that are capable of dioxygen activation, and details regarding their mechanistic pathways are limited. In an effort to garner further mechanistic understanding of O_2-activation processes, this report investigates two pentadentate monomeric Mn^{II} complexes that have been previously reported to react with O_2 to produce monomeric Mn^{III}-hydroxo species. One of the complexes, [Mn^{II}dpaq](OTf), activates dioxygen by a 4:1 Mn:O_2 stoichiometry. This stoichiometry suggests a mechanism in which a (μ-oxo)dimanganese(III, III) dimer is formed through the comproportionation of a Mn^{IV}-oxo species (either a terminal Mn-oxo or a bis(μ-oxo)dimanganese(IV, IV) dimer) and residual Mn^{II} complex in solution. This proposed comproportionation mechanism joins the majority of preceding systems described to form Mn^{III}-hydroxo complexes by O_2 oxidation of Mn^{II} precursors.[29-33, 46] In contrast, the bulkier [Mn^{II}dpaq^{2Me}](OTf) complex operates according to a 2:1 Mn:O_2 stoichiometry, suggesting a mechanism where a terminal Mn^{IV}-oxo species abstracts a hydrogen atoms from solvent. In support, oxygenation of [Mn^{II}(dpaq^{2Me})](OTf) in deuterated MeCN resulted in Mn^{III}–OD formation. The only other system for which a dioxygen activation mechanism involving hydrogen-atom abstraction from solvent was reported also employed a sterically-encumbered ligand.[28] Thus, simple steric modification of ligands may be an important approach to generate reactive, high-valent Mn species through O_2 activation. Studies investigating the oxidation of Mn^{II} complexes with PhIO reveal that the conversion of [Mn^{II}(dpaq^{2Me})]$^+$ to [Mn^{III}(OH)(dpaq^{2Me})]$^+$ only requires 0.5 equivalents of PhIO. This Mn:PhIO stoichiometry suggests a mechanism involving dimerization as opposed to HAT from a solvent molecule.

2.7 References.

1. A. J. Jasniewski and L. Que, *Chem. Rev.*, 2018, **118**, 2554-2592.

2. X. Huang and J. T. Groves, *Chem. Rev.*, 2018, **118**, 2491-2553.
3. A. T. Fiedler and A. A. Fischer, *J. Biol. Inorg. Chem.*, 2017, **22**, 407-424.
4. E. I. Solomon, D. E. Heppner, E. M. Johnston, J. W. Ginsbach, J. Cirera, M. Qayyum, M. T. Kieber-Emmons, C. H. Kjaergaard, R. G. Hadt and L. Tian, *Chem. Rev.*, 2014, **114**, 3659-3853.
5. K. D. Koehntop, J. P. Emerson and L. Q. Jr., *J. Biol. Inorg. Chem.*, 2005, **10**, 87-93.
6. W. A. Gunderson, A. I. Zatsman, J. P. Emerson, E. R. Farquhar, L. Que, J. D. Lipscomb and M. P. Hendrich, *J. Am. Chem. Soc.*, 2008, **130**, 14465-14467.
7. M. H. Glickman and J. P. Klinman, *Biochem.*, 1995, **34**, 14077-14092.
8. C. Su and E. H. Oliw, *J. Biol. Chem.*, 1998, **273**, 13072-13079.
9. C. Su, M. Sahlin and E. H. Oliw, *J. Biol. Chem.*, 2000, **275**, 18830-18835.
10. A. Wennman, S. Karkehabadi and E. H. Oliw, *Arch. Biochem. Biophys.*, 2014, **555-556**, 9-15.
11. A. Wennman, E. H. Oliw, S. Karkehabadi and Y. Chen, *J. Biol. Chem.*, 2016.
12. O. Opaleye, R.-S. Rose, M. M. Whittaker, E.-J. Woo, J. W. Whittaker and R. W. Pickersgill, *J. Biol. Chem.*, 2006, **281**, 6428-6433.
13. T. Borowski, A. Bassan, N. G. J. Richards and P. E. M. Siegbahn, *J. Chem. Theory Comp.*, 2005, **1**, 686-693.
14. A. Tanner, L. Bowater, S. A. Fairhurst and S. Bornemann, *J. Biol. Chem.*, 2001, **276**, 43627-43634.
15. L. C. Tabares, J. Gatjens, C. Hureau, M. R. Burell, L. Bowater, V. L. Pecoraro, S. Bornemann and S. Un, *J. Phys. Chem. B.*, 2009, **113**, 9016-9025.
16. M. Costas, M. P. Mehn, M. P. Jensen and L. Que, *Chem. Rev.*, 2004, **104**, 939-986.
17. C. E. Elwell, N. L. Gagnon, B. D. Neisen, D. Dhar, A. D. Spaeth, G. M. Yee and W. B. Tolman, *Chem. Rev.*, 2017, **117**, 2059-2107.
18. R. L. Shook, S. M. Peterson, J. Greaves, C. Moore, A. L. Rheingold and A. S. Borovik, *J. Am. Chem. Soc.*, 2011, **133**, 5810-5817.
19. M. K. Coggins, L. M. Brines and J. M. Kovacs, *Inorg. Chem.*, 2013, **52**, 12383-12393.
20. G. C. Wijeratne, B.; Day, V. W.; Jackson, T. A., *Inorg. Chem.*, 2014, **53**, 7622-7634.
21. P. Battioni, J. F. Bartoli, P. Leduc, M. Fontecave and D. Mansuy, *Chem. Comm.*, 1987, 791-792.
22. C. P. Horwitz, S. E. Creager and R. W. Murray, *Inorg. Chem.*, 1990, **29**, 1006-1011.
23. C. Zhang, Z. Xu, T. Shen, G. Wu, L. Zhang and N. Jiao, *Org. Lett.*, 2012, **14**, 2362-2365.
24. J. Christoffers, *J. Org. Chem.*, 1999, **64**, 7668-7669.
25. Y. Nishida, N. Tanaka, A. Yamazaki, T. Tokii, N. Hashimoto, K. Ide and K. Iwasawa, *Inorg. Chem.*, 1995, **34**, 3616-3620.
26. H. Komatsuzaki, Y. Nagasu, K. Suzuki, T. Shibasaki, M. Satoh, F. Ebina, S. Hikichi, M. Akita and Y. Moro-oka, *J. Chem. Soc., Dalton Trans.*, 1998, 511-512.
27. V. L. Pecoraro, M. J. Baldwin and A. Gelasco, *Chem. Rev.*, 1994, **94**, 807-826.
28. Z. Shirin, A. S. Borovik and V. G. Young Jr, *Chem. Commun.*, 1997, DOI: 10.1039/a703395h, 1967-1968.
29. M. K. Coggins, X. Sun, Y. Kwak, E. I. Solomon, E. Rybak-Akimova and J. A. Kovacs, *J. Am. Chem. Soc.*, 2013, **135**, 5631-5640.
30. M. K. Coggins, S. Toledo, E. Shaffer, W. Kaminsky, J. Shearer and J. A. Kovacs, *Inorg. Chem.*, 2012, **51**, 6633-6644.

31. J. A. Rees, V. Martin-Diaconescu, J. A. Kovacs and S. DeBeer, *Inorg. Chem.*, 2015, **54**, 6410-6422.
32. D. C. R. Brazzolotto, Fabian G.; Smith-Jones, Julian; Retegan, Marius; Amidani, Lucia; Faponle, Abayomi S.; Ray, Kallol; Philouze, Christian; de Visser, Sam P.; Gennari, Marcello; Duboc, Carole, *Angew. Chem.*, 2017, **56**, 8211-8215.
33. W.-Y. W. Chien-Ming Lee, Ming-Hsi Chiang, D. Scott Bohle, Gene-Hsiang Lee, *Inorg. Chem.*, 2017, **56**, 10559-10569.
34. D. B. Rice, S. D. Jones, J. T. Douglas and T. A. Jackson, *Inorg. Chem.*, 2018, **57**, 7825-7837.
35. D. B. Rice, G. B. Wijeratne, A. D. Burr, J. D. Parham, V. W. Day and T. A. Jackson, *Inorg. Chem.*, 2016, **55**, 8110-8120.
36. J. M. Achord and C. L. Hussey, *Anal. Chem.*, 1980, **52**, 601-602.
37. D. B. Rice, S. D. Jones, J. T. Douglas and T. A. Jackson, *Inorganic Chemistry*, 2018, DOI: 10.1021/acs.inorgchem.8b00917.
38. A. M. Massie, M. C. Denler, C. L. T.;, A. M. Walker, M. K. Hossain, V. W. Day, E. Nordlander and T. A. Jackson, *Angew. Chem. Int. Ed.*, 2017, **56**, 4178-4182.
39. A. A. Massie, A. Sinha, J. D. Parham, E. Nordlander and T. A. Jackson, *Inorg. Chem.*, 2018, **57**, 8253-8263.
40. M. C. Denler, A. A. Massie, R. Singh, E. Stewart-Jones, A. Sinha, V. W. Day, E. Nordlander and T. A. Jackson, *Dalton Trans.*, 2019, **48**, 5007-5021.
41. I. Garcia-Bosch, A. Company, C. W. Cady, S. Styring, W. R. Browne, X. Ribas and M. Costas, *Angew. Chem. Int. Ed.*, 2011, **50**, 5648-5653.
42. D. F. Leto, R. Ingram, V. W. Day and T. A. Jackson, *Chem. Comm.*, 2013, **49**, 5378-5380.
43. D. F. Leto, A. A. Massie, D. B. Rice and T. A. Jackson, *J. Am. Chem. Soc.*, 2016, **138**, 15413-15424.
44. T. H. Parsell, M.-Y. Yang and A. S. Borovik, *J. Am. Chem. Soc.*, 2009, **131**, 2762-2763.
45. K.-B. Cho, S. Shaik and W. Nam, *J. Phys. Chem. Let.*, 2012, **3**, 2851-2856.
46. M. Gennari, D. Brazzolotto, J. Pecaut, M. V. Cherrier, C. J. Pollock, S. DeBeer, M. Retegan, D. A. Pantazis, F. Neese, M. Rouzieres, R. Clerac and C. Duboc, *J. Am. Chem. Soc.*, 2015, **137**, 8644-8653.
47. C. P. Horwitz, P. J. Winslow, J. T. Warden and C. A. Lisek, *Inorg. Chem.*, 1993, **32**, 82-88.
48. D. F. Leto, S. Chattopadhyay, V. W. Day and T. A. Jackson, *Dalton Trans.*, 2013, **42**, 13014.
49. G. Berggren, A. Thapper, P. Huang, L. Eriksson, S. Styring and M. F. Anderlund, *Inorg. Chem.*, 2011, **50**, 3425-3430.
50. M. Sankaralingam, S. H. Jeon, Y.-M. Lee, M. S. Seo, K. Ohkubo, S. Fukuzumi and W. Nam, *Dalton Trans.*, 2016, **45**, 376-383.
51. M. Sankaralingam, Y.-M. Lee, Y. Pineda-Galvan, D. G. Karmalkar, M. S. Seo, S. H. Jeon, Y. Pushkar, S. Fukuzumi and W. Nam, *J. Am. Chem. Soc.*, 2019, **141**, 1324-1336.
52. D. J. Goebbert, L. Velarde, D. Khuseynov and A. Sanov, *J. Phys. Chem. Let.*, 2010, **1**, 792-795.
53. J. J. Warren, T. A. Tronic and J. M. Mayer, *Chem. Rev.*, 2010, **110**, 6961-7001.
54. Y. R. Luo, in *Comprehensive Handbook of Chemical Bond Energies.*, CRC Press, 2007, pp. 19-145.

55. G. B. Wijeratne, V. W. Day and T. A. Jackson, *Dalton Trans.*, 2015, **44**.
56. C. R. Goldsmith, A. P. Cole and T. D. P. Stack, *J. Am. Chem. Soc.*, 2005, **127**, 9904-9912.
57. D. B. Rice, A. Munasinghe, E. N. Grotemeyer, A. D. Burr, V. W. Day and T. A. Jackson, *Inorg. Chem.*, 2019, **58**, 622-636.

Chapter 3:

Spectroscopic and Structural Characterization of Mn(III)-alkylperoxo Complexes Supported by Pentadentate Amide-containing Ligands

Reproduced with permission from:
Joshua D. Parham, Gayan B. Wijeratne, Derek B. Rice, and Timothy A. Jackson *Inorg. Chem.* **2018**, *575*, 2489-2502.

3.1 Introduction. Manganese-dependent enzymes participate in a number of biologically important processes, including detoxification of reactive oxygen species by manganese superoxide dismutase (MnSOD) and manganese catalase,[1-4] oxalate degradation by oxalate oxidase and oxalate decarboxylase,[5] and water splitting by the oxygen-evolving complex of photosystem II.[6] Peroxo-level intermediates have been invoked in the catalytic cycles of many of these enzymes, although only a few examples have been spectroscopically or structurally characterized.[7] For MnSOD, a Mn^{III}-peroxo adduct has been proposed to form under conditions of high superoxide concentration.[1, 8-10] Intriguingly, X-ray crystallographic studies of MnSOD crystals soaked in hydrogen peroxide revealed a side-on peroxomanganese center in several of the enzyme active sites.[11] On the basis of rapid-freeze-quench EPR investigations, a Mn^{II}-alkylperoxo intermediate has been proposed for manganese-dependent homoprotocatechuate 2,3-dioxygenase (HPCD), which catalyzes oxidative aromatic ring cleavage in certain bacteria.[12] An analogous Fe^{II}-alkylperoxo adduct was crystallographically characterized in the iron-dependent HPCD by using the slow substrate 4-nitrocatechol.[13] For both the Fe- and Mn-forms of HPCD, the metal-alkylperoxo decays by a redox reaction to facilitate the dioxygenation of the homoprotocatechuate substrate.

Alkylperoxometal intermediates have also been proposed to form in the catalytic cycles of the iron- and manganese-dependent lipoxygenase enzymes (M-LOX; M = Fe or Mn).[14, 15] LOX enzymes convert fatty acids with *cis,cis*-1,4-diene motifs to the corresponding alkylhydroperoxide products. In both Fe- and Mn-LOX, this process is rate-controlled by a concerted proton-electron-transfer reaction between the fatty acid substrate and an active-site M^{III}-hydroxo moiety (M = Fe or Mn; Scheme 3.1(**I**)).[16-18] The nascent, carbon-based substrate radical (**II**) subsequently reacts with dioxygen to form a peroxyl radical. From this point in the catalytic cycle, the

alkylhydroperoxide product (**III**) could be formed by one of several pathways (*e.g.*, Scheme 1, A or B). The substrate radical could displace the aqua ligand and oxidize the M^{II} center, forming a M^{III}-alkylperoxo adduct (Scheme 3.1B).[15] This species would then undergo a ligand substitution reaction with water to form the product (**III**), and the M^{III}-hydroxo resting state (**I**). Circumstantial support for this pathway is provided by an X-ray crystal structure of the so-called purple soybean lipoxygenase, which contains an active-site Fe^{III}-alkylperoxo unit.[14] Alternatively, a proton-coupled electron transfer (PCET) from the M^{II}-aqua species to the substrate radical would yield the organic product (**III**), and regenerate the M^{III}-hydroxo oxidant (Scheme 3.1A, (**I**)).[19] The latter pathway has the advantage of being more direct, and the former invokes decay of a metal-alkylperoxo by a ligand substitution reaction, rather than a redox transformation.

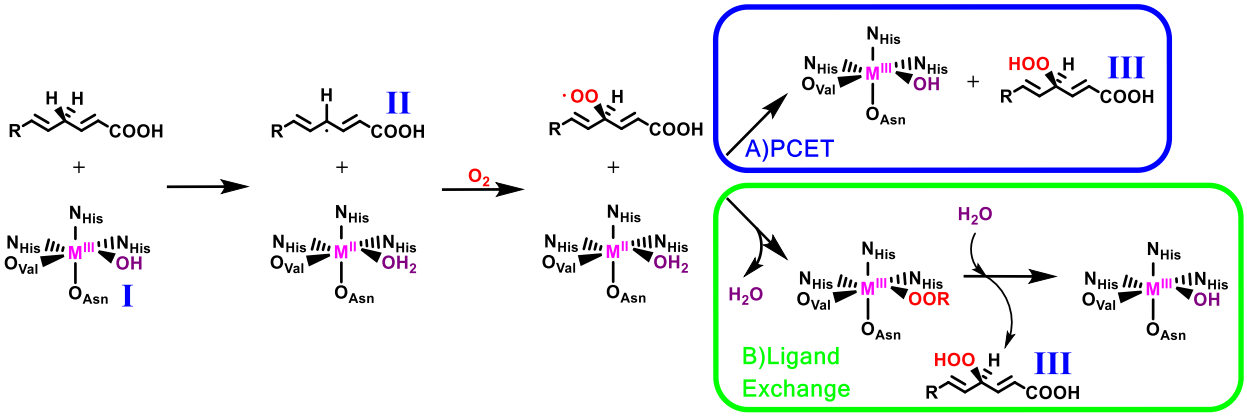

Scheme 3.1. Proposed mechanisms for fatty acid oxidation by lipoxygenase enzymes. M is either Fe or Mn.

Because of their relevance to important biochemical transformations, the properties and reactivity of Fe^{III}-alkylperoxo model complexes have been the subject of thorough experimental and theoretical investigation.[20-34] There is evidence that Fe^{III}-alkylperoxo complexes can decay by Fe–O bond cleavage,[23] with a high-spin state of the Fe^{III} center favoring this process against O–O cleavage.[35, 36]

Significantly less is known concerning the fundamental properties and reactivity of Mn^{III}-alkylperoxo species. Nonetheless, the reactivity proposed for the putative Mn^{III}-alkylperoxo intermediate in Mn-LOX (i.e., decay via Mn–O bond cleavage) stands in contrast to the O–O bond decay pathway proposed for related model complexes. Kovacs and co-workers have used a series of N_4S^- ligands to generate an array of Mn^{III}-alkylperoxo complexes, which have all been characterized structurally by X-ray crystallography.[37, 38] In those model systems, an analysis of the organic components of the decay products of two Mn^{III}-cumylperoxo complexes provided strong evidence for O–O bond homolysis.[37, 38] Further evidence for decay by O–O bond cleavage was provided by variable-temperature kinetic studies of the decay process. Both the enthalpy ($\Delta H^{\ddagger}$) and entropy ($\Delta S^{\ddagger}$) of activation for the decay process showed a linear correlation with the O–O distance determined by X-ray crystallography, with a decrease in both $\Delta H^{\ddagger}$ and $\Delta S^{\ddagger}$ with increasing O–O distance.[38] Unfortunately, the Mn-based products of the decay reaction could not be identified, although a black precipitate was observed and attributed to formation of a manganese oxide.

These prior studies demonstrate the need to advance understanding of the fundamental properties and chemical reactivity of Mn-alkylperoxo species. Kovacs and co-workers have elegantly established tuning of properties through subtle modifications *cis* to the alkylperoxo ligand,[37,38] and it is of interest to determine how more drastic changes in the primary coordination sphere could influence spectroscopic properties and reactivity. We have recently described two Mn^{III}-hydroxo complexes supported by pentadentate amide containing ligands, dpaq (dpaq = 2-[bis(pyridin-2-ylmethyl)]amino-N-quinolin-8-yl-acetamidate) and $dpaq^{2Me}$ ($dpaq^{2Me}$ = 2-[bis(pyridin-2- ylmethyl)]amino-*N*-2-methyl-quinolin-8-yl-acetamidate), which are able to carry out PCET reactions of relevance to the Mn-LOX mechanism (Figure 1).[39,40] Motivated by the

potential to mimic further the features of the proposed Mn-LOX mechanism, we set out to determine if these ligands would be able to support Mn^{III}-alkylperoxo species.

We report here the formation and characterization of the $[Mn^{III}(OO^tBu)(dpaq)]^+$ and $[Mn^{III}(OO^tBu)(dpaq^{2Me})]^+$ complexes, which contain a *t*-butylalkylperoxo ligand *trans* to the amide group of the supporting ligand (Figure 3.1). Spectroscopic experiments, including Mn K-edge X-ray absorption (XAS) measurements, support the formulation of these complexes. The spectroscopic data are interpreted with the aid of electronic structure calculations to understand differences in bonding between the $[Mn^{III}(OO^tBu)(dpaq)]^+$ and $[Mn^{III}(OO^tBu)(dpaq^{2Me})]^+$ complexes and Mn^{III}-alkylperoxo species with *cis*-thiolate ligation.[37-38]

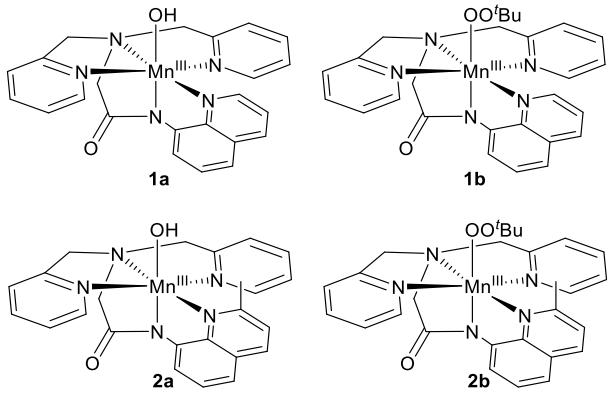

Figure 3.1. Mn^{III}-hydroxo and Mn^{III}-alkylperoxo complexes discussed in this work, **1a** = $[Mn^{III}(OH)(dpaq)]^+$, **2a** = $[Mn^{III}(OH)(dpaq^{2Me})]^+$, **1b** = $[Mn^{III}(OO^tBu)(dpaq)]^+$ and **2b** = $[Mn^{III}(OO^tBu)(dpaq^{2Me})]^+$.

3.2 Experimental Methods

Materials and Instrumentation. All chemicals were used as obtained from commercial sources unless noted otherwise. Acetonitrile, diethyl ether, and methanol were dried and degassed using a PureSolv Micro solvent purification system. $[Mn^{II}(dpaq)]OTf$ (**1**), $[Mn^{II}(dpaq^{2Me})]OTf$ (**2**),

[Mn^{III}(OH)(dpaq)]OTf (**1a**), and [Mn^{III}(OH)($dpaq^{2Me}$)]OTf (**2a**) were synthesized and characterized as reported previously.[39,40] The concentration of *tert*-butyl hydroperoxide (^{t}BuOOH) in decane stock solution was found to be 4.3 M by an iodometric titration procedure.[41] $^{t}Bu^{18}O^{18}OH$ was synthesized as previously described.[42] Electronic absorption spectroscopy was performed using a Varian Cary 50 Bio UV-Visible spectrophotometer equipped with a Unisoku cryostat and stirrer cooled with liquid N_2. Vibrational data were obtained using a PerkinElmer Spectrum100 FT-IR spectrometer with samples sealed in 0.1 mm gas-tight NaCl cells. ESI-MS experiments were performed using an LCT Premier MicroMass electrospray time-of-flight instrument. X-band EPR experiments were performed using a Bruker EMXplus with Oxford ESR900 continuous-flow liquid helium cryostat and an Oxford ITC503 temperature system.

Formation of [Mn^{III}(OH)($dpaq^{R}$)]$^{+}$ complexes from ^{t}BuOOH and Mn(II) complexes. A 2 mM solution of **1** in MeCN was prepared under inert atmosphere in a glovebox and transferred to a quartz cuvette with a stir bar and a septum. Upon cooling the solution to -15 °C, 10 equivalents of triethylamine (Et_3N) were added. Then, ^{t}BuOOH diluted in MeCN to 0.043 M was added via a gas-tight syringe in successive aliquots of 0.12 - 0.24 equivalents, up to 1 equivalent. The reaction of **1** with each aliquot of ^{t}BuOOH was monitored with electronic absorption spectroscopy at -15 °C until the spectra ceased to change, upon which the next aliquot was added. Full formation of the Mn^{III}-hydroxo complex **1a** was observed following the addition of 0.5 equivalents ^{t}BuOOH. Similar experiments monitoring the reaction of **2** with substoichiometric amounts of ^{t}BuOOH likewise revealed complete formation of the corresponding Mn^{III}-hydroxo complex, **2a**, following the addition of 0.5 equivalents ^{t}BuOOH. The percent formations of **1a** and **2a** were determined based on previously reported molar absorptivities.[39,40]

Formation of [Mn^{III}(OOtBu)($dpaq^{R}$)]$^{+}$ complexes. 2 mM solutions of **1a** or **2a** in MeCN were prepared and transferred to quartz cuvettes with stir bars and pierceable septa with 10 equivalents of Et_3N. In a typical experiment, the solution was cooled to -15 °C, and varied equivalencies of diluted ^{t}BuOOH in MeCN (0.43 M) were added via a gastight syringe. The amount of ^{t}BuOOH added was varied from 5 - 100 equivalents, and 100 equivalents were required to fully form [Mn^{III}(OO^{t}Bu)(dpaq)]$^{+}$ (**1b**) and [Mn^{III}(OO^{t}Bu)($dpaq^{2Me}$)]$^{+}$ (**2b**). The reaction mixture, maintained at -15 °C, was monitored by electronic absorption spectroscopy during each addition until the spectra ceased to change. An EPR sample was prepared for a solution after the reaction of **1a** (2 mM in MeCH) with 50 equivalents of ^{t}BuOOH in the presence of Et_3N. The EPR spectrum was collected at 20 K (9.64 GHz microwave frequency, 0.126 mW microwave power, 0.4 mT modulation amplitude, 100 kHz modulation frequency). Spin quantification of the signal was determined against a 0.54 mM frozen solution of [$Mn^{III}Mn^{IV}(\mu\text{-}O)_2(N4py)_2]^{+}$ in MeCN, prepared as reported previously.[43] FT-IR analyses of **1b** and **2b** were performed by injecting the cold solutions directly into gastight IR cells, which had been cleaned with CH_2Cl_2, and immediately collecting spectra. FT-IR experiments of isotopically labeled complexes were carried out using a similar procedure that employed $^{t}Bu^{18}O^{18}OH$ for the generation of **1b** and **2b**. Dry MeCN was used as a solvent background, and the IR spectrum of ^{t}BuOOH was acquired for comparison. At -15 °C, the complete decay of a 2 mM sample of both **1b** and **2b** occurred in approximately 2 hours after their maximum formation. The influence of base on the reactivity of the Mn centers with ^{t}BuOOH was evaluated by performing similar experiments to those described above in the absence of Et_3N. The products of these reactions were monitored using electronic absorption spectroscopy. EPR samples of **1b** and **2b** (each 2 mM in Mn in MeCN), as well as their decay products, were prepared upon their full formation in the presence of Et_3N and following

their full decay, respectively. EPR spectra for **1b**, **2b**, and their decay products were collected at 5K (9.64 GHz microwave frequency, 0.126 mW microwave power, 0.4 mT modulation amplitude, 100 kHz modulation frequency). The spectrum of **1b** was also collected at 77 K (9.64 GHz microwave frequency, 5 mW microwave power, 0.1 mT modulation amplitude, 100 kHz modulation frequency). Spin quantification of the spectrum of **1b** was determined against a TEMPO (2,2,6,6-tetramethylpiperidin-1-yl)oxyl) standard (9.64 GHz microwave frequency, 2 mW microwave power, 0.4 mT modulation amplitude, 100 kHz modulation frequency).

X-ray Absorption Data Collection and Analysis. Samples of **1a** and **2a** were prepared in MeCN (10 mM) and transferred to 2 mm pathlength cuvettes which were sealed with pierceable septa. Upon cooling the solution to -15 °C, 107 equivalents of ^{t}BuOOH (250 μL of 4.3 M stock solution) were added via a gas-tight syringe. The contents of the cuvette were thoroughly mixed with a pipette that was pre-chilled with liquid nitrogen. Formation of **1b** and **2b** was monitored by electronic absoprtion spectroscopy. Upon full formation, the solutions were injected into sample holders with a Kapton tape window using a pre-cooled syringe and frozen in liquid nitrogen immediately. Mn K-edge XAS data were collected at SSRL Beamline 2-2. Mn K-edge X-ray absorption spectra were collected at 15 K over a range in energy from 6.3 to 7.25 keV using a Si(111) monochromator. The fluorescence excitation spectra were obtained using a 13-element Ge array. Spectra of manganese foil were collected with each scan as a reference and were calibrated by assigning the zero crossing of the second derivative of the foil K-edge energy to 6539.0 eV. During data collection, the rising edge of each spectrum was monitored for evidence of photo-reduction. No photo-reduction was observed.

XAS data reduction and averaging was carried out using the Athena program.[44] A Gaussian function was fit to the pre-edge background and subtracted from the whole spectrum as a

background correction. The spectrum was then spline corrected to remove low-frequency background. EXAFS refinement was carried out on $k^3\chi(k)$ data, using phase and amplitude functions obtained from *FEFF*, version 6,[45] and structural models of **1b** and **2b** obtained from DFT geometry optimizations (vide infra). The EXAFS data were fit using the Artemis program.[44] The average distances between Mn and scattering atoms (*r*) and Debye-Waller factors□□□^{2}) were optimized for each fit, while the number of atoms in the shell (*n*) was kept fixed. *n* was systematically varied between fits. The threshold energy, E_0, in electronvolts (k = 0 point) was kept at a common, variable value for every shell of a given fit. The goodness of fit was evaluated using the R-factor:

$$R = \sum_{i=1}^{N}(\chi_i^{data} - \chi_i^{fit})^2 \,/\, \sum_{i=1}^{N}(\chi_i^{data})^2$$

Electronic Structure Calculations. Density functional theory (DFT) calculations were carried out using the ORCA 3.0.1 software package.[46] Initial coordinates for each Mn^{III}-alkylperoxo complex were based on crystal structure data of the respective hydroxide analogues.[39-40] The hydroxide ligands were replaced with a *t*-butylperoxo moiety and the resulting structure was subjected to unconstrained geometry optimization converged to the S = 2 spin state. In order to facilitate comparison with DFT computations performed for the Mn^{III}-alkylperoxo complexes of Kovacs and co-workers, we used the same level of theory;[38] *i.e.*, these calculations employed the TPSS functional[47,48] with the def2-TZVP(-f) basis set for all atoms,[49] along with the resolution of identity (RI) approximation[50] and def2-TZV/J auxiliary basis sets.[49] The ZORA approximation was employed to account for scalar relativistic effects,[51,52] and Grimme's atom-pairwise dispersion correction was included.[53] Acetonitrile solvation was accounted for using COSMO.[54] All geometry optimizations were carried out with an integration grid of 7 for the Mn atom and a grid of 5 for the remainder of the complex.

Electronic absorption spectra were calculated using the time-dependent (TD)-DFT method, as implemented in ORCA.[46] The TD-DFT calculations used the hybrid B3LYP functional[55-57] with the Ahlrichs TZVP basis set employed for manganese and all heteroatoms, and the SVP basis set for carbon and hydrogen.[58,59] The RIJCOSX approximation[60,61] was utilized with the TZVP/J and SVP/J auxiliary basis sets.[58,59] Acetonitrile solvation was accounted for using COSMO.[54] An integration grid of 5 and tight SCF convergence criteria were employed.

3.3 Results and Analysis

Reactions of [Mn^{II}(dpaq)](OTf) (1) and [Mn^{II}(dpaq^{2Me})](OTf) (2) with ^{t}BuOOH. In order to identify conditions for the formation of the Mn^{III}-alkylperoxo complex [Mn^{III}(OO^{t}Bu)(dpaq)]$^{+}$ (**1b**), we explored the reactivity of [Mn^{II}(dpaq)]$^{+}$ (**1**) with ^{t}BuOOH. These reactions were performed in MeCN at -15°C and monitored by electronic absorption spectroscopy. The addition of sub-stoichiometric amounts of ^{t}BuOOH to solutions of **1** resulted in the appearance of electronic absorption features at 550 and 780 nm (Figure 3.2). These absorption bands are consistent with the formation of [Mn^{III}(OH)(dpaq)]$^{+}$ (**1a**; Scheme 3.2). Using published extinction coeffecients for **1a**,[39] stoichiometric conversion of **1** to **1a** is suggested upon the addition of ~0.5 equivalents of ^{t}BuOOH (Figure 3.2, blue trace). However, while ESI-MS data collected for a MeCN solution of **1** treated with 0.5 equivalents of ^{t}BuOOH show the most prominent peak to be associated with **1a** (*m/z* of 454.1; see Figure A2.1), a weaker peak is also observed at 510.2 *m/z*. This peak can be attributed to the formation of [Mn^{III}(O^{t}Bu)(dpaq)]$^{+}$. As the Mn^{III}-methoxy analogue of **1a**, [Mn^{III}(OMe)(dpaq)]$^{+}$, shows electronic absorption signals nearly identical to those of **1a**,[62] we propose that a mixture of **1a** and [Mn^{III}(O^{t}Bu)(dpaq)]$^{+}$ would show an electronic absorption spectrum resembling that of a pure solution of **1a**. In addition, the [Mn^{III}(OMe)(dpaq)]$^{+}$ complex can be rapdily converted to **1a** by the addition of water.[62] By analogy, we propose that

$[Mn^{III}(O^tBu)(dpaq)]^+$ can be converted to **1a** by reaction with trace water in MeCN. The reaction pathway for this process is elaborated in the *Discussion* section.

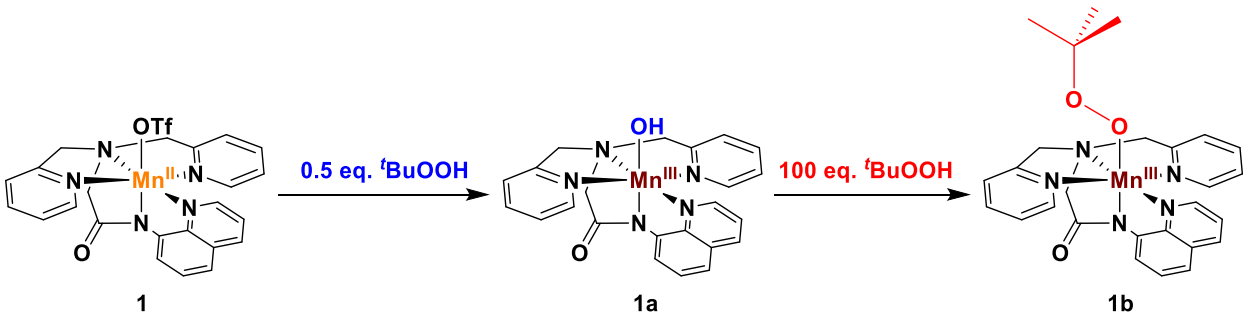

Scheme 3.2. Complex **1** reacts with ~0.5 eq. ^{t}BuOOH to predominantly form **1a** (a minor peak associated with $[Mn^{III}(O^tBu)(dpaq)]^+$ is observed by ESI-MS experiments; see Figure A2.1). When reacted with ~100 eq. ^{t}BuOOH, **1a** converts to **1b**.

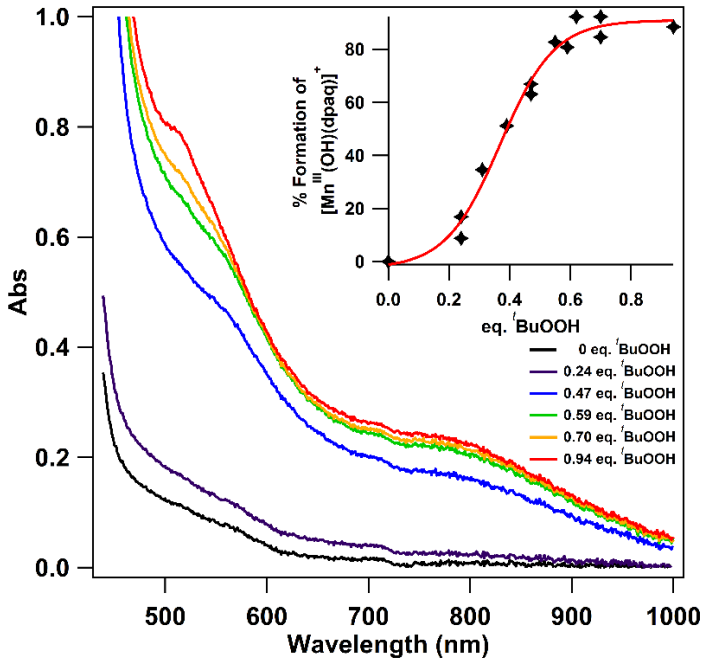

Figure 3.2. Electronic absorption changes upon the addition of sub-stoichiometric amounts of ^{t}BuOOH to solutions of **1** in MeCN at -15°C. The addition of ~0.5 equivalents of ^{t}BuOOH is required to fully form **1a** (blue trace and inset). Additional aliquots react with **1a** to produce a mixture of species. **Inset:** Plot of the titration data including a trendline (red).

Treatment of solutions of **1a** with additional equivalents of ^{t}BuOOH led to further spectral changes. For example, the addition of one equivalent of ^{t}BuOOH to **1a** resulted in a poorly-defined

electronic absorption spectrum lacking clear band maxima (Figure 3.3, orange trace). Reactions in the absence of a base resulted in the appearance of a similar chromophore, but with a better-defined electronic absorption spectrum with a maximum near 550 nm (Figure A2.2), showing the influence of added base on this chemistry. The addition of 10, 20, and 50 equivalents of ^{t}BuOOH to **1a** in the presence of 10 equivalents Et_3N resulted in the appearance of a new electronic absorption band centered near 700 nm, as shown in Figure 3. The temporal evolution of the electronic absorption signals of **1a** upon the addition of 50 equivalents of ^{t}BuOOH in the presence of 10 equivalents Et_3N are shown in Figures 4 and S3. Insight into the composition of this final solution was obtained through X-band EPR experiments. The 5 K perpendicular-mode EPR spectrum of **1a** following the addition of 50 equivalents of ^{t}BuOOH in the presence of Et_3N shows a 16-line signal (Figure 3.4, inset; g = 2.02, A = 7.81 mT); the corresponding parallel-mode spectrum is silent at X-band frequency. Because complex **1a** is EPR silent in both perpendicular and parallel-mode at X-band frequency, this sixteen-line signal must arise from a product of the reaction of **1a** and ^{t}BuOOH. Spin quantification of the sixteen-line signal associated with the $Mn^{III}Mn^{IV}$ center indicates that this signal represents 70 ± 20 % of the total Mn. The position and hyperfine splitting pattern of this EPR signal are within the range reported for $Mn^{III}Mn^{IV}(\mu\text{-}O)_2$ dimers, and the appearance of the EPR signal is strikingly similar to that of the $[Mn^{III}Mn^{IV}(\mu\text{-}O)_2(dpaq)_2]^+$ complex reported by Nam and co-workers.[43,63-65] This $[Mn^{III}Mn^{IV}(\mu\text{-}O)_2(dpaq)_2]^+$ complex was formed upon the addition of 5 equivalents of H_2O_2 with Et_3N to **1a**. The electronic absorption spectrum of $[Mn^{III}Mn^{IV}(\mu\text{-}O)_2(dpaq)_2]^+$ consisted of broad features extending from ~800 – 400 nm.[63] In contrast, the spectrum we observed following the addition of 50 equivalents ^{t}BuOOH to **1a** has sharper features (Figure 3.3). Thus, on the basis of the EPR and electronic absorption data, we

conclude that the addition of 50 equivalents of ^{t}BuOOH to **1a** results in a mixture of $[Mn^{III}Mn^{IV}(\mu\text{-}O)_2(dpaq)_2]^+$ and other, EPR-silent, products.

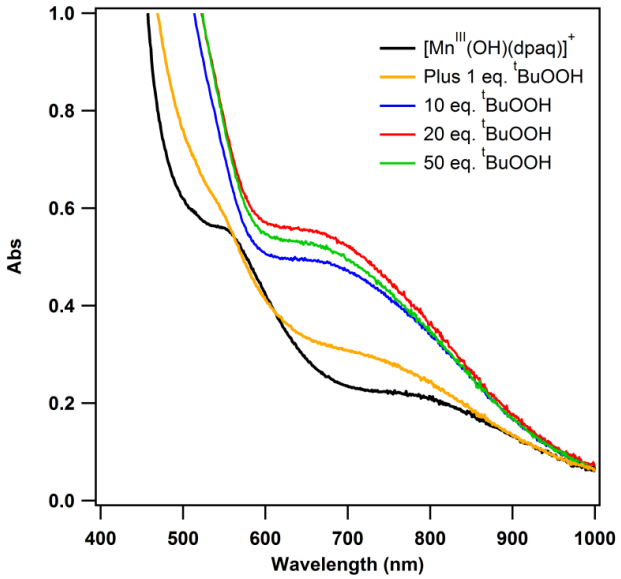

Figure 3.3. Electronic absorption spectra of the product of the reaction of **1a** (black line) with increasing equivalents ^{t}BuOOH in the presence of 10 equivalents Et_3N in MeCN at -15°C.

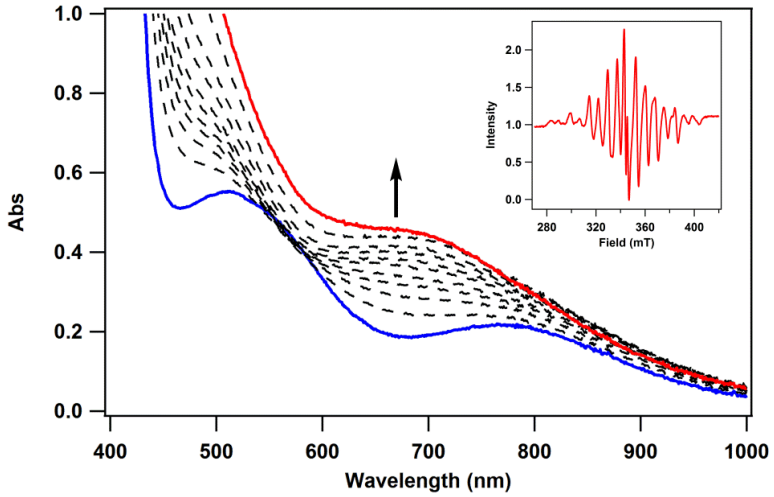

Figure 3.4. Electronic absorption spectra showing the time course of the reaction of **1a** with 50 equivalents ^{t}BuOOH in the presence of 10 equivalents Et_3N in MeCN at -15°C. **Inset.** 5K EPR spectrum of the final reaction mixture showing a sixteen line signal indicative of $[Mn^{III}Mn^{IV}(\mu\text{-}O)_2(dpaq)_2]^+$, which represents ca. 70% of Mn in the sample.

Additional experiments showed that the broad electronic absorption features observed following the addition of ^{t}BuOOH to **1a** became more defined with increased amounts of added ^{t}BuOOH. Species **1b** is maximally formed when approximately 100 equivalents of ^{t}BuOOH are added either in the presence or absence of Et_3N, and this conversion appears to proceed with isosbestic behavior (Figure 3.5, left and Figure A2.4). The rate of formation of **1b** in the presence or absence of base is essentially identical (Figure A2.5). The electronic absorption spectrum of **1b** has features at 710 and 500 nm (ε = 150 and 400 $M^{-1}cm^{-1}$, respectively; see Figure 3.5, left panel; Figure A2.6). Importantly, the perpendicular-mode EPR spectrum of **1b** lacks the sixteen-line signal from $[Mn^{III}Mn^{IV}(\mu\text{-}O)_2(dpaq)_2]^+$ and does not contain signals from mononuclear Mn^{II} species. Instead, the EPR spectrum now shows a radical signal with *g*-values, at 77 K, of 2.033, 2.007, and 2.002 (Figure A2.7). These *g*-values are identical to those of the ^{t}BuOO$^\bullet$ radical.[66] Spin quantification of the radical signal indicates ^{t}BuOO$^\bullet$ formation of ca. 10% relative to the total Mn concentration. The lack of any other signal in either perpendicular or parallel mode supports the assignment of **1b** as an EPR-silent species, potentially a mononuclear Mn(III) complex with a moderate zero-field splitting. An alternative route to **1b** was achieved by adding 50 equivalents ^{t}BuOOH to the Mn^{III}-hydroxo complex **1a** in the absence of any added Et_3N (Figure A2.8). However, in this case the conversion does not proceed with isobestic behavior, suggesting the formation of one or more intermediates with electronic absorption bands in the visible region.

It is important to note that these data do not necessarily provide evidence that **1b** is the only species present in solution under these conditions, as the presence of other EPR-silent species cannot be ruled out. ESI-MS experiments, which should, in principle, be useful for addressing this issue, are complicated by the thermal instability of **1b**. Our assessment that **1b** is maximally, if not exclusively, formed upon the addition of 100 equivalents of ^{t}BuOOH comes from the lack of EPR

signals associated with $Mn^{III}Mn^{IV}$ or mononuclear Mn^{II} species, the ability to fit EXAFS data for these solutions with metric parameters consistent with a Mn^{III}-OO^{t}Bu adduct (*vide infra*), and the analysis of the ratio of electronic absorption intensities at 710 nm (local maximum absorbance of **1b**) and 590 nm (local minimum absorbance for **1b**, but with absorbance contributions from **1a** and the $Mn^{III}Mn^{IV}$ dimer) as a function of added equivalents of ^{t}BuOOH. As shown in Figure A2.4, this ratio is maximized upon the addition of 100 equivalents of ^{t}BuOOH to **1a**.

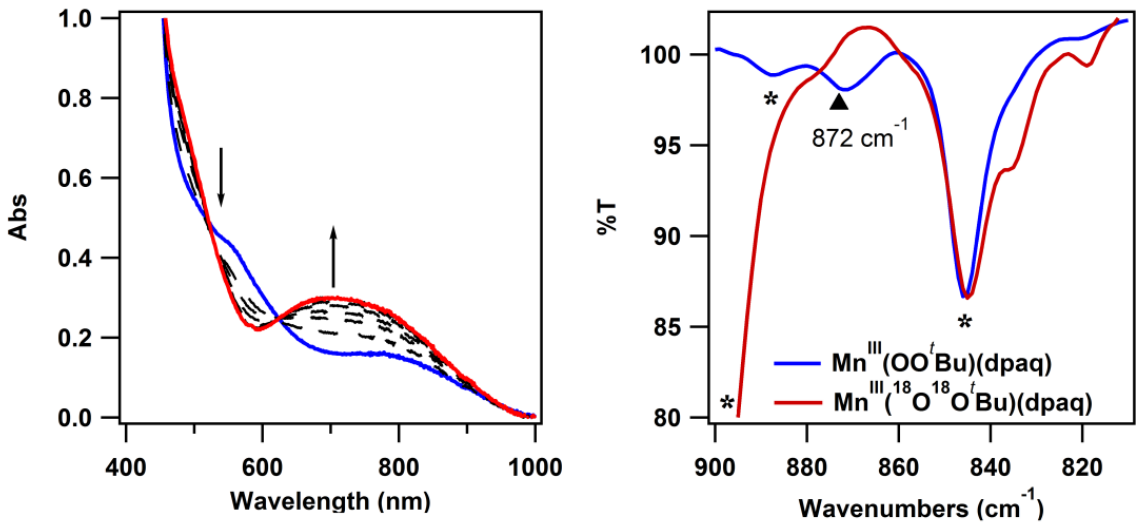

Figure 3.5. Characterization of **1b** generated from the reaction of **1a** (2 mM in MeCN) with 100 equivalents ^{t}BuOOH in the presence of Et_3N in MeCN at -15°C. **Left:** Electronic absorption spectra showing the appearance of features at 710 and 500 nm (red trace) with the disappearance of features at 550 and 780 nm that correspond to **1a** (blue trace). **Right:** Solution FT-IR spectrum showing a signal at 872 cm^{-1} corresponding to the O–O stretch of the alkylperoxo complex. The signal is lost when **1a** reacts with labeled ^{t}Bu^{18}O^{18}OH. Asterisks (*****) denote background signals from ^{t}BuOOH (846 and 887 cm^{-1}) and CH_2Cl_2 contaminant (900 cm^{-1}).[67,68]

Similar ^{t}BuOOH titration experiments were performed for **2**, and the observed reaction chemistry parallels that described for **1**. For example, ~0.5 equivalents of ^{t}BuOOH are required to convert **2** into the Mn^{III}-hydroxo complex **2a** in the presence of Et_3N (Figure A2.9). The addition

of approximately 100 equivalents of ^{t}BuOOH to **2a** in the presence of Et_3N leads to the maximum formation of a new chromophore, **2b**, which shows a prominent absorption band of 690 nm (ε = 115 $M^{-1}cm^{-1}$, Figure A2.10). The perpendicular-mode EPR spectrum of **2b** has a sharp signal near g = 2.0 attributable to the ^{t}BuOO$^\bullet$ radical (Figure A2.11).

Characterization of 1b and 2b. The electronic absorption spectra of both **1b** and **2b** bear resemblance to spectra previously reported for Mn^{III}-alkylperoxo complexes (Table 3.1). For example, the Mn^{III}-alkylperoxo complexes reported by Kovacs *et al.* show broad absorption features with λ_{max} values from 585 to 600 nm (extinction coefficients from 320 to 575 $M^{-1}cm^{-1}$), which were tentatively attributed to Mn^{III} ligand-field transitions.[37,38] In comparison, **1b** and **2b** show weak bands near 700 nm (Figure 3.5, left and Table 3.1). In addition, the Mn^{III}-alkylperoxo complexes of Kovacs and co-workers showed more intense, higher energy absorption features with λ_{max} values ranging from 355 to 420 nm (extinction coefficients from 240 to 1060 $M^{-1}cm^{-1}$).[37,38] These bands were attributed to alkylperoxo $\pi_{ip}^* \rightarrow Mn^{III}$ charge-transfer (CT) transitions, where the alkylperoxo π_{ip}^* MO is the O–O π-antibonding MO that lies in-plane with the Mn–O bond axis (*vide infra*). The analogous bands for **1b** and **2b** appear as shoulders at ~475 nm, with significant overlap with more intense bands in the near-UV region (Figure 3.5, left and Table 3.1).

Further support for the assignment of **1b** as the Mn^{III}-*t*-butylperoxo complex, $[Mn^{III}(OO^tBu)(dpaq)]^+$, comes from FT-IR experiments. The solution FT-IR spectrum of **1b** is dominated by vibrations from the large excess of ^{t}BuOOH (100 equivalents) required for the formation of **1b**. However, the FT-IR spectrum of the still cold reaction solution of **1b** shows a feature at 872 cm^{-1} (Figure 3.5, right panel), which is not observed in the FT-IR spectrum of ^{t}BuOOH or **1a** in MeCN (Figure A2.12). The FT-IR spectrum of **1b** also includes a weak feature at 821 cm^{-1} that could be due to a small amount of residual **1a** in solution (Figure A2.12). The band

at 872 cm^{-1} is absent in a sample of **1b** prepared using $^{t}Bu^{18}O^{18}OH$, further supporting the assignment of this feature as an O–O vibration (Figure 3.5, right). The isotopically-labeled sample of **1b** displays two new features at 836 and 819 cm^{-1}. Assuming the O–O vibration behaves as a harmonic oscillator, a $^{16}O/^{18}O$ isotopic shift of 51 cm^{-1} is expected. The 819 cm^{-1} vibration observed for isotopically-labeled **1b** would correspond to an isotopic shift of 53 cm^{-1}, in good agreement with the prediction. While the appearance of the second new band at 836 cm^{-1} for isotopically-labeled **1b** is difficult to rationalize, we note that coupling of the O–O and *t*-butyl C–C vibrations in high-spin Fe^{III}-alkylperoxo adducts has been observed to give rise to two vibrations near 850 cm^{-1}.[69] On the basis of these collective observations, we assign the 872 cm^{-1} mode to the O–O stretching vibration of **1b**. The energy of this vibration is comparable to O–O vibrations reported for other Mn^{III}-alkylperoxo complexes (875 to 893 cm^{-1}).[37,38] Corresponding FT-IR experiments performed for **2b** did not result in the observation of any bands attributable to the O–O vibration, presumably because this vibration overlaps with one of the intense vibrations of free ^{t}BuOOH (Figure A2.13).

Table 3.1. Comparison of Electronic Absorption Band Maxima (nm), Mn–O and O–O Distances (Å), and O–O Stretching Frequencies ($\nu_{O\text{-}O}$; cm^{-1}) for Mn^{III}-alkylperoxo Complexes.

Complex	λ_{max}		O–O	Mn–O	$\nu_{O\text{-}O}$
$[Mn^{III}(OO^{t}Bu)(dpaq)]^{+}$	~475	710	1.477[a]	1.837[a]	872
$[Mn^{III}(OO^{t}Bu)(dpaq^{2Me})]^{+}$	~475	690	1.477[a]	1.840[a]	--
$[Mn^{III}(S^{Me2}N_4(6\text{-Me-DPPN}))(OO^{t}Bu)]^{+}$ [b]	420	585	1.431	1.843	893
$[Mn^{III}(S^{Me2}N_4(QuinoPN))(OO^{t}Bu)]^{+}$ [b]	415	590	1.438	1.840	895
$[Mn^{III}(S^{Me2}N_4(QuinoEN))(OO^{t}Bu)]^{+}$ [b]	385	590	1.457	1.848	888
$[Mn^{III}(S^{Me2}N_4(6\text{-Me-DPEN}))(OO^{t}Bu)]^{+}$ [b]	355	600	1.468	1.853	875

[a] From DFT computations. [b] From ref. 37 and 38.

The formulations of **1b** and **2b** were further bolstered by analysis of Mn K-edge X-ray absorption (XAS) data. The XAS technique was previously used to characterize the related Mn^{II} complexes **1** and **2**, as well as the Mn^{III}-hydroxo species **1a** and **2a**,[70] making it straightforward to compare Mn oxidation state and metric parameters for **1b** and **2b** relative to these structurally well-defined complexes. The Mn K-edge energies of **1b** and **2b** (6550.4 and 6549.5 eV, respectively) are essentially identical to those observed for the Mn^{III}-hydroxo complexes **1a** and **2a** (Figure 6), and 1.5-2.5 eV higher in energy than the Mn^{II} complexes **1** and **2** (Table 3.2). In addition, the pre-edge features observed for **1b** and **2b** are of similar energy and area as those of **1a** and **2a** (Table 3.2). Because the energetic position of the Mn K-edge and pre-edge features are very sensitive to changes in Mn oxidation data, and the pre-edge areas are reflective of Mn geometry, these similarities provide strong support that **1b** and **2b** contain Mn^{III} centers with Mn-ligand metric parameters comparable to those of **1a** and **2a**. More detailed structural comparisons were afforded by analysis of extended X-ray absorption fine structure (EXAFS) data collected for **1b** and **2b**.

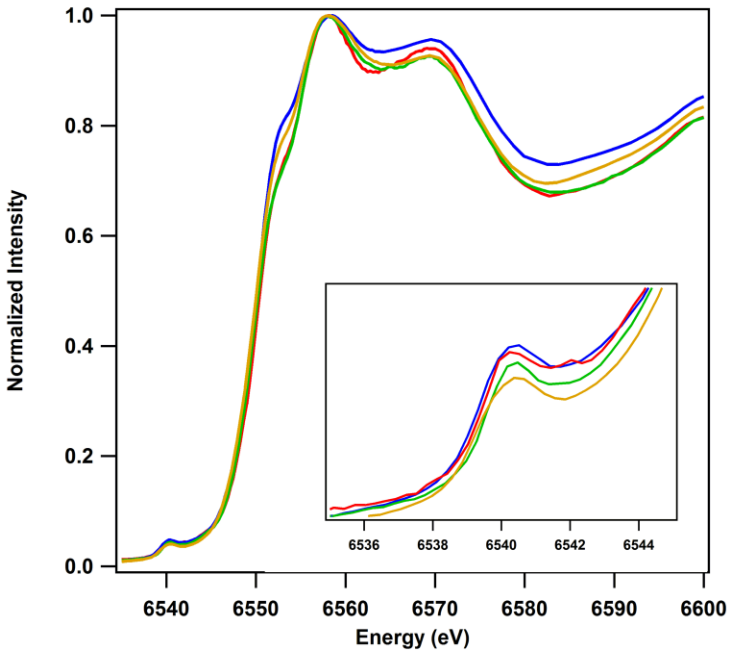

Figure 3.6. Comparison of Mn K-edge near-edge spectra of **1a** (blue)**, 1b** (red)**, 2a** (orange)**, 2b** (green) collected for frozen solutions in MeCN at 15 K. **Inset:** Pre-edge features of the four complexes.

Table 3.2. Comparison of XANES data between **1**, **1a**, **1b**, **2**, **2a**, and **2b**. All data are from sample solutions frozen in MeCN.

Complex	Pre-edge energy (eV)	Pre-edge area	Edge energy (eV)
$[Mn^{II}(dpaq)]^+$ (**1**)[a]	6540.2	4.9	6547.9
$[Mn^{II}(dpaq^{2Me})]^+$ (**2**) [a]	6540.2	4.3	6548.6
$[Mn^{III}(OH)(dpaq)]^+$ (**1a**) [a]	6540.2	4.3	6550.6
	6541.8		
$[Mn^{III}(OH)(dpaq^{2Me})]^+$ (**2a**) [a]	6540.2	4.1	6550.0
	6541.6		
$[Mn^{III}(OO^tBu)(dpaq)]^+$ (**1b**)	6540.2	4.6	6550.4
	6542.0		
$[Mn^{III}(OO^tBu)(dpaq^{2Me})]^+$ (**2b**)	6540.5	4.1	6549.5
	6541.7		

[a]Data from reference 65.

The Fourier transform of the EXAFS data of **1b** consists of an intense peak at 1.79 Å that has shoulders at 1.18, 1.43, 2.10, and 2.41 Å (Figure 3.7). This set of EXAFS peaks is best fit using a shell of two O/N atoms at 1.90 Å and a shell of five N atoms at 2.17 Å (Table 3.3). The Mn^{III}-OOR series of complexes previously reported by Kovacs and co-workers displayed Mn–OO^tBu distances ranging from 1.840 – 1.861 Å.[38] In addition, the X-ray structure of **1a** displays a Mn–N(amide) distance of 1.975 Å.[39] Because we are fitting EXAFS data for **1b** within a k-window of 2 – 14 $Å^{-1}$, the Mn–OO^tBu and Mn–N(amide) shells are expected to fall within the resolution of 0.13 Å. Accordingly, the shell at 1.90 Å likely includes contributions from both axial ligands; *i.e.*, the *t*-butylperoxo oxygen and the amide nitrogen. The EXAFS data of **1a** in MeCN were also best fit including a shell at 1.92 Å that accounted for both axial ligands.[70] The shell of five nitrogen scatterers at 2.17 Å is attributed to the equatorial nitrogen ligands. In support, the X-ray diffraction structure of **1a** shows an average Mn–N distance of 2.18 Å.[39] It is important to note that the goodness of fit does not change appreciably when going from a fit including four N scatterers to a fit including five N scatterers (Table 3.3). This insensitivity to the number of scatterers is consistent with the low sensitivity of EXAFS fits to the number of scatterers within a given shell, which has been reported to have an intrinsic uncertainty of ±1.[71] A shell of 6 C atoms at ~2.97 Å was included to account for the second coordination sphere. For comparison, crystal structure data of **1a** show an average Mn---C distance of 3.02 Å for atoms within the same radius as the EXAFS fitting shell.[39]

The Fourier transform of the EXAFS data for **2b** is very similar to that of **1b** (Figure 3.7). Therefore, fits of the EXAFS data for **2b** resulted in similar Mn-scatter distances; specifically, two O/N atoms at 1.89 Å, four N atoms at 2.16 Å, and six C atoms at 2.93 Å (Table 3.3). Collectively,

our analysis of XAS data for **1b** and **2b** support the formulation of these complexes as Mn^{III}-alkylperoxo adducts.

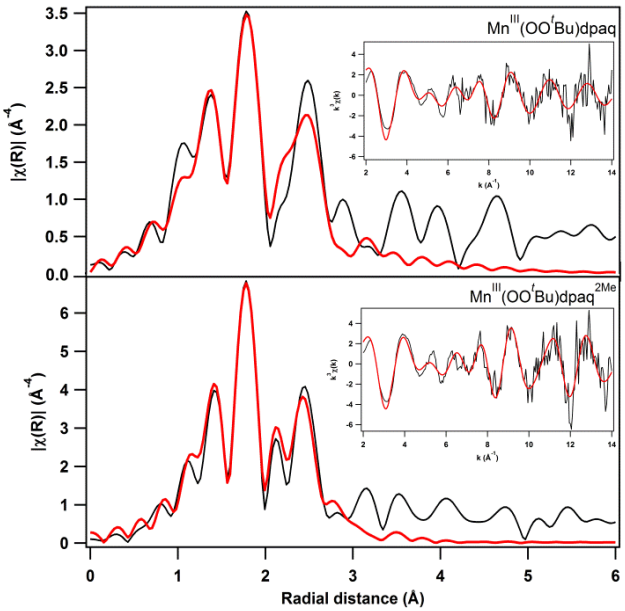

Figure 3.7. Fourier transforms of Mn K-edge EXAFS data, and EXAFS spectra (inset), for **1b** (top) and **2b** (bottom) in frozen MeCN. Experimental data are in black, while (black line) and fits (red lines).

Table 3.3. Fits of EXAFS data of **1b** and **2b**.[a]

Fit	Mn─N			Mn─O/N			Mn─C			Goodness of Fit[b]
	n	r(Å)	σ^2 (Å^2)	n	r(Å)	σ^2 (Å^2)	n	r(Å)	σ^2 (Å^2)	
$[Mn^{III}(OO^tBu)(dpaq)]^+$ **(1b)**										
1	6	2.47	0.032							0.685
2	4	2.16	0.007	2	1.89	0.005				0.402
3	4	2.17	0.007	2	1.90	0.005	6	2.97	0.010	0.225
4	***5***	***2.17***	***0.009***	***2***	***1.90***	***0.004***	***6***	***2.97***	***0.010***	***0.212***
$[Mn^{III}(OO^tBu)(dpaq^{2Me})]^+$ **(2b)**										
1	6	1.84	0.022							0.900
2	4	2.15	0.004	2	1.89	0.003				0.386
3	***4***	***2.16***	***0.004***	***2***	***1.89***	***0.003***	***6***	***2.93***	***0.005***	***0.255***

[a] Fits highlighted in bold, italic font represent the best fits to the EXAFS data. [b] Evaluated using the R-factor.

Table 3.4. Comparison of EXAFS fits of **1b** and **2b** to DFT-optimized structures (distances in Å).

	$[Mn^{III}(OO^tBu)(dpaq)]^+$ (**1b**)		$[Mn^{III}(OO^tBu)(dpaq^{2Me})]^+$ (**2b**)	
	EXAFS	DFT	EXAFS	DFT
Mn–O/N_{ax}	1.90	1.837(O), 1.992(N)	1.89	1.840(O), 1.985(N)
Mn–O_{distal}	ND[a]	2.709	ND[a]	2.766
O–O	ND[a]	1.477	ND[a]	1.477
∠Mn–O–O	NA[b]	109.16°	NA[b]	112.54°
Mn–N_{eq}	2.17	2.079(N_Q[c]), 2.177(avg.)	2.16	2.149(N_Q[c]), 2.182 (avg.)
Mn---C	2.97	3.005[d]	2.93	2.979[e]

[a] Not determined. [b] Not applicable. [c] N_Q refers to the nitrogen donor atom of the quinoline ring. [d] Average distance of 9 carbon atoms ranging from 2.901 to 3.070 Å. [e] Average distance of 9 carbon atoms ranging from 2.881 to 3.059 Å.

Thermal Decay of 1b and 2b. Complexes **1b** and **2b** have half lives of $t_{1/2}$ = 3200 and 3600 seconds, respectively, at -15 °C (for 2 mM solutions in MeCN). Unfortunately, the large excess of ^{t}BuOOH required to generate **1b** and **2b** complicates investigation of the decay mechanism. The decay is characterized by a loss of electronic absorption intensity at ~710 nm, with the final decay spectrum of **1b** showing no clearly defined bands (Figure 3.8 and S14). Although no precipitation was observed, the thermal decay of both **1b** and **2b** is accompanied by significant gas evolution. The gas is presumed to be dioxygen, as alkylperoxyl radicals are known to undergo decomposition that leads to the production of O_2 (Equation 3.1).[72]

$$2\ {\bullet}OO^tBu \rightarrow {}^tBuO{-}O^tBu + O_2 \qquad (3.1)$$

The presence of O_2 in the headspace of a decaying sample of **1b** was confirmed by allowing the headspace gas to pass through an anaerobic 2 mM solution of **1** in MeCN. The Mn^{II} complex **1** is known to react with O_2 to produce the Mn^{III}-hydroxo **1a**.[39] After stirring for 2 hours while continuing to pass the headspace gas through the solution, formation of **1a** was confirmed by

electronic absorption spectroscopy (~40% yield relative to the initial concentration of **1**). EPR analysis of frozen solutions of the decay products revealed a loss of intensity of the sharp signal due to ^{t}BuOO$^{\bullet}$ radical (Figures A2.15 and A2.16), consistent with the decay of this radical to give dioxygen.[66,72] The EPR spectra of the decay solutions of **1b** and **2b** also display six-line signals corresponding to mononculear Mn^{II} products (Figures A2.15 and A2.16), although the intensity of these signal are modest. No signals associated with a $Mn^{III}Mn^{IV}$ dimer are observed. Analysis of the decayed reaction solutions by electrospray ionization mass spectrometry revealed weak signals associated with the Mn^{III}-hydroxo species **1a**, which could be formed by O_2 oxidation of a Mn^{II} product (Figure A2.17). Collectively, the electronic absorption and EPR characterization of the decay solutions of **1b** and **2b** provide limited insight into the nature of the decay products, rendering it challenging to determine by which mechanism(s) the Mn^{III}-alkylperoxo adducts decay.

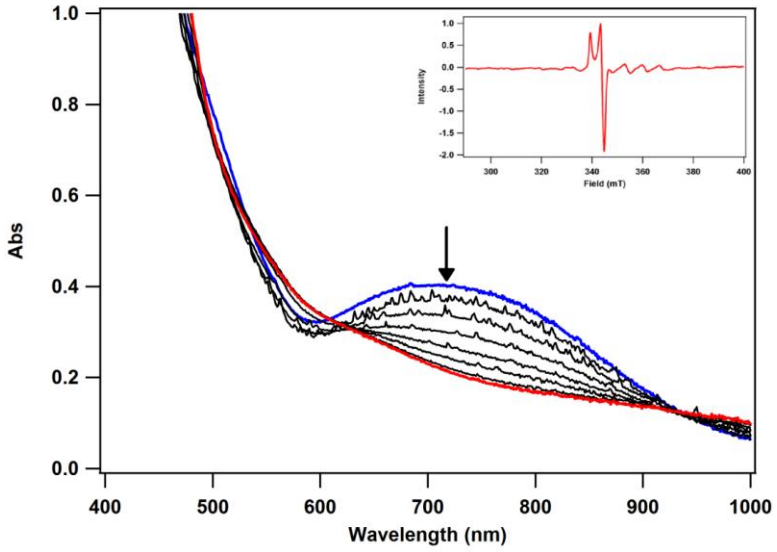

Figure 3.8. UV-Vis spectra of the decay of **1b** in MeCN at -15°C. Inset: X-band EPR spectrum of reaction solution showing a less intense radical signal from excess ^{t}BuOOH and a weak six-line signal typical of a Mn^{II} species.

DFT Calculations of 1b and 2b. In order to compare the bonding in the Mn–OO^{t}Bu units of **1b** and **2b** with those of the previously reported Mn^{III}-alkylperoxo adducts with N_4S^- ligation, we performed DFT calculations for complexes **1b** and **2b**. The structures afforded by these computations, which are shown in Figure 3.9, have the alkylperoxo ligand *trans* to the dpaq amide group, giving six-coordinate Mn^{III} centers. The DFT-computed Mn–OO^{t}Bu distances are 1.837 and 1.840 Å for **1b** and **2b**, respectively, which are within the range of, or just shorter than, the Mn–OO^{t}Bu distances previously observed by X-ray crystallography for complexes with N_4S^- ligation (1.840 – 1.861 Å).[38] The comparatively short Mn–O distances are somewhat surprising, given that the *trans* amide donor of the dpaq and dpaq^{2Me} ligands might be expected to exert a *trans* influence, elongating the Mn–OO^{t}Bu bond length. The computed Mn^{III}–OO^{t}Bu distances for **1b** and **2b** are also longer than the crystallographic distances of the corresponding Mn^{III}-hydroxo complexes **1a** and **2a** (1.806(13) and 1.819(3), respectively),[39,40] but the Mn^{III}–N_{amide} distances are quite similar (1.99 Å versus 1.98 Å for Mn^{III}-alkylperoxo and Mn^{III}-hydroxo complexes, respectively).[39,40] The DFT-computed Mn–OO^{t}Bu and Mn^{III}–N(amide) distances lead to average Mn–N/O_{axial} distances of 1.91 Å for both **1b** and **2b**, which are in good agreement with the EXAFS distances obtained for the two-atom N/O scattering shells (~1.9 Å; see Table 3.4). In addition, the average Mn–$N_{equatorial}$ distances for the DFT-computed structures of **1b** and **2b** (2.18 Å for both), are in good agreement with the corresponding distances of four-atom EXAFS shells (Table 4). The calculated Mn–$N_{equatorial}$ distances of **1b** cover the range of 2.08 - 2.27 Å, while the calculated distances of **2b** fall in a more narrow range of 2.13 - 2.26 Å. The DFT optimized O–O distances for **1b** and **2b** were both calculated to be 1.477 Å (Table 3.4), which are longer than those reported for previous Mn^{III}-alkylperoxo complexes (1.431-1.468 Å).[37,38]

The calculated Mn^{III} 3*d* orbital splitting patterns of **1b** and **2b** are shown in Figure 3.10. The Mn^{III} 3*d* orbitals are labeled according to a coordinate system with the *z*-axis along the Mn–O bond and the *y*-axis along the Mn–$N_{quinoline}$ bond (Figure 3.9). Calculations suggest substantial mixing of the Mn^{III} 3*d*-orbitals with both dpaq and alkylperoxo ligand orbitals (Tables A2.3 and A2.4). In many cases, Mn^{III} 3*d* orbital character is distributed over several molecular orbitals (MOs). Surface contour plots of the frontier MOs of **1b** show that the Mn $3d_{z^2}$ MO (a σ-type orbital) has significant contributions from the strongly donating *trans* amide N (7.1%) and the in plane π^* orbital of the alkylperoxo moiety (12.8% oxygen character; Figure 11). In contrast, little contribution from the out of plane π^* orbitals of the alkylperoxo ligand is observed in the π-type Mn^{III} $3d_{xz}$ and $3d_{yz}$ orbitals (3.4% and 2.7% oxygen character, respectively; Table A2.3, Figure A2.18). Thus, the Mn^{III}–alkylperoxo bonding in **1b** is dominated by a Mn–OO^{t}Bu σ-interaction, with little apparent Mn=OO^{t}Bu character. Frontier MO calculations for **2b** predict similar alkylperoxo bonding as compared to that observed for **1b** (Figure A2.19, Table A2.4), consistent with the spectroscopic similarities between the two species.

The TD-DFT calculated absorption spectrum for **1b** corresponds well to the experimental spectrum (Figure 3.12). Band **i**, which is predicted at 731 nm, is in good agreement with the feature at 710 nm in the experimental spectrum. This low-intensity feature arises from a d-d transition from Mn $d_{x^2-y^2}$ to d_{z^2}, which is the lowest energy Mn^{III} d-d transition (Figure 3.10 and Table A2.5). Band **ii**, which corresponds to the poorly defined experimental band around 475 nm, is calculated to include contributions from both dpaq-to-Mn^{III} ligand-to-metal charge transfer (LMCT) and alkylperoxo-to-Mn^{III} LMCT transitions. The TD-DFT-calculated absorption spectrum of **2b** also corresponds well to experiment (Figure A2.20). Mn d-d transitions and LMCT features are observed at similar energies to **1b** and to previously reported Mn^{III}-alkylperoxo complexes.[38] For

both complexes, TD-DFT calculations predict additional alkylperoxo-to-Mn CT transitions and another Mn d-d transition (d_{xy} to d_{z^2}) at higher energies (band **iii** in Figures 12 and S20; see also Tables A2.5 and A2.6).

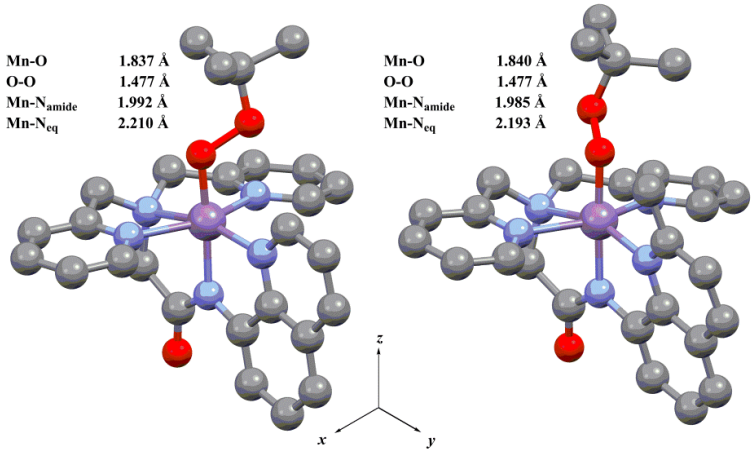

Figure 3.9. DFT optimized structures of **1b** (left) and **2b** (right).

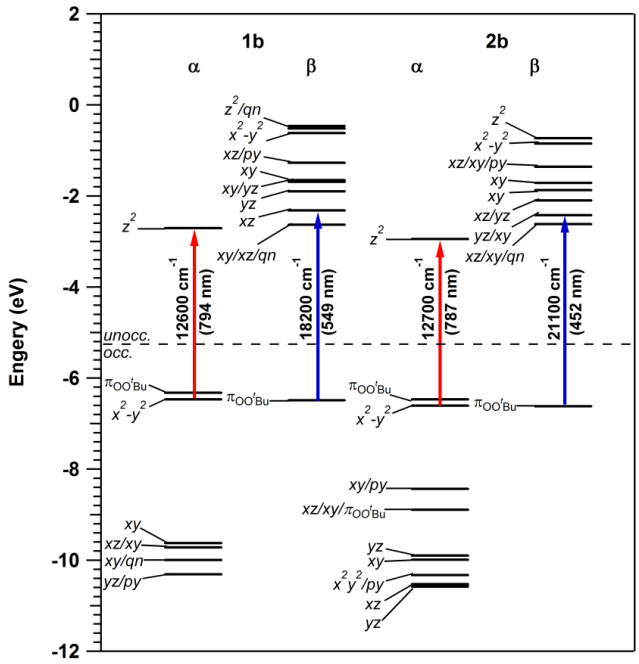

Figure 3.10. Molecular orbital (MO) energy-level diagrams for **1b** (left) and **2b** (right) obtained from DFT calculations. MOs are labeled according to their principal contributors, which reveal a high degree of mixing (py = pyridine, qn = quinoline). For clarity, only Mn^{III} d-based and OO^tBu π*-based MOs are included. TD-DFT-calculated transition energies of prominent electronic transitions are also displayed.

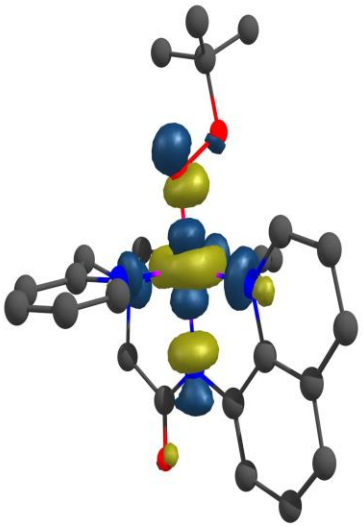

Figure 3.11. Surface contour plot of spin up, unoccupied Mn^{III} $3d_{z^2}$ MO of **1b** as calculated by DFT calculations. The contour plot reveals significant contribution from the alkylperoxo moiety and the *trans*-amide N of the dpaq ligand.

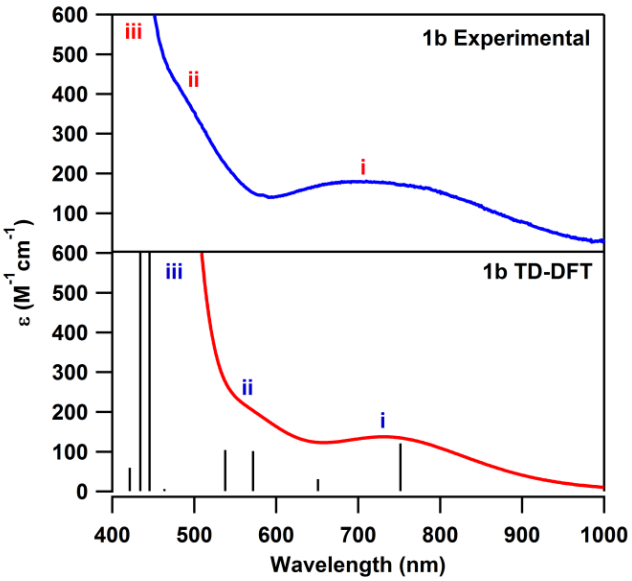

Figure 3.12. Comparison of experimental (top) and simulated (bottom) absorption spectra of **1b** based on TD-DFT calculations. Calculated spectra show a feature arising from a Mn $d_{x^2-y^2}$ to d_{z^2} transition (**i**), higher energy features arising from ligand-to-metal charge transfer from both dpaq and the alkylperoxo moiety to Mn^{III} (**ii**)**,** and higher intensity features corresponding to additional ligand-to-metal charge transfers and a d_{xy} to d_{z^2} transition (**iii**).

3.4 Discussion. At present, knowledge of both synthetic and biological Mn^{III}-alkylperoxo intermediates is quite limited. Although a Mn^{III}-alkylperoxo adduct has been proposed as a potential intermediate in Mn-LOX (Scheme 3.1), there is no direct evidence for the formation of such a species.[15,17,18] To date, only a handful of synthetic Mn^{III}-alkylperoxo complexes have been isolated and characterized. Of these complexes, all feature N_4S^- supporting ligands with the thiolate donor *cis* to the alkylperoxo ligand.[37,38] In this present work, we have generated and characterized two new Mn^{III}-alkylperoxo species supported by N_5^- ligands that feature a strongly donating anionic amide ligand *trans* to the alkylperoxo unit. Although the Mn^{III}-alkylperoxo complexes **1b** and **2b** were able to be characterized by an array of spectroscopic methods, the extreme excess of oxidant necessary for their full formation rendered it difficult to determine the decay mechanism, and prevented any meaningful investigations of reactivity with substrates. However, the reaction pathway for formation of the Mn^{III}-alkylperoxo complexes **1b** and **2b** from their Mn^{II} precursors is informative when compared to formation reactions of other metal-alkylperoxo adducts. Additionally, a structural and spectroscopic comparison of **1b** and **2b** with previously reported Mn^{III}-alkylperoxo species with N_4S^- ligations provides insight into spectro-structural correlations for this class of compounds.

Reactions of 1 and 2 with ^{t}BuOOH. Initial treatment of the Mn^{II} complexes **1** or **2** with 0.5 equivalents of ^{t}BuOOH led to the quantitative formation of the mononuclear Mn^{III}-hydroxo complexes **1a** and **2a** (Figure 3.2). On the basis of the stoichiometry of this reaction, as well as the observation of $[Mn^{III}(O^tBu)(dpaq)]^+$ by ESI-MS experiments (Figure A2.1), we postulate a reaction pathway involving homolytic cleavage of the O–O bond of ^{t}BuOOH to initially give Mn^{III}-hydroxo and Mn^{III}-^{t}butoxide species (Scheme 3.3, top). We have previously generated and characterized the Mn^{III}-methoxide complex $[Mn^{III}(OMe)(dpaq)]^+$, which has electronic absorption

signals nearly identical to those of **1a**.[62] Thus, under the reasonable assumption that the $[Mn^{III}(OMe)(dpaq)]^+$ and $[Mn^{III}(O^tBu)(dpaq)]^+$ complexes would have similar electronic absorption band maxima and intensities, formation of a mixture of Mn^{III}-hydroxo and Mn^{III}-*t*-butoxide species in the reaction of **1** with ^{t}BuOOH would be compatible with our electronic absorption data (Figure 3.2). Because ESI-MS experiments on solutions of **1** with 0.5 equivalents ^{t}BuOOH predominantly show peaks associated with **1a**, we propose that water present in the MeCN and/ or ^{t}BuOOH solutions converts the majority of the initially formed Mn^{III}-^{t}butoxide species to **1a** through a ligand substitution reaction. In support, we have previously demonstrated that **1a** and the Mn^{III}-methoxy analogue $[Mn^{III}(OMe)(dpaq)]^+$ can be readily interconverted by the addition of MeOH or H_2O.[62]

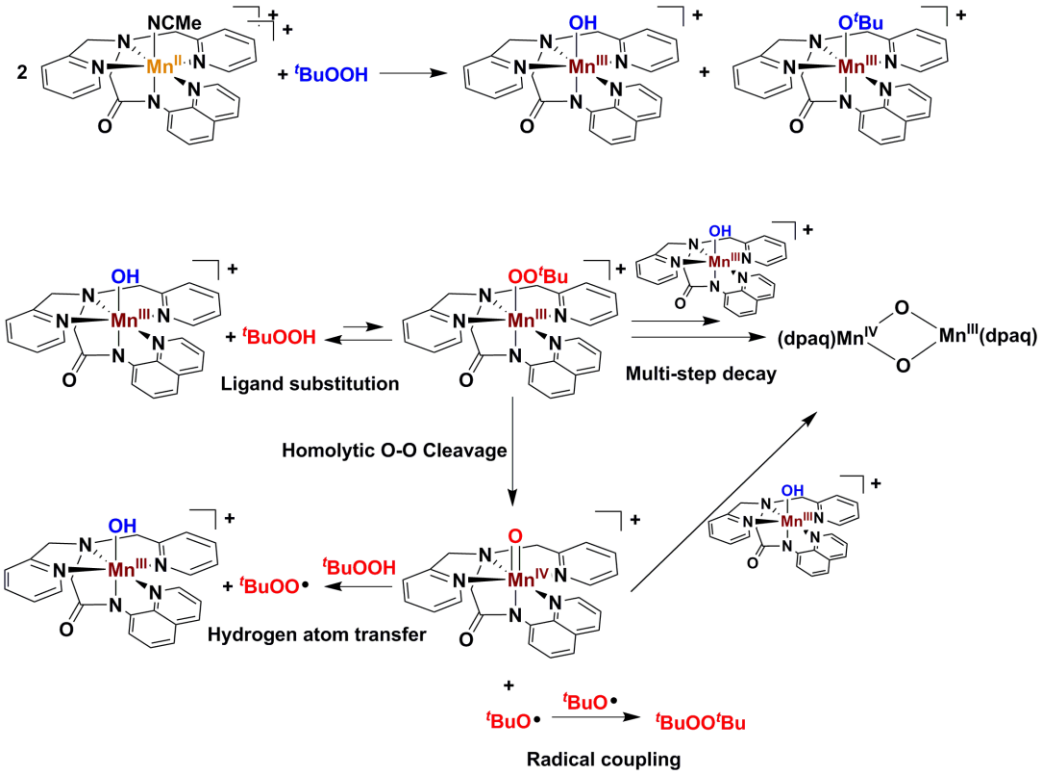

Scheme 3.3. Postulated reaction pathways for formation of Mn^{III}-hydroxo, bis-μ-oxo-dimanganese(III,IV), and Mn^{III}-alkylperoxo species formed from the reaction of **1** with ^{t}BuOOH.

Formation of a metal(III)-hydroxo species by ^{t}BuOOH oxidation of a metal(II) precursor has been reported for other systems. For example, Que and co-workers observed that the addition of 0.5 equivalents of ^{t}BuOOH to the Fe^{II} complex $[Fe^{II}(6\text{-Me-TPA})(O_2CAr)]^+$ (TPA = trispyridylmethylamine) resulted in complete conversion to the mononuclear Fe^{III}-hydroxo complex $[Fe^{III}(OH)(6\text{-Me-TPA})(O_2CAr)]^+$.[73] Further addition of five equivalents ^{t}BuOOH to $[Fe^{III}(OH)(6\text{-Me-TPA})(O_2CAr)]^+$ gave the corresponding Fe^{III}-alkylperoxo complex $[Fe(OO^tBu)(6\text{-Me-TPA})(O_2CAr)]^+$.[73] This result stands in contrast to the reactivity we have described here, where treatment of the Mn^{III}-hydroxo complex **1a** leads to different products depending on the amount of ^{t}BuOOH added.

Electronic absorption experiments suggest that treatment of **1a** with excesses of ^{t}BuOOH below 100 equivalents in the presence of a base results in a mixture of products (Figure 3.3). At 50 equivalents of ^{t}BuOOH and 10 equivalents Et_3N, a bis-μ-oxo-dimanganese(III,IV) dimer is formed. For comparison, Nam and co-workers observed that the addition of H_2O_2 to **1a** results in formation of the $[Mn^{III}Mn^{IV}(\mu\text{-O})(dpaq)]^{2+}$ complex.[63] In contrast, when **1a** is treated with 100 equivalents of ^{t}BuOOH and 10 equivalents Et_3N, formation of the Mn^{III}-alkylperoxo species **1b** is observed. Under these conditions, EPR experiments show no signals associated with the bis-μ-oxo-dimanganese(III,IV) dimer. Species **1b** could also be observed following the addition of 50 equivalents of ^{t}BuOOH to **1a** in the absence of added base (Figure A2.8); however, the spectral evolution for the reaction of **1a** and ^{t}BuOOH differs from that observed with the addition of 100 equivalents of ^{t}BuOOH (cf. Figures 3.5 and A2.8).

We propose a reaction pathway, summarized in Scheme 3.3, that accounts for these observations. First, the addition of ^{t}BuOOH to **1a** establishes an equilibrium between the Mn^{III}-hydroxo and Mn^{III}-alkylperoxo species, which are related by a ligand substitution (Scheme 3.3).

This step is influenced by the presence of Et_3N, which serves to deprotonate ^{t}BuOOH, facilitating exchange of ^{t}BuOO$^-$ with the hydroxide ligand. At small excesses of ^{t}BuOOH and base, this equilibrium lies predominantly to the left, in favor of the Mn^{III}-hydroxo species **1a**. Under these conditions, the Mn^{III}-alkylperoxo adduct **1b** could react directly with **1a**, forming the bis-μ-oxo-dimanganese(III,IV) dimer in a multistep process. An alternative decay pathway for **1b** could involve O–O homolysis to yield a Mn^{IV}-oxo species that could react with **1a** to again give the bis-μ-oxo-dimanganese(III,IV) dimer. Additionally, this Mn^{IV}-oxo species could be capable of abstracting a H atom from ^{t}BuOOH to generate **1a** and ^{t}BuOO radical. These scenarios are illustrated in Scheme 3.3.

In contrast, when **1a** is treated with a large excesses of ^{t}BuOOH (100 equivalents or greater), the ligand substitution equilibrium favors the Mn^{III}-alkylperoxo species **1b**. This relatively straightforward reaction is supported by the apparent isosbestic behavior observed by electronic absorption spectroscopy for this reaction (Figure 3.5, left). Under similar reaction conditions, but lacking added base, the formation of **1b** is more complex, as evidenced by the lack of isosbestic points for these reactions (Figure A2.8). In addition, EPR spectra collected for solutions of **1a** treated with 100 equivalents of ^{t}BuOOH and base lack any signals associated with the bis-μ-oxo-dimanganese(III,IV) dimer. The only signals observed are from a small amount of ^{t}BuOO·, which could result from homolytic decay of the Mn–OO^{t}Bu bond of **1b**. ^{t}BuOO· radicals are known to couple to form O_2 and relatively stable ^{t}BuOO^{t}Bu species.[72] Thus, the evolution of O_2 during the decay of **1b** could support a Mn–O homolysis pathway. This decay mechanism would yield the $[Mn^{II}(dpaq)]^+$ starting material, which could react further with O_2 in solution to generate **1a**. Although ESI-MS experiments for the decay solutions show the presence of **1a**, the electronic absorption spectrum of the corresponding solution is not consistent with the clean

conversion of **1b** to **1a** during the thermal decay of the former (Figure 3.8). Thus, the decay pathway is likely more complex than simple Mn–O homolysis.

The seemingly complex pathway required for the formation of **1b** and **2b** stands in sharp contrast to previously reported routes for generating Mn^{III}-alkylperoxo adducts reported by Kovacs and co-workers. In those examples, the $[Mn^{II}(N_4S)]^+$ complexes (where N_4S^- represent a variety of pentadentate ligands with thiolate, amine, imine, and bis-2-Me-pyridine or bis-quinoline ligation) yield the corresponding $[Mn^{III}(OO^tBu)(N_4S)]^+$ species in high yield when treated with only 2 equivalents of ^{t}BuOOH and base.[37,38] There was no evidence for formation of a mononuclear Mn^{III}-hydroxo intermediate or multinuclear intermediates, suggesting that particular properties of the supporting ligands influence the stabilities and/ or rates of formation and decay of such species. In addition, a large body of experimental evidence suggests that the $[Mn^{III}(OO^tBu)(N_4S)]^+$ complexes decay by O–O cleavage, while there is indirect, and circumstantial, evidence that **1b** decays by Mn–O cleavage. An understanding of how ligand properties modulate Mn reactivity towards ^{t}BuOOH is clearly in its infancy.

Spectroscopic and structural comparison with previous Mn^{III}-alkylperoxo complexes. The Mn^{III}-alkyperoxo complexex **1b** and **2b** show very similar spectroscopic properties, consistent with their nearly identical coordination spheres (Figure 3.9). The only notable spectroscopic difference between the two is a 20 nm (400 cm^{-1}) blue-shift in the lowest-energy electronic absorption band for **2b** compared to **1b**. TD-DFT computations allowed us to assign this absorption band as the Mn^{III} $3d_{x^2-y^2}$ to $3d_{z^2}$ transition. Because the Mn^{III}-alkylperoxo bonding descriptions afforded by DFT computations are quite similar, we can attribute the modest shift in this electronic transition to the subtly different properties of the dpaq and $dpaq^{2Me}$ ligands. The inclusion of the 2-methyl-quinoline group in **2b** leads to a weaker $Mn–N_{quinoline}$ interaction, as described

previously.[40] This weakened interaction should stabilize the energy of the $3d_{x^2-y^2}$ MO, which is largely Mn^{III}-dpaq -antibonding, causing the observed blue-shift for **2b** relative to **1b**.

For comparison, the $[Mn^{III}(OO^tBu)(N_4S)]^+$ complexes of Kovacs and co-workers show a corresponding electronic absorption feature that ranges from 600 – 585 nm, at significantly higher energy than the bands of **1b** and **2b**. The $[Mn^{III}(OO^tBu)(N_4S)]^+$ complexes contain two 6-Me-pyridine or quinoline donors in the equatorial plane *cis* to the alkylperoxo ligand. X-ray structures show highly elongated Mn^{III}–N distances of 2.354 to 2.522 Å, suggesting very weak interactions.[38] Accordingly, we attribute the more substantial blue-shift of these bands to further stabilization of the Mn^{III} $3d_{x^2-y^2}$ donor orbitals due to the equatorial bond elongations.

The O–O vibrational frequency observed for **1b** is on the low end of O–O vibrations reported for the $[Mn^{III}(OO^tBu)(N_4S)]^+$ series (Table 3.1). While this observation is consistent with the relatively long O–O bond of **1b** predicted by DFT computations, this comparison must be made with caution. The $^{16}O/^{18}O$ isotopic shifts observed for the $[Mn^{III}(OO^tBu)(N_4S)]^+$ complexes did not follow that predicted on the basis of a harmonic oscillator model, suggesting some vibrational coupling. In addition, isotopic labeling of **1b** led to the appearance of two additional IR features (Figure 5, right), also suggestive of coupling. Thus, care should be taken in relating the O–O vibrational frequencies of these complexes to the O–O bond strength.

3.5 Conclusions. Spectroscopic and structural studies of two new Mn^{III}-alkylperoxo complexes described in this work add to the otherwise limited knowledge base for this class of compound. The axial donating amide motif employed herein is unique among model manganese-alkylperoxo complexes, and the variety of species apparent in reactions of **1** with ^{t}BuOOH reveals the versatility of this platform in supporting biologically relevant intermediates. Complexes **1** and **2** were shown to react with ^{t}BuOOH to generate the previously characterized Mn^{III}-hydroxo

species **1a** and **2a.** These Mn^{III}-hydroxo adducts could react with ^{t}BuOOH to form the Mn^{III}-alkylperoxo species **1b** and **2b**. However, this conversion required a large excess of ^{t}BuOOH. Structural comparison with previously reported Mn^{III}-alkylperoxo complexes revealed a relatively short Mn–O bond, and DFT calculations suggest a long, and therefore more activated, O–O bond. Although the large excess of ^{t}BuOOH needed for full formation of the Mn^{III}-alkylperoxo species complicated investigations of reactivity, structural and spectroscopic characterization of these species points to the potential of the dpaq system, as well as other similar platforms that feature strongly donating *trans* ligand motifs, for the formation and activation Mn^{III}-alkylperoxo complexes.

3.6 References.

1. Sheng, Y.; Abreu, I. A.; Cabelli, D. E.; Maroney, M. J.; Miller, A.-F.; Teixeira, M.; Valentine, J. S. *Chem. Rev.* **2014,** *114*, 3854-3918.
2. Miller, A.-F. *Curr. Opin. Chem. Biol.* **2004,** *8*, 162-168.
3. Grove, L. E.; Brunold, T. C. *Comm. Inorg. Chem.* **2008,** *29*, 134-168.
4. Wu, A. J.; Penner-Hahn, J. E.; Pecoraro, V. L. *Chem. Rev.* **2004,** *104*, 903-938.
5. Svedružic, D.; Jónsoon, S.; Toyota, C. G.; Reinhardt, L. A.; Ricagno, S.; Lindqvist, Y.; Richards, N. G. J. *Arch. Biochem. Biophys.* **2005,** *433*, 176-192.
6. Yano, J.; Yachandra, V. *Chem. Rev.* **2014,** *114*, 4175-4205.
7. Leto, D. F.; Jackson, T. A. *J. Biol. Inorg. Chem.* **2014,** *19*, 1-15.
8. Sheng, Y.; Butler Gralla, E.; Schumacher, M.; Cascio, D.; Cabelli, D. E.; Selverstone Valentine, J. *Proc. Natl. Acad. Sci. U.S.A.* **2012,** *109*, 14314-14319.
9. Bull, C.; Niederhoffer, E. C.; Yoshida, T.; Fee, J. A. *J. Am. Chem. Soc.* **1991,** *113*, 4069-4076.
10. Hearn, A. S.; Tu, C. K.; Nick, H. S.; Silverman, D. N. *J. Biol. Chem.* **1999,** *274*, 24457-24460.
11. Porta, J.; Vahedi-Faridi, A.; Borgstahl, G. E. O. *J. Mol. Biol.* **2010,** *399*, 377-384.
12. Gunderson, W. A.; Zatsman, A. I.; Emerson, J. P.; Farquhar, E. R.; Que, L.; Lipscomb, J. D.; Hendrich, M. P. *J. Am. Chem. Soc.* **2008,** *130*, 14465-14467.
13. Kovaleva, E. G.; Lipscomb, J. D. *Science* **2007,** *316*, 453-457.
14. Skrzypczak-Jankun, E.; Bross, R. A.; Carroll, R. T.; Dunham, W. R.; Funk, M. O. *J. Am. Chem. Soc.* **2001,** *123*, 10814-10820.
15. Company, A.; Lloret-Fillol, J.; Costas, M. In *Small molecule models for nonporphyrinic iron and manganese oxygenases*, Elsevier B.V.: 2013; pp 487-564.
16. Glickman, M. H.; Klinman, J. P. *Biochemistry* **1995,** *34*, 14077-14092.
17. Su, C.; Sahlin, M.; Oliw, E. H. *J. Biol. Chem.* **2000,** *275*, 18830-18835.
18. Wennman, A.; Karkehabadi, S.; Oliw, E. H. *Arch. Biochem. Biophys.* **2014,** *555–556*, 9-15.
19. Lehnert, N.; Solomon, E. I. *J. Biol. Inorg. Chem.* **2003**, *8*, 294-305.
20. Costas, M.; Mehn, M. P.; Jensen, M. P.; Que, L., Jr. *Chem. Rev.* **2004,** *104*, 939-986.
21. Namuswe, F.; Hayashi, T.; Jiang, Y.; Kasper, G. D.; Sarjeant, A. A. N.; Moënne-Loccoz, P.; Goldberg, D. P. *J. Am. Chem. Soc.* **2010,** *132*, 157-167.

22. Namuswe, F.; Kasper, G. D.; Sarjeant, A. A. N.; Hayashi, T.; Krest, C. M.; Green, M. T.; Moënne-Loccoz, P.; Goldberg, D. P. *J. Am. Chem. Soc.* **2008,** *130*, 14189-14200.
23. Kim, J.; Larka, E.; Wilkinson, E. C.; Que, L. J. *Angew. Chem. Int. Ed.* **1995,** *34*, 2048-2051.
24. Rohde, J.-U.; Torelli, S.; Shan, X.; Lim, M. H.; Klinker, E. J.; Kaizer, J.; Chen, K.; Nam, W.; Que, L., Jr. *J. Am. Chem. Soc.* **2004,** *126*, 16750-16761.
25. Zang, Y.; Elgren, T. E.; Dong, Y.; Que, L. J. *J. Am. Chem. Soc.* **1993,** *115*, 811-813.
26. Hong, S.; Lee, Y.-M.; Cho, K.-B.; Seo, M. S.; Song, D.; Yoon, J.; Garcia-Serres, R.; Clemancey, M.; Ogura, T.; Shin, W.; Latour, J.-M.; Nam, W. *Chem. Sci.* **2014,** *5*, 156-162.
27. Jensen, M. P.; Mairata i. Payeras, A.; Fiedler, A. T.; Costas, M.; Kaizer, J.; Stubna, A.; Muenck, E.; Que, L., Jr. *Inorg. Chem.* **2007,** *46*, 2398-2408.
28. Krishnamurthy, D.; Kasper, G. D.; Namuswe, F.; Kerber, W. D.; Narducci Sarjeant, A. A.; Moeenne-Loccoz, P.; Goldberg, D. P. *J. Am. Chem. Soc.* **2006,** *128*, 14222-14223.
29. Ogihara, T.; Hikichi, S.; Akita, M.; Uchida, T.; Kitagawa, T.; Moro-oka, Y. *Inorg. Chim. Acta* **2000,** *297*, 162-170.
30. Shan, X.; Rohde, J.-U.; Koehntop, K. D.; Zhou, Y.; Bukowski, M. R.; Costas, M.; Fujisawa, K.; Que, L., Jr. *Inorg. Chem.* **2007,** *46*, 8410-8417.
31. Sobolev, A. P.; Babushkin, D. E.; Talsi, E. P. *J. Mol. Catal. A: Chem.* **2000,** *159*, 233-245.
32. Stasser, J.; Namuswe, F.; Kasper, G. D.; Jiang, Y.; Krest, C. M.; Green, M. T.; Penner-Hahn, J.; Goldberg, D. P. *Inorg. Chem.* **2010,** *49*, 9178-9190.
33. Wada, A.; Ogo, S.; Watanabe, Y.; Mukai, M.; Kitagawa, T.; Jitsukawa, K.; Masuda, H.; Einaga, H. *Inorg. Chem.* **1999,** *38*, 3592-3593.
34. Widger, L. R.; Jiang, Y.; McQuilken, A. C.; Yang, T.; Siegler, M. A.; Matsumura, H.; Moenne-Loccoz, P.; Kumar, D.; de Visser, S. P.; Goldberg, D. P. *Dalton Trans.* **2014,** *43*, 7522-7532.
35. Lehnert, N.; Ho, R. Y. N.; Que, L. J.; Solomon, E. I. *J. Am. Chem. Soc.* **2001,** *123*, 8271-8290.
36. Lehnert, N.; Ho, R. Y. N.; Que, L. J.; Solomon, E. I. *J. Am. Chem. Soc.* **2001,** *123*, 12802-12816.
37. Coggins, M. K.; Kovacs, J. A. *J. Am. Chem. Soc.* **2011,** *133*, 12470-12473.
38. Coggins, M. K.; Martin-Diaconescu, V.; DeBeer, S.; Kovacs, J. A. *J. Am. Chem. Soc.* **2013,** *135*, 4260-4272.
39. Wijeratne, G. B.; Corzine, B.; Day, V. W.; Jackson, T. A. *Inorg. Chem.*, **2014,** 53, 7622-7634.
40. Rice, D. B.; Wijeratne, G. B.; Burr, A. D.; Parham, J. D.; Day, V. W.; Jackson, T. A. *Inorg. Chem.*, **2016**, 55, 8110–8120.
41. Kokatnur, V. R.; Jelling, M. *J. Am. Chem. Soc.* **1941,** 63, 1432-1433.
42. Walling, C.; Buckler, S. A. *J. Am. Chem. Soc.* **1955,** 77, 6032-6038.
43. Leto, D. F.; Chattopadhyay, S.; Day, V. W.; Jackson, T. A. *Dalton Trans.* **2013**, 42, 13014-13025.
44. Ravel, B.; Newville, M. ATHENA, ARTEMIS, HEPHAESTUS: data analysis for X-ray absorption spectroscopy using IFEFFIT. *J. Synchrotron Rad.* **2005,** 12, 537-541.
45. Rehr, J. J.; Mustre de Leon, J.; Zabinsky, S. I.; Albers, R. C. *J. Am. Chem. Soc.* **1991,** 113, 5135-5140.
46. Neese, F., *ORCA - an ab initio, DFT and Semiempirical SCF-MO Package, Version 3.0.3*, Max-Planck-Institute for Chemical Energy Conversion, 2013.
47. Roemelt, M.; Beckwith, M. A.; Duboc, C.; Collomb, M.-N.; Neese, F.; DeBeer, S. *Inorg. Chem.* **2012,** 51, 680−687.
48. Buhl, M.; Kabrede, H. *J. Chem. Theory Comput*. **2006,** 2, 1282− 1290.
49. Weigend, F.; Ahlrichs, R. *Phys. Chem. Chem. Phys.* **2005,** 7, 3297-3305.
50. Neese, F. *J. Comput. Chem.* **2003,** 24, 1740-1747.
51. Lenthe, E. v.; Baerends, E. J.; Snijders, J. G. *J. Chem. Phys.* **1993,** 99, 4597-4610.
52. van Wüllen, C. *J. Chem. Phys.* **1998,** 109, 392-399.
53. Grimme, S.; Antony, J.; Ehrlich, S.; Krieg, H. *J. Chem. Phys.* **2010,** 132, 154104-154122.

54. Klamt, A.; Schuurmann, G. *J. Chem. Soc., Perkin Trans.* **1993**, 2, 799-805.
55. Becke, A. D. *J. Chem. Phys.* **1993,** 98, 1372-1377.
56. Becke, A. D. *J. Chem. Phys.* **1993,** 98, 5648-5652.
57. Lee, C.; Yang, W.; Parr, R. G. *Phys. Rev. B* **1988,** 37, 785-789.
58. Schäfer, A.; Horn, H.; Ahlrichs, R. *J. Chem. Phys.* **1992,** 97, 2571-2577.
59. Schäfer, A.; Huber, C.; Ahlrichs, R. *J. Chem. Phys.* **1994,** 100, 5829-5835.
60. Izsák, R.; Neese, F. J*Chem. Phys.* **2011**, 135, 144105-144116.
61. Neese, F.; Wennmohs, F.; Hansen, A.; Becker, U. *Chem. Phys.* **2009**, 356, 98-109.
62. Wijeratne, G. B.; Day, V. W.; and Jackson, T. A. O–H bond oxidation by a monomeric MnIII–OMe complex. *Dalton Trans*., **2015**, 44, 3295-3306.
63. Sankaralingam, M.; Jeon, S. H.; Lee, Y.; Seo, M. S.; Ohkubo, K.; Fukuzumi, S.; Nam, W. *Dalton Trans.*, **2016,** 45, 376-383.
64. Triller, M. U.; Hsieh, W.Y.; Pecoraro, V. L.; Rompel, A.; Krebs, B. *Inorg. Chem.* **2002**, 41, 5544-5554.
65. Hureau, C.; Blondin, G.; Charlot, M.-F.; Philouze, C.; Nierlich, M.; Ceario, M.; Anxolabehere-Mallart, E. *Inorg. Chem.* **2005**, 44, 3669-3683.
66. Jomová, K.; Kysel, O.; Madden, J. C.; Morris, H.; Enoch, S. J.; Budzak, S.; Young, A. J.; Cronin, M. T. D.; Mazur, M.; Valko, M*Chem. Phys. Lett.* **2009**, 478, 266-270.
67. Shreve, O. D.; Heether, M. R. *Anal. Chem.* **1951**, 23, 282-285.
68. NIST Mass Spec Data Center; Stein, S. E., director "Infrared Spectra" In *NIST Chemistry WebBook, NIST Standard Reference Database Number 69*, Linstrom, P.J., Mallard, W.G. , Eds.; National Institute of Standards and Technology, Gaithersburg, MD, doi:10.18434/T4D303.
69. Lehnert, N.; Ho, R. Y. N.; Que, L.; Solomon, E. I. *J. Am. Chem. Soc.*, **2001**, 123, 12802-12816.
70. Rice, D. B.; Wijeratne, G. W.; Jackson, T. A. Mn K-edge X-ray absorption studies of mononuclear Mn(III)-hydroxo complexes. *J. Biol. Inorg. Chem.* **2017**. DOI: 10.1007/s00775-017-1501-0
71. Penner-Hahn, J. E. In *Comprehensive Coordination Chemistry II;* McCleverty, J. A., Meyer, T.J., Eds.; Elsevier: Oxford, UK, **2003**, Volume 2, pp 159-186.
72. Chamulitrat, W.; Takahashi, N.; Mason, R. P. *J. Biol. Chem.,* **1989**, 264, 7889-7899.
73. Kim, J.; Zang, Y.; Costas, M.; Harrison, R. G.; Wilkinson, E. C.; Que, L. *J. Biol. Inorg. Chem.* **2001**, 6, 275-284.

Chapter 4

Synthesis, Characterization, and Reactivity of the First Room Temperature-Stable Mn^{III}-alkylperoxo Species

X-ray diffraction data collection and analysis were carried out by Dr. Victor W. Day.

4.1 Introduction. Mn-alkylperoxo species have been proposed as important intermediates in certain enzymatic pathways, though none have been isolated.[1-7] Mn-dependent dioxygenases, such as homoprotocatechuate 2,3-dioxygenase (Mn-HPCD), are proposed to generate a Mn^{II}-alkylperoxo intermediate during substrate oxidation.[2] The formation of this intermediate is proposed to occur through the reaction of a Mn^{II} center with dioxygen to form a Mn^{III}-superoxo species that is able to react with a bound substrate molecule and form the proposed Mn^{II}-alkylperoxo intermediate. This Mn^{II}-alkylperoxo intermediate is proposed to decay through a redox reaction that results in the dioxygenation of the substrate molecule.[2]

Mn-dependent lipoxygenases (Mn-LOX) have also been proposed to form Mn-alkylperoxo intermediates during the hydroperoxidation of fatty acid substrates.[4-6, 8] In contrast to what is proposed for Mn-HPCD, the formation of the Mn^{III}-alkylperoxo intermediate of Mn-LOX is not the result of a direct reaction between the Mn center and dioxygen. Instead, an active-site Mn^{III}-hydroxo center abstracts a hydrogen atom from the substrate, generating a Mn^{II}-aqua complex and a substrate radical. This substrate radical then reacts with dioxygen to form a peroxyl radical, which is proposed to react with the Mn^{II} center and form a Mn^{III}-alkylperoxo species.[8] The Mn^{III} resting state of the enzyme is regenerated through ligand substitution of the alkylperoxo moiety with a water molecule, concurrently yielding the final oxidized product.[8]

In light of the suggested biological importance of Mn-alkylperoxo species in biology, efforts employing synthetic model complexes as investigative tools into the properties and reactivity of this class of intermediates have been underway.[9-12] A report from Komatsuzaki and coworkers stand as the only example of a synthetic Mn^{II}-alkylperoxo species.[12] However, there are a couple ligand systems capable of supporting Mn^{III}-alkylperoxo complexes.[9-11] Kovacs and coworkers have reported a series of metastable Mn^{III}-alkylperoxo complexes supported by

pentadentate N_4S^- ligands. These complexes have been well characterized both spectroscopically and structurally by X-ray diffraction.[9, 10] The complexes all feature strongly donating thiolate ligation *cis* to the alkylperoxo moiety. In addition, these complexes featured sterically bulky quinolyl or 6-methylpyridyl substituents *cis* to the alkylperoxo moiety, resulting in elongated Mn-N bonds in the equatorial plane.[9, 10] These Mn^{III}-alkylperoxo complexes decay rapidly, even at temperatures as low as -15 °C. Analysis of the thermal decay products suggested a decay mechanism involving the homolytic cleavage of the alkylperoxo O-O bond.[10] In support of this proposed mechanism, variable-temperature kinetic analysis of the thermal decay of this series of complexes revealed that both the enthalpy ($\Delta H^{\ddagger}$) and the entropy ($\Delta S^{\ddagger}$) of the decay process trended with the O-O bond distance.[10] This homolytic cleavage pathway is different than that proposed in Mn-LOX.

More recently, our group has reported two Mn^{III}-alkylperoxo complexes supported by the pentadentate dpaq and $dpaq^{2Me}$ ligands, both of which feature strongly donating amide groups *trans* to the alkylperoxo moiety (dpaq = 2-[bis(pyridin-2-ylmethyl)]amino-*N*-quinolin-8-yl-acetamidate, $dpaq^{2Me}$ = 2-[bis(pyridin-2-ylmethyl)]amino-*N*-2-methyl-quinolin-8-yl-acetamidate).[11] $[Mn^{III}(OO^tBu)(dpaq)]^+$ and $[Mn^{III}(OO^tBu)(dpaq^{2Me})]^+$ were unstable ($t_{1/2}$ = 3200 and 3600 sec, respectively) and were characterized by electronic absorbance and FT-IR spectroscopies. Structural information was obtained from an analysis of extended X-ray absorption fine structure (EXAFS) data collected at the Mn K-edge. The formation of these complexes required a large excess (~100 equivalents) of ^{t}BuOOH that made detailed studies of reactivity or decay mechanisms difficult. However, the observation of ^{t}BuOO• in EPR analysis of the complexes served as indirect evidence of homolytic Mn-O bond cleavage during thermal decay of the complexes, potentially mimicking the proposed decay pathway of Mn-LOX.[11]

Taking note of the inherent difference in stability between the Mn^{III}-alkylperoxo complexes of the sterically encumbered N_4S^- ligand and our dpaq series, we sought to develop a derivative of the dpaq ligand that would stabilize such a species. Herein, we report the synthesis of the 2-(bis((6-methylpyridin-2-yl)methyl)amino)-N-(quinolin-8-yl)acetamide (H^{6Me}dpaq) ligand, a derivative of the dpaq ligand that incorporates steric bulk at the 6 position of the pyridyl substituents in the equatorial plane (Figure 4.1). Structural characterization of $[Mn^{III}(OH)(^{6Me}dpaq)](OTf)$ reveals that the 6-methylpyridinyl groups lead to elongations in the Mn-N distance of 0.11 Å relative to the unsubstituted analogue. This Mn^{III}-hydroxo species reacts with stoichiometric amounts of ^{t}BuOOH to generate the first room-temperature stable Mn^{III}-alkylperoxo species, $[Mn^{III}(OO^tBu)(^{6Me}dpaq)]^+$. This Mn^{III}-alkylperoxo complex is characterized by a battery of spectroscopic techniques, including X-ray absorption spectroscopy.

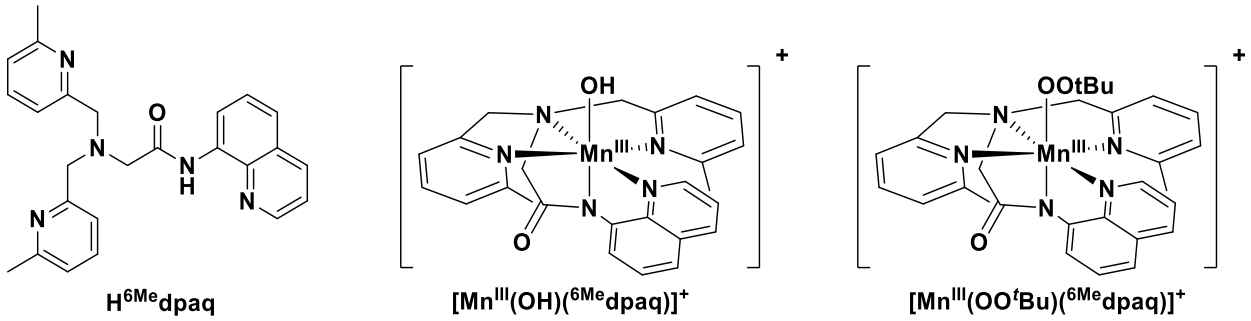

Figure 4.1. H^{6Me}dpaq ligand (left), $[Mn^{III}(OH)(^{6Me}dpaq)]^+$ (center), and $[Mn^{III}(OO^tBu)(^{6Me}dpaq)]^+$ (right).

4.2 Experimental Methods. All chemicals were used as obtained from commercial sources unless noted otherwise. Acetonitrile, diethyl ether, and methanol were dried and degassed using a PureSolv Micro solvent purification system. Bis((6-methylpyridin-2-yl)methyl)amine was synthesized according to a reported procedure.[13] The concentration of tert-butyl hydroperoxide (^{t}BuOOH) in decane stock solution was found to be 4.3 M by an iodometric titration procedure.[14]

Electronic absorption spectroscopy was performed using a Varian Cary 50 Bio UV−visible spectrophotometer equipped with a Unisoku cryostat and stirrer. Vibrational data were obtained using a PerkinElmer Spectrum100 FTIR spectrometer with samples sealed in 0.1 mm gastight NaCl cells. Electrospray ionization mass spectrometry (ESI-MS) experiments were performed using an LCT Premier MicroMass electrospray time-of-flight instrument. X-band EPR experiments were performed using a Bruker EMXplus with Oxford ESR900 continuous-flow liquid helium cryostat and an Oxford ITC503 temperature system. ^{1}H and ^{31}P NMR spectra were obtained on a Bruker DRX 400 MHz NMR spectrometer. ^{13}C and HSQC NMR spectra were obtained on a Avance AVIII 500 MHz NMR spectrometer.

Synthesis of 2-(bis((6-methylpyridin-2-yl)methyl)amino)-N-(quinolin-8-yl)acetamide (H^{6Me}dpaq). The H^{6Me}dpaq ligand was synthesized according to a modified literature procedure.[15] Under inert atmosphere in a Schlenk flask, 8-aminoquinoline and sodium carbonate were dissolved in MeCN. The solution was cooled to 0°C in an ice bath. Bromoacetyl bromide was added dropwise to the cooled solution. The reaction was allowed to stir for one hour at 0°C. The reaction mixture was filtered through an ultrafine frit, and the solvent removed under vacuum. The resulting orange solid was combined in a flask along with sodium carbonate and dissolved in MeCN under inert atmosphere. The solution was cooled to 0°C in an ice bath. Bis((6-methylpyridin-2-yl)methyl)amine was added slowly while stirring. The reaction mixture was allowed to stir overnight at 0°C. After the reaction was complete, the reaction mixture was filtered through a fine frit and the solvent removed under vacuum. The resulting red solid was purified through column chromatography on alumina and eluted with a DCM:MeOH solvent gradient. The final product was obtained as a dark yellow solid in 80% yield and characterized by ^{1}H, ^{13}C, and HSQC NMR. ^{1}H NMR data (400 MHz) for H^{6Me}dpaq ($CDCl_3$, δ) = 11.61 (s, 1H), 8.94 (dd; J = 4.2, 1.7 Hz;1H),

8.75 (dd; *J* = 6.1, 2.9 Hz; 1H), 8.19 (dd; *J* = 8.3, 1.7 Hz; 1H), 7.82 (d; *J* = 7.7 Hz; 2H), 7.52 (m, 5H), 7.02 (m, 2H), 3.99 (s, 4H), 3.52 (s, 2H), 2.47 (s, 6H) ppm. ^{13}C NMR data (125 MHz) for H^{6Me}dpaq ($CDCl_3$, δ) = 169.92 (s, C=O), 157.88 (s, Py), 157.80 (s, Py), 148.19 (s, Qu), 139.02 (s, Qu), 137.01 (s, Qu), 136.42 (s, Qu), 134.58 (s, Qu), 128.22 (s, Qu), 127.58 (s; Qu), 121.98 (s; Py), 121.73 (d; Py,Qu), 120.30 (s, Py), 116.65 (s, Qu), 61.48 (-CH_2Py), 59.39 (-CH_2CO-), 24.50 (CH_3Py) ppm.

Synthesis of [Mn^{II}(NCMe)(^{6Me}dpaq)](OTf). The Mn^{II} complex of the H^{6Me}dpaq ligand was generated under inert atmosphere in a glovebox. Separate solutions of $Mn(OTf)_2$ and NaO^{t}Bu in MeOH were added to a sequentially added to a solution of H^{6Me}dpaq in MeOH in a schlenk flask. The reaction was allowed to stir overnight. The resultant orange solution was filtered, and the solvent was removed under reduced pressure. The orange solid product was purified by recrystallization from MeCN by layering with diethyl ether. An EPR sample was prepared by injecting a 2 mM solution of the orange solid in MeCN into an EPR tube and immediately freezing the solution with liquid nitrogen. The magnetic moment of the compound was also measured using the Evans ^{1}H NMR method for a 2.5 mM solution of [Mn^{II}(NCMe)(^{6Me}dpaq)](OTf) in d_3-MeCN at 298 K. The μ_{eff} with diamagnetic correction was found to be 5.7 μ_B. The complex was also characterized by ESI-MS: *m/z* = 465.1196 (calculated *m/z* = 465.1361, Figure A3.4).

Preparation of [Mn^{III}(OH)(^{6Me}dpaq)](OTf). The Mn^{III}-hydroxo complex [Mn^{III}(OH)(^{6Me}dpaq)]$^+$ was generated through the oxidation of the Mn^{II} complex with PhIO in MeCN. In a typical experiment, a 2 mM solution of [Mn^{II}(NCMe)(^{6Me}dpaq)]$^+$ in MeCN was allowed to stir with 0.5 equivalents of PhIO and monitored by electronic absorption spectrometry until the spectra ceased to change. Larger scale preparations of [Mn^{III}(OH)(^{6Me}dpaq)](OTf), in which a saturated MeCN solution of 20 mg of [Mn^{II}(NCMe)(^{6Me}dpaq)]$^+$ was treated with 0.5

equivalents of PhIO, were carried out to obtain material for X-ray diffraction analysis. The formation of $[Mn^{III}(OH)(^{6Me}dpaq)](OTf)$ was assessed through electronic absorption spectroscopy. After repetitive crystallizations in MeCN/Et_2O, dark grey crystals of X-ray crystallographic quality were obtained. Fourier transform-infrared (FT-IR) analysis was performed for $[Mn^{III}(OH)(^{6Me}dpaq)]^+$ by injecting a 2 mM solution of $[Mn^{III}(OH)(^{6Me}dpaq)]^+$ in MeCN into a gas tight IR cell and collecting the FT-IR spectrum at 298 K. A sample for ^1H NMR was prepared by dissolving crystalline material in d_3-MeCN (10 mM). The magnetic moment of the compound was also measured using the Evans ^1H NMR method for a 1 mM solution of $[Mn^{III}(OH)(^{6Me}dpaq)](OTf)$ in d_3-MeCN at 298 K. The μ_{eff} with diamagnetic correction was found to be 4.5 μ_B. The complex was also characterized by ESI-MS: *m/z* = 482.1340 (calculated *m/z* = 482.1389, Figure A3.5).

X-ray diffraction data collection and analysis for $[Mn^{III}(OH)(^{6Me}dpaq)](OTf)$. A set of 4121 unique reflections were collected[16] for a 92/8 racemically-twinned crystal of $[Mn(C_{25}H_{24}N_5O)(OH)][O_3SCF_3]$ using 1.0º-wide ω- or ϕ-scan frames with scan times of 8-30 seconds and monochromated CuKα radiation (λ= 1.54178 Å) on a Bruker Proteum Single Crystal Diffraction System equipped with dual CCD area detectors. Data collection utilized a Platinum 135 CCD detector and Helios high-brilliance multilayer optics. X-rays were provided with a Bruker MicroStar microfocus Cu rotating anode x-ray source operating at 45kV and 60mA. The integrated data[17] were corrected empirically for variable absorption effects using equivalent reflections. The Bruker software package SHELXTL was used to solve the structure using "direct methods" techniques. All stages of weighted full-matrix least-squares refinement were conducted using F_o^2 data with the SHELXTL XL v2014 software package[18].

The asymmetric unit of $[Mn(C_{25}H_{24}N_5O)(OH)][O_3SCF_3]$ contains an ordered $[Mn(C_{25}H_{24}N_5O)(OH)]^+$ cation and an ordered triflate anion. All nonhydrogen atoms of $[Mn(C_{25}H_{24}N_5O)(OH)][O_3SCF_3]$ were included in the structural model with anisotropic thermal parameters that were allowed to vary along with their positional parameters in least-squares refinement cycles. The hydrogen atom of the coordinated hydroxyl group was located from a difference Fourier and included in the structural model as an independent isotropic atom whose parameters was also allowed to vary. Methyl groups for $[Mn(C_{25}H_{24}N_5O)(OH)][O_3SCF_3]$ were incorporated into the structural model as idealized rigid rotors (using sp^3-hybridized geometry and a C–H bond length of 0.98 Å) that were permitted to rotate freely about their C–C bonds in least-squares refinement cycles. The remaining non-methyl hydrogen atoms for $[Mn(C_{25}H_{24}N_5O)(OH)][O_3SCF_3]$ were included in the structural model as idealized riding-model atoms (assuming sp^2- or sp^3-hybridization of the carbon atoms with C–H bond lengths of 0.95 or 0.99 Å). The isotropic thermal parameters of all idealized hydrogen atoms were fixed at values 1.2 (nonmethyl) or 1.5 (methyl) times the equivalent isotropic thermal parameter of the carbon atom to which they are covalently bonded. Cartesian coordinates are presented in Table A3.2, and final crystallographic details are summarized in Table A3.3.

Preparation of [Mn^{III}(OO^{t}Bu)(^{6Me}dpaq)](OTf). A Mn^{III}-alkylperoxo complex was generated from either the Mn^{II} complex or the Mn^{III}-hydroxo complex by reacting with ^{t}BuOOH. To determine the minimum amount of ^{t}BuOOH required for full conversion, aliquots of ^{t}BuOOH (0.5, 1.0, 1.5, 2.5, or 5 equivalents) were added to a 2 mM solution of the Mn^{II} complex in MeCN while monitoring by electronic absorption spectroscopy and comparing the absorbance of the spectra collected with different aliquots. In this manner, the maximum formation of $[Mn^{III}(OO^tBu)(^{6Me}dpaq)](OTf)$ from $[Mn^{II}(NCMe)(^{6Me}dpaq)](OTf)$ was found to require the

addition of 1.5 equivalents of ^{t}BuOOH (Figure A3.3). The formation of [Mn^{III}(OO^{t}Bu)(^{6Me}dpaq)](OTf) from [Mn^{III}(OH)(^{6Me}dpaq)](OTf) was found to require 1 equivalent ^{t}BuOOH.

FT-IR analysis of [Mn^{III}(OO^{t}Bu)(^{6Me}dpaq)](OTf) was performed by injecting the solution following the reaction between [Mn^{III}(OH)(^{6Me}dpaq)](OTf) and 1 equivalent of ^{t}BuOOH directly into gastight IR cells, and immediately collecting FT-IR data. A ^{1}H NMR sample was prepared by injecting the solution following the reaction between [Mn^{III}(OH)(^{6Me}dpaq)](OTf) and 1 equivalent of ^{t}BuOOH into an NMR tube. The magnetic moment of the compound was also measured using the Evans ^{1}H NMR method for a 1 mM solution of [Mn^{III}(OH)(^{6Me}dpaq)](OTf) in d_3-MeCN at 298 K. The μ_{eff} with diamagnetic correction was found to be 4.5 μ_B. The Mn^{III}-alkylperoxo complex was also characterized by ESI-MS: *m/z* =554.1968 (calculated *m/z* = 554.1964, Figure A3.8). The thermal decay of [Mn^{III}(OO^{t}Bu)(^{6Me}dpaq)](OTf) and was monitored at 298 K and 328 K by electronic absorption spectroscopy.

X-ray Absorption Data Collection and Analysis. A 10 mM solution of [Mn^{II}(^{6Me}dpaq)](OTf) was prepared in MeCN and immediately injected into sample holders with a Kapton tape window and frozen in liquid nitrogen. A 10 mM sample of [Mn^{III}(OO^{t}Bu)(^{6Me}dpaq)](OTf) was prepared by a similar procedure. Full formation of [Mn^{III}(OO^{t}Bu)(^{6Me}dpaq)](OTf) was confirmed by electronic absoprtion spectroscopy. Mn Kedge XAS data were collected at Stanford Synchrotron Radiation Lightsource (SSRL) Beamline 9-3. Mn K-edge XAS spectra were collected at 10 K over a range in energy from 6.3 to 7.25 keV using a Si(111) monochromator. The fluorescence excitation spectra were obtained using a 100-element Ge array. Spectra of manganese foil were collected with each scan as a reference and were calibrated by assigning the zero crossing of the second derivative of the foil K-edge energy to

6539.0 eV. During data collection, the rising edge of each spectrum was monitored for evidence of photoreduction. No photoreduction was observed for either the Mn^{II} or the Mn^{III}-alkylperoxo samples. XAS data reduction and averaging was performed using the Athena program.[19] Each data set was normalized using the edge-step normalization procedure. A Gaussian function was fit to the pre-edge background and subtracted from the whole spectrum as a background correction. The spectrum was then spline-corrected to remove low-frequency background contributions. EXAFS refinement was performed on $k^3\chi(k)$ data, using phase and amplitude functions obtained from FEFF, version 6,[20] and structural models of $[Mn^{II}(^{6Me}dpaq)]^+$ and $[Mn^{III}(OO^tBu)(^{6Me}dpaq)]^+$ obtained from density functional theory (DFT) geometry optimizations (vide infra). The EXAFS data were fit using the Artemis program.[19] The average distances between Mn and scattering atoms (r) and Debye−Waller factors (σ^2) were optimized for each fit, while the number of atoms in the shell (n) was kept fixed. n was systematically varied between fits. The threshold energy E_0, in electronvolts (k = 0 point), was kept at a common, variable value for every shell of a given fit. The goodness-of-fit was evaluated using the R-factor:

$$R = \sum_{i=1}^{N} (\chi_i^{data} - \chi_i^{fit})^2 / \sum_{i=1}^{N} (\chi_i^{data})^2$$

Electronic Structure Computations. All computations were performed using the ORCA 4.0.1.2 software program.[21] Initial coordinates for $[Mn^{II}(NCMe)(^{6Me}dpaq)]^+$ were obtained through modification of the X-ray crystal structure of $[Mn^{II}(dpaq)]^+$ by adding methyl substituents to the 6 position of the pyridine arms. The polymeric structure from the X-ray crystal structure of $[Mn^{II}(dpaq)]^+$ was truncated by replacing the amide donor of a nearby Mn^{II} complex with an acetonitrile molecule. The resulting structure was subjected to unconstrained geometry optimization converged to the S = 5/2 spin state. The geometry optimization of

$[Mn^{II}(NCMe)(^{6Me}dpaq)]^+$ was performed using the B3LYP functional[22-24] with the SVP basis set for C and H atoms, and the TZVP basis set for manganese, oxygen, and nitrogen atoms.[25, 26] The integration grid was set to 4, with RI integral transformation approximations and the SVP/J and TZVP/J auxiliary basis sets.[25-27] Tight convergence criteria were employed. Cartesian coordinates are presented in Table A3.1.

Initial coordinates for $[Mn^{III}(OO^tBu)(^{6Me}dpaq)]^+$ were obtained by modifying the X-ray crystal structure coordinates of $[Mn^{III}(OH)(^{6Me}dpaq)]^+$ to replace the hydroxo ligand with a ^{t}butylperoxo ligand, and the resulting structure was subjected to unconstrained geometry optimization converged to the S = 2 spin state. The geometry optimization of $[Mn^{III}(OO^tBu)(^{6Me}dpaq)]^+$ was performed using the TPSS functional with D3 dispersion correction,[28, 29] the def2-SVP basis set for carbon and hydrogen atoms, and the def2-TZVP basis set was for manganese, nitrogen, and oxygen atoms.[25, 26, 30] The integration grid was set to 4, with RI integral transformation approximations[27] and the def2/J auxiliary basis set.[27] Cartesian coordinates are presented in Table A3.4.

Reaction of $[Mn^{III}(OO^tBu)(^{6Me}dpaq)](OTf)$ with H_2O. The formation of $[Mn^{III}(OO^tBu)(^{6Me}dpaq)](OTf)$ was achieved by adding 1 equivalent of ^{t}BuOOH to a 2 mM solution of $[Mn^{III}(OH)(^{6Me}dpaq)](OTf)$ in MeCN while monitoring by electronic absorption spectroscopy. Upon full formation of the Mn^{III}-alkylperoxo species, 100 equivalents of H_2O were added via syringe at 298 K. The resulting reaction was monitored by electronic absorption spectroscopy. The products of the reaction were analyzed by ESI-MS and ^{1}H NMR analyses.

Reaction of $[Mn^{III}(OO^tBu)(^{6Me}dpaq)](OTf)$ with 9,10-dihydroanthracene. The formation of $[Mn^{III}(OO^tBu)(^{6Me}dpaq)](OTf)$ was achieved by adding 1 equivalent of ^{t}BuOOH to a 1.25 mM MeCN solution of $[Mn^{III}(OH)(^{6Me}dpaq)](OTf)$ in a quartz cuvette with a pierceable septum. Upon

full formation of the Mn^{III}-alkylperoxo species, 175 equivalents of 9,10-dihydroanthracene (DHA), which had been dissolved in 100 µL of dichloromethane, were added via gas-tight syringe. The resulting reaction was allowed to stir for 30 hours at 323 K while monitoring by electronic absorption spectroscopy. The organic products of the reaction were separated by passing the solution through a 1 inch silica plug and eluting with dichloromethane. The solvent was removed, and a sample for ^{1}H NMR analysis was prepared in $CDCl_3$ using 1,4-benzoquinone as an internal reference.

Reaction of [Mn^{III}($OO^{t}Bu$)(^{6Me}dpaq)](OTf) with triphenylphosphine. The formation of [Mn^{III}($OO^{t}Bu$)(^{6Me}dpaq)](OTf) was achieved under inert atmosphere by adding 1 equivalent of ^{t}BuOOH to a 1.25 mM solution of [Mn^{III}(OH)(^{6Me}dpaq)](OTf) in MeCN that had been sealed in a quartz cuvette with a pierceable septum in a glovebox. Upon full formation of the Mn^{III}-alkylperoxo species, 100 equivalents of triphenylphosphine (PPh_3), which had been dissolved in 100 µL of O_2-free MeCN, were added. The resulting reaction was allowed to stir at 298 K while monitoring by electronic absorption spectroscopy until the spectra ceased to change. The organic products of the reaction were separated by evaporating the solvent and dissolving the organic products in diethyl ether. Diethyl ether was removed, and the resulting white crystals were dissolved in $CDCl_3$ and injected into an NMR tube for ^{31}P NMR analysis.

4.3 Results and discussion.

Synthesis of (H^{6Me}dpaq). The synthesis of H^{6Me}dpaq was carried out according to a modified procedure of the synthesis of the Hdpaq ligand (Scheme 4.1).[15] The alkylation of 8-aminoquinoline was achieved through the addition of bromo acetyl bromide in MeCN under inert atmosphere at 273 K. Bis((6-methylpyridin-2-yl)methyl)amine, which was synthesized according to a published procedure,[13] was subsequently added to the reaction solution and allowed to stir

overnight at 273 K. The product was purified by column chromatography and obtained in 80% yield. Analysis by ^{1}H, ^{13}C, and HSQC NMR confirmed the formation of H^{6Me}dpaq (Figure A3.1-3).

Scheme 4.1. Synthesis of H^{6Me}dpaq.

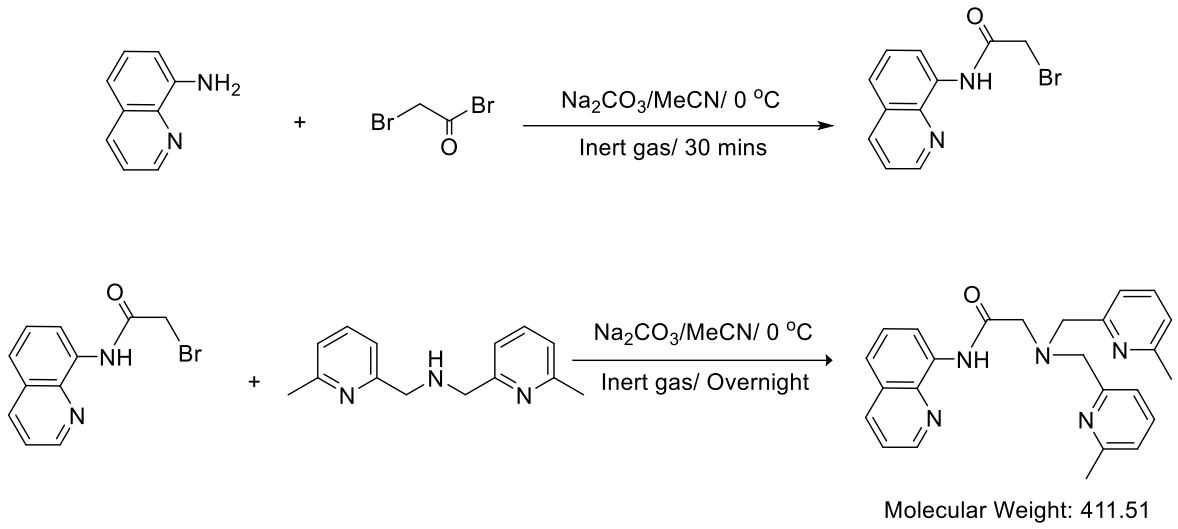

Characterization of [Mn^{II}(NCMe)(^{6Me}dpaq)]$^{+}$. Metallation of the H^{6Me}dpaq ligand with $Mn^{II}(OTf)_2$ results in the formation of a bright orange solid. Mass-spectral analysis of the orange solid revealed a peak at *m/z* = 465.1196, consistent with the $[Mn^{II}(^{6Me}dpaq)]^{+}$ ion (calculated *m/z* = 465.1361, Figure A3.4). We presume that the Mn^{II} center is six-coordinate in solution with an acetonitrile ligand, $[Mn^{II}(NCMe)(^{6Me}dpaq)]^{+}$. An EPR spectrum obtained for a 2 mM solution of $[Mn^{II}(NCMe)(^{6Me}dpaq)]^{+}$ in MeCN revealed a 6-line signal (g = 2.00, A = 9.39 mT; Figure 4.2). The g-value and hyperfine splitting observed in this EPR spectrum are similar to those reported for the high-spin $[Mn^{II}(N4S)]^{+}$ complexes (g = 1.98 - 2.00, A = 9.0 – 10.0 mT) and $[Mn^{II}(NCMe)(dpaq^{2Me})]^{+}$ (g = 2.04).[31, 32] The magnetic moment of $[Mn^{II}(NCMe)(^{6Me}dpaq)]^{+}$ was measured to be 5.7 μ_B using the Evans method with diamagnetic correction, consistent with the

assignment of this species as a high-spin Mn^{II} complex (the calculated spin-only value for an S = 5/2 species is 5.91 μ_B).

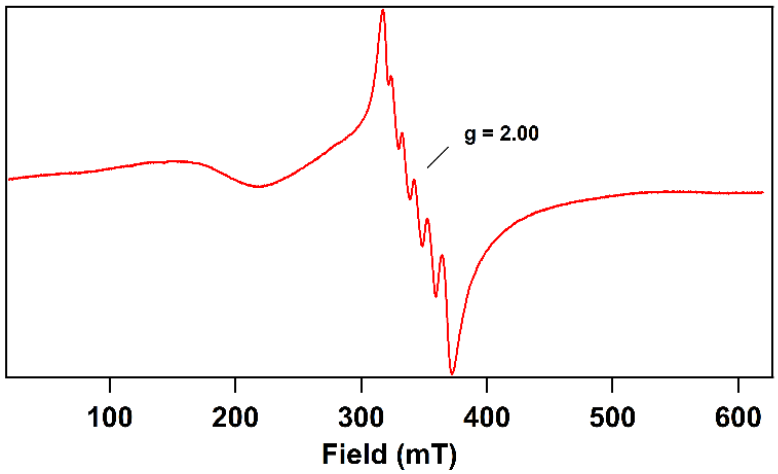

Figure 4.2. EPR spectrum obtained for a 2 mM solution of $[Mn^{II}(NCMe)(^{6Me}dpaq)]^+$ in MeCN showing a six-line signal consistent with the assignment of a Mn^{II} species (g = 2.00 , A = 9.39 mT).

$[Mn^{II}(NCMe)(^{6Me}dpaq)]^+$ was also subjected to Mn K-edge XAS analysis. This technique was used previously to characterize the Mn^{II} complexes of other dpaq derivatives, and as such served as a good method to validate our formulation of the orange species as a Mn^{II} complex.[33] The Mn K-edge energy of the spectrum was found to be 6547.1 eV, similar to the edge energies reported for $[Mn^{II}(NCMe)(dpaq)](OTf)$ and $[Mn^{II}(NCMe)(dpaq^{2Me})](OTf)$ (6547.9 and 6548.6, respectively; Table 1; Figure 4.3). The pre-edge features of the three Mn^{II}-complexes are of similar energy, though the area under the pre-edge feature of $[Mn^{II}(NCMe)(^{6Me}dpaq)]^+$ is higher (Table 4.1, Figure 4.3 inset).[33] As the energy of the pre-edge features and the Mn K-edge are sensitive to oxidation state, these findings support our assignment of the orange species as containing a Mn^{II} center. However, the difference in the area of the pre-edge feature suggests that there are geometric differences between $[Mn^{II}(NCMe)(^{6Me}dpaq)]^+$ and the previously reported $[Mn^{II}(NCMe)(dpaq)]^+$ and $[Mn^{II}(NCMe)(dpaq^{2Me})]^+$.

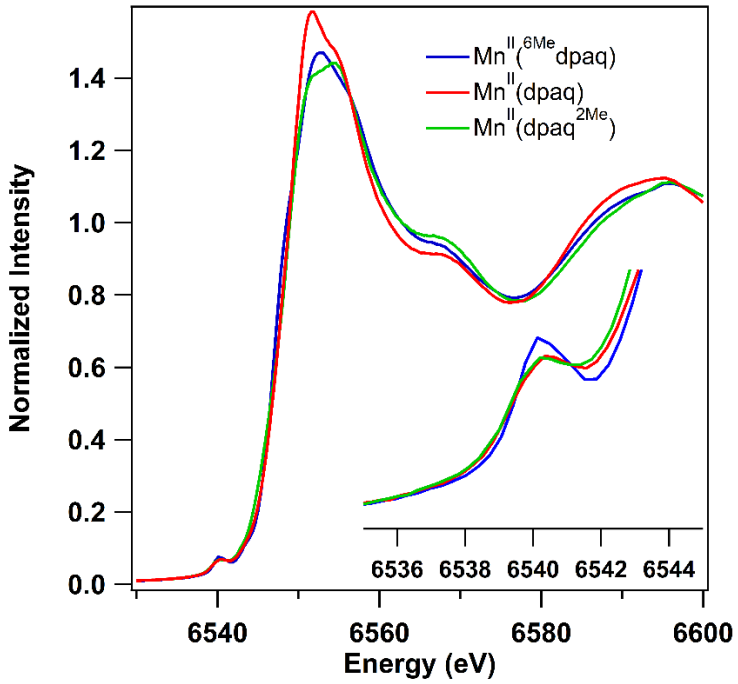

Figure 4.3. Mn K-edge near-edge spectra of $[Mn^{II}(NCMe)(^{6Me}dpaq)]^+$ (blue), $[Mn^{II}(NCMe)(dpaq)]^+$ (red), and $[Mn^{II}(NCMe)(dpaq^{2Me})]^+$ (green) collected for frozen solutions in MeCN at 10 K. Inset: Expanded view of the pre-edge region.

Table 4.1. Experimental pre-edge and Mn K-edge properties for Mn^{II} complexes in frozen MeCN.

Complex	Pre-edge energy	Pre-edge area	Edge energy	Reference
$[Mn^{II}(MeCN)(^{6Me}dpaq)]^+$	6540.1	5.3	6547.1	*This work*
$[Mn^{II}(MeCN)(dpaq)]^+$	6540.2	4.9	6547.9	*30*
$[Mn^{II}(MeCN)(dpaq^{2Me}]^+$	6540.2	4.3	6548.6	*30*

Insight into possible structural differences between $[Mn^{II}(NCMe)(^{6Me}dpaq)]^+$ and the previously reported Mn^{II} complexes can be garnered from the analysis of the extended X-ray absorption fine structure (EXAFS) data collected for $[Mn^{II}(NCMe)(^{6Me}dpaq)]^+$. The Fourier

transform of the EXAFS spectrum of $[Mn^{II}(NCMe)(^{6Me}dpaq)]^+$ consists of an intense peak at 1.81 Å with shoulders at 1.01 and 1.44 Å, as well as a smaller peak at 2.61 Å with a shoulder at 2.19 Å (Figure 4.4). This set of peaks is best fit using a shell of 6 N/O atom scatterers at an average distance of 2.25 Å (Table 4.2.) The distance for this scattering shell agrees well with the average Mn-N/O distance from a DFT-optimized structure of $[Mn^{II}(NCMe)(^{6Me}dpaq)]^+$ (Table 4.3). While splitting the N/O shell improves the goodness of fit, the resulting Debye-Waller factor is smaller than expected (Table 4.2). It is important to note that the EXAFS spectra of $[Mn^{II}(NCMe)(dpaq)]^+$ and $[Mn^{II}(NCMe)(dpaq^{2Me})]^+$ were also best fit using single shells of N atom scatterers.[33] A shell of 6 C atoms at 3.09 Å was included to account for the second coordination sphere (Table 4.2).

Table 4.2. Fits of EXAFS data of $[Mn^{II}(NCMe)(^{6Me}dpaq)]^+$.[a]

Fit	Mn-N/O			Mn-N/O			Mn-C			Goodness of fit[b]
	n	*r (Å)*	σ^2	*n*	*r (Å)*	σ^2	*n*	*r (Å)*	σ^2	
1	6	2.25	0.005							0.358
2	5	2.25	0.004							0.359
3	5	2.26	0.003	1	2.49	0.003				0.361
4	4	2.27	0.003	2	2.50	0.003				0.429
5	***6***	***2.25***	***0.005***				***6***	***3.10***	***0.005***	***0.285***
6	6	2.25	0.005				4	3.10	0.003	0.286

[a]Fit highlighted in bold, italicized font represents the best fit to the EXAFS data. [b]Evaluated using the R-factor.

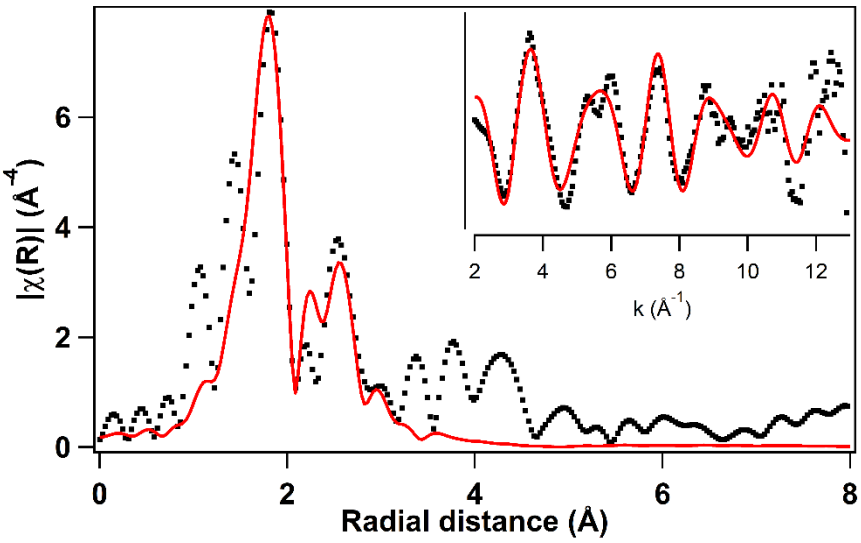

Figure 4.4. Fourier transform of the Mn K-edge EXAFS data, and EXAFS spectra (inset), for [Mn^{II}(NCMe)(^{6Me}dpaq)]$^{+}$ in frozen MeCN. Experimental data are in black, while fit 5 (see table 2) is in red.

The DFT-optimized structure of [Mn^{II}(NCMe)(^{6Me}dpaq)]$^{+}$ that was used for EXAFS data refinement has a six-coordinate Mn center, similar to those reported in the crystal structures of [Mn^{II}(dpaq)](OTf) and [Mn^{II}(dpaq^{2Me})](OTf).[31, 34] The calculated distances between the Mn center and the pyridine substituents are 2.40 and 2.43 Å (Table 4.3). These distances are longer than the Mn-pyridine distances reported for the crystal structures of [Mn^{II}(dpaq)](OTf) and [Mn^{II}(dpaq^{2Me})](OTf) by 0.11 to 0.19 Å, presumably due to the steric bulk imparted by the methyl substitutions adjacent to the donor nitrogen atom (Figure 4.5, Table 4.3).[31, 34] The calculated structure of [Mn^{II}(NCMe)(^{6Me}dpaq)]$^{+}$ also has a Mn-amide N bond distance of 2.09 Å which is shorter than what is observed for [Mn^{II}(dpaq)](OTf) and [Mn^{II}(dpaq^{2Me})](OTf) by 0.10 and 0.08 Å, respectively (Table 4.3).[31, 34] The remaining Mn-ligand bond lengths of the calculated structure of [Mn^{II}(NCMe)(^{6Me}dpaq)]$^{+}$ are similar to that reported for [Mn^{II}(dpaq)](OTf) and [Mn^{II}(dpaq^{2Me})](OTf) (Table 4.3).[31, 34]

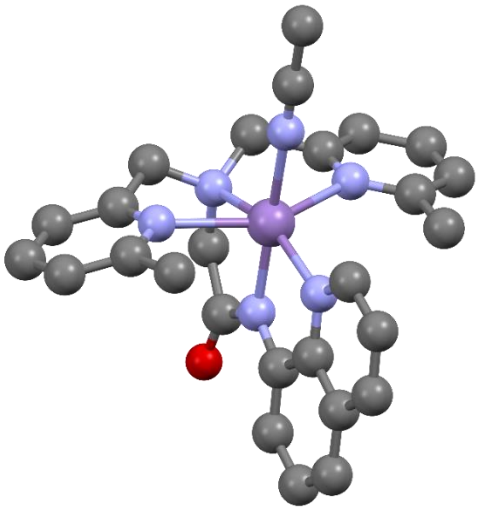

Figure 4.5. DFT-optimized structure of $[Mn^{II}(NCMe)(^{6Me}dpaq)]^{+}$.

Table 4.3. Comparison of the scattering distance from the EXAFS fit of $[Mn^{II}(NCMe)(^{6Me}dpaq)]^{+}$ to bond lengths obtained from a DFT-optimized structure of $[Mn^{II}(NCMe)(^{6Me}dpaq)]^{+}$ and bond lengths obtained from the X-ray structures of $[Mn^{II}(dpaq)](OTf)$ and $[Mn^{II}(dpaq^{2Me})](OTf)$ (distances in Å).

	$[Mn^{II}(NCMe)(^{6Me}dpaq)]^{+}$		**$[Mn^{II}(dpaq)](OTf)^{a}$**	**$[Mn^{II}(dpaq^{2Me})](OTf)^{a}$**
	EXAFS	DFT		
$Mn\text{-}N_{amide}$	--	2.09	2.191(3)	2.172(3)
$Mn\text{-}N_{Py}$	--	2.40, 2.43	2.244(3), 2.286(3)	2.275(3), 2.286(3)
$Mn\text{-}N_{amine}$	--	2.32	2.314(3)	2.317(3)
$Mn–N_{Qu}$	--	2.24	2.214(3)	2.268(3)
Mn-N (avg.)	2.25	2.30	2.250	2.264
Mn---C (avg.)	3.10	3.07	3.08	3.08

[a] From references [31, 34].

Formation and characterization of $[Mn^{III}(OH)(^{6Me}dpaq)](OTf)$. Previously reported Mn^{II} complexes from our group have shown varying reactivity with dioxygen to generate Mn^{III} species.[31, 34, 35] The $[Mn^{II}(dpaq)](OTF)$ complex, along with the $[Mn^{II}(dpaq^{5OMe})](OTF)$ and $[Mn^{II}(dpaq^{5Cl})](OTF)$ complexes, react with dioxygen to generate mononuclear Mn^{III}-hydroxo

complexes that exist in equilibria with (μ-oxo)dimanganese(III, III) species.[35] The sterically modified [Mn^{II}(dpaq^{2Me})](OTF) also reacts with dioxygen, but in this case strictly forms a monomeric Mn^{III}-hydroxo complex.[31, 35] When the dpaq ligand is functionalized with and electron-withdrawing NO_2 group, [Mn^{II}(dpaq^{5NO_2})](OTF) reacts with dioxygen very slowly (only partial conversion was observed after 24 hours of reaction), and instead requires the use of iodosylbenzene (PhIO) to form an equilibrium mixture of Mn^{III}-hydroxo and (μ-oxo)dimanganese(III, III) species.[35] These Mn^{III} species all exhibit similar electronic absorption spectra with a feature around 770 nm that has been assigned to the Mn^{III} $d_{x^2-y^2}$ to d_{z^2} transition.[31, 34, 35]

[Mn^{II}(NCMe)(^{6Me}dpaq)]$^+$ reacts very slowly with dioxygen, with only partial oxidation being observed after a period of 48 hours. Presumably, the elongation of the Mn-N_{Py} bond, and resultant withdrawal of electron density at the metal center, raises the $Mn^{III/II}$ reduction potential enough to reduce reactivity with dioxygen. However, the reaction between [Mn^{II}(NCMe)(^{6Me}dpaq)]$^+$ and PhIO is rapid, resulting in the formation of a dark orange solution with a single electronic absorption feature at 500 nm (Figure 4.6). Mass spectral analysis of the dark orange solution shows a peak at *m/z* = 482.1340, consistent with the Mn^{III}-hydroxo complex [Mn^{III}(OH)(^{6Me}dpaq)]$^+$ (calculated *m/z* = 482.1389, Figure A3.5). The magnetic moment of [Mn^{III}(OH)(^{6Me}dpaq)]$^+$ as determined using the Evans ^{1}H NMR method with diamagnetic correction supported the assignment of this species as a high-spin Mn^{III} center (μ_{eff} = 4.5 μ_B, expected spin-only value of μ_{eff} = 4.90 μ_B).

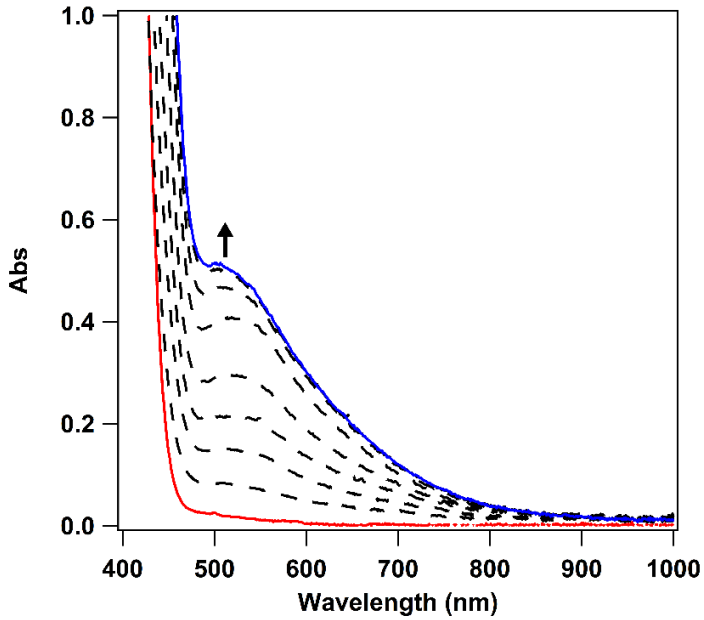

Figure 4.6. Electronic absorption spectra monitoring the reaction of a 2 mM solution of $[Mn^{II}(NCMe)(^{6Me}dpaq)]^{+}$ with 0.5 equivalents of PhIO in MeCN at 298 K.

Repeated recrystallizations of the dark orange solution obtained following the reaction of $[Mn^{II}(NCMe)(^{6Me}dpaq)]^{+}$ with PhIO resulted in the formation of dark grey crystals that were suitable for XRD analysis. The X-ray crystal structure of $[Mn^{III}(OH)(^{6Me}dpaq)](OTf)$ contains a six-coordinate Mn^{III} center with a distorted octahedral geometry (Figure 4.7). The ^{6Me}dpaq ligand is coordinated to the metal center in a pentadentate fashion, with the amide function *trans* to the hydroxo ligand. This coordination mode is identical that observed in Mn^{III}-hydroxo complexes of other dpaq derivatives.[31, 34, 35] The Mn-O distance is 1.806(6) Å, which is identical to that observed for $[Mn^{III}(OH)(dpaq)](OTf)$ (Table 4.4).[34]. These Mn-O distances are on the low end of the range of Mn-O bond lengths reported for Mn^{III}-hydroxo complexes (1.81-1.86 Å).[31, 36-44] Inspection of the extended structure of $[Mn^{III}(OH)(^{6Me}dpaq)]^{+}$ reveals that the hydrogen atom of the hydroxo ligand is involved in a hydrogen-bonging interaction with the amide oxygen of a neighboring $[Mn^{III}(OH)(^{6Me}dpaq)]^{+}$ complex (H···O distance of 2.008 Å, Figure A3.6). A free triflate ion is also

present in the asymmetric unit, though not directly associated with the Mn center (Mn-O distance of ~7.5 Å).

The Mn-$N_{Pyridine}$ distances in the crystal structure of [Mn^{III}(OH)(^{6Me}dpaq)](OTf) are 0.114 Å longer than the corresponding distances in [Mn^{III}(OH)(dpaq)]$^{+}$ (Table 4.4).[34] This elongation is caused by the steric bulk of the methyl functions. Similar bond lengths have been observed in the crystal structures of Mn^{III} complexes of the $N4S^{-}$ class of ligands. These complexes featured 6-methylpyridinyl or quinolinyl substituents in the equatorial field, with the Mn-N bond length ranging from 2.352 – 2.581 Å.[9, 10, 32] For [Mn^{III}(OH)(^{6Me}dpaq)](OTf), the longer Mn-$N_{Pyridine}$ distances are accompanied by modest contractions of the Mn-N_{amide}, Mn-$N_{Quinoline}$, and Mn-N_{amine} bonds by 0.013, 0.029, and 0.043 Å, respectively, relative to [Mn^{III}(OH)(dpaq)](OTf) (Table 4). The paired elongation of Mn-$N_{Pyridine}$ distances and contraction of the other Mn-N distances is consistent with our calculated structure of the Mn^{II} complex (Figure 4.5, Table 4.3).

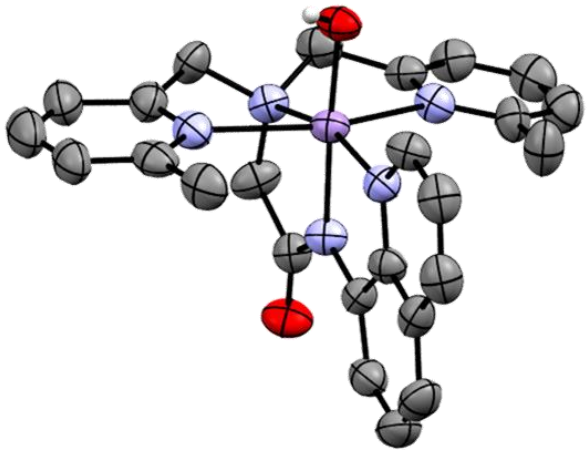

Figure 4.7. ORTEP diagram of cationic portion of [Mn^{III}(OH)(^{6Me}dpaq)](OTf)showing 50% probability thermal ellipsoids. Hydrogen atoms of the ^{6Me}dpaq ligand have been omitted for clarity.

Table 4.4. Manganese-ligand bond lengths (Å) from the crystal structures of $[Mn^{III}(OH)(^{6Me}dpaq)](OTf)$ and $[Mn^{III}(OH)(dpaq)](OTf)$.

Bond	$[Mn^{III}(OH)(^{6Me}dpaq)](OTf)$	$[Mn^{III}(OH)(dpaq)](OTf)^a$
Mn-O(H)	1.806(6)	1.806(13)
$Mn\text{-}N_{amide}$	1.962(6)	1.975(14)
$Mn\text{-}N_{Pyidine}$	2.322(6), 2.381(7)	2.260(14), 2.216(15)
$Mn\text{-}N_{Quinoline}$	2.041(7)	2.072(14)
$Mn\text{-}N_{amine}$	2.130(6)	2.173(14)

[a] From reference 26.

The Mn^{III}-hydroxo complex $[Mn^{III}(OH)(^{6Me}dpaq)](OTf)$ was also characterized by ^1H NMR spectroscopy in MeCN at 298 K. The spectrum exhibits seven hyperfine-shifted peaks, as well as two peaks in the 0 - 10 ppm region (Figure 4.8, red trace and Table 4.5). The ^1H NMR data suggest that the oxidation of $[Mn^{II}(NCMe)(^{6Me}dpaq)]^+$ with PhIO does not result in the formation of an equilibrium mixture of a Mn^{III}-hydroxo species and a to (μ-oxo)dimanganese(III, III) dimer. The chemical shifts for the hyperfine-shifted peaks of $[Mn^{III}(OH)(^{6Me}dpaq)]^+$ are quite similar to that observed in the ^1H NMR spectra of $[Mn^{III}(OH)(dpaq)]^+$ (Figure 4.8, red and blue traces and Table 4.5).[35, 45] The four most strongly up-field-shifted peaks of $[Mn^{III}(OH)(dpaq)]^+$, at -15.5, -33.7, -53.8, and -63.4 ppm (Figure 4.8), were previously assigned to protons from the quinolinyl moiety.[46] The upfield region of the ^1H NMR spectrum of $[Mn^{III}(OH)(^{6Me}dpaq)]^+$ shows three sharp peaks at -19.3, -45.0, and -61.6 ppm that resemble the peaks of $[Mn^{III}(OH)(dpaq)]^+$ at -15.5, -33.7, -53.8 ppm. The ^1H NMR spectrum of $[Mn^{III}(OH)(^{6Me}dpaq)]^+$ lacks a broad, highly upfield-shifted peak analogous to the weak, broad -63.4 ppm signal of $[Mn^{III}(OH)(dpaq)]^+$. The overall similarities between the upfield region of the ^1H NMR spectra of $[Mn^{III}(OH)(^{6Me}dpaq)]^+$ to that of $[Mn^{III}(OH)(dpaq)]^+$ are expected given the lack of changes to the quinolinyl group in the former complex. The ^1H NMR signals of $[Mn^{III}(OH)(dpaq)]^+$ at 130.5, 60.9, 54.3, and -4.6 ppm were

attributed to pyridyl protons.[46] Consequently, the larger perturbations in the down-field regions of the ^{1}H NMR spectra of $[Mn^{III}(OH)(dpaq)]^+$ and $[Mn^{III}(OH)(^{6Me}dpaq)]^+$ can be rationalized by changes in chemical shifts of pyridyl protons. The peak at 130.5 ppm for $[Mn^{III}(OH)(dpaq)]^+$ was assigned to the α-H of the pyridine substituent. The lack of a corresponding peak in the ^{1}H NMR spectrum of $[Mn^{III}(OH)(^{6Me}dpaq)]^+$ is consistent with the 6-methyl-pyridine functionalization of the ligand. The ^{1}H NMR spectrum of $[Mn^{III}(OH)(^{6Me}dpaq)]^+$ contains a broad, up-field-shifted peak at -9.5 ppm, lacking in the ^{1}H NMR spectrum of $[Mn^{III}(OH)(dpaq)]^+$, that could arise from the protons of the 6-methyl-pyridyl groups.

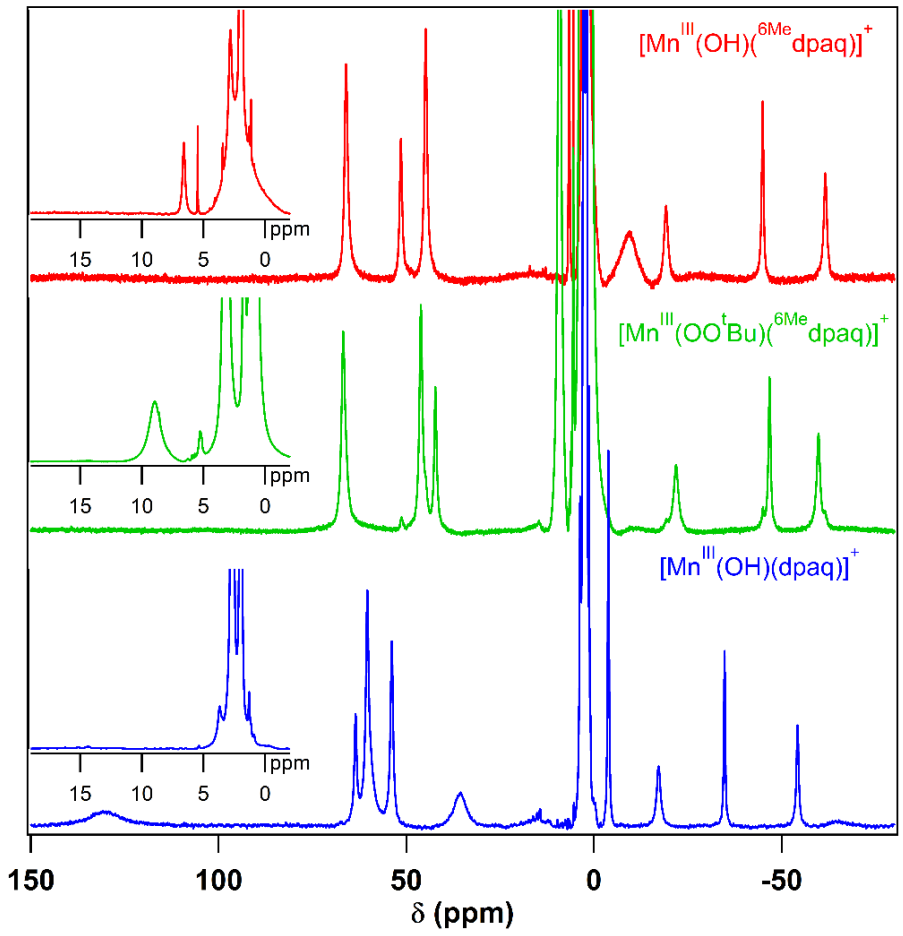

Figure 4.8. ^{1}H NMR spectra of 2 mM solutions of $[Mn^{III}(OH)(^{6Me}dpaq)]^+$ (top), $[Mn^{III}(OO^tBu)(^{6Me}dpaq)]^+$ (center), and a 15 mM solution of $[Mn^{II}(OH)(dpaq)]^+$ (bottom) with 45 µL D_2O in d_3-MeCN at 298 K. Inset: expanded view of the 0 to 20 ppm region.

Table 4.5. ^{1}H NMR Chemical Shifts (ppm) for $[Mn^{III}(OH)(^{6Me}dpaq)]^{+}$, $[Mn^{III}(OO^{t}Bu)(^{6Me}dpaq)]^{+}$, and $[Mn^{III}(OH)(dpaq)]^{+}$ in CD_3CN.

$[Mn^{III}(OH)(^{6Me}dpaq)]^{+}$	$[Mn^{III}(OO^{t}Bu)(^{6Me}dpaq)]^{+}$	$[Mn^{III}(OH)(dpaq)]^{+a,b}$
		130.5 (H-py)
66.0	66.8	62.7 (H-qn)
51.4	46.1	60.9 (H-py)
44.8	42.2	54.3 (H-py)
		40.5
8.9	9.2	
5.5	5.5	
-9.6	-10	-4.6 (H-py)
-19.3	-22	-15.5 (H-qn)
		-33.7 (H-qn)
-45	-46.9	-53.8 (H-qn)
-61.6	-60	-63.4 (H-qn)

a From the spectrum of $[Mn^{III}(OH)(dpaq)]^{+}$ in d_3-MeCN with 880 equivalents of D_2O.[35] *b* Tentative assignments of $[Mn^{III}(OH)(dpaq)]^{+}$ ^{1}H-NMR peaks are shown in parentheses (py = pyridine, qn = quinoline).

The electronic absorption spectrum of $[Mn^{III}(OH)(^{6Me}dpaq)]^{+}$ reveals stark differences to that observed in $[Mn^{III}(OH)(dpaq)]^{+}$ and its previously reported derivatives (Figure 4.9). While the previous Mn^{III}-hydroxo complexes have all exhibited an electronic absorption feature around 770 nm, such a signal is not observed for $[Mn^{III}(OH)(^{6Me}dpaq)]^{+}$.[31, 34, 35] This is presumed to be an effect of the distorted geometric environment around the Mn center (Figure 4.7, Table 4.4). Namely, the methyl functionalization adjacent to the coordinating N atom of the pyridine arms results in an elongation of the Mn-N_{Py} bond. This withdrawal of electron density as a result of this weakened coordination stabilizes the d_{x2-y2} orbital. As the feature observed around 770 nm for $[Mn^{III}(OH)(dpaq)]^{+}$ was assigned as a d_{x2-y2} to d_{z2} transition, stabilization of the d_{x2-y2} orbital would blue-shift this electronic transition. A significant enough shift in energy may cause this band to be obstructed by other more intense bands.

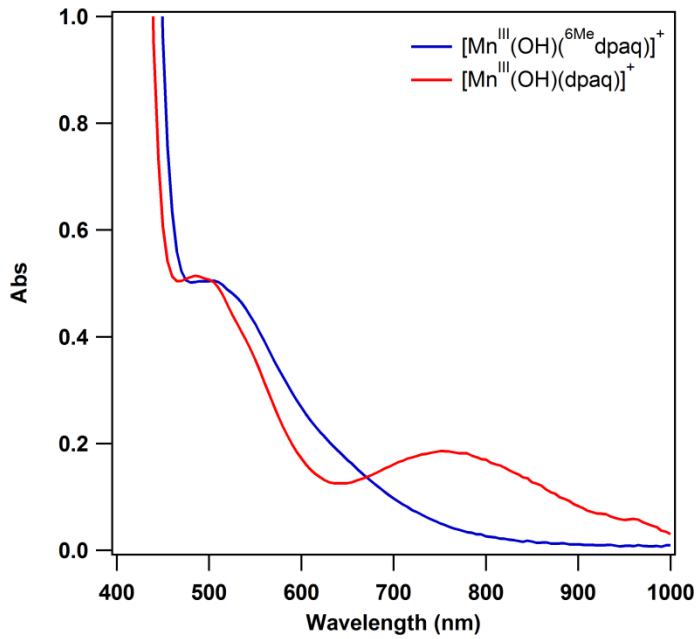

Figure 4.9. The electronic absorption spectrum of $Mn^{III}(OH)(^{6Me}dpaq)]^+$ (red trace) consists of an intense feature at 510 nm and a weak shoulder around 620 nm. Electronic absorption spectrum of $[Mn^{III}(OH)(dpaq)]^+$ shown for comparison (red trace).

Reactions of $[Mn^{II}(^{6Me}dpaq)]^+$ and $[Mn^{III}(OH)(^{6Me}dpaq)]^+$ with ^{t}BuOOH. Species $[Mn^{II}(NCMe)(^{6Me}dpaq)]^+$ reacts with ^{t}BuOOH in MeCN at 298 K to form a green species (species **1**). The electronic absorption spectrum of this green chromophore has a shoulder near 500 nm and prominent band at 650 nm (Figure 4.10, left). The maximum formation of **1**, as assessed by the lack of further growth of electronic absorption features, was observed with the addition of 1.5 equivalents of ^{t}BuOOH (Figure A3.7). The addition of ^{t}BuOOH to $[Mn^{II}(NCMe)(^{6Me}dpaq)]^+$ initially results in the formation of a broad, featureless spectrum, with the eventual appearance of bands around 510 and 650 nm (Figure 4.10, left). While the intensity of the 650 nm band maximizes at ca. 60 minutes after ^{t}BuOOH addition, the band at 510 nm reaches a maximum at 80 minutes and then drops in intensity over the course of 40 minutes (Figure 4.10, left inset). The observation of the initial growth and subsequent disappearance of a band at 510 nm suggests that

the reaction between $[Mn^{II}(NCMe)(^{6Me}dpaq)]^{+}$ and ^{t}BuOOH proceeds through the $[Mn^{III}(OH)(^{6Me}dpaq)]^{+}$, which reacts with ^{t}BuOOH to generate species **1**. The formation of a Mn^{III}-hydroxo intermediate during the reactivity of Mn^{II} complexes with ^{t}BuOOH has been observed in a previous report.[11]

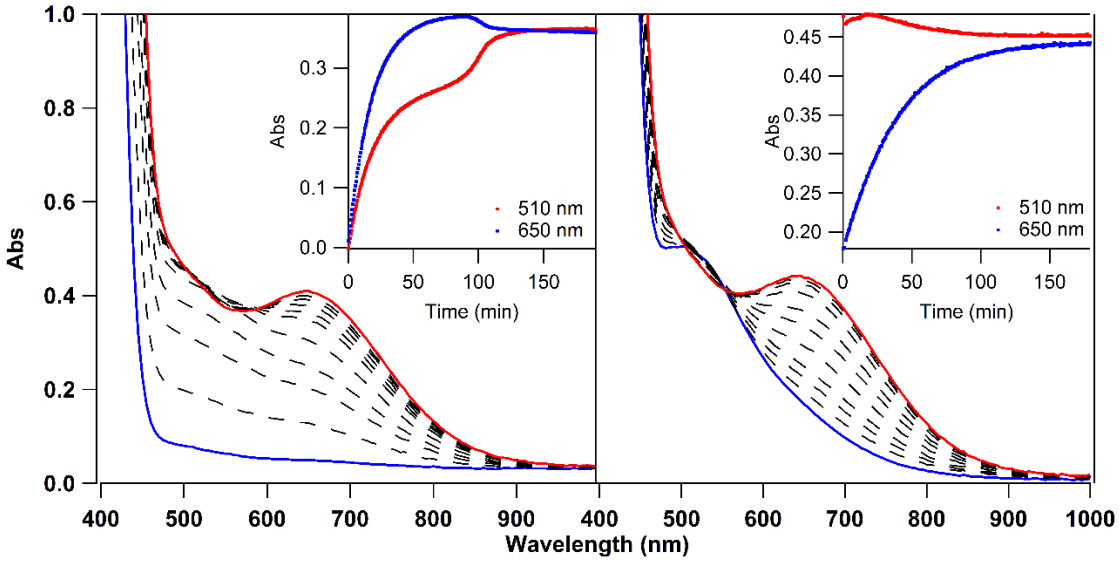

Figure 4.10. Left: Electronic absorption spectra showing the formation of a weak shoulder around 500 nm and a feature at 650 nm following the reaction of $[Mn^{II}(NCMe)(^{6Me}dpaq)]^{+}$ (blue trace) with 1.5 equivalents of ^{t}BuOOH (red trace). Right: Electronic absorption spectra showing the formation of a weak shoulder around 500 nm and a feature at 650 nm following the reaction of $[Mn^{III}(OH)(^{6Me}dpaq)]^{+}$ (blue trace) with 1 equivalent of ^{t}BuOOH (red trace). Time course of the reactions are shown in the insets.

To test our proposal that $[Mn^{III}(OH)(^{6Me}dpaq)]^{+}$ reacts with ^{t}BuOOH to form species **1**, we treated this Mn^{III}-hydroxo complex with 1 equivalent of ^{t}BuOOH From monitoring this reaction by electronic absorption spectroscopy, we observed the formation of the 650 nm electronic absorption band of **1** along with the decay of the 510 nm band of $[Mn^{III}(OH)(^{6Me}dpaq)]^{+}$ (Figure 4.10, right). This conversion is accompanied with isosbestic points at 505 and 555 nm, indicating the lack of an intermediate species in this reaction. The absorption features of this green species are within the range of previously reported Mn^{III}-alkylperoxo complexes (Table 4.6).[9-11] Kovacs

and coworkers report well-defined electronic absorption features ranging from 585 to 600 nm, and shoulders from 355 to 420 nm, for their crystallographically characterized Mn^{III}-alkylperoxo complexes.[9, 10] The electronic absorption spectra of $[Mn^{III}(OO^tBu)(dpaq)]^+$ and $[Mn^{III}(OO^tBu)(dpaq^{2Me})]^+$ exhibit features at 710 and 690 nm, respectively, as well as shoulders around 475 nm.[11]

Table 4.6. Comparison of electronic absorption band maxima (nm) and O-O stretching frequencies ($\nu_{O\text{-}O}$, cm^{-1}) for Mn^{III}-alkylperoxo complexes.

Complex	λ		ν	Reference
1	~500	650	877	*This work*
$[Mn^{III}(OO^tBu)(dpaq)]^+$	~475	710	872	*11*
$[Mn^{III}(OO^tBu)(dpaq^{2Me})]^+$	~475	690	NR	*11*
$[Mn^{III}(OO^tBu)(S^{Me2}N_4(6\text{-Me-DPPN}))]^+$	420	585	893	*10*
$[Mn^{III}(OO^tBu)(S^{Me2}N_4(QuinoPN))]^+$	415	590	895	*10*
$[Mn^{III}(OO^tBu)(S^{Me2}N_4(QuinoEN))]^+$	385	590	888	*9, 10*
$[Mn^{III}(OO^tBu)(S^{Me2}N_4(6\text{-Me-DPEN}))]^+$	355	600	875	*10*

Mass spectral analysis of **1** showed a peak at *m/z* = 554.1968 that is consistent with the formulation of this species as $[Mn^{III}(OO^tBu)(^{6Me}dpaq)]^+$ (calculated *m/z* = 554.1964, see appendix). The magnetic moment of **1**, as determined using the Evans ^1H NMR method with diamagnetic correction, supports the assignment of this species as a high-spin Mn^{III} center (μ_{eff} = 4.5 μ_B). The ^1H NMR spectrum of **1** is qualitatively similar to that observed for $[Mn^{III}(OH)(^{6Me}dpaq)]^+$ (Figure 4.8). Three upfield-shifted-peaks at -22, -46.9, and -60 ppm are only slightly perturbed from those observed in the ^1H NMR spectrum of $[Mn^{III}(OH)(^{6Me}dpaq)]^+$ (Table 4.5). The broad signal at -10 ppm is still present in the ^1H NMR spectrum of **1**, but much less intense than the analogous feature observed in the ^1H NMR spectrum of $[Mn^{III}(OH)(^{6Me}dpaq)]^+$ (Figure 4.8). Similar to that observed for the up-field-shifted peaks, the down-field-shifted peaks at 66.8, 46.1, and 42.2 ppm in the ^1H NMR spectrum of **1** only show slight deviations from those observed ^1H NMR spectrum of $[Mn^{III}(OH)(^{6Me}dpaq)]^+$ (Table 4.5).

The similarities in the ^{1}H NMR spectra of [Mn^{III}(OH)(^{6Me}dpaq)]$^{+}$ and **1** suggest structural similarities between the two species.

Further support of the formulation of **1** as a Mn^{III}-alkylperoxo species comes from FT-IR experiments. The solution FT-IR spectrum obtained following the reaction between [Mn^{III}(OH)(^{6Me}dpaq)]$^{+}$ with 1 equivalent of ^{t}BuOOH shows a feature at 877 cm^{-1} that is not observed in the spectrum of [Mn^{III}(OH)(^{6Me}dpaq)]$^{+}$ (Figure 4.11). This band has an energy similar to those of O-O vibrations reported for Mn^{III}-alkylperoxo complexes (872 – 895 cm^{-1}; Table 4.6).[9-11] As such, we tentatively assign this feature as the O-O stretch of [Mn^{III}(OO^{t}Bu)(^{6Me}dpaq)]$^{+}$. Confirmation of this assignment will come from FT-IR analysis of **1** that is generated using ^{t}Bu^{18}O^{18}OH.

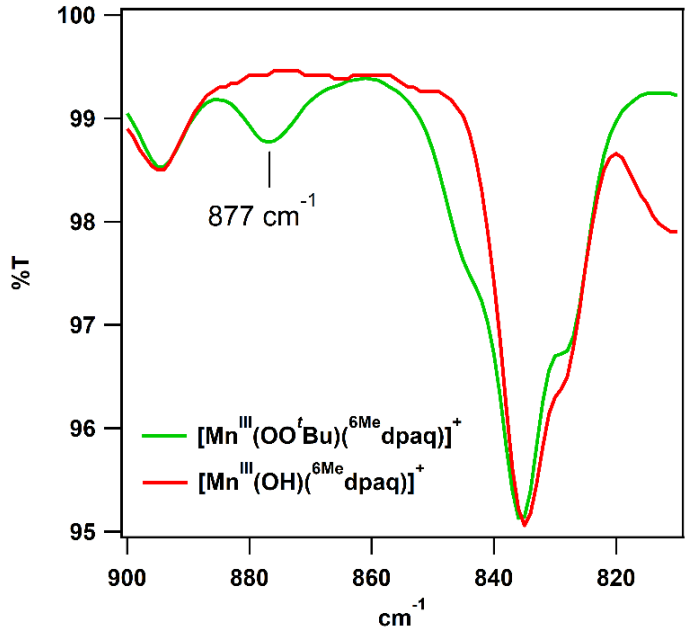

Figure 4.11. Solution FT-IR spectrum obtained following the reaction between a 2 mM solution of [Mn^{III}(OH)(^{6Me}dpaq)]$^{+}$ in MeCN and 1 equivalent of ^{t}BuOOH, showing a signal at 877 cm^{-1} tentatively assigned as the O–O stretch of the alkylperoxo complex (green trace). The spectrum of [Mn^{III}(OH)(^{6Me}dpaq)]$^{+}$ (red trace) is shown for comparison.

Additional support for the formulation of **1** as a Mn^{III}-alkylperoxo species comes from an XAS analysis of frozen MeCN solutions following the reaction between a 10 mM solution of $[Mn^{III}(OH)(^{6Me}dpaq)]^+$ and 1 equivalent of ^{t}BuOOH at 50°C. The Mn K-edge energy of **1** is 6549.4 eV, similar to the edge energies reported for $[Mn^{III}(OO^tBu)(dpaq)]^+$ and $[Mn^{III}(OO^tBu)(dpaq^{2Me})]^+$ (6550.4 and 6549.5, respectively; Table 4.7; Figure 4.12). The pre-edge features of the three Mn^{III}-complexes are of similar energy and area (Table 4.7, Figure 4.12 inset).[11] Taken together with the electronic absorption, mass spectrometry, and FT-IR data, this analysis of the XAS data supports our assignment of **1** as $[Mn^{III}(OO^tBu)(^{6Me}dpaq)]^+$.

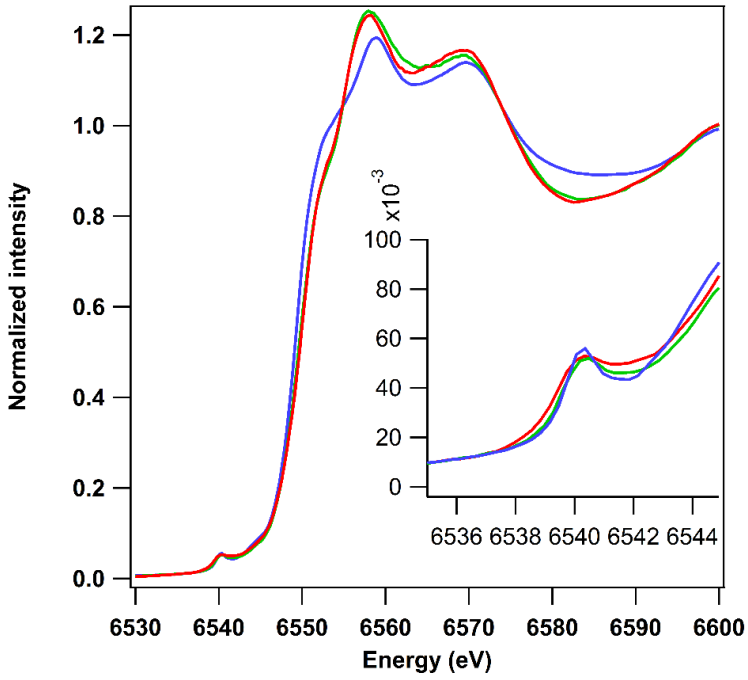

Figure 4.12. Comparison of Mn K-edge near-edge spectra of **1** (blue), $[Mn^{III}(OO^tBu)(dpaq)]^+$ (red), and $[Mn^{III}(OO^tBu)(dpaq^{2Me})]^+$ (green) collected for frozen solutions in MeCN at 10 K. (Inset) Pre-edge features of the three complexes.

Table 4.7. Experimental pre-edge and Mn K-edge properties for Mn^{III}-alkylperoxo complexes.

Complex	Pre-edge energy	Pre-edge area	Edge energy	Reference
1	6540.1 6543.1	4.7	6549.4	*This work*
$[Mn^{III}(OO^tBu)(dpaq)]^+$	6540.2 6542.0	4.6	6550.4	*35*
$[Mn^{III}(OO^tBu)(dpaq^{2Me})]^+$	6540.5 6541.7	4.1	6549.5	*35*

Structural information for previously reported $[Mn^{III}(OO^tBu)(dpaq)]^+$ and $[Mn^{III}(OO^tBu)(dpaq^{2Me})]^+$ was afforded through extended X-ray absorption fine structure (EXAFS) analysis of frozen MeCN solutions. A similar analysis was performed for a 10 mM sample of **1** in MeCN that was formed at 50°C and subsequently frozen. The Fourier transform of the EXAFS data of **1** consists of an intense peak at 1.99 Å with a shoulder at 1.87 Å, a peak at 2.45 Å, and smaller features at 3.00 and 3.34 Å (Figure 4.13). The first coordination sphere was fit by including a shell of 2 O/N atoms at 2.00 Å and a shell of 3 N atoms at 2.35 Å (Table 4.8). This combination of shells results in a more intense peak than that observed in the experimental data (Figure 4.13). Numerous combinations of N atom and O atom shells were evaluated in an effort to better model the intensity of the peak at 1.99 Å, but the variations either did not improve the quality of the fit, or resulted in unreasonable distances or Debye-Waller factors (Table 4.8). The fit was improved by including a shell of 6 C atoms at 2.91 Å to account for the second coordination sphere, but modeling of peak intensities remained poor (Figure 4.13). The inclusion of a multiscattering pathway comprised of a C atom and a N atom greatly improved the fit, but resulted in negative Debye-Waller factors (Table 4.8).

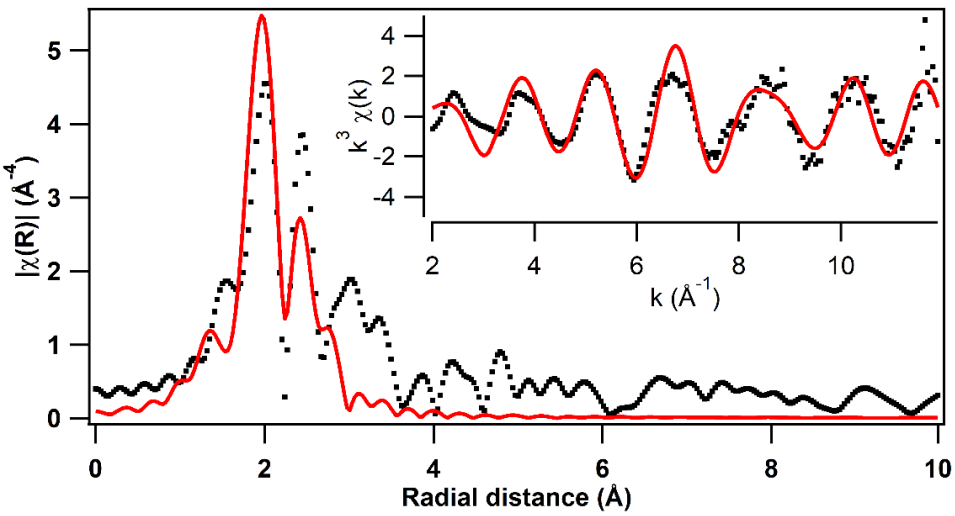

Figure 4.13. Fourier transform of the Mn K-edge EXAFS data, and EXAFS spectra (inset), for 10 mM **1** in frozen MeCN. Experimental data is in black, while fits of the data are shown in red.

Table 4.8. Fits of EXAFS data of **1**.[a]

Fit	Mn-N/O			Mn-N			Mn-N			Mn-C			Mn-C-N			Goodness of fit[b]
	n	*r* (Å)	σ^2	*n*	*r* (Å)	σ^2	*n*	*r* (Å)	σ^2	*n*	*r* (Å)	σ^2	*n*	*r* (Å)	σ^2	
1	6	1.71	0.073													0.999
2	1	1.99	0.008	5	2.3	0.006										0.714
3	1	2.01	0.005	4	2.38	0.006										0.613
4	2	2.02	0.010	4	2.37	0.005										0.574
5	4	2.03	0.036	2	2.36	-0.001										0.505
6	2	2.05	0.015	3	2.36	0.002										0.508
7	3	2.02	0.020	3	2.36	0.002										0.529
8	2	2.01	0.016	2	2.70	-0.001										0.490
9	2	2.05	0.016	3	2.55	0.007	1	2.38	-0.004							0.384
10	2	2.07	0.012	2	2.61	-0.001	2	2.41	-0.001							0.324
13	***2***	***2***	***0.014***	***3***	***2.35***	***0.002***				***6***	***2.91***	***0.006***				***0.369***
17	2	2	0.010	3	2.35	0.003				6	2.91	0.005	2	3.32	-0.0006	0.263

[a]Fit highlighted in bold, italicized font represents the best fit as shown in Figure A3.13 (red trace).
[b]Evaluated using the R-factor.

Fits of the EXAFS data within different *k* ranges converged on shells of similar distances, supporting the model described above as a reasonable fit to the data (Table A3.1). EXAFS data of the previously reported $[Mn^{III}(OO^tBu)(dpaq)]^+$ were similarly fit with two shells of 2 O/N atoms and 4 N atoms for the first coordination sphere, and a shell of 6 C atoms for the second coordination sphere.[11] In that case, the shell of 2 O/N atoms was attributed to contributions from the axial amide and alkylperoxo ligands, and the shell of 4 N atoms was attributed to the equatorial ligands. The structural parameters obtained from fitting the EXAFS data of $[Mn^{III}(OO^tBu)(dpaq)]^+$ were very similar to those reported in the crystal structure of its Mn^{III}-hydroxo counterpart (Chapter 3).[11] If the shells used in the fitting of EXAFS data of **1** are assigned similarly, the analysis suggests unexpected deviations in Mn-ligand bond lengths between **1** and $[Mn^{III}(OH)(^{6Me}dpaq)](OTf)$ (Table 4.9). This may indicate that different structural models need to be considered for $[Mn^{III}(OO^tBu)(^{6Me}dpaq)]^+$. Alternatively, since the sample of **1** was formed at 50°C at a relatively high concentration of 10 mM, there is a possibility of some thermal decay product being present. Such inhomogeneity would complicate the analysis of the EXAFS data. As such, we plan to prepare a new sample of **1** for XAS analysis at a later time.

Table 4.9. Comparison of the bond lengths obtained from the EXAFS analysis of **1**, a DFT-optimized structure of $[Mn^{III}(OO^tBu)(^{6Me}dpaq)]^+$, the EXAFS analysis of $[Mn^{III}(OO^tBu)(dpaq)]^+$, and the crystal structure of $[Mn^{III}(OH)(^{6Me}dpaq)](OTf)$ (distances in Å).

	1	$[Mn^{II}(OO^tBu)(^{6Me}dpaq)]^+$	$[Mn^{III}(OO^tBu)(dpaq)]^+$ [a]	$[Mn^{III}(OH)(^{6Me}dpaq)](OTf)$
	EXAFS	DFT	EXAFS	XRD
Mn-O/N_{amide}	2.00	1.84(O), 1.97(N)	1.90	1.806(6) (O),1.962(6) (N)
Mn-N_{Py}		2.41, 2.27	--	2.322(6), 2.381(7)
Mn-N_{amine}		2.14	--	2.130(6)
Mn–N_{Qu}		2.03	--	2.041(7)
Mn-N_{eq} (avg.)	2.34	2.21	2.17	2.22
Mn---C (avg.)	2.91	2.95	2.97	2.96

[a] From reference [11].

The DFT-optimized structure of $[Mn^{III}(OO^tBu)(^{6Me}dpaq)]^+$ used for refinement of the EXAFS data predicts similar metrical parameters to those observed in the XRD structure of $[Mn^{III}(OH)(^{6Me}dpaq)](OTf)$ (Table 4.9). The calculated structure has a six-coordinate Mn center, similar to the crystal structure of $[Mn^{III}(OH)(^{6Me}dpaq)](OTf)$ (Figures 4.7 and 4.14). The calculated structure of $[Mn^{III}(OO^tBu)(^{6Me}dpaq)]^+$ has a Mn-O(O^tBu) distance of 1.84 Å which is longer than the Mn-O(H) distance observed in the crystal structure of $[Mn^{III}(OH)(^{6Me}dpaq)]^+$ by ~0.03 Å. A similar Mn-O bond length was calculated for $[Mn^{III}(OO^tBu)(dpaq)]^+$.[11] The calculated O-O bond length of $[Mn^{III}(OO^tBu)(^{6Me}dpaq)]^+$ is 1.48 Å, identical to the O-O bond lengths calculated for $[Mn^{III}(OO^tBu)(dpaq)]^+$ and $[Mn^{III}(OO^tBu)(dpaq^{2Me})]^+$.[11] The calculated distances between the Mn center and the pyridine substituents are 2.41 and 2.27 Å (Table 4.9). These distances are longer than the Mn-pyridine distances calculated for $[Mn^{III}(OO^tBu)(dpaq)]^+$ and $[Mn^{III}(OO^tBu)(dpaq^{2Me})]^+$ by 0.08 to 0.23 Å, due to the steric bulk imparted by the methyl substitutions adjacent to the donor nitrogen atom (Figure 4.14, Table 4.9).[31, 34] The DFT-calculated Mn-N_{amide} bond length of 1.97 Å is similar to that observed in the crystal structure of $[Mn^{III}(OH)(^{6Me}dpaq)](OTf)$ and slightly shorter than that calculated for $[Mn^{III}(OO^tBu)(dpaq)]^+$ (1.99 Å, Table 4.9).[11] The Mn-$N_{Quinline}$ and Mn-N_{amine} bond lengths of $[Mn^{III}(OO^tBu)(^{6Me}dpaq)]^+$ are calculated to be essentially identical to those observed in the crystal structure of $[Mn^{III}(OH)(^{6Me}dpaq)](OTf)$ (Table 4.9).

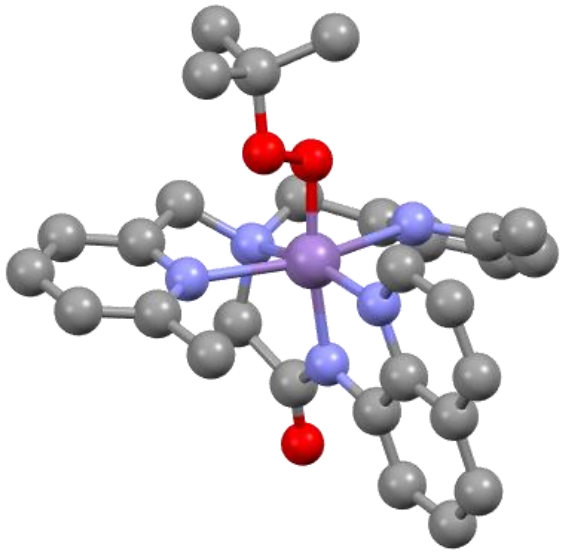

Figure 4.14. DFT-optimized structure of $[Mn^{III}(OO^tBu)(^{6Me}dpaq)]^+$.

Reactivity and decay of $[Mn^{III}(OO^tBu)(^{6Me}dpaq)](OTf)$. The thermal decay of $[Mn^{III}(OO^tBu)(^{6Me}dpaq)]^+$ occurs over a period of days at 298 K to yield a brown solution. An estimate of the half-life was determined by monitoring the decay with electronic absorption spectroscopy. After a period of 116 hours, the intensity of the electronic absorption feature at 650 nm had decayed by 44% in MeCN at 298 K. Assuming a constant rate of decay, the half-life of $[Mn^{III}(OO^tBu)(^{6Me}dpaq)]^+$ is estimated to be 5 days. The decay is quicker at 328 K ($t_{1/2} \approx 10$ hours), allowing the complete decay pathway to be monitored using electronic absorption spectroscopy over the course of 46 hours (Figure 4.15). Monitoring the disappearance of the electronic absorption feature at 650 nm reveals an initial relatively slow rate of decay, followed by a more rapid process. Thus, the decay of $[Mn^{III}(OO^tBu)(^{6Me}dpaq)]^+$ does not follow first-order kinetic behavior, precluding the determination of a pseudo-first-order rate constant for this process. The final spectrum of the decay is featureless (Figure 4.15).

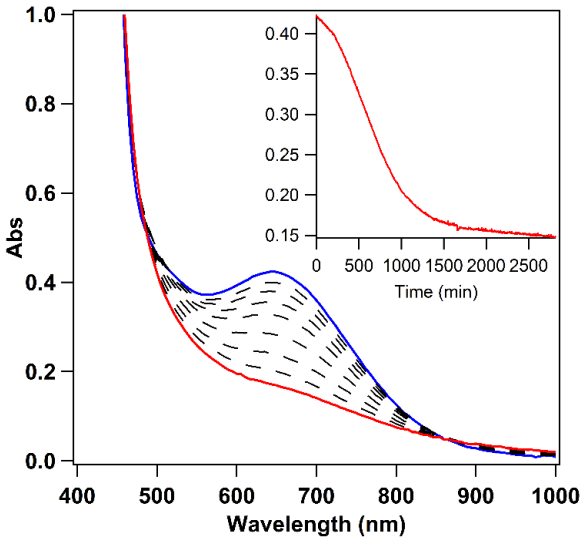

Figure 4.15. Electronic absorption spectra following the decay of a 2 mM solution of **1** in MeCN (blue trace) at 328 K over the course of 46 hours to result in a featureless spectrum (red trace).

^{1}H NMR analysis of the solution following thermal decay reveals the loss of signals corresponding to **1** along with the appearance of hyperfine-shifted peaks that are consistent with the formation of $[Mn^{III}(OH)(^{6Me}dpaq)]^{+}$. Multiple other hyperfine-shifted peaks are also observed, indicating the formation of one or more paramagnetic species also being formed through a presumably complex decay mechanism (Figure 4.16, blue trace). There are very few peaks in the 0-12 ppm region, none of which correspond to the free ligand (Figure A3.9). Mass spectral analysis of the solution following the decay of $[Mn^{III}(OO^{t}Bu)(^{6Me}dpaq)]^{+}$ revealed peaks associated with free ^{6Me}dpaq ligand, $[Mn^{III}(OH)(^{6Me}dpaq)]^{+}$, and $[Mn^{III}(OO^{t}Bu)(^{6Me}dpaq)]^{+}$ (Figure A3.10).

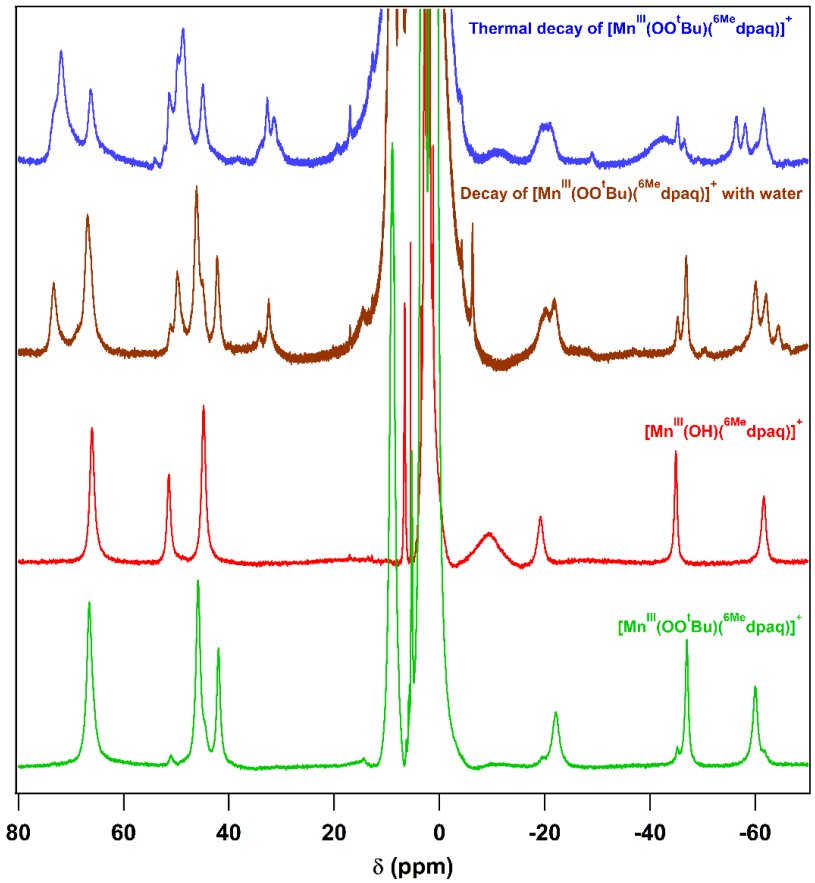

Figure 4.16. ^{1}H NMR spectra obtained of $[Mn^{III}(OH)(^{6Me}dpaq)]^{+}$ (red trace) and $[Mn^{III}(OO^{t}Bu)(^{6Me}dpaq)]^{+}$ in d_3-MeCN (green trace), as well as ^{1}H NMR spectra obtained following the thermal decay of a 2 mM solution $[Mn^{III}(OO^{t}Bu)(^{6Me}dpaq)]^{+}$ in d_3-MeCN (blue trace), as well as after the reaction of $[Mn^{III}(OO^{t}Bu)(^{6Me}dpaq)]^{+}$ with 100 equivalents of H_2O in d_3-MeCN (brown trace).

Taking inspiration from the proposed catalytic cycle of Mn-LOX, in which a proposed Mn^{III}-alkylperoxo intermediate undergoes ligand exchange with H_2O to form the Mn^{III}-hydroxo resting state of the enzyme,[8] we also investigated the reactivity of $[Mn^{III}(OO^{t}Bu)(^{6Me}dpaq)]^{+}$ with H_2O. The addition of 100 equivalents of H_2O to $[Mn^{III}(OO^{t}Bu)(^{6Me}dpaq)]^{+}$ results in the loss of intensity at 650 nm, resulting in an electronic absorption spectrum with a feature at ~500 nm, similar to what is observed in the spectrum of $[Mn^{III}(OH)(^{6Me}dpaq)]^{+}$ (Figure 4.17). However, the precipitation of an insoluble brown solid is also observed during this process, possibly indicative

of demetallation. ^{1}H NMR analysis of the filtered solution following thermal decay reveals a similar set of peaks to that observed in the thermal decay of [Mn^{III}(OO^{t}Bu)(^{6Me}dpaq)]$^{+}$, including hyperfine-shifted signals that can be attributed to both [Mn^{III}(OO^{t}Bu)(^{6Me}dpaq)]$^{+}$ and [Mn^{III}(OH)(^{6Me}dpaq)]$^{+}$, as well as additional hyperfine-shifted peaks that have not been identified (Figure 4.16). Mass spectral analysis of the solution following the decay of [Mn^{III}(OO^{t}Bu)(^{6Me}dpaq)]$^{+}$ revealed peaks associated with free ^{6Me}dpaq ligand, [Mn^{II}(^{6Me}dpaq)]$^{+}$, [Mn^{III}(OH)(^{6Me}dpaq)]$^{+}$, and [Mn^{III}(OO^{t}Bu)(^{6Me}dpaq)]$^{+}$ (Figure A3.10). While the observation of [Mn^{II}(^{6Me}dpaq)]$^{+}$ as a major decay product may support a mechanism proceeding through Mn-O homolysis, the observation of other products points to a more complicated array of decay reactions taking place.

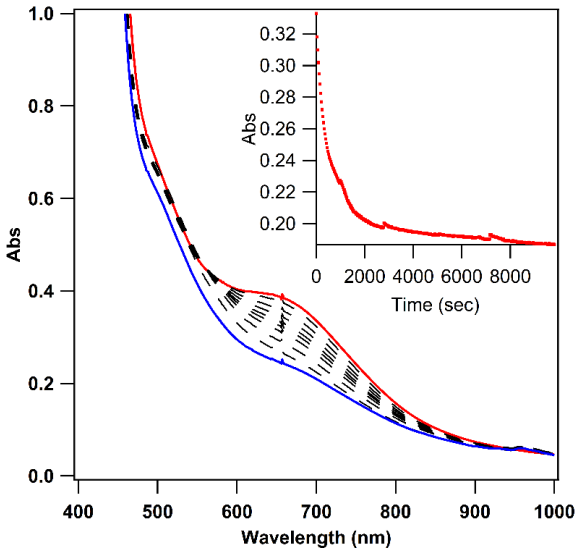

Figure 4.17. Electronic absorption spectra monitoring the reaction of a 2 mM solution of [Mn^{III}(OO^{t}Bu)(^{6Me}dpaq)]$^{+}$ in MeCN with 100 equivalents of H_2O at 298 K. (Inset) time course for the spectral changes.

As previous studies have employed phosphines as a probe of homolytic O-O bond cleavage, the reactivity of [Mn^{III}(OO^{t}Bu)(^{6Me}dpaq)]$^{+}$ with PPh_3 was investigated.[10, 47] The addition

of 100 equivalents of PPh_3 to an anaerobic solution of $[Mn^{III}(OO^tBu)(^{6Me}dpaq)]^+$ (0.5 mM in MeCN) at 298 K resulted in the loss of intensity at 650 nm over the course of two hours, resulting in an electronic absorption spectrum consistent with the generation of Mn^{II} products (Figure 4.18). A ^{31}P NMR analysis of the organic products revealed the formation of Ph_3PO (Figure A3.11). Previously reported Mn^{III}-alkylperoxo complexes supported by N_4S^- ligands are also able to react with a phosphine substrate and yield the phosphine oxide product.[10] In those cases, the addition of PPh_3 did not have an effect on the decay rate of the Mn^{III}-alkylperoxo species, indicative of the Mn^{III}-alkylperoxo decay product being responsible for the reativity.[10] Since the addition of PPh_3 does affect the decay rate of $[Mn^{III}(OO^tBu)(^{6Me}dpaq)]^+$, it is likely that the oxidation of PPh_3 follows a different pathway in which the substrate reacts directly with the Mn^{III}-alkylperoxo species.

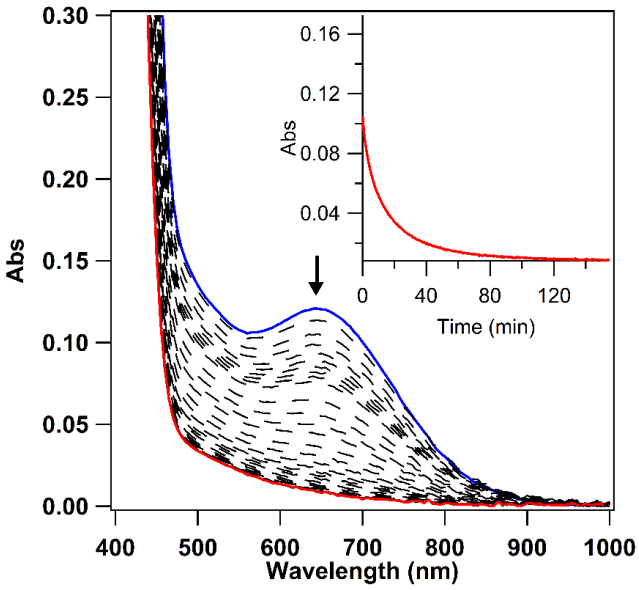

Figure 4.18. Electronic absorption spectra monitoring the reaction of a 0.5 mM anaerobic solution of $[Mn^{III}(OO^tBu)(^{6Me}dpaq)]^+$ (blue trace) in MeCN with 100 equivalents of PPh_3 at 298 K. (Inset) time course for the spectral changes.

The reaction between $[Mn^{III}(OO^{t}Bu)(^{6Me}dpaq)]^{+}$ and the hydrogen-atom donor 9,10-dihydroanthracene (DHA) was also explored. 75 equivalents of DHA were added to a 1.25 mM solution of $[Mn^{III}(OO^{t}Bu)(^{6Me}dpaq)]^{+}$ in MeCN and allowed to stir for 30 hours while monitoring with electronic absorption spectroscopy. The slow disappearance of the electronic absorption feature at 650 nm was observed (Figure 4.19). ^{1}H NMR analysis of the organic products revealed the formation of 14.5 equivalents of anthracene, 7 equivalents of anthrone, and 1.5 equivalents of anthraquinone (Figure A3.12). The total amount of oxidized products corresponds to 23 equivalents of DHA being consumed during the reaction. The products observed can arise from the reactivity of DHA with a high-valent Mn complex and/ or an alkoxyl or peroxyl radical generated through the different possible decay pathways of $[Mn^{III}(OO^{t}Bu)(^{6Me}dpaq)]^{+}$. Furthermore, the presence of O_2 likely has an effect on the product distribution. As such, the reaction between $[Mn^{III}(OO^{t}Bu)(^{6Me}dpaq)]^{+}$ and DHA has not proven insightful towards the decay mechanism of $[Mn^{III}(OO^{t}Bu)(^{6Me}dpaq)]^{+}$. Future experiments in which O_2 is absent from the reaction mixture should prove more illuminating. It should be noted that DHA oxidation experiments with previously reported Mn^{III}-alkylperoxo complexes supported by $N4S^{-}$ ligands did exhibit the formation of hydrogen atom transfer products. However, the presence of a substrate did not affect the rate of Mn^{III}-alkylperoxo decay, suggesting that a proposed Mn^{IV}-oxo decay product was responsible for substrate oxidation.[10]

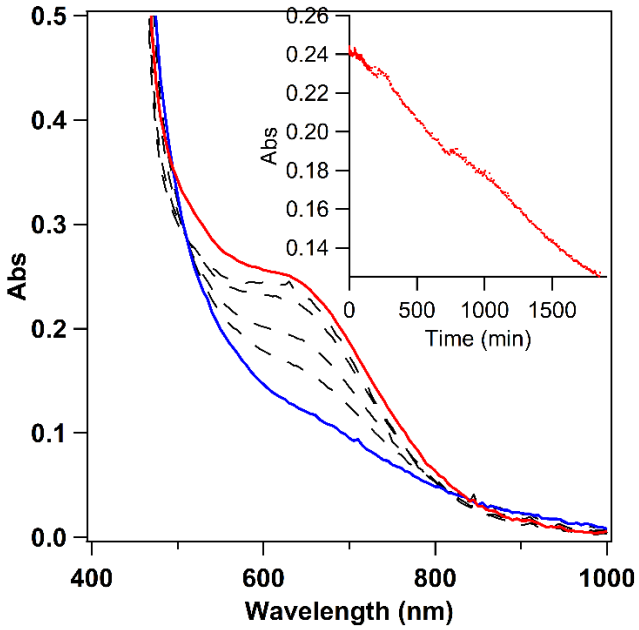

Figure 4.19. Electronic absorption spectra following the reaction of a 1.25 mM solution of $[Mn^{III}(OO^tBu)(^{6Me}dpaq)]^+$ (red trace) with 9,10-dihydroanthracene in MeCN at 328 K. (Inset) time course for the spectral changes.

4.4 Conclusion. In this work, a new derivative of the dpaq ligand platform was developed in order to stabilize a Mn^{III}-alkylperoxo species. The Mn^{II} complex of this new ligand featuring methyl functionalization of pyridine donors, $[Mn^{II}(NCMe)(^{6Me}dpaq)]^+$, was characterized by XAS, mass spectrometry, and EPR spectroscopy. $[Mn^{II}(NCMe)(^{6Me}dpaq)]^+$ was oxidized by PhIO to form the Mn^{III}-hydroxo complex, $[Mn^{III}(OH)(^{6Me}dpaq)]^+$. XRD analysis of $[Mn^{III}(OH)(^{6Me}dpaq)]^+$ revealed that the methyl functionalization of the pyridine ligand substituents resulted in the predicted Mn-N elongation *cis* to the hydroxyl ligand moiety. Both $[Mn^{II}(NCMe)(^{6Me}dpaq)]^+$ and $[Mn^{III}(OH)(^{6Me}dpaq)]^+$ react with stoichiometric amounts of ^{t}BuOOH to generate a new intermediate, species **1**. This room temperature-stable compound is assigned to be $[Mn^{III}(OO^tBu)(^{6Me}dpaq)]^+$, based on characterization by electronic absorption, mass spectrometry, XAS, and ^{1}H NMR spectroscopy. The stability of **1**, combined with the ability to use only stoichiometric amounts of peroxide during formation, will aid in more thorough investigations of

the reactivity and decay of this class of compounds. The reaction of **1** with PPh_3 occurs much faster than the thermal decay of **1**, suggesting a direct reaction between the substrate and the alkylperoxo moiety of **1** as opposed to a high-valent Mn decay product.

4.5 References.

1. A. T. Fiedler and A. A. Fischer, *J. Biol. Inorg. Chem.*, 2017, **22**, 407-424.
2. W. A. Gunderson, A. I. Zatsman, J. P. Emerson, E. R. Farquhar, L. Que, J. D. Lipscomb and M. P. Hendrich, *J. Am. Chem. Soc.*, 2008, **130**, 14465-14467.
3. M. W. Vetting, L. P. Wackett, L. Que, Jr., J. D. Lipscomb and D. H. Ohlendorf, *J. Bacteriol.*, 2004, **186**, 1945-1958.
4. M. H. Glickman and J. P. Klinman, *Biochem.*, 1995, **34**, 14077-14092.
5. C. Su, M. Sahlin and E. H. Oliw, *J. Biol. Chem.*, 2000, **275**, 18830-18835.
6. A. Wennman, S. Karkehabadi and E. H. Oliw, *Arch. Biochem. Biophys.*, 2014, **555-556**, 9-15.
7. A. Wennman, E. H. Oliw, S. Karkehabadi and Y. Chen, *J. Biol. Chem.*, 2016.
8. A. L.-F. Company, J.; Costas, M., Elsevier B.V., 2013, pp. 487-564.
9. M. K. Coggins and J. A. Kovacs, *J. Am. Chem. Soc.*, 2011, **133**, 12470-12473.
10. M. K. Coggins, V. Martin-Diaconescu, S. DeBeer and J. A. Kovacs, *J. Am. Chem. Soc.*, 2013, **135**.
11. J. D. Parham, G. B. Wijeratne, D. B. Rice and T. A. Jackson, *Inorg. Chem.*, 2018, **57**, 2489-2502.
12. H. Komatsuzaki, N. Sakamoto, M. Satoh, S. Hikichi, M. Akita and Y. Moro-oka, *Inorg. Chem.*, 1998, **37**, 6554-6555.
13. H. Nagao, N. Komeda, M. Mukaida, M. Suzuki and K. Tanaka, *Inorg. Chem.*, 1996, **35**, 6809-6815.
14. V. R. Kokatnur and M. Jelling, *J. Am. Chem. Soc.*, 1941, **63**, 1432-1433.
15. Y. Hitomi, K. Arakawa, T. Funabiki and M. Kodera, *Angew. Chem. Int. Ed.*, 2012, **51**, 3448-3452.
16. Data Collection: SMART Software in APEX2 v2014.11-0 Suite. Bruker-AXS, 5465 E. Cheryl Parkway, Madison, WI 53711-5373 USA.
17. Data Reduction: SAINT Software in APEX2 v2014.11-0 Suite. Bruker-AXS, 5465 E. Cheryl Parkway, Madison, WI 53711-5373 USA.
18. Refinement: SHELXTL Software in APEX2 v2014.11-0 Suite. Bruker-AXS, 5465 E. Cheryl Parkway, Madison, WI 53711-5373 USA.
19. B. N. Ravel, M., *J. Synchrotron Rad.*, 2005, **12**, 537-541.
20. J. J. Rehr, J. Mustre de Leon, S. I. Zabinsky and R. C. Albers, *J. Am. Chem. Soc.*, 1991, **113**, 5135-5140.
21. F. Neese, *W. Int. Rev. Comp. Mol. Sci.*, 2018, **8**, e1327.
22. A. D. Becke, *J. Chem. Phys.*, 1993, **98**, 1372-1377.
23. A. D. Becke, *J. Chem. Phys.*, 1993, **98**, 5648-5652.

24. C. Lee, W. Yang and R. G. Parr, *Phys. Rev. B*, 1988, **37**, 785-789.
25. A. Schäfer, H. Horn and R. Ahlrichs, *J. Chem. Phys.*, 1992, **97**, 2571-2577.
26. A. Schäfer, C. Huber and R. Ahlrichs, *J. Chem. Phys.*, 1994, **100**, 5829-5835.
27. F. Neese, *J. Comput. Chem.*, 2003, **24**, 1740-1747.
28. S. Grimme, J. Antony, S. Ehrlich and H. Krieg, *J. Chem. Phys.*, 2010, **132**, 154104.
29. J. Tao, J. P. Perdew, V. N. Staroverov and G. E. Scuseria, *Phys. Rev. Lett.*, 2003, **91**, 146401.
30. F. Weigend and R. Ahlrichs, *Phys. Chem. Chem. Phys.*, 2005, **7**, 3297-3305.
31. D. B. Rice, G. B. Wijeratne, A. D. Burr, J. D. Parham, V. W. Day and T. A. Jackson, *Inorg. Chem.*, 2016, **55**, 8110-8120.
32. M. K. Coggins, S. Toledo, E. Shaffer, W. Kaminsky, J. Shearer and J. A. Kovacs, *Inorg. Chem.*, 2012, **51**, 6633-6644.
33. D. B. Rice, G. W. Wijeratne and T. A. Jackson, *J. Biol. Inorg. Chem.*, 2017, **22**, 1281-1293.
34. G. B. Wijeratne, B. Corzine, V. W. Day and T. A. Jackson, *Inorg. Chem.*, 2014, **53**, 7622-7634.
35. D. B. Rice, A. Munasinghe, E. N. Grotemeyer, A. D. Burr, V. W. Day and T. A. Jackson, *Inorg. Chem.*, 2019, **58**, 622-636.
36. C. R. Goldsmith, A. P. Cole and T. D. P. Stack, *J. Am. Chem. Soc.*, 2005, **127**, 9904-9912.
37. S. El Ghachtouli, B. Lassalle-Kaiser, P. Dorlet, R. Guillot, E. Anxolabéhère-Mallart, C. Costentin and A. Aukauloo, *Ener. Env. Sci.*, 2011, **4**, 2041-2044.
38. Z. Shirin, B. S. Hammes, V. G. Young and A. S. Borovik, *J. Am. Chem. Soc.*, 2000, **122**, 1836-1837.
39. B. Cheng, P. H. Fries, J.-C. Marchon and W. R. Scheidt, *Inorg. Chem.*, 1996, **35**, 1024-1032.
40. A. A. Eroy-Reveles, Y. Leung, C. M. Beavers, M. M. Olmstead and P. K. Mascharak, *J. Am. Chem. Soc.*, 2008, **130**, 4447-4458.
41. D. M. Eichhorn and W. H. Armstrong, *J. Chem. Soc., Chem. Commun.*, 1992, 85-87.
42. T. J. Hubin, J. M. McCormick, N. W. Alcock and D. H. Busch, *Inorg. Chem.*, 2001, **40**, 435-444.
43. M. K. Coggins, L. M. Brines and J. A. Kovacs, *Inorg. Chem.*, 2013, **52**, 12383-12393.
44. Z. Shirin, A. S. Borovik and V. G. Young Jr, *Chem. Comm.*, 1997, 1967-1968.
45. D. B. Rice, S. D. Jones, J. T. Douglas and T. A. Jackson, *Inorg. Chem.*, 2018, **57**, 7825-7837.
46. D. B. Rice, S. D. Jones, J. T. Douglas and T. A. Jackson, *Inorg. Chem.*, 2018, **57**, 7825-7837.
47. A. G. DiPasquale, D. A. Hrovat and J. M. Mayer, *Organometallics*, 2006, **25**, 915-924.

Chapter 5

The Reactivity of $[Mn^{III}(OH)(dpaq^{2Me})](OTf)$ and $[Mn^{III}(OH)(^{6Me}dpaq)](OTf)$ with H_2O_2

5.1 Introduction. There are several examples of Mn-dependent enzymes that are proposed to form peroxo intermediates as part of their catalytic cycles.[1, 2] For example, the formation of a dimeric $(\mu\text{-O})_2Mn^{III}Mn^{IV}$ species in Mn-ribonucleotide reductase (Mn-RNR) from superoxide is proposed to proceed through a Mn^{III}-peroxo intermediate.[3-6] For Mn-dependent dioxygenases and Mn-lipoxygenases, it has been proposed that to O_2-derived Mn-alkylperoxo intermediates form during substrate oxidation.[7-11] The product-inhibited complex of manganese superoxide dismutase is presumed to be a Mn^{III}-peroxo adduct,[12-14] but the exact nature of this species (i.e. side-on Mn^{III}-peroxo versus end-on Mn^{III}-hydroperoxo complex) is a matter of contention.[15-17] Water oxidation by the oxygen evolving complex of Photosystem II results in a putative Mn-OO(H)-M intermediate (M = Mn or Ca) during O-O bond formation.[18-23] The majority of these proposed intermediates have not been observed.

The importance of peroxo-level intermediates in biological pathways has led to the development of synthetic model complexes as investigative tools. While there have been numerous examples of synthetic side-on Mn-peroxo species,[24-44] examples of end-on Mn-hydroperoxo or Mn-alkylperoxo complexes are rare. Reports investigating Mn^{III}-hydroperoxo complexes are especially limited in number, with only two examples having been reported.[45, 46] The formation of the Mn^{III}-hydroperoxo complexes $[Mn^{III}(OOH)(14\text{-tmc})]^{2+}$ and $[Mn^{III}(OOH)(13\text{-tmc})]^{2+}$ was achieved through the addition of perchloric acid to their side-on Mn^{III}-peroxo counterparts in MeCN at -40°C (14-tmc = 1,4,8,11-tetramethyl-1,4,8,11-tetraaza-cyclotetradecane, 13-tmc = 1,4,8,11-tetramethyl-1,4,8,11-tetraaza-cyclotridecane).[45] The Mn^{III}-hydroperoxo complexes were characterized by electronic absorption, resonance Raman, electron paramagnetic resonance (EPR), and X-ray absorption spectroscopy.[45, 46] These complexes were only stable at -40°C, and rapidly carried out oxygen atom transfer (OAT) reactions with thioanisole and its derivatives at this

temperature.[45, 46] In addition to OAT reactivity, $[Mn^{III}(OOH)(13\text{-tmc})]^{2+}$ was also capable of performing hydrogen atom transfer (HAT) reactions with the hydrocarbons with weak C-H bonds, including xanthene, 9,10-dihydroanthracene (DHA), and 1,4-cyclohexadiene.[46] Aldehyde deformylation of cyclohexane carboxaldehyde by $[Mn^{III}(OOH)(13\text{-tmc})]^{2+}$ was also observed.[46]

Synthetic Mn^{III}-alkylperoxo complexes have also been studied, both for their own relevance to biological pathways and as analogues of the highly unstable metal-hydroperoxo intermediates discussed above.[47-51] In work by Kovacs and coworkers, a series of Mn^{III}-alkylperoxo complexes supported by N_4S^- type ligands were formed through the reaction of Mn^{II} complexes with ^{t}BuOOH at -15°C in dichloromethane. These complexes were only stable at -15 °C. The X-ray diffraction structures of these complexes revealed thiolate ligands *cis* to the alkylperoxo moiety, along with elongated equatorial Mn-N bonds.[49, 50] Investigations of the decay of these complexes, both in the presence and absence of various substrates, suggested a decay mechanism involving homolytic O–O bond cleavage.[50] More recently, our group reported the formation of two Mn^{III}-alkylperoxo species that featured amide groups *trans* to the alkylperoxo moiety (Chapter 3).[51] The formation of these complexes, $[Mn^{III}(OO^tBu)(dpaq)]^+$ and $[Mn^{III}(OO^tBu)(dpaq^{2Me})]^+$, was achieved through the reaction of the Mn^{II} or Mn^{III}-hydroxo counterparts with ^{t}BuOOH (dpaq = 2-(bis((pyridin-2-yl)methyl)amino)-*N*-(quinolin-8-yl)acetamidate, $dpaq^{2Me}$ = 2-(bis(pyridin-2-ylmethyl)amino)-*N*-(2-methylquinolin-8-yl)acetamidate, Chapter 3).[51] Maximal conversion to the Mn^{III}-alkylperoxo species was only achieved through the addition of 100 equivalents of ^{t}BuOOH, complicating investigations into the reactivity or decay pathways of these complexes. Nonetheless, the observation of $\bullet OO^tBu$ radical in EPR analyses of the Mn^{III}-alkylperoxo species provided circumstantial evidence of a decay mechanism that involves Mn-O bond homolysis.[51] Building from these recent advancements in Mn-alkylperoxo chemistry, the development of a new

derivative of the dpaq ligand featuring methyl functionalization on the pyridine positions adjacent to the nitrogen atom, ^{6Me}dpaq, has led to the formation of a room temperature stable Mn^{III}-akylperoxo complex (Chapter 4). Investigations of the reactivity and decay of this new complex are ongoing.

Knowing that the $[Mn^{III}(OH)(dpaq^{2Me})]^+$ and $[Mn^{III}(OH)(^{6Me}dpaq)]^+$ complexes are capable of reacting with ^{t}BuOOH to generate end-on Mn^{III}-alkylperoxo species (Chapters 3 and 4), we were interested in the possibility of generating an end-on Mn^{III}-hydroperoxo complex by treating the $[Mn^{III}(OH)(dpaq^{2Me})]^+$ or $[Mn^{III}(OH)(^{6Me}dpaq)]^+$ complexes with H_2O_2. As described below, the addition of H_2O_2 to the Mn^{III}-hydroxo complexes in the presence of a base results in the formation of new intermediates (intermediates $\mathbf{1^{2Me}}$ and $\mathbf{1^{6Me}}$) that have been characterized by electronic absorption, EPR, and ^{1}H NMR spectroscopy. $\mathbf{1^{2Me}}$ and $\mathbf{1^{6Me}}$ decay over the course of minutes. $\mathbf{1^{2Me}}$ is observed to decay to form a $(\mu\text{-}O)_2Mn^{III}Mn^{IV}$ species, which then decays to regenerate $[Mn^{III}(OH)(dpaq^{2Me})]^+$. $\mathbf{1^{6Me}}$ decays to $[Mn^{III}(OH)(^{6Me}dpaq)]^+$ without the formation of any intermediates.

5.2 Materials and methods. All chemicals were used as obtained from commercial sources unless noted otherwise. Acetonitrile and diethyl ether were dried and degassed using a PureSolv Micro solvent purification system. $[Mn^{III}(OH)(dpaq)](OTf)$, $[Mn^{III}(OH)(dpaq^{2Me})](OTf)$, and $[Mn^{III}(OH)(^{6Me}dpaq)]^+$ were synthesized and characterized as reported previously (for synthesis of $[Mn^{III}(OH)(^{6Me}dpaq)]^+$, see Chapter 4).[52, 53] Electronic absorption experiments were performed using a Varian Cary 50 Bio UV-Visible spectrophotometer. Electrospray ionization-mass spectrometry (ESI-MS) experiments were performed using an LCT Premier MicroMass electrospray time-of-flight instrument. X-band EPR experiments were performed using a Bruker EMXplus with Oxford ESR900 continuous-flow

liquid helium cryostat and an Oxford ITC503 temperature system. ^{1}H NMR spectra were obtained on a Bruker DRX 400 MHz NMR spectrometer.

Reactions between [Mn^{III}(OH)(dpaq^{2Me})](OTf) and H_2O_2 in the presence of a base. A 3 mM solution of [Mn^{III}(OH)(dpaq^{2Me})]$^{+}$ was prepared in MeCN and transferred to a quartz cuvette. 10 equivalents of H_2O_2 and Et_3N were simultaneously added to the cuvette at 25°C while monitoring the reaction by electronic absorption spectroscopy. After the addition of H_2O_2 and Et_3N, the purple solution of [Mn^{III}(OH)(dpaq^{2Me})]$^{+}$ instantly changed color to a bright green. The same reaction was performed in 1:1 MeCN:Toluene in order to prepare an EPR sample. Immediately after formation of the bright green species, the MeCN:Toluene solution was transferred to an EPR tube and frozen with liquid nitrogen. The EPR spectrum was collected at 10 K (9.64 GHz microwave frequency, 0.126 mW microwave power, 0.4 mT modulation amplitude, 100 kHz modulation frequency). A sample for ^{1}H NMR was prepared by simultaneously adding 10 equivalents of H_2O_2 and Et_3N to a 3 mM solution of [Mn^{III}(OH)(dpaq^{2Me})]$^{+}$ in *d3*-MeCN in an NMR tube. The ^{1}H NMR spectrum was collected at 298 K immediately after the formation of the green species.

Reactions between [Mn^{III}(OH)(^{6Me}dpaq)](OTf) and H_2O_2 in the presence of a base. A 3 mM solution of [Mn^{III}(OH)(^{6Me}dpaq)]$^{+}$ was prepared in MeCN and transferred to a quartz cuvette. 20 equivalents of both H_2O_2 and Et_3N were simultaneously added to the cuvette at 25°C while monitoring by electronic absorption spectroscopy. Upon the addition of H_2O_2 and Et_3N, the dark orange solution of [Mn^{III}(OH)(^{6Me}dpaq)]$^{+}$ was observed to turn a bright green.

Formation and decay of [Mn^{III}Mn^{IV}(μ-O)$_2$(dpaq^{2Me})$_2$]$^{2+}$. A 3 mM solution of [Mn^{III}(OH)(dpaq^{2Me})]$^{+}$ was prepared in MeCN and transferred to a quartz cuvette. 1 equivalent of H_2O_2 was added to the cuvette at 25°C while monitoring the reaction by electronic absorption

spectroscopy. The purple solution of $[Mn^{III}(OH)(dpaq^{2Me})]^{+}$ changed color to an amber solution. After the electronic absorption spectra ceased to change, the MeCN solution was transferred to an EPR tube and frozen with liquid nitrogen. The EPR spectrum was collected at 10 K (9.64 GHz microwave frequency, 2 mW microwave power, 0.4 mT modulation amplitude, 100 kHz modulation frequency). Spin quantification of the 16-line EPR signal was determined against a sample of $[Mn^{III}Mn^{IV}(\mu\text{-}O)_2(N4Py)_2]^{+}$ prepared by the addition of 5 equivalents of H_2O_2 to a 10 mM solution of $[Mn^{II}(N4Py)(OTf)](OTf)$ in 2,2,2-trifluoroethanol.[44] A sample of $[Mn^{III}Mn^{IV}(\mu\text{-}O)_2(dpaq^{2Me})_2]^{2+}$ for ^1H NMR measurement was prepared by adding 1 equivalent of H_2O_2 to a 3 mM solution of $[Mn^{III}(OH)(dpaq^{2Me})]^{+}$ in *d3*-MeCN in an NMR tube. The thermal decay of $[Mn^{III}Mn^{IV}(\mu\text{-}O)_2(dpaq^{2Me})_2]^{2+}$ was also monitored using electronic absorption spectroscopy at 25°C.

Reaction of $[Mn^{III}Mn^{IV}(\mu\text{-}O)_2(dpaq^{2Me})_2]^{2+}$ with 2,4-ditertbutylphenol. A 3 mM solution of $[Mn^{III}Mn^{IV}(\mu\text{-}O)_2(dpaq^{2Me})_2]^{2+}$ was prepared in MeCN in a quartz cuvette, as described above. Upon full formation of $[Mn^{III}Mn^{IV}(\mu\text{-}O)_2(dpaq^{2Me})_2]^{2+}$, 100 equivalents of 2,4-ditertbutylphenol, dissolved in 100 µL of MeCN, was added to the cuvette via syringe while monitoring the reaction by electronic absorption spectroscopy at 25°C.

Formation and decay of $[Mn^{III}Mn^{IV}(\mu\text{-}O)_2(dpaq)_2]^{2+}$. The $[Mn^{III}Mn^{IV}(\mu\text{-}O)_2(dpaq)_2]^{2+}$ complex was generated by following a previously reported protocol.[54] A 0.5 mM solution of $[Mn^{III}(OH)(dpaq)]^{+}$ was prepared in MeCN and transferred to a quartz cuvette. 5 equivalents of H_2O_2 and 5 equivalents of Et_3N were added to the cuvette at 25°C, while monitoring the reaction by electronic absorption spectroscopy.[54] The complex was allowed to thermally decay at 25°C while monitoring with electronic absorption spectroscopy.

5.3 Results and discussion.

Reactions of [Mn^{III}(OH)(dpaq^{2Me})](OTf) and H_2O_2 in the presence of a base. Upon the addition of 2.5 equivalents of both H_2O_2 and Et_3N to [Mn^{III}(OH)(dpaq^{2Me})]$^+$ in MeCN at 25 °C, the purple Mn^{III}-hydroxo complex is rapidly converted to a bright green species (termed **1^{2Me}**). This conversion can be monitored by electronic absorption, where the features of [Mn^{III}(OH)(dpaq^{2Me})]$^+$ at 515 and 770 nm are immediately replaced by new signals at 615 and 450 nm upon the addition of H_2O_2 and Et_3N (Figure 5.1, left). The electronic absorption signals of **1^{2Me}** are similar to those of side-on Mn^{III}-peroxo complexes (Table 5.1).[24, 34, 35, 39, 40, 44] Under these conditions, **1^{2Me}** decays over a period of 60 seconds, resulting in the formation of an amber species (**2^{2Me}**) with intense UV-Vis signals around 500 and 710 nm (Figure 5.1, center). **2^{2Me}** decays over the course of three hours to yield the [Mn^{III}(OH)(dpaq^{2Me})]$^+$ starting complex in 89% yield (Figure 5.1, right).

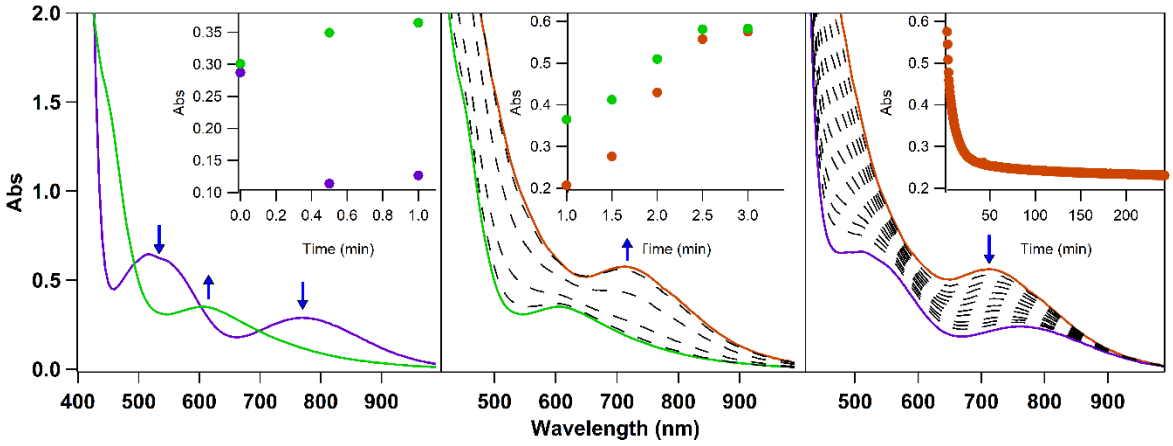

Figure 5.1. Left: The reaction of a 3 mM MeCN solution of [Mn^{III}(OH)(dpaq^{2Me})]$^+$ with 2.5 equivalents of both H_2O_2 and Et_3N at 25 °C results in the formation of **1^{2Me}** (green trace). Center: **1^{2Me}** rapidly converts to **2^{2Me}** with a feature at 710 nm (brown trace). Right: **2^{2Me}** decays back to [Mn^{III}(OH)(dpaq^{2Me})]$^+$ (blue trace). Time courses of the transformations are shown in the figure insets.

Table 5.1. Comparison of spectroscopic characteristics of select Mn^{III}-peroxo species.

Complex	*λ (nm)*	*g*	*A*	*Reference*
$\mathbf{1^{2Me}}$	450, 615	8.6	--	*This work.*
$\mathbf{1^{6Me}}$	450, 610	--	--	*This work.*
$[Mn^{III}(O_2)(Me_2EBC)]_+$	400, 650	7.96	6.84	*40*
$[Mn^{III}(O_2)(N4Py)]^+$	617	7.85	6.8	*34, 44*
$[Mn^{III}(O_2)(mL_5{}^2)]^+$	585	8.1	6.6	*34*
$[Mn^{III}(O_2)(Tp^{Ph2})(THF)]$	379, 435	8.3	9.1	*35*
$[Mn^{III}(O_2)(Pro_3Py)]^+$	580	8.3	--	*39*
$[Mn^{III}(O_2)(H_2bupa)]^-$	490, 660	8.2	5.7	*24*

Intermediate $\mathbf{1^{2Me}}$ is more stable when formed through the reaction of a 3 mM solution of $[Mn^{III}(OH)(dpaq^{2Me})]^+$ with 10 equivalents of both H_2O_2 and Et_3N in MeCN at 25 °C. Under these formation conditions, the feature of $\mathbf{1^{2Me}}$ at 450 nm is more resolved, either suggesting more complete formation of $\mathbf{1^{2Me}}$ or the lack of some impurity that absorbs in the UV region (Figure 5.2). When formed in this manner, $\mathbf{1^{2Me}}$ persists for 6 minutes before decaying over the period of half an hour to result in an amber solution with a brown precipitate. Since the formation of $\mathbf{1^{2Me}}$ under these conditions results in a more stable complex, analysis of $\mathbf{1^{2Me}}$ through ^{1}H NMR was attempted by collecting the ^{1}H NMR spectrum immediately after the initial formation of $\mathbf{1^{2Me}}$. However, the ^{1}H NMR spectrum primarily consists of peaks that arise from free $Hdpaq^{2Me}$ ligand, indicating that the sample had decayed during collection of the spectrum (Figure 5.3).

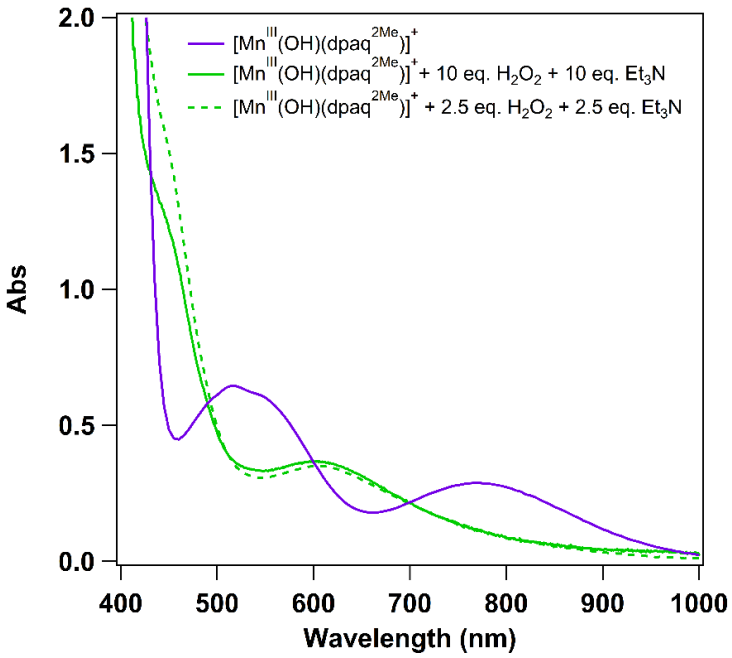

Figure 5.2. Electronic absorption spectra of a 3 mM solution of $[Mn^{III}(OH)(dpaq^{2Me})]^{+}$ (purple trace) in MeCN, solutions of **1**$^{\mathbf{2Me}}$ in MeCN, formed by the addition of 10 equivalents of H_2O_2 and 10 equivalents Et_3N (green solid trace) and 2.5 equivalents of H_2O_2 and 2.5 equivalents Et_3N (green dashed trace).

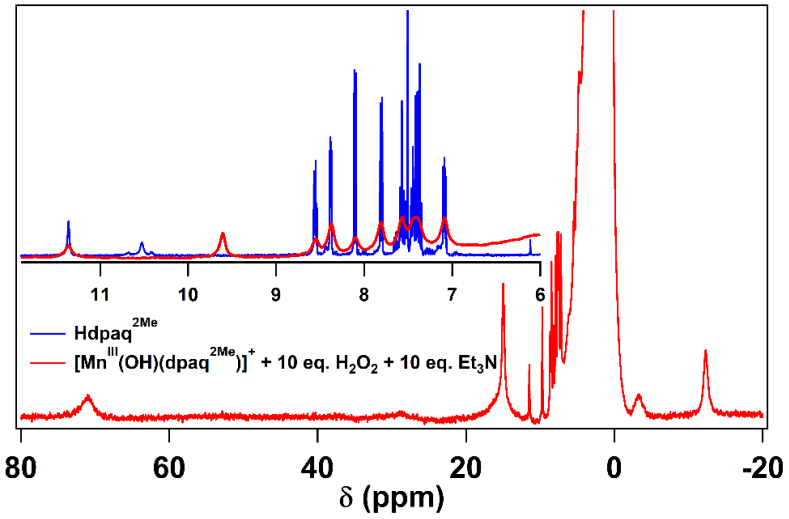

Figure 5.3. ^{1}H NMR spectrum obtained following the reaction of a 3 mM solution of $[Mn^{III}(OH)(dpaq^{2Me})]^{+}$ with 10 equivalents of both H_2O_2 and Et_3N in *d3*-MeCN (red trace). Inset: expanded view of the 12 to 6 ppm region comparing the spectrum obtained after the reaction of $[Mn^{III}(OH)(dpaq^{2Me})]^{+}$ with 10 equivalents of H_2O_2 and Et_3N in *d3*-MeCN to the spectrum of the free ligand (blue trace).

An EPR sample of **1**$^{\mathbf{2Me}}$ was prepared through the reaction of a 3 mM solution of $[Mn^{III}(OH)(dpaq^{2Me})]^{+}$ with 10 equivalents of both H_2O_2 and Et_3N in 1:1 MeCN:Toluene at 25 °C. After formation of **1**$^{\mathbf{2Me}}$, the solution was transfered to an EPR tube and frozen with liquid nitrogen. The EPR spectrum of **1**$^{\mathbf{2Me}}$ at 10 K reveals an intense, broad, derivative-shaped signal with a *g* value of 8.6 (Figure 5.4). Mononuclear, $S = 2$ Mn^{III} centers often exhibit parallel-mode EPR signals at similar *g* values.[24, 34, 35, 40] However, the strong derivative shape of the EPR signal of **1**$^{\mathbf{2Me}}$, and the absence of a six-line hyperfine splitting makes the EPR signature of this complex distinct from that usually seen for Mn^{III}-peroxo complexes.[35, 39, 40] While the shape of the signal is unusual for a mononuclear Mn^{III} complex, a Mn^{III}-peroxo complex reported by Borovik and coworkers also exhibited a derivative-shaped EPR signal, though with resolved hyperfine splitting.[24] Similarly shaped signals, without observable hyperfine splitting, have been observed in trimeric Mn(III) complexes reported by Agapie and coworkers.[55] However, in these cases, the derivative-shaped signals were centered around 40-50 mT, which would correspond to a much higher *g* value than that of **1**$^{\mathbf{2Me}}$.[55] Thus, while the field position of the EPR signal of **1**$^{\mathbf{2Me}}$ is consistent with that of a mononuclear Mn^{III} center, further investigations, including studies of the temperature-dependence of the EPR signal, are required to confirm this proposal.

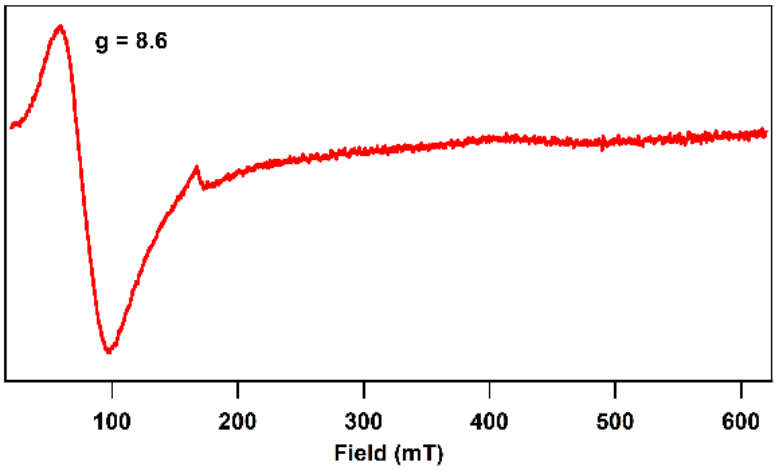

Figure 5.4. The parallel-mode EPR spectrum obtained at 10 K following the reaction of a 3 mM solution of $[Mn^{III}(OH)(dpaq^{2Me})]^+$ in 1:1 MeCN:Toluene with 10 equivalents of both H_2O_2 and Et_3N at 25°C.

Based on the knowledge that $[Mn^{III}(OH)(^{6Me}dpaq)]^+$ reacts with ^{t}BuOOH to form a stable Mn^{III}-alkylperoxo species (Chapter 4), similar reactions between $[Mn^{III}(OH)(^{6Me}dpaq)]^+$ and H_2O_2 were investigated. A 3 mM solution of $[Mn^{III}(OH)(^{6Me}dpaq)]^+$ in MeCN reacts with 20 equivalents of H_2O_2 and Et_3N at 25 °C to form a green species (**1**^{6Me}) with a well-defined electronic absorption feature at 610 nm, and a shoulder around 450 nm (Figure 5.5, red trace). **1**^{6Me} decays back to $[Mn^{III}(OH)(^{6Me}dpaq)]^+$ over the course of 3 minutes (Figure 5.5). Attempts to form **1**^{6Me} using less than 20 equivalents of H_2O_2 and Et_3N did not result in the observation of **1**^{6Me}, presumably due to the rapid decay of this transient species. Unlike **1**^{2Me}, demetallation is not observed upon the decay of **1**^{6Me}. This finding is unexpected considering the elongated Mn-pyridine bonds of the $[Mn^{III}(OH)(^{6Me}dpaq)]^+$ complex, which might be expected to favor ligand dissociation.

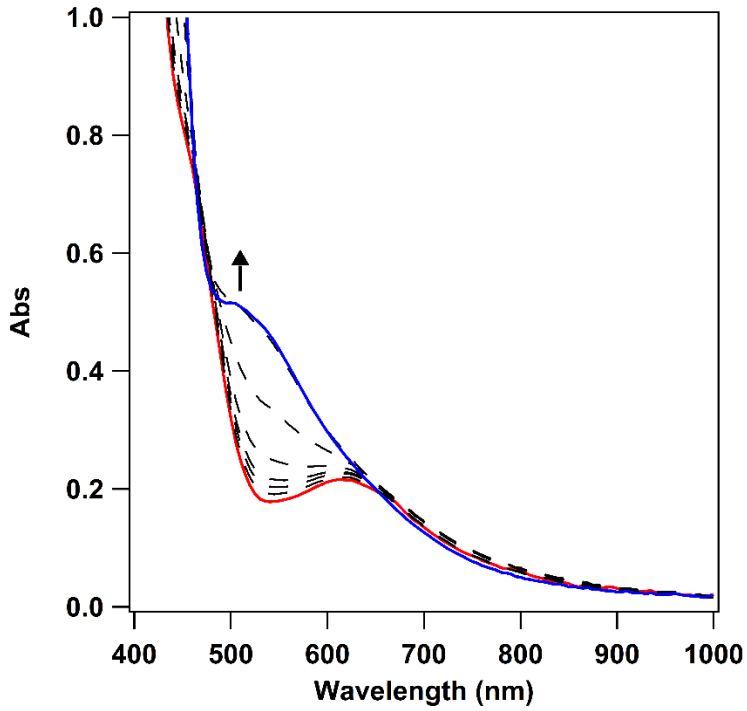

Figure 5.5. Electronic absorption of **1^{6Me}** (red trace) and its decay to form [Mn^{III}(OH)(^{6Me}dpaq)]$^{+}$ (blue trace) over the course of 3 minutes.

Reaction between [Mn^{III}(OH)(dpaq^{2Me})](OTf) and H_2O_2 in the absence of a base. Intermediate **2^{2Me}** is directly formed when a 3 mM solution of [Mn^{III}(OH)(dpaq^{2Me})]$^{+}$ in MeCN is treated with 1 equivalent of H_2O_2 in the absence of Et_3N at 25 °C. Over the course of one minute after the addition of H_2O_2, intense electronic absorption features around 500 and 710 nm are formed, indicative of the formation of **2^{2Me}** (Figure 5.6). Perpendicular-mode EPR investigation of a frozen MeCN solution of **2^{2Me}** reveals a 16-line signal (Figure 5.7; g = 2.01, A = 7.70 mT). The electronic absorption features and the position and hyperfine splitting pattern of the EPR signal are similar to those previously reported for (μ-oxo)$_2$dimanganese(III,IV) complexes (Table 5.2).[44, 54, 56-59] Spin quantification of the EPR signal of **2^{2Me}** indicates that this signal accounts for 80 ± 20% of total Mn in solution. Based on the spectroscopic similarities to previously reported

(μ-oxo)$_2$dimanganese(III,IV) complexes,[44, 54, 56-59] we assign **2^{2Me}** as [Mn^{III}Mn^{IV}(μ-O)$_2$(dpaq^{2Me})$_2$]$^+$.

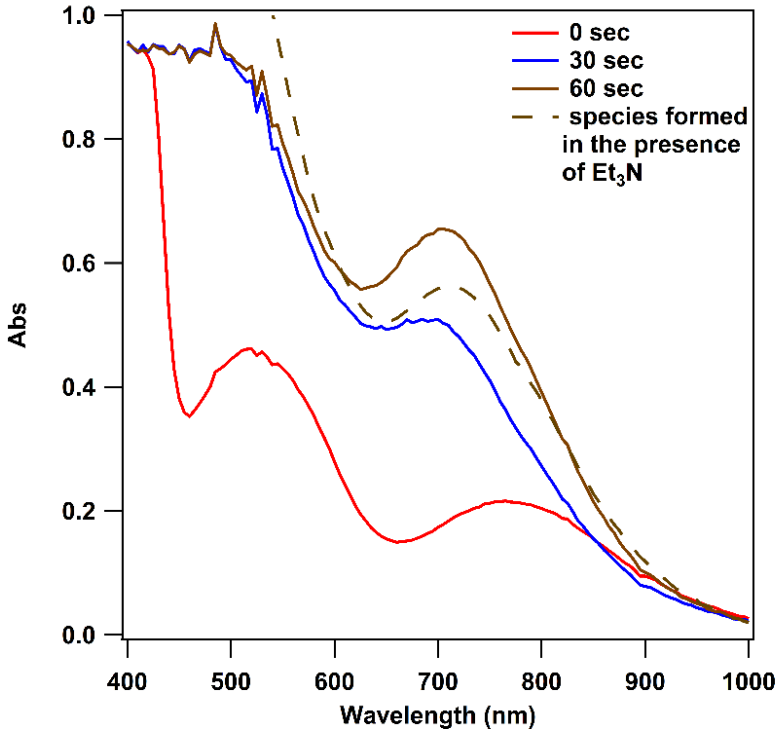

Figure 5.6. Electronic absorption spectra following the reaction of a 3 mM solution of [Mn^{III}(OH)(dpaq^{2Me})]$^+$ in MeCN at 25 °C (red trace) with 1 equivalent of H_2O_2. An amber solution, characterized by an intense feature at 710 nm is formed over the course of 60 seconds (brown solid trace). The electronic absorption spectrum of the species formed through the reaction of [Mn^{III}(OH)(dpaq^{2Me})]$^+$ with 2.5 equivalents of H_2O_2 in the presence of Et_3N is shown for comparison (brown dashed trace).

Table 5.2. Comparison of spectroscopic characteristics of select Mn^{III}Mn^{IV}(μ-O)$_2$ species.

Complex	*λ (nm)*	*g*	*A (mT)*	*Reference*
2^{2Me}	~500, 710	2.01	7.7	*This work*
[Mn^{III}Mn^{IV}(μ-O)$_2$(N4Py)$_2$]$^{3+}$	439, 562, 667	2.01	7.7	*44*
[Mn^{III}Mn^{IV}(μ-O)$_2$(^{DMM}N4Py)$_2$]$^{3+}$	440, 562, 667	2.01	7.7	*56*
[Mn^{III}Mn^{IV}(μ-O)$_2$(dpaq)$_2$]$^+$	540, 660	1.996	A_x = 16.7[a] A_y = 14.9[a] A_z = 14.3[a]	*54*

[a] From simulation of the experimental spectrum.

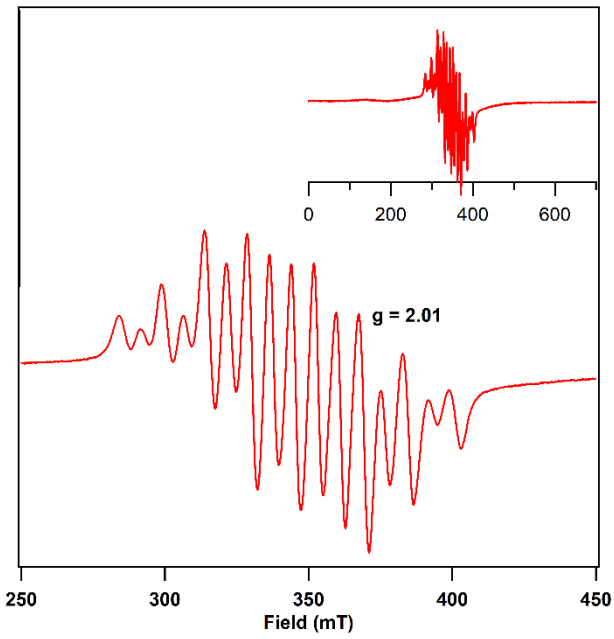

Figure 5.7. 10 K perpendicular-mode EPR spectrum obtained following the reaction of a 3 mM solution of $[Mn^{III}(OH)(dpaq^{2Me})]^+$ with 1 equivalent of H_2O_2 in MeCN at 25°C showing a 16-line signal consistent with a $(\mu\text{-}O)_2Mn^{III}Mn^{IV}$ dimer, which accounts for ca. 80% of total Mn in the sample. Inset: full range of the collected spectrum.

2^{2Me} undergoes thermal decay over the course of 24 hours to regenerate $[Mn^{III}(OH)(dpaq^{2Me})]^+$ in 99% yield (Figure 5.8). **2^{2Me}** is much more stable in the absence of a base ($t_{1/2} \approx 2$ hours) than in the presence 10 equivalents of Et_3N ($t_{1/2} \approx 8$ minutes). For comparison, a solution of $[Mn^{III}Mn^{IV}(\mu\text{-}O)_2(dpaq)_2]^+$ was prepared according to a previously reported procedure and allowed to decay while monitoring by electronic absorption spectroscopy.[54] The decay of $[Mn^{III}Mn^{IV}(\mu\text{-}O)_2(dpaq)_2]^+$ resulted in the formation of Mn^{III}-hydroxo complex in 98% yield, similar to that seen for the decay of **2^{2Me}** (Figure 5.9). **2^{2Me}** is more stable than $[Mn^{III}Mn^{IV}(\mu\text{-}O)_2(dpaq)_2]^+$ ($t_{1/2} \approx 30$ minutes).[54]

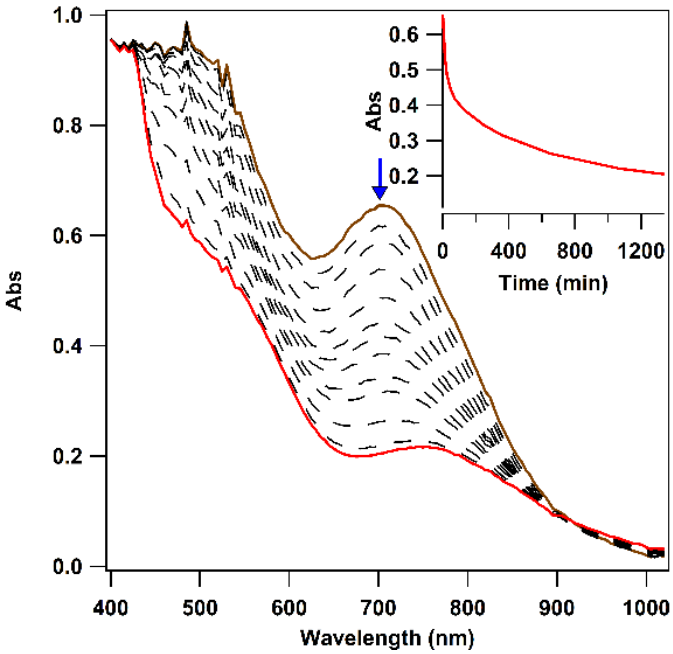

Figure 5.8. Electronic absorption spectra monitoring the thermal decay of $[Mn^{III}Mn^{IV}(\mu\text{-}O)_2(dpaq^{2Me})_2]^+$ (brown trace) in MeCN to regenerate $[Mn^{III}(OH)(dpaq^{2Me})]^+$ (red trace). Inset: time course of the decay.

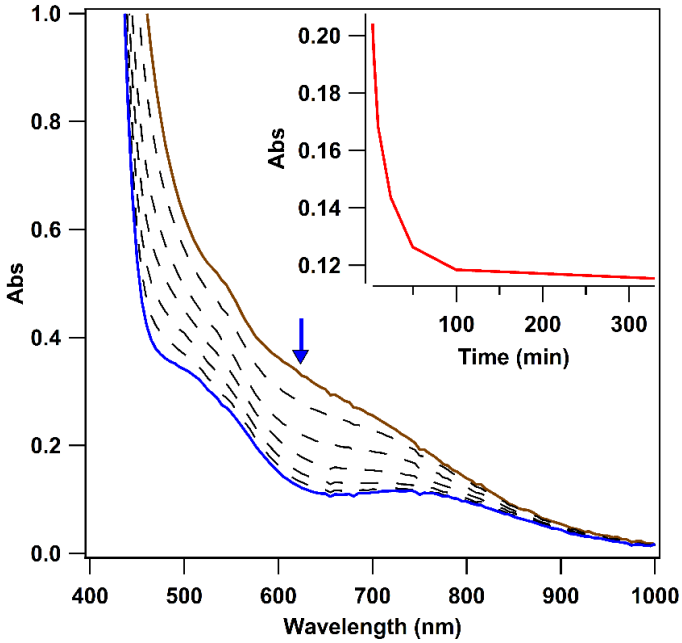

Figure 5.9. Electronic absorption spectra obtained while monitoring the thermal decay of $[Mn^{III}Mn^{IV}(\mu\text{-}O)_2(dpaq)_2]^+$ (brown trace) to yield $[Mn^{III}(OH)(dpaq)]^+$ (blue trace). Inset: time course of the decay.

In MeCN, **2**$^{\mathbf{2Me}}$ reacts with 100 equivalents of 2,4-ditertbutyl phenol over the course of 2 minutes (Figure 10). The resulting electronic absorption spectrum is poorly defined with a broad feature around 750 nm (Figure 5.10, red trace). This spectrum is different than what is observed following the reaction of $[Mn^{III}Mn^{IV}(\mu\text{-}O)_2(dpaq)_2]^+$ with phenol substrates, during which a Mn^{III}-hydroxo complex is generated.[54] In a previous report from our group, $[Mn^{III}Mn^{IV}(\mu\text{-}O)_2(N4Py)]^{3+}$ and $[Mn^{III}Mn^{IV}(\mu\text{-}O)_2(^{DMM}N4Py)]^{3+}$ were seen to react with phenol substrates to generate a mixture of Mn^{II} and Mn^{III} products.[56] The amorphous electronic absorption features observed following the reaction of $[Mn^{III}Mn^{IV}(\mu\text{-}O)_2(dpaq^{2Me})]^+$ may be indicative of similar Mn products being formed. Alternatively, it is possible that $[Mn^{III}(OH)(dpaq^{2Me})]^+$ is the sole Mn product formed, but subsequently reacts with the phenol substrate to result in a mixture of Mn^{II} and Mn^{III} products.[52]

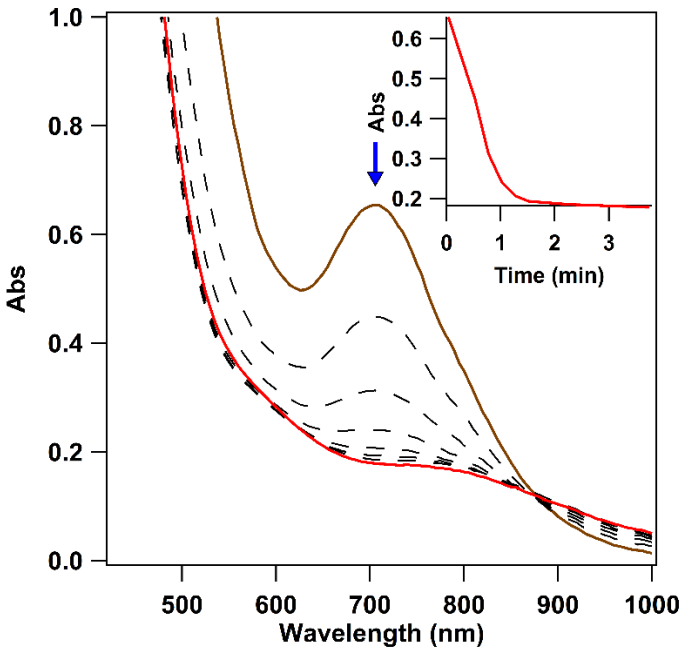

Figure 5.10. Electronic absorption spectra obtained while monitoring the reaction of $[Mn^{III}Mn^{IV}(\mu\text{-}O)_2(dpaq^{2Me})_2]^+$ (brown trace) with 2,4-ditertbutyl phenol in MeCN to result in a poorly defined spectrum with a feature ~750 nm (red trace). Inset: time course of the reaction.

5.4 Outlook and future work. Both $[Mn^{III}(OH)(dpaq^{2Me})]^+$ and $[Mn^{III}(OH)(^{6Me}dpaq)]^+$ react with H_2O_2 to form new intermediates, $\mathbf{1^{2Me}}$ and $\mathbf{1^{6Me}}$. The electronic absorption features of $\mathbf{1^{2Me}}$ and $\mathbf{1^{6Me}}$ (λ_{max} = 615 and 610 nm, respectively) are within the range of those reported for Mn^{III}-peroxo complexes (λ_{max} = 435 to 660 nm, Table 5.1). Additionally, the EPR spectrum of $\mathbf{1^{2Me}}$ is consistent with the complex containing a Mn^{III} center. However, confident formulation of these species requires more characterization.

$\mathbf{1^{2Me}}$ is much more stable at lower temperatures, persisting for two hours at -40°C, potentially allowing for additional characterization. ^{1}H NMR analysis of $\mathbf{1^{2Me}}$ at -40°C would allow for characterization of the complex without signals associated with decay products dominating the spectrum, as is observed in experiments carried out at room temperature (Figure 3). Comparison of the ^{1}H NMR spectrum of $\mathbf{1^{2Me}}$ to that obtained for $[Mn^{III}(OH)(dpaq^{2Me})]^+$ can give some insight into solution-phase structure.[60] If $\mathbf{1^{2Me}}$ is an end-on Mn^{III}-hydroperoxo species, the ^{1}H NMR spectrum would likely look similar to that observed for $[Mn^{III}(OH)(dpaq^{2Me})]^+$ due to a similar molecular symmetry. The ^{1}H NMR spectrum of a side-on Mn^{III}-peroxo species may be significantly different, reflective of geometric distortion that occurs in accommodating the η^2 binding mode of the peroxo ligand. Similar experiments carried out with $\mathbf{1^{6Me}}$ would have the added benefit of being able to compare to $[Mn^{III}(OO^tBu)(^{6Me}dpaq)]^+$, a possible structural analogue to an end-on Mn^{III}-hydroperoxo (Chapter 4). Collection of the EPR spectrum of $\mathbf{1^{2Me}}$ at a range of temperatures will help to determine the zero-field splitting parameters of the complex, which can subsequently be compared to those reported for Mn^{III}-peroxo complexes.[1]

Characterization of $\mathbf{1^{2Me}}$ and $\mathbf{1^{6Me}}$ by FTIR, either by analysis of cold solutions or by way of ReactIR instrumentation, would allow for a comparison of O-O bond vibration energy to those reported for the end-on Mn^{III}-alkylperoxo complexes and $[Mn^{III}(OO^tBu)(dpaq^{2Me})]^+$ and

$[Mn^{III}(OO^tBu)(^{6Me}dpaq)]^+$ (Chapter 4).[51] The O-O bonds of side-on Mn^{III}-peroxo complexes tend to be shorter than those reported for end-on Mn^{III}-alkylperoxo complexes, potentially resulting in a higher energy O-O bond vibration.[1] Similar trends have also been seen in iron systems.[47, 48] Notably, the O-O vibrational frequency measured for $[Mn^{III}(OOH)(tmc)]^{2+}$, one of only two reported Mn^{III}-hydroperoxo species (ν_{O-O} = 792 cm^{-1}),[45] is much lower than those reported for Mn^{III}-alkylperoxo complexes (ν_{O-O} = 872 – 893 cm^{-1}, Chapters 3 and 4).[49-51]

A comparison of XAS data of $\mathbf{1^{2Me}}$ and $\mathbf{1^{6Me}}$ and their respective Mn^{II} or Mn^{III}-hydroxo analogues would give additional insight into the oxidation state, geometry, and Mn-ligand distances of the complexes. Mn K-edge energy is sensitive to oxidation state and could confirm our tentative assignment of $\mathbf{1^{2Me}}$ and $\mathbf{1^{6Me}}$ containing a Mn^{III} center. Analysis of any pre-edge features is often used to probe geometric differences between complexes. Finally, fitting the extended X-ray absorption fine structure region of the spectrum will give structural information regarding the distance between the Mn center and surrounding ligand.

Mass spectral analysis of a cold solution of $\mathbf{1^{2Me}}$ may be helpful in determining whether or not these new species are peroxo-level intermediates. If $\mathbf{1^{2Me}}$ is cationic end-on Mn^{III}-hydroperoxo species, we would expect to see a peak near the calculated *m/z* of 484.12. If $\mathbf{1^{2Me}}$ is a side-on Mn^{III}-peroxo species, the overall charge of the complex would be neutral. Charged species are required in order to see a mass spectral signal. As such, the mass spectrum of a side-on Mn^{III}-peroxo species would have to include the association of a proton or a Na^+ ion, resulting in signals near the calculated *m/z* of 484.12 or 506.10. While the two possible formulations of $\mathbf{1^{2Me}}$ share a peak at *m/z* = 484.12, the presence of a peak at *m/z* = 506.10 could be indicative of $\mathbf{1^{2Me}}$ being a side-on Mn^{III}-peroxo species.

5.5 Conclusion. Drawing from the ability of $[Mn^{III}(OH)(dpaq^{2Me})]^+$ and $[Mn^{III}(OH)(^{6Me}dpaq)]^+$ to react with alkylhydroperoxides to form end-on Mn^{III}-alkylperoxo complexes, this work exploredsimilar reactivity between the Mn^{III}-hydroxo complexes and H_2O_2 in an attempt to form end-on Mn^{III}-hydroperoxo complexes. Through the reactions of $[Mn^{III}(OH)(dpaq^{2Me})]^+$ and $[Mn^{III}(OH)(^{6Me}dpaq)]^+$ with H_2O_2, two new species are generated, $\mathbf{1^{2Me}}$ and $\mathbf{1^{6Me}}$. These species were characterized by electronic absorption spectroscopy and exhibited features similar to those reported for Mn^{III}-peroxo complexes. The EPR spectrum of complex $\mathbf{1^{2Me}}$ showed a signal at a field position consistent with a mononuclear Mn^{III} complex. However, the exact nature of this species remains unclear, warranting further characterization. The lifetime of $\mathbf{1^{2Me}}$ is short at room temperature (ca. 30 seconds) and decays to form a $(\mu\text{-}O)_2Mn^{III}Mn^{IV}$ dimer, which in turn decays to form $[Mn^{III}(OH)(dpaq^{2Me})]^+$. Complex $\mathbf{1^{6Me}}$ is also short lived, decaying over a three minute period to form $[Mn^{III}(OH)(^{6Me}dpaq)]^+$.

5.6 References.

1. D. F. Leto and T. A. Jackson, *J. Biol. Inorg. Chem.*, 2014, **19**, 1-15.
2. A. T. Fiedler and A. A. Fischer, *J. Biol. Inorg. Chem.*, 2017, **22**, 407-424.
3. J. A. Cotruvo, T. A. Stich, R. D. Britt and J. Stubbe, *J. Am. Chem. Soc.*, 2013, **135**.
4. A. K. Boal, J. A. Cotruvo, J. Stubbe and A. C. Rosenzweig, *Science*, 2010, **329**, 1526.
5. J. A. Cotruvo and J. Stubbe, *Proc. Natl. Acad. Sci.*, 2008, **105**, 14383.
6. J. A. Cotruvo and J. Stubbe, *Biochem.*, 2011, **50**, 1672-1681.
7. W. A. Gunderson, A. I. Zatsman, J. P. Emerson, E. R. Farquhar, L. Que, J. D. Lipscomb and M. P. Hendrich, *J. Am. Chem. Soc.*, 2008, **130**, 14465-14467.
8. M. H. Glickman and J. P. Klinman, *Biochem.*, 1995, **34**, 14077-14092.
9. C. Su, M. Sahlin and E. H. Oliw, *J. Biol. Chem.*, 2000, **275**, 18830-18835.
10. A. Wennman, S. Karkehabadi and E. H. Oliw, *Arch. Biochem. Biophys.*, 2014, **555-556**, 9-15.
11. A. Wennman, E. H. Oliw, S. Karkehabadi and Y. Chen, *J. Biol. Chem.*, 2016.
12. Y. Sheng, E. Butler Gralla, M. Schumacher, D. Cascio, D. E. Cabelli and J. Selverstone Valentine, *Proc. Natl. Acad. Sci.*, 2012, **109**, 14314.
13. C. Bull, E. C. Niederhoffer, T. Yoshida and J. A. Fee, *J. Am. Chem. Soc.*, 1991, **113**, 4069-4076.
14. A. S. Hearn, C. K. Tu, H. S. Nick and D. N. Silverman, *J. Biol. Chem.*, 1999, **274**, 24457-24460.

15. T. A. Jackson, A. Karapetian, A.-F. Miller and T. C. Brunold, *Biochem.*, 2005, **44**, 1504-1520.
16. I. A. Abreu, J. A. Rodriguez and D. E. Cabelli, *J. Phys. Chem. B*, 2005, **109**, 24502-24509.
17. R. Carrasco, I. Morgenstern-Badarau and J. Cano, *Inorg. Chim. Acta*, 2007, **360**, 91-101.
18. J. P. McEvoy and G. W. Brudvig, *Chem. Rev.*, 2006, **106**, 4455-4483.
19. N. Cox, D. A. Pantazis, F. Neese and W. Lubitz, *Acc. Chem. Res.*, 2013, **46**, 1588-1596.
20. J. Wang, M. Askerka, G. W. Brudvig and V. S. Batista, *ACS Energy Let.*, 2017, **2**, 2299-2306.
21. P. E. M. Siegbahn, *Chem. Eur. J.*, 2006, **12**, 9217-9227.
22. M. Suga, F. Akita, M. Sugahara, M. Kubo, Y. Nakajima, T. Nakane, K. Yamashita, Y. Umena, M. Nakabayashi, T. Yamane, T. Nakano, M. Suzuki, T. Masuda, S. Inoue, T. Kimura, T. Nomura, S. Yonekura, L.-J. Yu, T. Sakamoto, T. Motomura, J.-H. Chen, Y. Kato, T. Noguchi, K. Tono, Y. Joti, T. Kameshima, T. Hatsui, E. Nango, R. Tanaka, H. Naitow, Y. Matsuura, A. Yamashita, M. Yamamoto, O. Nureki, M. Yabashi, T. Ishikawa, S. Iwata and J.-R. Shen, *Nature*, 2017, **543**, 131.
23. N. Schuth, I. Zaharieva, P. Chernev, G. Berggren, M. Anderlund, S. Styring, H. Dau and M. Haumann, *Inorg. Chem.*, 2018, **57**, 10424-10430.
24. R. L. Shook, W. A. Gunderson, J. Greaves, J. W. Ziller, M. P. Hendrich and A. S. Borovik, *J. Am. Chem. Soc.*, 2008, **130**, 8888-8889.
25. R. L. Shook, S. M. Peterson, J. Greaves, C. Moore, A. L. Rheingold and A. S. Borovik, *J. Am. Chem. Soc.*, 2011, **133**, 5810-5817.
26. N. Kitajima, H. Komatsuzaki, S. Hikichi, M. Osawa and Y. Moro-oka, *J. Am. Chem. Soc.*, 1994, **116**, 11596-11597.
27. U. P. Singh, A. K. Sharma, S. Hikichi, H. Komatsuzaki, Y. Moro-oka and M. Akita, *Inorg. Chim. Acta*, 2006, **359**, 4407-4411.
28. J. Annaraj, J. Cho, Y.-M. Lee, S. Y. Kim, R. Latifi, S. P. de Visser and W. Nam, *Angew. Chem. Int. Ed.*, 2009, **48**, 4150-4153.
29. H. Kang, J. Cho, K.-B. Cho, T. Nomura, T. Ogura and W. Nam, *Chem. Eur*, 2013, **19**.
30. J. Cho, R. Sarangi and W. Nam, *Acc. Chem. Res.*, 2012, **45**, 1321-1330.
31. S. Groni, G. Blain, R. Guillot, C. Policar and E. Anxolabéhère-Mallart, *Inorg. Chem.*, 2007, **46**, 1951-1953.
32. S. Groni, P. Dorlet, G. Blain, S. Bourcier, R. Guillot and E. Anxolabéhère-Mallart, *Inorg. Chem.*, 2008, **47**, 3166-3172.
33. R. A. Geiger, S. Chattopadhyay, V. W. Day and T. A. Jackson, *J. Am. Chem. Soc.*, 2010, **132**, 2821-2831.
34. R. A. Geiger, D. F. Leto, S. Chattopadhyay, P. Dorlet, E. Anxolabéhère-Mallart and T. A. Jackson, *Inorg. Chem.*, 2011, **50**, 10190-10203.
35. H. E. Colmer, R. A. Geiger, D. F. Leto, G. B. Wijeratne, V. W. Day and T. A. Jackson, *Dalton Trans.*, 2014, **43**, 17949-17963.
36. R. A. Geiger, G. Wijeratne, V. W. Day and T. A. Jackson, *Eur. J. Inorg. Chem.*, 2012, 1598-1608.
37. M. C. Denler, G. B. Wijeratne, D. B. Rice, H. E. Colmer, V. W. Day and T. A. Jackson, *Dalton Trans.*, 2018, **47**, 13442-13458.
38. J. Du, C. Miao, C. Xia and W. Sun, *Chin. Chem. Lett.*, 2018, **29**, 1869-1871.

39. J. Du, D. Xu, C. Zhang, C. Xia, Y. Wang and W. Sun, *Dalton Trans.*, 2016, **45**, 10131-10135.
40. H. E. Colmer, A. W. Howcroft and T. A. Jackson, *Inorg. Chem.*, 2016, **55**, 2055-2069.
41. P. Barman, P. Upadhyay, A. S. Faponle, J. Kumar, S. S. Nag, D. Kumar, C. V. Sastri and S. P. de Visser, *Angew. Chem. Int. Ed.*, 2016, **55**, 11091-11095.
42. M. F. Sisemore, M. Selke, J. N. Burstyn and J. S. Valentine, *Inorg. Chem.*, 1997, **36**, 979-984.
43. M. S. Seo, J. Y. Kim, J. Annaraj, Y. Kim, Y.-M. Lee, S.-J. Kim, J. Kim and W. Nam, *Angew. Chem. Int. Ed.*, 2007, **46**, 377-380.
44. D. F. Leto, S. Chattopadhyay, V. W. Day and T. A. Jackson, *Dalton Trans.*, 2013, **42**, 13014.
45. H. So, J.-H. Park, K.-B. Cho, Y.-M. Lee, M. S. Seo, J. Cho, R. Sarangi and W. Nam, *J. Am. Chem. Soc.*, 2014, **136**, 12229−12232.
46. M. Sankaralingam, Y.-M. Lee, S. H. Jeon, M. S. Seo, K.-B. Cho and W. Nam, *Chem. Comm.*, 2018, **54**, 1209-1212.
47. A. L.-F. Company, J.; Costas, M., Elsevier B.V., 2013, pp. 487-564.
48. M. Costas, M. P. Mehn, M. P. Jensen and L. Que, *Chem. Rev.*, 2004, **104**, 939-986.
49. M. K. Coggins and J. A. Kovacs, *J. Am. Chem. Soc.*, 2011, **133**, 12470-12473.
50. M. K. Coggins, V. Martin-Diaconescu, S. DeBeer and J. A. Kovacs, *J. Am. Chem. Soc.*, 2013, **135**.
51. J. D. Parham, G. B. Wijeratne, D. B. Rice and T. A. Jackson, *Inorg. Chem.*, 2018, **57**, 2489-2502.
52. D. B. W. Rice, Gayan B.; Burr, Andrew D.; Parham, Joshua D.; Day, Victor W.; Jackson, Timothy A., *Inorg. Chem.*, 2016, **55**, 8110-8120.
53. G. B. Wijeratne, B. Corzine, V. W. Day and T. A. Jackson, *Inorg. Chem.*, 2014, **53**, 7622-7634.
54. M. Sankaralingam, S. H. Jeon, Y.-M. Lee, M. S. Seo, K. Ohkubo, S. Fukuzumi and W. Nam, *Dalton Trans.*, 2016, **45**, 376-383.
55. D. Lionetti, S. Suseno, E. Y. Tsui, L. Lu, T. A. Stich, K. M. Carsch, R. J. Nielsen, W. A. Goddard, R. D. Britt and T. Agapie, *Inorg. Chem.*, 2019, **58**, 2336-2345.
56. Y. Lee and T. A. Jackson, *Chem. Sel.*, 2018, **3**, 13507-13516.
57. C. Hureau, G. Blondin, M.-F. Charlot, C. Philouze, M. Nierlich, M. Césario and E. Anxolabéhère-Mallart, *Inorg. Chem.*, 2005, **44**, 3669-3683.
58. P. A. Goodson, J. Glerup, D. J. Hodgson, K. Michelsen and E. Pedersen, *Inorg. Chem.*, 1990, **29**, 503-508.
59. H. Chen, R. Tagore, S. Das, C. Incarvito, J. W. Faller, R. H. Crabtree and G. W. Brudvig, *Inorg. Chem.*, 2005, **44**, 7661-7670.
60. D. B. Rice, S. D. Jones, J. T. Douglas and T. A. Jackson, *Inorg. Chem.*, 2018, **57**, 7825-7837.

Chapter 6

Summary and Outlook

6.1 Summary. This work has served to expand our understanding of the reactivity of Mn complexes with dioxygen and its reduced derivatives. Major findings include:

- A steric effect on the activation of dioxygen by Mn^{II} complexes.
- The synthesis and characterization of three new Mn^{III}-alkylperoxo complexes.
- The development of a new derivative of the dpaq ligand with steric functionalization to the equatorial pyridine donors.
- Supported by this new ligand, the formation of a new Mn^{II} complex, its Mn^{III}-hydroxo counterpart and the first room-temperature stable Mn^{III}-alkylperoxo complex.
- The reaction of two Mn^{III}-hydroxo complexes with H_2O_2 and Et_3N to generate two new species that bear spectroscopic similarities to Mn^{III}-peroxo species.
- The formation of a new $(\mu\text{-}O)_2Mn^{III}Mn^{IV}$ dimer.

6.2 Outlook. Through the development of model complexes, we have a powerful tool to aid in the understanding of metalloenzyme mechanisms. New synthetic complexes are continually being published exhibiting one exciting property or another, and I'm proud to have been a part of this effort over the past five years. While the work presented in the previous chapters adds new insight towards the reactivity and stability of Mn complexes, our quest for knowledge remains a major undertaking. Though the potential effects of steric bulk on O_2 reactivity by $[Mn^{II}(dpaq^{2Me})]^+$ have been established, the intermediates along the pathway remain unknown. Though we have three more examples of rare Mn^{III}-alkylperoxo complexes, the intricacies of how they react and what governs their (in)stability remain unclear. Though we have realized the reactivity of Mn^{III}-hydroxo complexes with reactive oxygen species, the products formed remain unidentified. I discuss a few potential approaches to answering some of these remaining questions in this chapter.

The control afforded by a simple steric modification on the activation of O_2 is exciting. However, intermediates have so far gone unobserved in the oxygenation of $[Mn^{II}(dpaq)]^+$ and its derivatives. The design of new ligand derivatives with more significant perturbations is worth exploring within the context of gaining control over the intermediates formed. Noting the effect of a simple methyl group on the O_2-activation mechanism, developing a ligand that features even greater steric bulk around the active site may help to favor the formation of a terminal high-valent Mn-oxo by preventing dimerization. Building off of previous work in which hydrogen bond donors are able to stabilize Mn^{IV}-oxo species, such modifications to the dpaq ligand may be of interest, though certainly synthetically challenging.

It is obvious that the mechanism involved in the reaction of $[Mn^{II}(dpaq^{2Me})]^+$ with PhIO as an oxidant differs from that with dioxygen. In fact, this reaction has resulted in the formation of a new, as-of-yet unidentified, intermediate not seen in the reaction of the Mn^{II} complex with O_2. As such, this reactivity should be more thoroughly investigated. Spectroscopic characterization of the new intermediate is paramount to our understanding, as it is likely too unstable to isolate. Upon characterization, investigations of the reactivity of this intermediate with hydrogen atom and oxygen atom substrates, as well as probing its thermal decay, may lend insight into the unknowns of dioxygen activation by this series of complexes.

The development of a room-temperature stable Mn^{III}-alkylperoxo species is a promising result in and of itself, inching towards a structural and reactive model of the proposed intermediate of Mn-lipoxygenase. That being said, investigations towards how these complexes decay and how the decay pathways compare to the proposed enzyme mechanism are still in their infancy. Expanding upon the limited investigations into substrate reactivity reported in this work, as well as computational studies to analyze the electronic structure of the complex in regards to

alkylperoxo binding and decay pathways, will serve as a means to compare with and add to the limited understanding of this class of compounds. Additionally, modifications to the ^{6Me}dpaq ligand in which the 5-position of the quinoline is functionalized with electron withdrawing or donating groups will be carried out to investigate the effects of modulating the donation of the amide nitrogen *trans* to the alkylperoxo moiety, thereby influencing the energy of the d_{z^2} orbital and potentially affecting alkylperoxo binding (Figure 6.1).

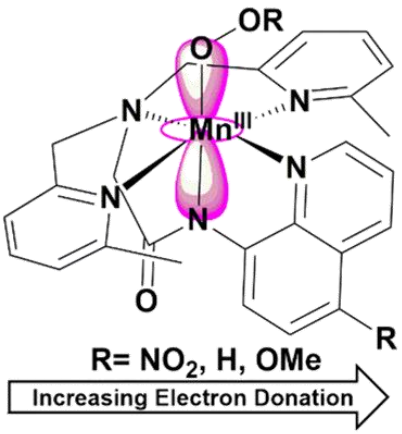

Figure 6.1. Electron donating and withdrawing functionalization of the ^{6Me}dpaq ligand results in modulation of the donating properties of the amide nitrogen *trans* to the alkylperoxo moiety.

In short, while our understanding of the reactivity of Mn^{II} complexes with O_2 and its derivatives remains in the early stages, there are clear ways forward towards learning more about these processes. As new ligands and their metal complexes are developed and new sets of reactions are performed on these complexes, our knowledge set grows and the importance of model chemistry grows with it. I look forward to seeing where the investigations lead over the coming years.

Appendix 1

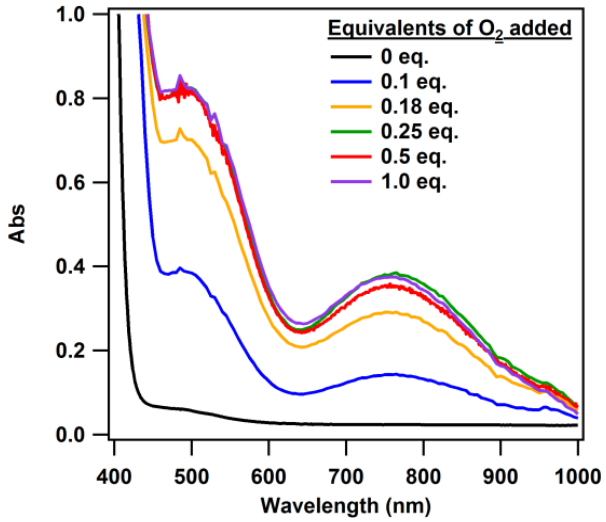

Figure A1.1. Overlay of electronic absorption spectra obtained during O_2-titration experiments for $[Mn^{II}(dpaq)]^+$ (6 mM in MeCN, 20°C).

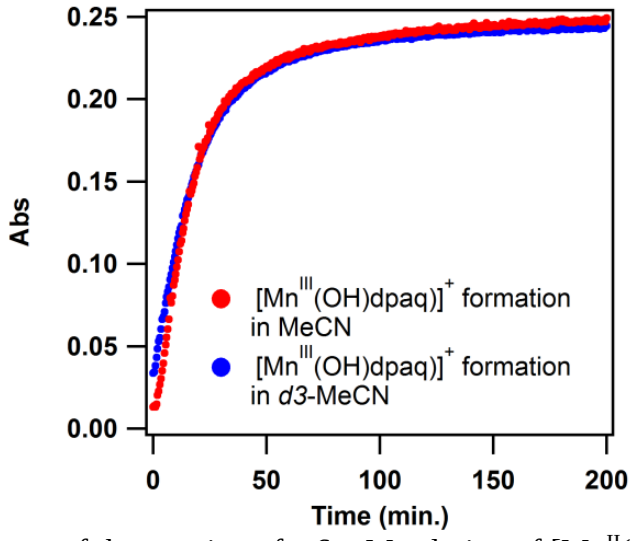

Figure A1.2. Time course of the reaction of a 6 mM solution of $[Mn^{II}(dpaq)]^+$ with excess O_2 in non-deuterated MeCN (red trace) or in d_3-MeCN (blue trace) at 25°C, monitored at 750 nm).

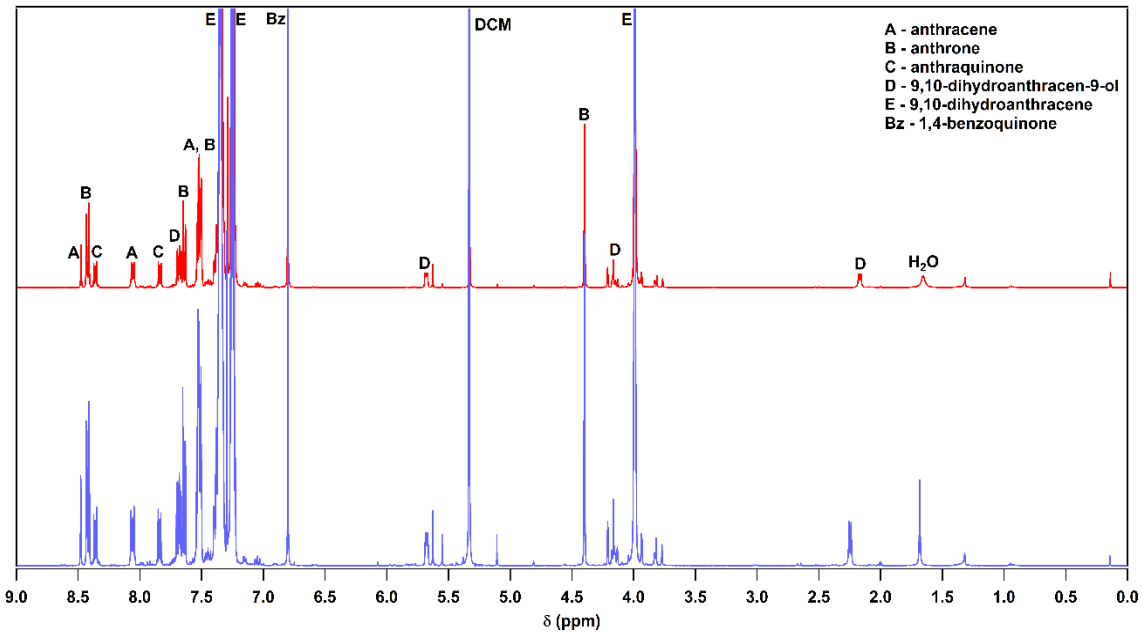

Figure A1.3. ^{1}H-NMR analysis of the oxidation of 9,10-dihydroanthracene in the presence of $[Mn^{II}(dpaq)]^{+}$ (top) or $[Mn^{III}(OH)(dpaq)]^{+}$ (bottom) and excess O_2 in d_3-MeCN (6 mM) at 25°C. Quantification of products was obtained by using 1,4-benzoquinone (10 molar equivalent relative to starting Mn^{II} complex) as an internal concentration reference.

Table A1.1. Experimental yield of DHA oxidation products during oxygenation experiments.

Complex	Anthracene yield[a]	Anthrone yield[a]	Anthraquinone yield[a]	9,10-dihydroanthran-9-ol yield[a]	Total DHA converted[a]
O_2 present					
$[Mn^{II}(dpaq)]^{+}$	3.0	12.9	2.0	7.9	25.8
$[Mn^{II}(dpaq^{2Me})]^{+}$	3.0	11.5	1.5	7.5	23.5
$[Mn^{III}(OH)(dpaq)]^{+}$	3.1	15.0	2.4	9.4	29.9
$[Mn^{III}(OH)(dpaq^{2Me})]^{+}$	4.0	15.7	2.6	11.5	33.8

[a] Molar equivalents relative to starting Mn concentration.

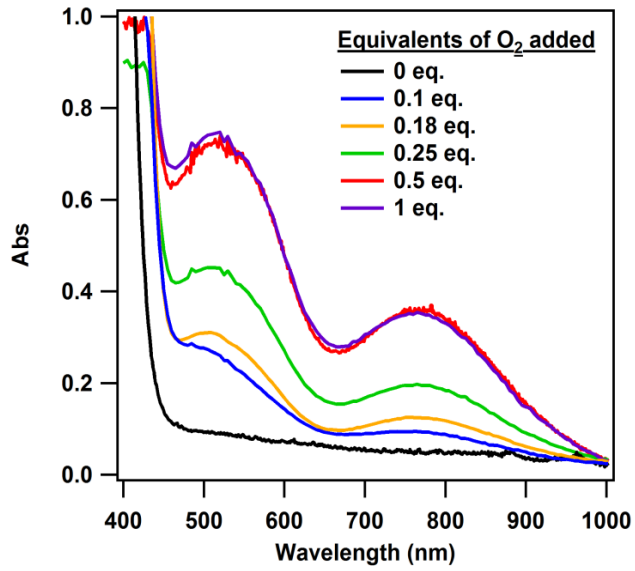

Figure A1.4. Overlay of electronic absorption spectra obtained during O_2-titration experiments for $[Mn^{II}(dpaq^{2Me})]^+$ (6 mM in MeCN, 20°C).

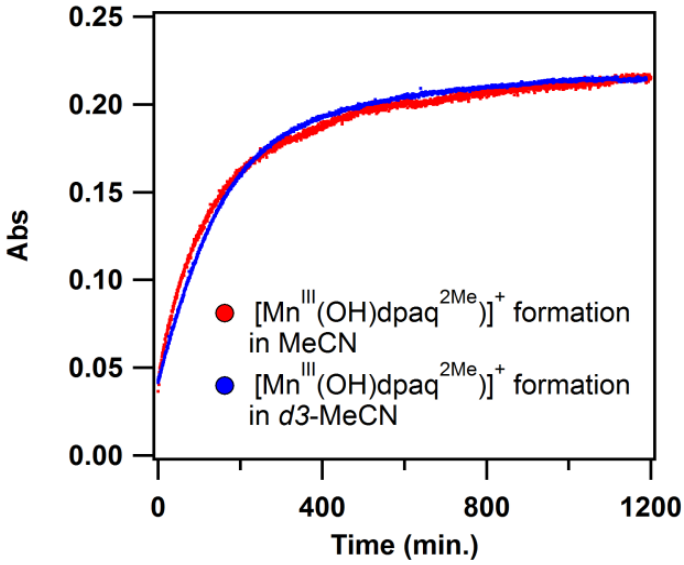

Figure A1.5. Time course of the reaction of a 6 mM solution of $[Mn^{II}(dpaq^{2Me})]^+$ with excess O_2 in non-deuterated MeCN (red trace) or in d_3-MeCN (blue trace) at 25°C, monitored at 750 nm).

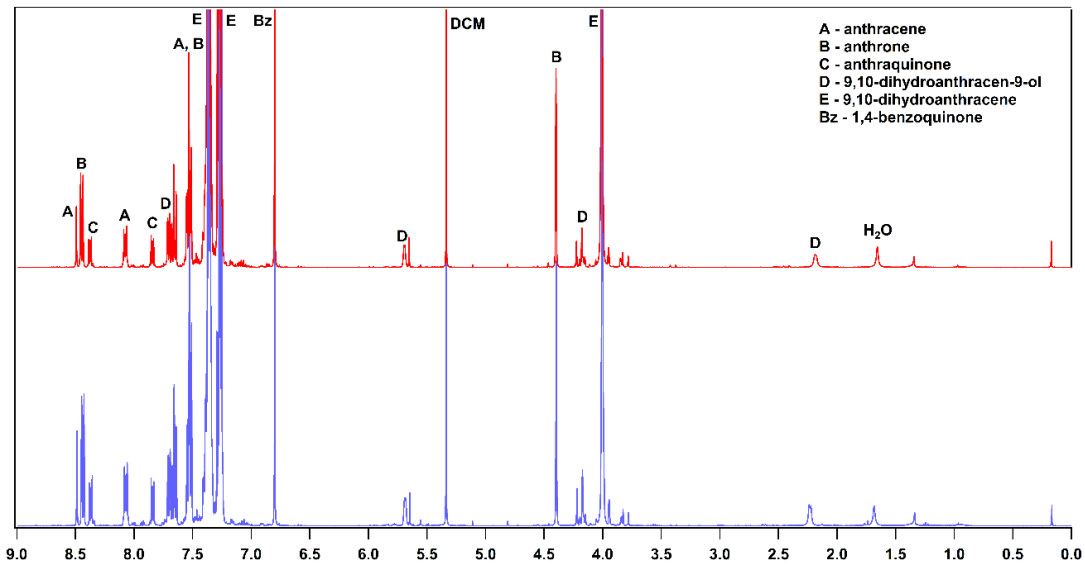

Figure A1.6. ^{1}H-NMR spectra after the treatment of $[Mn^{II}(dpaq^{2Me})]^{+}$ (top) or $[Mn^{III}(OH)(dpaq^{2Me})]^{+}$ (bottom) with 9,10-dihydroanthracene in the presence of and excess O_2 in d_3-MeCN (6 mM) at 25°C. Quantification of products was obtained by using 1,4-benzoquinone (10 molar equivalent relative to starting Mn^{II} complex) as an internal concentration reference.

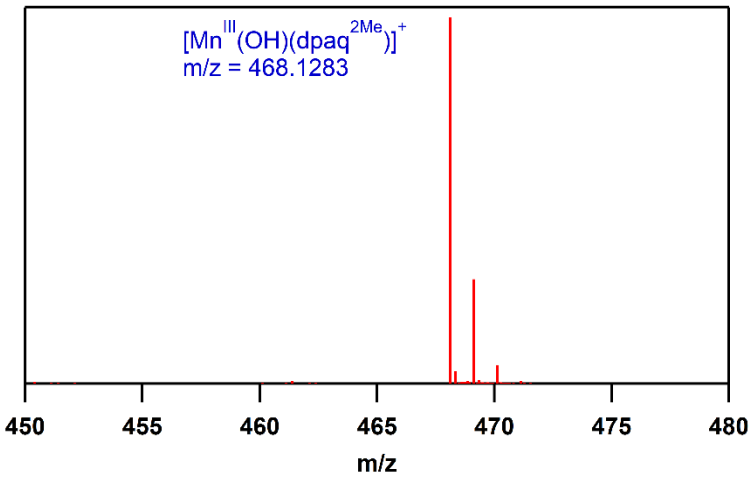

Figure A1.7. ESI-MS data for $[Mn^{III}(OH)(dpaq^{2Me})]^{+}$ from the reaction of $[Mn^{II}(dpaq^{2Me})](OTf)$ with 1 equivalent of O_2 in the presence of 100 equivalents of DHA in deuterated MeCN.

Appendix 2

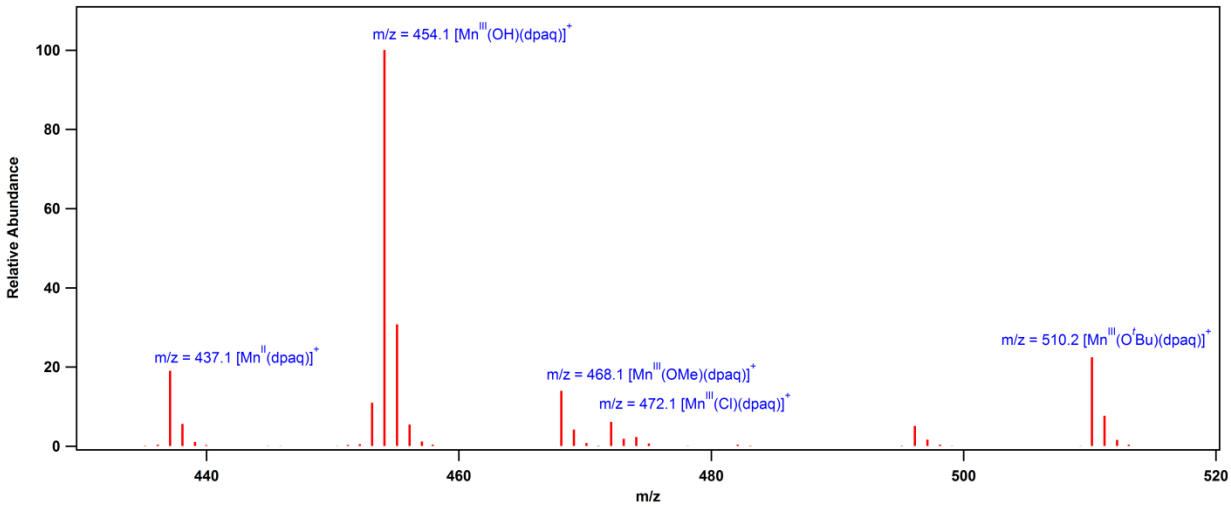

Figure A2.1: ESI-MS data of the reaction solution of **1** and 0.5 equivalents of ^{t}BuOOH in MeCN at -15°C in the presence of Et_3N. The spectra reveal peaks associated with several Mn^{III} species, including **1a** and $[Mn^{III}(O^{t}Bu)(dpaq)]^{+}$. Peaks associated with the Mn^{III}-OMe and Mn^{III}-Cl adducts are commonly observed in ESI-MS data of solution of **1a**.

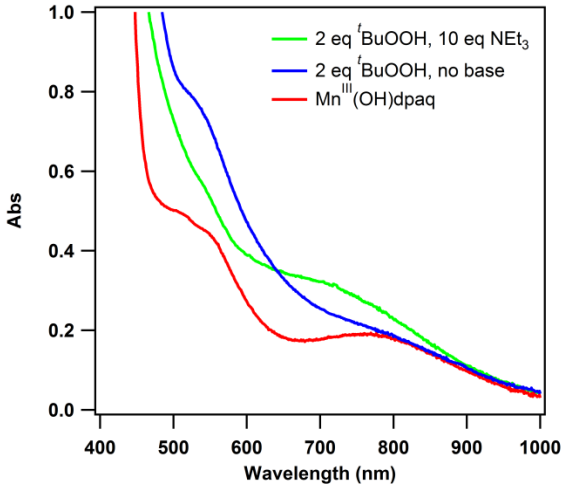

Figure A2.2: Electronic absorption spectra of the reaction of **1a** (red trace) with 2 equivalents of ^{t}BuOOH in the presence (green trace), or absence (blue trace), of Et_3N in MeCN at -15°C.

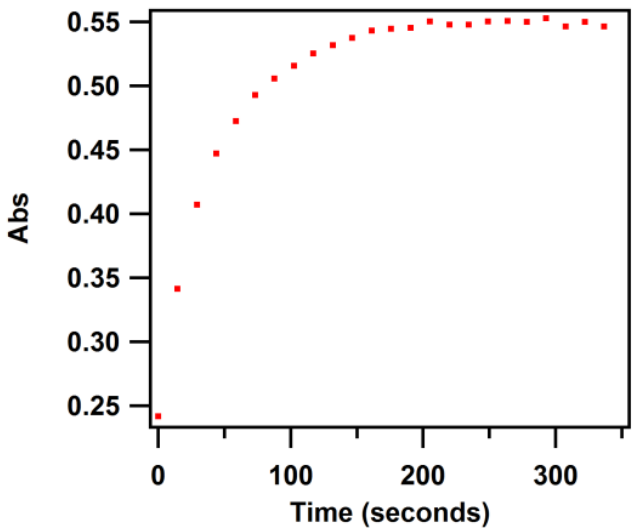

Figure A2.3: Time course of the reaction of **1a** with 50 equivalents of ^{t}BuOOH in MeCN at -15°C in the presence of Et_3N monitored at 700 nm (cf. Figure 4).

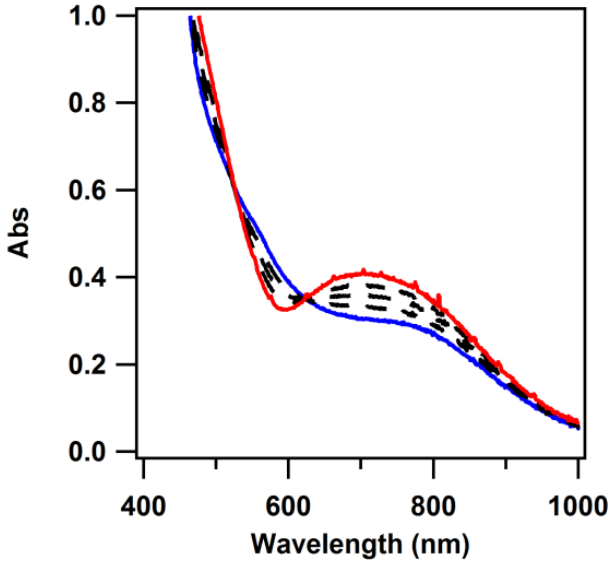

Figure A2.4: Electronic absorption spectra showing the formation of **1b** from the reaction of **1a** (2 mM) with 100 equivalents ^{t}BuOOH in the absence of Et_3N in MeCN at -15°C.

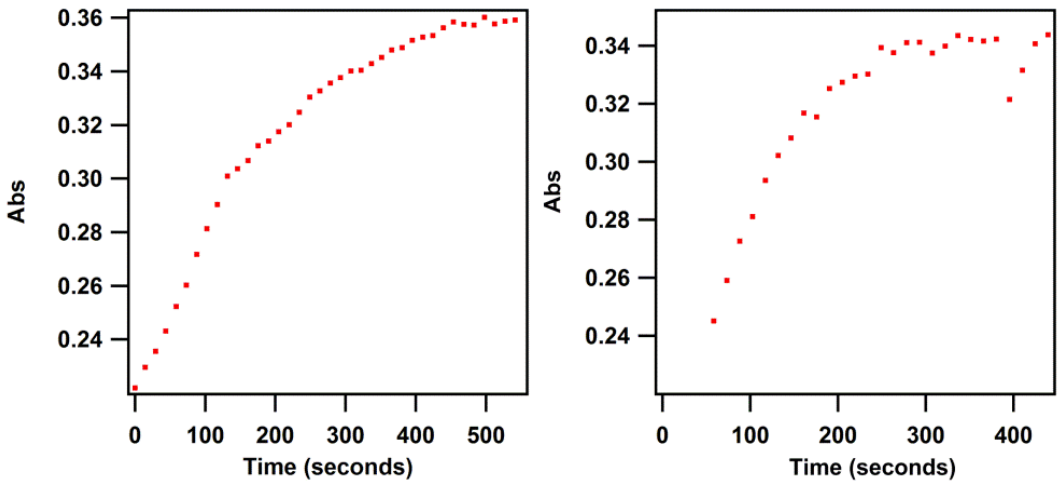

Figure A2.5: Time course of the reaction of **1a** with 100 equivalents of ^{t}BuOOH in MeCN at -15°C in the presence (left) and absence (right) of Et_3N, monitored at 700 nm.

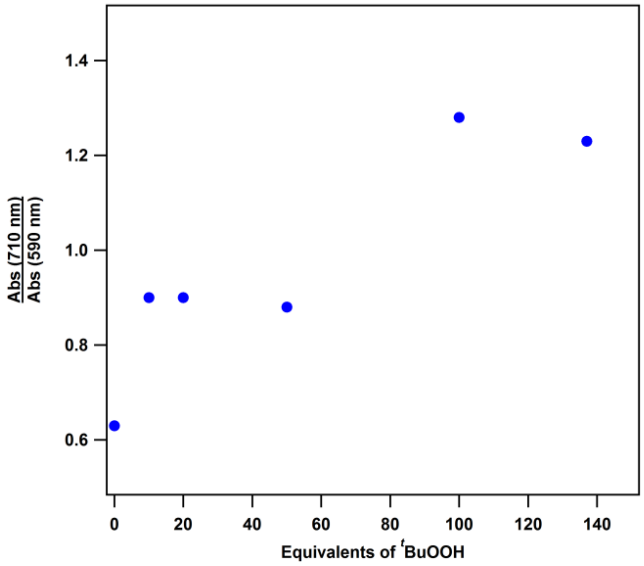

Figure A2.6: Plot comparing the ratio of intensities at 710 nm and 590 nm as a metric of **1b** formation. The low initial ratio marks near 100% formation of **1a** in solution. The first change in the ratio (10 to 50 equivalents ^{t}BuOOH) marks solutions dominated by the $Mn^{III}Mn^{IV}$ dimer, as assessed by EPR spectrosscopy. The highest ratios, observed upon addition of 100 and 140 equivalents ^{t}BuOOH, are associated with EPR-silent solutions that consist primarily of **1b**.

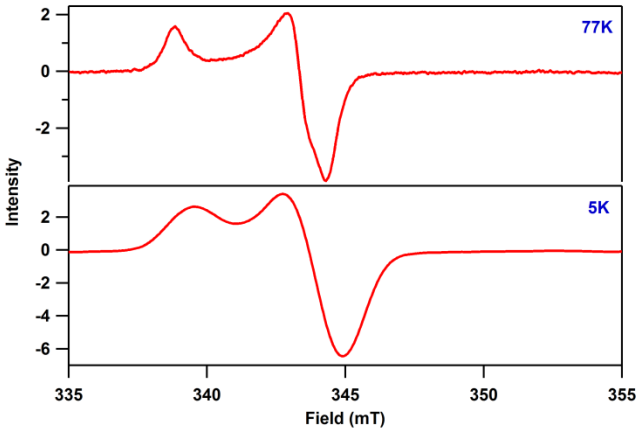

Figure A2.7. EPR spectrum of **1b** reaction mixture at 77 K (top) and 5 K (bottom), showing a rhombic signal with g values of 2.033, 2.007, and 2.002 that correspond to the ^{t}BuOO$^{\bullet}$ radical.

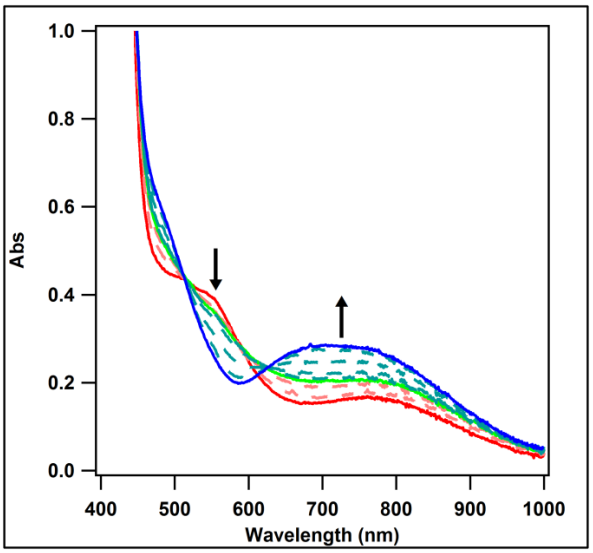

Figure A2.8. Electronic absorption spectra of the reaction of **1a** (red trace) with 50 equivalents of ^{t}BuOOH in the absence of Et_3N to form **1b** at -15 °C in MeCN (blue trace). The reaction proceeds through the initial formation of a species with broad, poorly defined spectroscopic features (green trace).

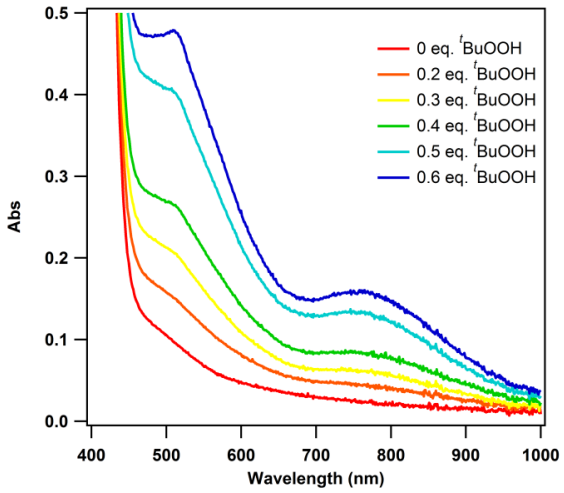

Figure A2.9. Electronic absorption spectra of reactions between **2** and ^{t}BuOOH in the presence of 10 equivalents of Et_3N showing full formation of **2a** with the addition of ~0.5 eq of ^{t}BuOOH at -15 °C in MeCN.

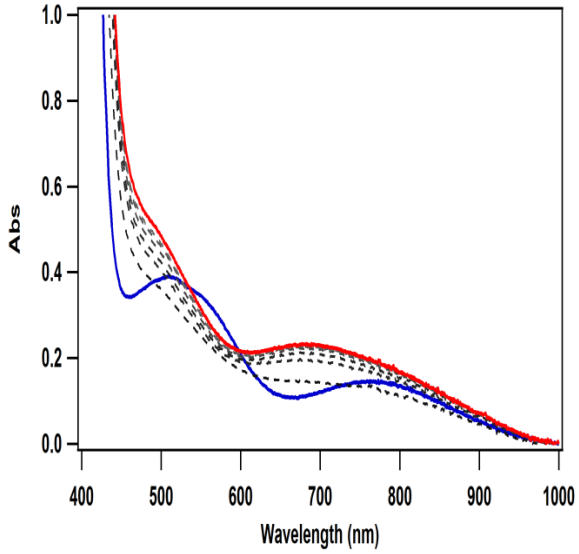

Figure A2.10. Electronic absorption spectrum showing the formation of **2b** (red trace) from **2a** (blue trace) upon the reaction with ~100 eq. of ^{t}BuOOH in the presence of 10 equivalents of Et_3N at -15°C in MeCN.

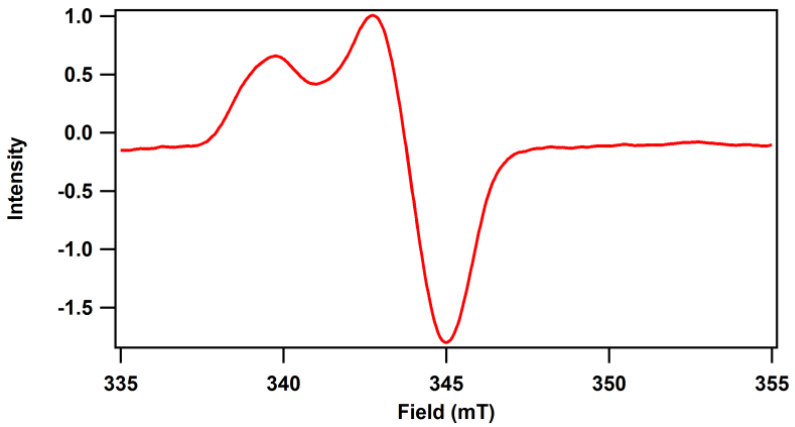

Figure A2.11. 5 K EPR spectrum of **2b** reaction mixture showing signals at g = 2.03 and 2.003 corresponding to ^{t}BuOO$^{\bullet}$ radical.

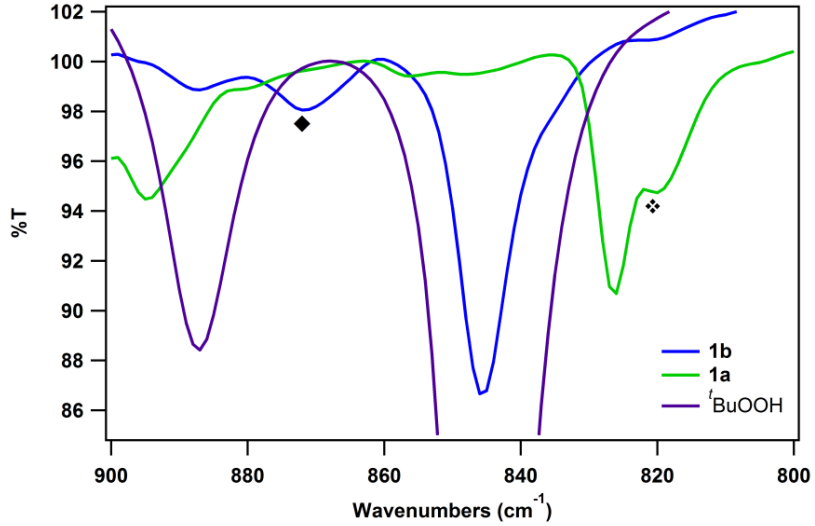

Figure A2.12. Solution FT-IR spectra of ^{t}BuOOH and **1a**. ◆ corresponds to the assigned O–O vibration of **1b**. ❖ corresponds to stretches ~820 cm^{-1} seen in **1a**.

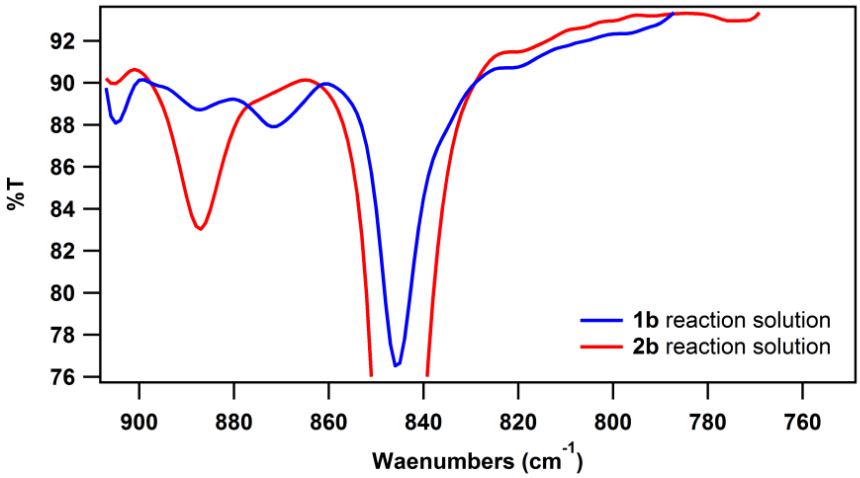

Figure A2.13. Comparison of solution FT-IR spectra of **1b** (blue) and **2b** (red) in MeCN. No signal corresponding to the O–O vibration of **2b** could be identified, presumably due to the signal overlapping with one of the intense vibrations of free ^{t}BuOOH.

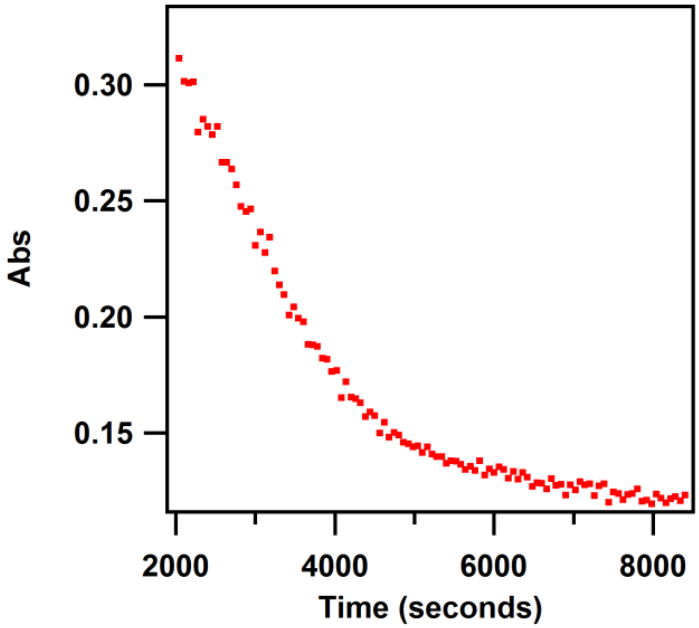

Figure A2.14. Time course of the decay of **1b** in MeCN at -15°C in the presence of Et_3N monitored at 700 nm.

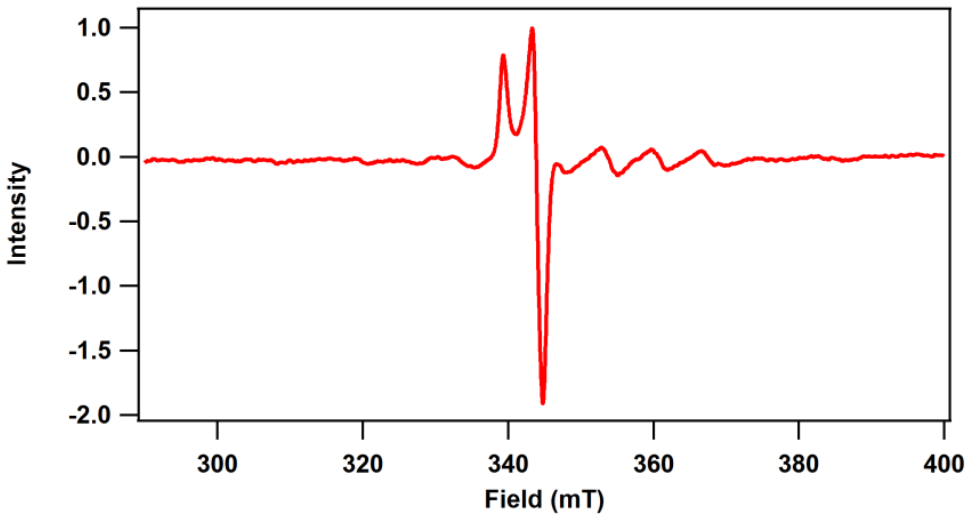

Figure A2.15. 5 K EPR spectrum of decay solution of **1b** showing a less intense ^{t}BuOO$^{\bullet}$ signal and the appearance of a weak six-line signal proposed to be a Mn(II) species.

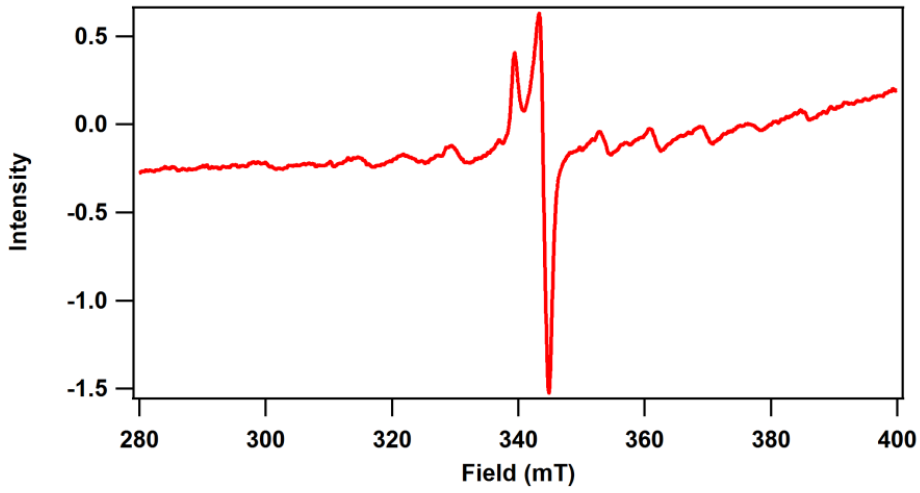

Figure A2.16. 5 K EPR spectrum of decay solution of **2b** showing a less intense ^{t}BuOO$^{\bullet}$ signal and the appearance of a six-line signal proposed to be a Mn(II) species.

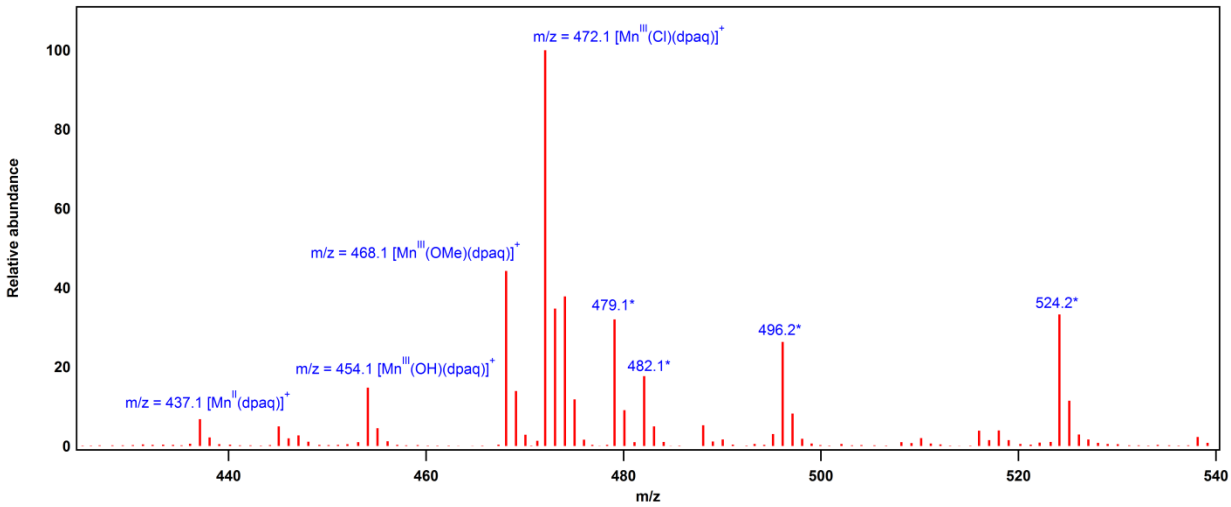

Figure A2.17: ESI-MS data of the solution following the decay of **1b** in MeCN at -15°C in the presence of Et_3N, revealing peaks associated with both **1** and **1a**. Asterisk (*) denotes unidentified products.

Table A2.1. Cartesian coordinates (Å) for DFT energy minimized $[Mn^{III}(OO^tBu)(dpaq)]^+$ model.

Atom	x	y	z
Mn	-0.151764	-0.044942	-0.941100
O	-0.123922	-1.229666	3.013223
O	-0.208315	0.255084	-2.752633
C	0.790374	-0.791350	-4.663368
N	-0.114053	2.011581	-0.636806
N	-0.133478	0.017106	1.049476
N	-0.162952	-2.275144	-0.517387
N	1.948242	-0.600816	-0.892484
N	-2.265844	-0.597020	-0.867768
C	-0.105911	2.958348	-1.574243
C	-0.068510	4.324218	-1.250999
C	-0.037994	4.703603	0.075593
C	-0.044798	3.722018	1.095130
C	-0.014332	4.015577	2.480809
C	-0.023565	2.977722	3.388353
C	-0.062341	1.623530	2.985449
C	-0.092788	1.291450	1.632754
C	-0.084303	2.359835	0.689046
C	-0.145301	-1.132705	1.775202
C	-0.202901	-2.426657	0.967084
C	1.072595	-2.850540	-1.096131
C	2.238156	-1.915912	-0.887883
C	3.546735	-2.371784	-0.755879
C	4.577524	-1.442398	-0.637864
C	4.270539	-0.082036	-0.645983
C	2.941070	0.297689	-0.770347
C	-1.381787	-2.828429	-1.155818
C	-2.552897	-1.912605	-0.901265
C	-3.855628	-2.378076	-0.749531
C	-4.885360	-1.456535	-0.571795
C	-4.582716	-0.095640	-0.545381
C	-3.257531	0.293494	-0.693305
H	-0.129469	2.611081	-2.602536
C	0.065112	0.193034	-5.579095
C	0.839529	-2.194412	-5.270898
O	-0.025207	-1.027388	-3.462546
C	2.180895	-0.293057	-4.279494
H	-0.063491	5.057907	-2.048902
H	-0.008227	5.754074	0.350103
H	0.015748	5.050651	2.806498
H	-0.000165	3.194423	4.452288
H	-0.067932	0.838473	3.727125
H	-1.124337	-2.943018	1.253415
H	0.629167	-3.056390	1.295865
H	1.290013	-3.839248	-0.677358
H	0.906981	-2.959379	-2.171464
H	3.748020	-3.437965	-0.746348
H	5.605090	-1.775294	-0.533709
H	5.041936	0.673666	-0.550739
H	2.647674	1.342622	-0.775515
H	-1.597985	-3.842253	-0.800822
H	-1.195958	-2.869089	-2.233319
H	-4.053312	-3.444784	-0.768049
H	-5.908566	-1.796402	-0.448299
H	-5.353640	0.653530	-0.404209
H	-2.967303	1.339448	-0.669946
H	-0.940748	-0.171531	-5.809223
H	-0.012166	1.172944	-5.101061
H	0.621171	0.305635	-6.515251
H	-0.169150	-2.556509	-5.490451
H	1.409995	-2.160139	-6.203812
H	1.332464	-2.895815	-4.590670
H	2.699475	-1.028739	-3.658595
H	2.772780	-0.123679	-5.184482
H	2.106366	0.648605	-3.730650

Table A2.2. Cartesian coordinates (Å) for DFT energy minimized $[Mn^{III}(OO^{t}Bu)(dpaq^{2Me})]^{+}$ model.

Atom	x	y	z
Mn	-0.229079	-0.052843	0.017737
O	-0.363260	-1.554686	3.856195
O	-0.180712	0.082483	-1.816887
C	1.312551	-0.543670	-3.577367
N	-0.331604	2.034664	0.518314
N	-0.247858	-0.153327	2.000588
N	-0.368996	-2.292214	0.274598
N	1.815875	-0.626742	0.196164
N	-2.367313	-0.517892	-0.084343
C	-0.466966	3.104807	-0.277404
C	-0.230472	4.409016	0.215527
C	0.140532	4.602570	1.523977
C	0.255829	3.493757	2.394624
C	0.601474	3.608934	3.762754
C	0.667555	2.473103	4.540743
C	0.389594	1.195656	4.010883
C	0.046808	1.042024	2.668676
C	-0.005558	2.208159	1.847264
C	-0.395213	-1.349521	2.631408
C	-0.693767	-2.526823	1.707354
C	0.932978	-2.879827	-0.112691
C	2.079886	-1.947448	0.204159
C	3.366763	-2.422727	0.443161
C	4.395883	-1.513411	0.673521
C	4.110987	-0.148207	0.668817
C	2.804991	0.254870	0.430368
C	-1.478490	-2.711693	-0.615947
C	-2.660248	-1.793061	-0.409808
C	-3.976682	-2.219532	-0.558303
C	-5.009557	-1.301719	-0.378791
C	-4.698852	0.014173	-0.038165
C	-3.362387	0.364896	0.105341
C	-0.878996	2.912667	-1.705317
C	0.382346	0.113515	-4.595701
C	1.919230	-1.839160	-4.121251
O	0.526022	-1.049416	-2.449626
C	2.394270	0.416232	-3.087767
H	-0.350817	5.248730	-0.460283
H	0.332124	5.601749	1.904754
H	0.805374	4.591450	4.177174
H	0.934256	2.550586	5.590567
H	0.436031	0.323886	4.646839

Atom	x	y	z
H	-1.766168	-2.728553	1.794048
H	-0.165535	-3.408243	2.082666
H	1.088973	-3.848447	0.374474
H	0.916578	-3.037723	-1.193497
H	3.551699	-3.491880	0.450733
H	5.404533	-1.865617	0.863328
H	4.880485	0.593304	0.850590
H	2.527918	1.304083	0.418950
H	-1.770007	-3.753536	-0.440295
H	-1.122251	-2.614659	-1.646266
H	-4.183363	-3.255666	-0.805310
H	-6.043067	-1.612544	-0.491772
H	-5.473098	0.755794	0.122920
H	-3.063747	1.370983	0.382798
H	-1.557048	2.064387	-1.814290
H	-0.001714	2.711503	-2.329897
H	-1.361424	3.819389	-2.076804
H	-0.403391	-0.585640	-4.897837
H	-0.082850	1.004750	-4.167230
H	0.951440	0.409457	-5.482822
H	1.133016	-2.535362	-4.427888
H	2.539701	-1.606409	-4.991813
H	2.548430	-2.317589	-3.364358
H	3.081802	-0.092425	-2.406846
H	2.965235	0.795358	-3.941173
H	1.941664	1.264278	-2.5675

Table A2.3. DFT calculated Energies (eV) and Compositions (%) of O and N 2p-based MOs and the Mn 3d-based MOs of **1b**.

MO		Spin	Occupancy	Energy (eV)	% Contribution		
					Mn 3d	OOtBu	N dpaq
112	(Mn *yz*/py[a])	α	1	-10.3105	15.2	2.7	4.6
116	(Mn *xy*/qn[a])	α	1	-9.9976	26.7	1.8	9.9
120	(Mn *xz*/*xy*)	α	1	-9.7213	45.8	3.4	5.8
121	(Mn *xy*)	α	1	-9.6262	29	2	5.5
136	(Mn x^2-y^2)	α	1	-6.4694	35.6	4.2	34.2
137	(O_p)	α	1	-6.3241	8.2	74.2	3.7
139	(Mn z^2)	α	0	-2.7084	54.7	12.8	12.8
127	(O_p)	β	1	-8.0848	2.2	58.7	7.6
133	(O_p)	β	1	-6.4901	8.5	79.6	0.6
135	(Mn *xy*/*xz*/qn[a])	β	0	-2.633	26.9	0.5	9.3
136	(Mn *xz*)	β	0	-2.3198	56	4.8	6.1
137	(Mn *yz*)	β	0	-1.8989	54.6	8.8	8.1
138	(Mn *xy*/*yz*)	β	0	-1.6911	32.7	1.4	11.3
139	(Mn *xy*)	β	0	-1.6522	38.2	1.1	11
140	(Mn *xz*/py[a])	β	0	-1.2709	22.5	1.4	13.3
144	(Mn x^2-y^2)	β	0	-0.6198	78.6	0.5	8.5
145	(Mn z^2)	β	0	-0.5196	53.8	4.5	9.3
146	(Mn z^2/qn[a])	β	0	-0.4665	27.8	2.8	8.6

[a]qn = quinoline, py = pyridine

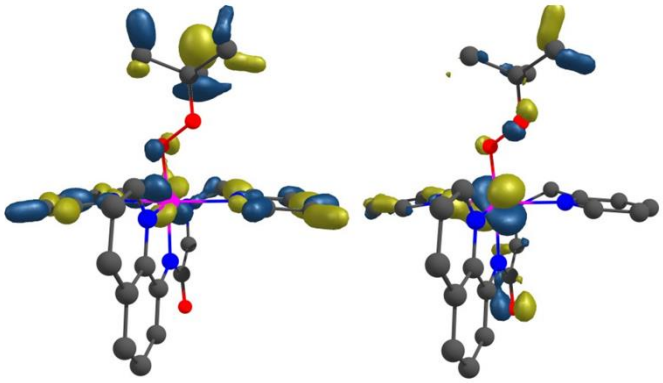

Figure A2.18. Surface contour plots of π-type Mn 3d_{yz} (left) and 3d_{xz} (right) MOs (isovalue = 0.05) calculated for **1b** showing minor alkylperoxo contributions.

Table A2.4. DFT calculated Energies (eV) and Compositions (%) of O and N 2p-based MOs and the Mn 3d-based MOs of **2b**.

MO		Spin	Occupancy	Energy (eV)	% Contribution		
					Mn 3d	OOtBu	N dpaq
113	(Mn *yz*)	α	1	-10.5807	16.2	7.9	2.6
114	(Mn *xz*)	α	1	-10.528	16.1	2.8	7.1
117	(Mn x^2-y^2/py[a])	α	1	-10.33	26.7	0.8	4.8
120	(Mn *xy*)	α	1	-9.9901	47.5	0.8	7.4
122	(Mn *yz*)	α	1	-9.8999	50	6.9	2.9
129	(Mn *xz*/*xy*/O_p)	α	1	-8.8937	18.4	17.9	6
133	(Mn *xy*/py[a])	α	1	-8.4342	20.3	8.1	26.7
140	(Mn x^2-y^2)	α	1	-6.6088	33.7	1.1	39.5
141	(O_p)	α	1	-6.4684	5.9	37.5	4
143	(Mn z^2)	α	0	-2.9457	55.3	13.1	16.4
131	(O_p)	β	1	-8.0843	3.6	50.3	8.9
137	(O_p)	β	1	-6.6203	7.6	76.5	0.2
139	(Mn *xz*/*xy*/qn[a])	β	0	-2.6198	31.4	0.9	8.3
140	(Mn *yz*/*xy*)	β	0	-2.4242	66.4	5.7	4.3
141	(Mn *xz*/*yz*)	β	0	-2.1	55.1	8.7	7.2
142	(Mn *xy*)	β	0	-1.8747	25.1	0.1	13.2
143	(Mn *xy*)	β	0	-1.7131	29.7	0.6	15.2
144	(Mn *xz*/*xy*/py[a])	β	0	-1.3599	30.5	2.2	13.6
148	(Mn x^2-y^2)	β	0	-0.8508	71.4	0.8	8.5
149	(Mn z^2)	β	0	-0.732	68.1	6.2	9.7

[a]qn = quinoline, py = pyridine

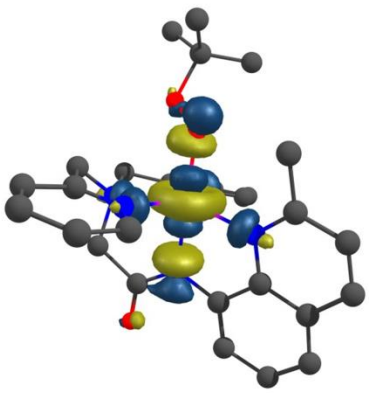

Figure A2.19. Surface contour plot of Mn 3d_{z^2} frontier MO (isovalue = 0.05) calculated for **2b**.

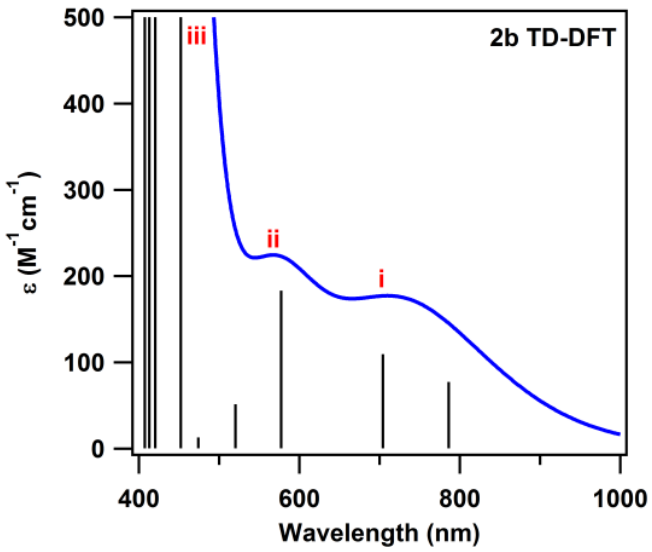

Figure A2.20. TD-DFT predicted electronic absorbtion spectrum of **2b** showing a feature arising from a Mn $3d_{x^2-y^2}$ to $3d_{z^2}$ transition (**i**), higher energy features arising from ligand-to-metal charge transfer from both dpaq and the alkylperoxo moiety to Mn^{III} (**ii**)**,** and higher intensity features corresponding to additional ligand-to-metal charge transfers and a $3d_{xy}$ to $3d_{z^2}$ transition (**iii**).

Table A2.5. TD-DFT Calculated Energies, Percent Contributions from Dominant One-electron Excitations, and Oscillator Strengths for the Major Electronic Transitions of **1b**.

	State	Energy (cm^{-1})[a]	f_{osc}	Transition[b]	%	donor MO	Acceptor MO	comments
	1	12600	0.001801	136a → 139a	75.3	Mn $3d_{x^2-y^2}$	Mn $3d_{z^2}$	d-d
		(794 nm)		137a → 139a	14.6	O1 p_y	Mn $3d_{z^2}$	
i	2	15200	0.000748	136a → 139a	14.6	Mn $3d_{x^2-y^2}$	Mn $3d_{z^2}$	LMCT
		(658 nm)		137a → 139a	54.7	O1 p_y	Mn $3d_{z^2}$	
				138a → 139a	17.4	N p_x	Mn $3d_{z^2}$	
	3	18200	0.001639	137a → 139a	17.6	O1 p_y	Mn $3d_{z^2}$	LMCT
		(549 nm)		138a → 139a	69.9	N p_x	Mn $3d_{z^2}$	
ii								
	4	19200	0.000879	138a → 140a	38.1	N p_x	C p_x	LMCT
		(520 nm)		134b → 135b	51.1	C p_x	Mn $3d_{xy}$	
	5	21200	0.000157	133b → 135b	31.0	O1 p_y	Mn $3d_{xy}$	LMCT
		(472 nm)		133b → 136b	56.1	O1 p_y	Mn $3d_{xz}$	
	6	22900	0.00270	133b → 135b	53.2	O1 p_y	Mn $3d_{xy}$	LMCT
		(437 nm)		133b → 136b	28.6	O1 p_y	Mn $3d_{xz}$	
iii	8	23900	0.009660	138a → 140a	16.2	N p_x	C p_x	LMCT
		(418 nm)		134b → 136b	62.8	C p_x	Mn $3d_{xz}$	
	14	28600	0.014191	129a → 139a	16.6	Mn $3d_{xy}$	Mn $3d_{z^2}$	d-d
		(350 nm)		133b → 137b	19.8	O1 p_y	Mn $3d_{yz}$	

[a]Transition energies rounded to the nearest 100 cm^{-1}. [b]Composition of MOs are listed in Table A2.4.

Table A2.6. TD-DFT Calculated Energies, Percent Contributions from Dominant One-electron Excitations, and Oscillator Strengths for the Major Electronic Transitions of **2b**.

	State	Energy (cm^{-1})[a]	f_{osc}	Transition[b]	%	donor MO	acceptor MO	Comments
i	1	12700 (787 nm)	0.001248	140a → 143a	86.6	Mn 3 $d_{x^2-y^2}$	Mn $3d_{z^2}$	d-d
	2	14200	0.001767	141a → 143a	50.6	O p_x	Mn $3d_{z^2}$	LMCT
		(704 nm)		142a -> 143a	35.4	N p_x	Mn $3d_{z^2}$	
ii	3	17300	0.002954	142a → 143a	54.6	N p_x	Mn $3d_{z^2}$	LMCT
		(578 nm)		141a → 143a	35.3	O p_x	Mn $3d_{z^2}$	
	4	19200	0.000827	142a → 144a	35.3	N p_x	N p_x	LMCT
		(521 nm)		138b → 139b	48.5	C p_x	Mn $3d_{yz/xz}$	
iii	6	22100 (452 nm)	0.010782	138b → 140b	77.5	C p_x	Mn $3d_{yz}$	LMCT
	7	23800	0.012161	142a → 144a	14.5	N p_x	N p_x	LMCT
		(420 nm)		137b → 139b	16.6	O p_x	Mn $3d_{yz/xz}$	
				138b → 139b	21.1	C p_x	Mn $3d_{yz/xz}$	
	9	24500	0.015256	137b → 139b	49.3	O p_x	Mn $3d_{yz/xz}$	LMCT
		(408 nm)		137b → 140b	13.4	O p_x	Mn $3d_{yz}$	
	11	26700	0.005050	133a → 143a	43.4	Mn $3d_{xy}$	Mn $3d_{z^2}$	d-d
		(375 nm)		120a → 143a	18.4	Mn $3d_{xy}$	Mn $3d_{z^2}$	

[a]Transition energies rounded to the nearest 100 cm^{-1}. [b]Composition of MOs are listed in Table A2.5.

Appendix 3

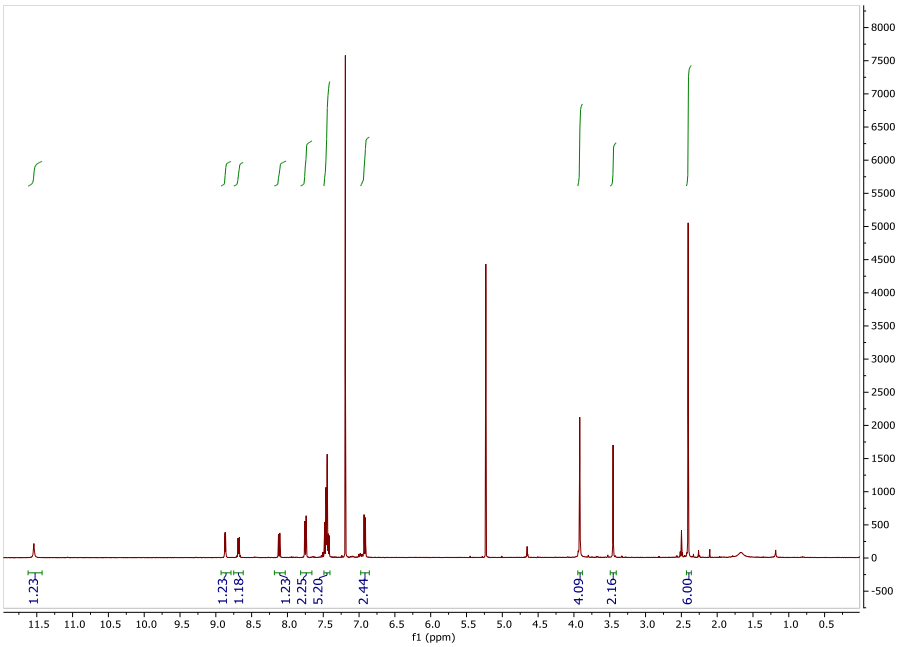

Figure A3.1. ^{1}H NMR spectrum of H^{6Me}dpaq

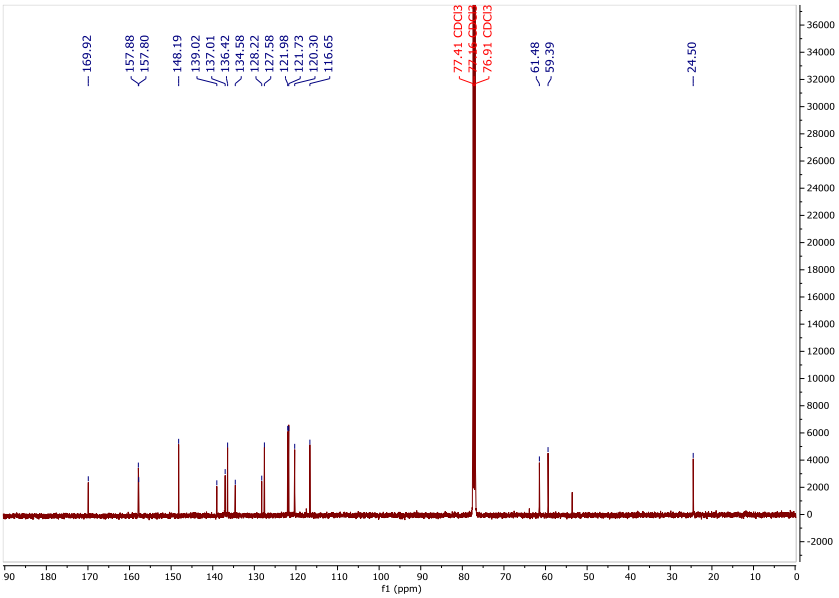

Figure A3.2. ^{13}C NMR spectrum of H^{6Me}dpaq.

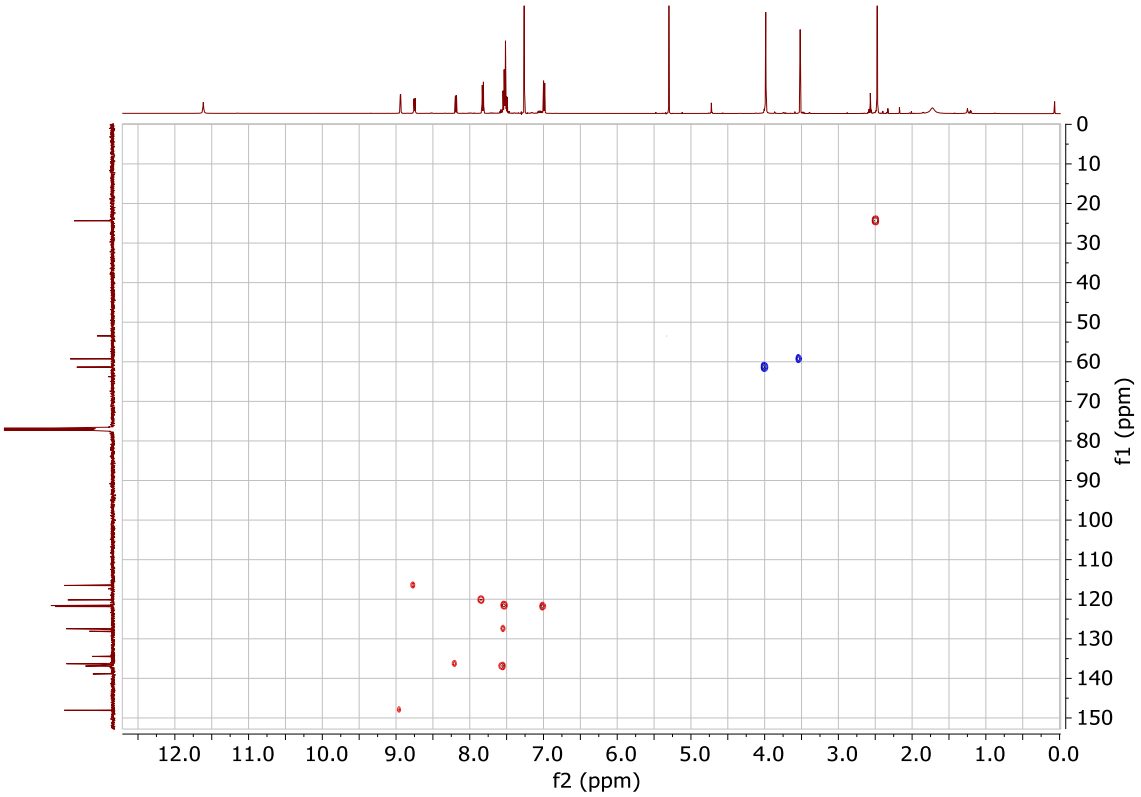

Figure A3.3. HSQC NMR of H^{6Me}dpaq.

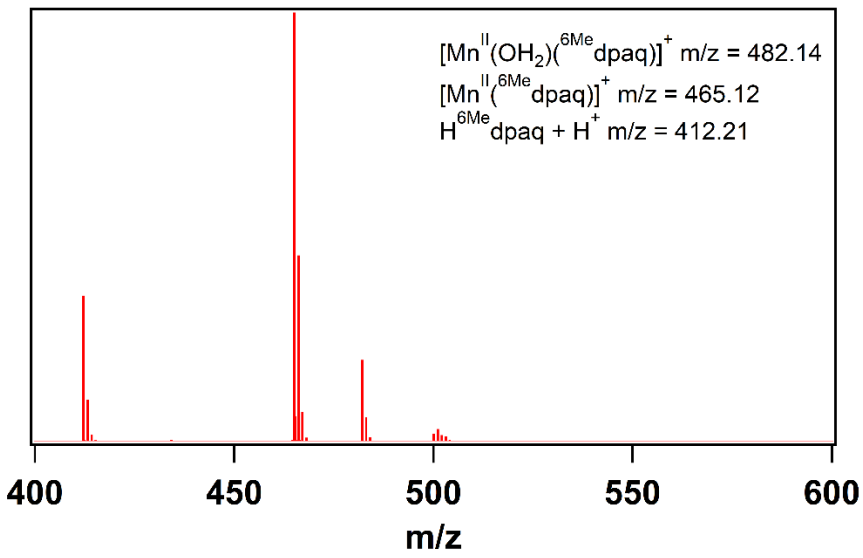

Figure A3.4. ESI-MS of $[Mn^{II}(^{6Me}dpaq)]^+$ in MeCN.

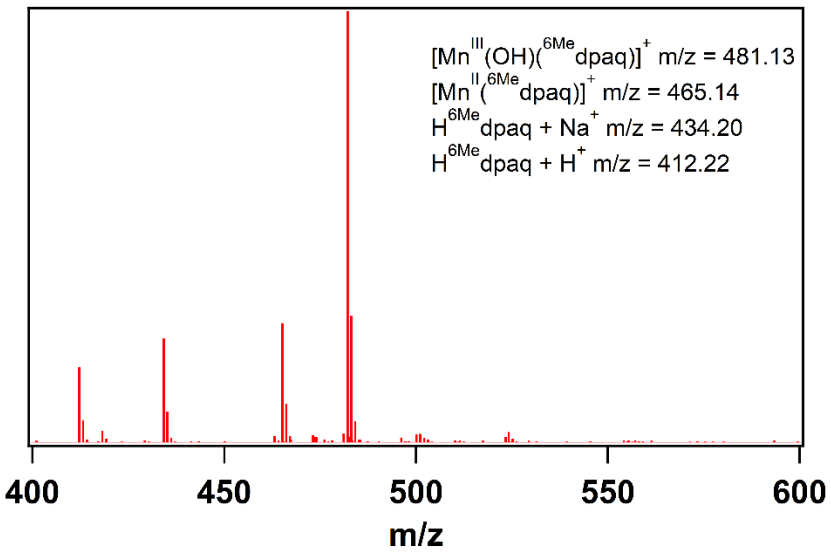

Figure A3.5. ESI-MS of $[Mn^{III}(OH)(^{6Me}dpaq)]^+$ in MeCN.

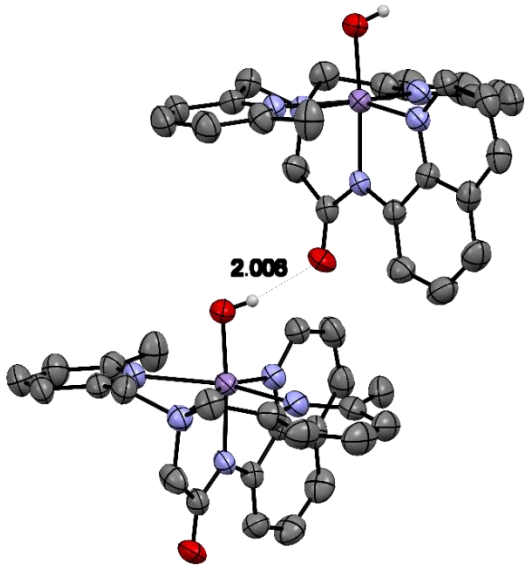

Figure A3.6. ORTEP diagram showing the hydrogen bonding interaction between two $[Mn^{III}(OH)(^{6Me}dpaq)]^+$ subunits.

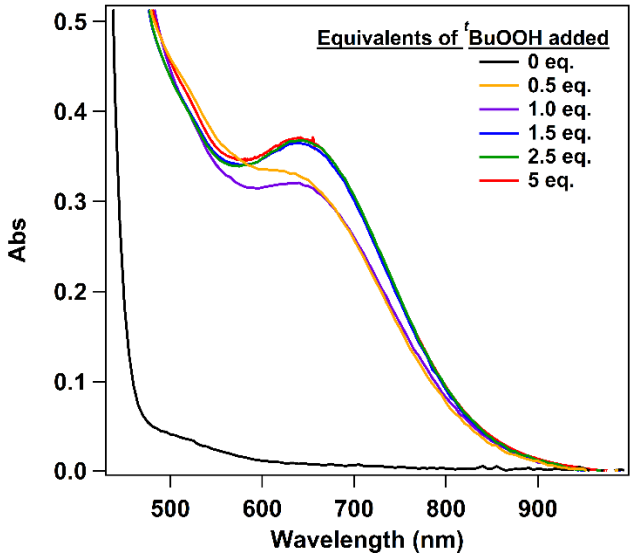

Figure A3.7. Electronic absorption spectra obtained upon the addition of varying amounts of ^{t}BuOOH to a solution of [Mn^{II}(MeCN)(^{6Me}dpaq)]$^{+}$ in MeCN at 293 K. Full formation of [Mn^{III}(OO^{t}Bu)(^{6Me}dpaq)]$^{+}$ is achieved upon the addition of 1.5 equivalents of ^{t}BuOOH.

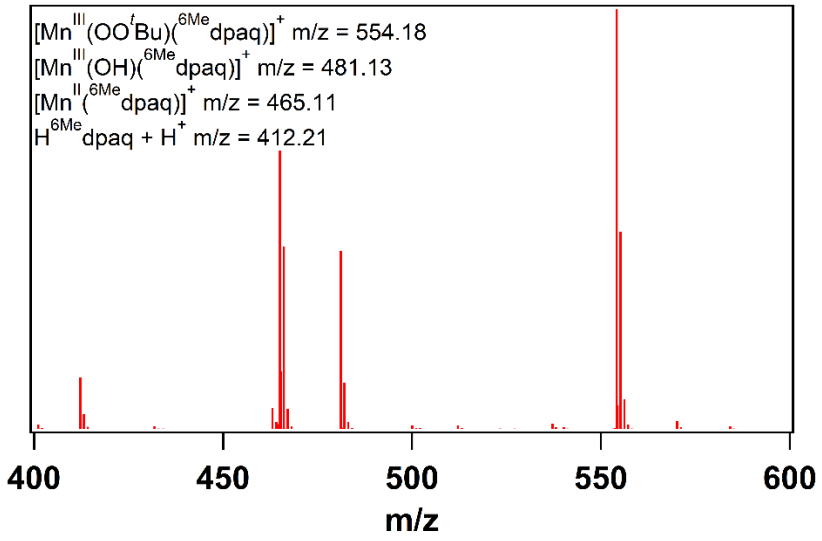

Figure A3.8. ESI-MS of [Mn^{III}(OO^{t}Bu)(^{6Me}dpaq)]$^{+}$ in MeCN.

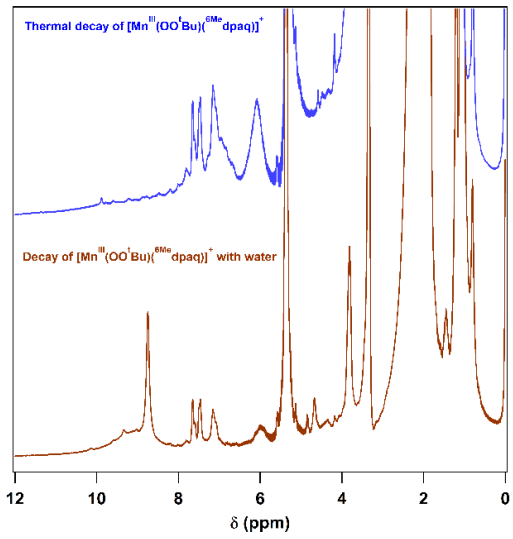

Figure A3.9. Expanded view of the 0 – 12 ppm region of the ^{1}H NMR spectra obtained following the thermal decay of $[Mn^{III}(OO^{t}Bu)(^{6Me}dpaq)]^{+}$ (blue trace) and the reaction of $[Mn^{III}(OO^{t}Bu)(^{6Me}dpaq)]^{+}$ with water (brown trace).

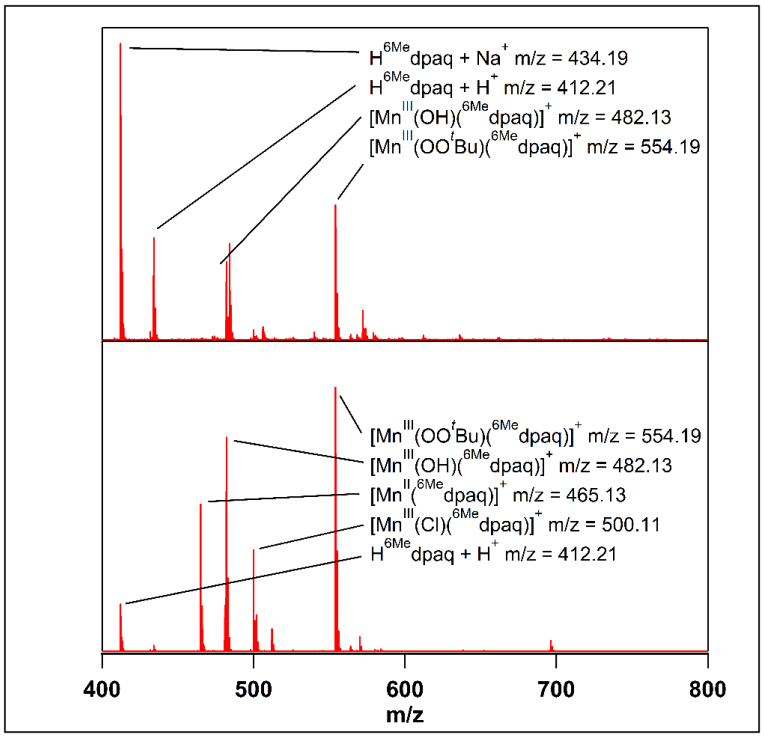

Figure A3.10. Top: ESI-MS analysis of the thermal decay products of $[Mn^{III}(OO^{t}Bu)(^{6Me}dpaq)]^{+}$. Bottom: ESI-MS analysis of the products from the reaction of $[Mn^{III}(OO^{t}Bu)(^{6Me}dpaq)]^{+}$ with water.

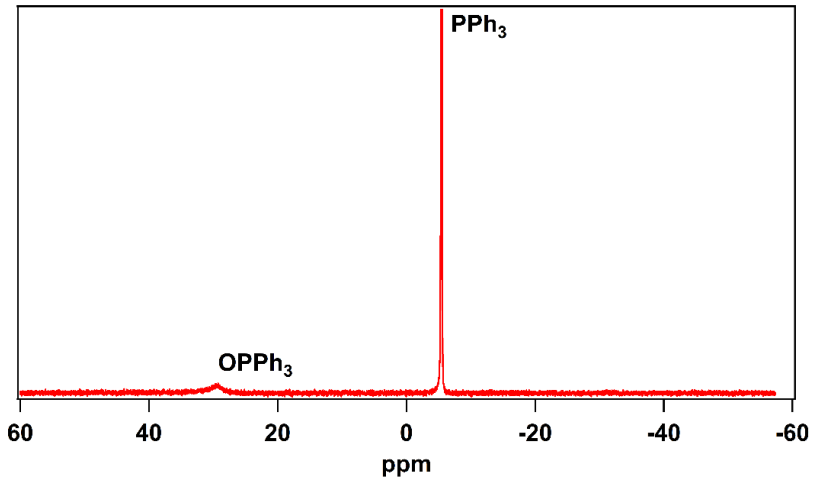

Figure A3.11. ^{31}P NMR analysis of the oxidation of PPh_3 by $[Mn^{III}(OO^tBu)(^{6Me}dpaq)]^+$ in d_3-MeCN at 298 K.

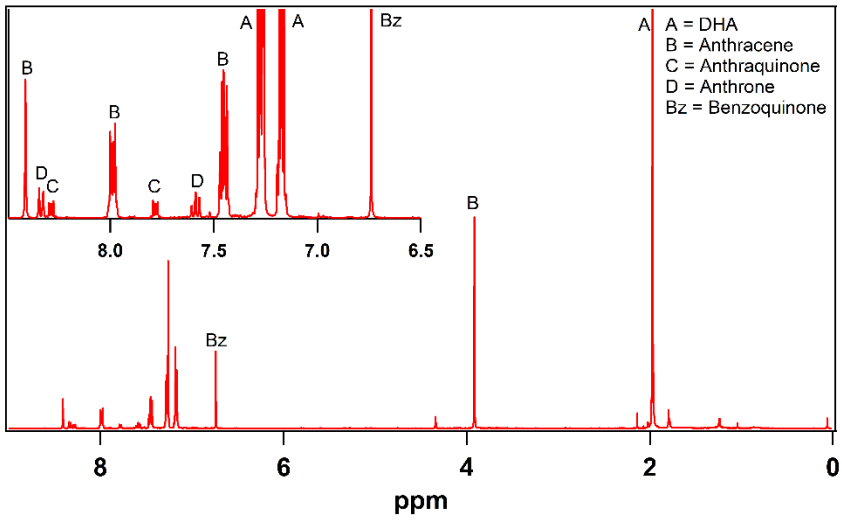

Figure A3.12. ^{1}H-NMR analysis of the oxidation of 9,10-dihydroanthracene in the presence of $[Mn^{III}(OO^tBu)(^{6Me}dpaq)]^+$ and O_2 in d_3-MeCN (6 mM) at 25°C. Quantification of products was obtained by using 1,4-benzoquinone (10 molar equivalent relative to starting Mn^{II} complex) as an internal concentration reference.

Table A3.1. Cartesian coordinates (Å) for DFT energy minimized $[Mn^{II}(NCMe)(^{6Me}dpaq)]^+$ model.

Atom	x	y	z
Mn	2.15602548217922	7.46295424269347	8.19202491377767
O	3.50770763845712	3.57175447202422	7.37581953820193
H	1.24391078981109	9.05306068889888	10.93025953793888
H	5.61121665559816	9.37150670068334	10.66699941412803
N	1.94449613915688	7.18996512944906	10.40336728178133
N	2.82620615657731	5.50318309118796	8.49240135372917
N	2.66463107128470	6.87513587657535	6.00951966927692
N	4.31065905016550	8.40870096248932	7.72185809800856
N	0.08618649542393	6.58316149103237	7.27573014903808
C	1.51780858599440	8.06089971638517	11.30183314303751
C	1.40567088378433	7.76155280307500	12.67365732986173
H	1.04812675284421	8.52142147120179	13.37107442280863
C	1.75544306038964	6.49541576210509	13.09997206019657
H	1.68148521412163	6.22121421995783	14.15603581331577
C	2.21599993782425	5.53031700591559	12.16788196679292
C	2.58587351257352	4.21180929186273	12.53959060180259
H	2.52041745135521	3.91047953602503	13.58759154593645
C	3.01968244897337	3.33573142186253	11.56518986886231
H	3.30534802442507	2.31717846183598	11.84108606933748
C	3.10909498259431	3.71273307019892	10.20567618639165
H	3.45244908577013	2.99735143450870	9.46197887423207
C	2.76347009219031	5.00021114433863	9.78352003095573
C	2.30202387888840	5.92685557371501	10.79171198152248
C	3.20586424850626	4.76175573008272	7.42551202419680
C	3.34773966645768	5.55271059160065	6.10552796756830
H	3.02685339526506	4.88986760896914	5.28648984009178
H	4.43000801908591	5.70345052823538	5.97304401146531
C	3.54603079904907	7.92056839255703	5.46302889177170
H	3.97764254720605	7.62867857885512	4.48790646420382
H	2.93018586516592	8.81749065683212	5.28122871246634
C	4.65071563062300	8.29734499536038	6.42493883329210
C	5.94121200482267	8.56253513709214	5.96442649658565
H	6.18078666817278	8.44653091038558	4.90548188357910
C	6.90845665019292	8.97389377680667	6.88191635111147
H	7.92911372518491	9.18933362251897	6.55645394534177
C	6.54938675426331	9.09893335507714	8.22116319105261
H	7.27919730881921	9.41689845264749	8.96797642564531
C	5.23724527737671	8.80271720523842	8.61767080916931
C	4.82556147024779	8.90313290458448	10.05920626761811
C	1.40550164239418	6.79870293689996	5.24885303322700
H	1.55083824278964	6.28747060641525	4.28008037480154

H	1.08918546112329	7.83042803802915	5.02306414144507
C	0.28335716363725	6.14166695324974	6.01900976965485
C	-0.54479041327072	5.19524835121001	5.41780606248257
H	-0.34082873250596	4.85192047889950	4.40172200763710
C	-1.63588784437824	4.70663295353864	6.13945809550316
H	-2.30482408950039	3.96199344179977	5.70125671741943
C	-1.85867006131122	5.19292589853583	7.42330984995761
H	-2.71102273632153	4.84752550835660	8.01160092180582
C	-0.97320854588194	6.13377347567664	7.97290773469130
C	-1.18454576381744	6.65769404213062	9.36627603177769
H	3.90354720630522	9.49330905043215	10.16493472860039
H	4.62243737299525	7.90330650551495	10.47314610367208
H	-0.55846593464899	6.10618024167276	10.08531666814477
H	-0.91021698073491	7.71922512167019	9.43500735586743
H	-2.23185344982929	6.54097025107603	9.67826692735709
C	0.86494005136532	10.59393905624052	7.96153739898651
N	1.29847337926877	9.53373304638078	8.04866503166463
C	0.31316157983020	11.93491579455562	7.85051809197128
H	0.37612919180278	12.44876343635712	8.82199948628504
H	-0.74190468383347	11.88338146178019	7.54075129795379
H	0.87828552370025	12.51409233471252	7.10425620299988

Table A3.2. Cartesian coordinates (Å) for XRD structure of [Mn^{III}(OH)(^{6Me}dpaq)](OTf).

Atom	**x**	**y**	**z**
Mn	4.942504	1.025872	2.950393
O	5.113484	1.483793	4.688828
H	5.365861	2.229268	4.751408
O	5.500008	-1.008284	-0.538879
N	3.340021	2.172002	2.417424
N	4.701950	0.405972	1.104413
N	6.602738	-0.305757	2.863592
N	3.997112	-0.973515	3.658584
N	6.761895	2.428675	2.324713
C	2.710215	3.065755	3.166060
H	2.971687	3.177218	4.072304
C	1.655232	3.860315	2.648041
H	1.216413	4.496372	3.199668
C	1.286897	3.698744	1.358207
H	0.602523	4.249926	0.996637
C	1.900788	2.719093	0.535403
C	1.543822	2.435833	-0.813534
H	0.882184	2.960427	-1.245796

C	2.144071	1.421414	-1.484525
H	1.853041	1.208713	-2.364115
C	3.194506	0.669803	-0.898132
H	3.596946	-0.035791	-1.389497
C	3.637872	0.954086	0.384748
C	2.930761	1.960324	1.117160
C	5.545481	-0.513345	0.579440
C	6.673221	-0.900911	1.521609
H	6.677769	-1.886697	1.616638
H	7.532669	-0.639125	1.106730
C	6.391286	-1.342674	3.922809
H	6.582275	-0.947950	4.810511
H	7.021093	-2.092240	3.777949
C	4.972516	-1.867268	3.901949
C	4.722413	-3.182331	4.209052
H	5.438619	-3.791801	4.350436
C	3.410505	-3.596484	4.307557
H	3.201327	-4.492282	4.545127
C	2.412364	-2.686370	4.054921
H	1.502896	-2.962472	4.080416
C	2.726130	-1.369261	3.762883
C	7.835067	0.456080	3.201985
H	8.628578	-0.089989	2.972527
H	7.853256	0.624809	4.177762
C	7.907824	1.754782	2.480003
C	9.167437	2.290624	2.081348
H	9.970043	1.791595	2.189124
C	9.187900	3.550467	1.538993
H	10.013243	3.937010	1.267815
C	8.005592	4.262197	1.384862
H	8.010139	5.132429	1.004749
C	6.802821	3.670111	1.799741
C	1.664326	-0.324164	3.577463
H	1.803020	0.399837	4.222959
H	0.782142	-0.726046	3.722323
H	1.714347	0.034768	2.667742
C	5.525018	4.455468	1.689647
H	4.870201	3.944168	1.168151
H	5.702364	5.309339	1.241160
H	5.168052	4.626242	2.585461

Table A3.3. Crystal data and structure refinement for [Mn(OH)(C25H24N5O)][O3SCF3].

Identification code	v60d	
Empirical formula	C26 H25 F3 Mn N5 O5 S	
Formula weight	631.51	
Temperature	200(2) K	
Wavelength	1.54178 Å	
Crystal system	Orthorhombic	
Space group	$Pna2_1$	
Unit cell dimensions	a = 22.7367(9) Å	α= 90°.
	b = 10.2260(4) Å	β= 90°.
	c = 11.5888(4) Å	γ = 90°.
Volume	2694.46(18) $Å^3$	
Z	4	
Density (calculated)	1.557 Mg/m^3	
Absorption coefficient	5.315 mm^{-1}	
F(000)	1296	
Crystal size	0.100 x 0.050 x 0.030 mm^3	
Theta range for data collection	3.888 to 68.257°.	
Index ranges	-26<=h<=24, -12<=k<=8, -13<=l<=13	
Reflections collected	9990	
Independent reflections	4121 [R(int) = 0.0477]	
Completeness to theta = 66.000°	99.5 %	
Absorption correction	Multi-scan	
Max. and min. transmission	1.000 and 0.699	
Refinement method	Full-matrix least-squares on F^2	
Data / restraints / parameters	4121 / 1 / 378	
Goodness-of-fit on F^2	1.162	
Final R indices [I>2sigma(I)]	R1 = 0.0603, wR2 = 0.1696	
R indices (all data)	R1 = 0.0659, wR2 = 0.1757	
Absolute structure parameter	0.082(14)	
Extinction coefficient	0.0012(4)	
Largest diff. peak and hole	0.398 and -0.752 e.$Å^{-3}$	

Table A3.4. Cartesian coordinates (Å) for DFT energy minimized $[Mn^{III}(OO^{t}Bu)(^{6Me}dpaq)]^{+}$ model.

Atom	x	y	z
Mn	0.20788856685387	-0.06877261869516	-0.01971964192381
O	0.19885371085901	-0.15933770481435	1.81712414885873
O	0.58052633953373	1.14108597773279	2.39605864778137
O	0.90672330498638	-1.12865715155843	-3.90966205765125
N	-1.45684142992269	1.07365133218609	-0.24464378124565
N	0.02828819574899	-0.16728447541523	-1.97467718971810
N	1.83741786060127	-1.40740471659932	-0.38680489300892
N	-0.87804416763294	-2.21542646203937	-0.00963791635814
N	2.05762693840085	1.25247239360241	-0.07527568012501
C	-2.12970498557802	1.69747408518598	0.72206055738680
H	-1.71195145452423	1.61675134753181	1.72786735459437
C	-3.31155609469838	2.41950238703521	0.45438926184590
H	-3.83039639386978	2.91599203940850	1.27810449341117
C	-3.79522893520917	2.48094336041484	-0.84497702808377
H	-4.71400506433023	3.03009388368087	-1.07326930210411
C	-3.09454348326991	1.82637896568247	-1.89630968270667
C	-3.50242575393783	1.82195948574107	-3.26108878292065
H	-4.41484235001659	2.35192695537757	-3.54996410380613
C	-2.73478995850563	1.14546124532922	-4.19824946118130
H	-3.04607866491542	1.13902709213629	-5.24795535056745
C	-1.54558825945074	0.45353812164044	-3.84737728012931
H	-0.96488136251189	-0.06566917583334	-4.60924593725589
C	-1.11188151232541	0.43520615055110	-2.51737855738744
C	-1.90175874584403	1.12491098080579	-1.54396716092378
C	0.94123427229524	-0.88824564814082	-2.69507039609399
C	2.13423196364131	-1.33788728413477	-1.85416051878059
H	2.51102763579265	-2.30675912089936	-2.21782099860613
H	2.93000272524082	-0.59186382212491	-2.01256024122496
C	1.45733072477176	-2.78869455727618	0.02523948774553
H	1.49699515091454	-2.81629624277177	1.12556878532123
H	2.18224950588466	-3.51865830407298	-0.36994656988776
C	0.05162313797589	-3.11531053007874	-0.40666780765804
C	-0.27552531860913	-4.28279967492528	-1.09712403726994
H	0.51005472732023	-4.97659668581890	-1.40862788169109
C	-1.62863210236687	-4.53800818194086	-1.36472700015796
H	-1.92656833527487	-5.43771784487540	-1.91181873793046
C	-2.58979718365490	-3.63898694623947	-0.90110478930203
H	-3.65585180004173	-3.82718854301669	-1.05824877169233
C	-2.18738866770021	-2.47667608386328	-0.21333470018957
C	2.98520603152837	-0.92647339550133	0.42851259348390

H	3.90766872444472	-1.47478363782696	0.17324823959324
H	2.74203677349919	-1.13529044468686	1.48290871065489
C	3.16878424909834	0.55826219446276	0.24306094272392
C	4.41060111469390	1.17517561386782	0.42396929226151
H	5.29011179092805	0.57420350770622	0.67025034140863
C	4.48903409157460	2.56388104052706	0.27827890832702
H	5.44185291452171	3.08406871966001	0.41621823020434
C	3.33529989925165	3.27720067337239	-0.06253999502472
H	3.36620698450704	4.36150010567823	-0.20009441688364
C	2.12161679465832	2.59445520704301	-0.24119534350879
C	-3.20393226764729	-1.51375369181876	0.33639259236694
H	-2.79353345799657	-0.96886767037659	1.19849746241080
H	-4.11092809777345	-2.05538935534780	0.64989897672459
H	-3.51368747498270	-0.78147575931671	-0.43004153184853
C	0.85846728629360	3.31857184632367	-0.60661620595893
H	0.36822054879245	2.83884241372617	-1.46948540855704
H	1.06796474574749	4.36870544001288	-0.85862848073187
H	0.14946746160680	3.30185623630354	0.23874184328402
C	0.73257498231338	0.98253784117370	3.84426162207099
C	-0.60021393070324	0.55441989590626	4.46705496431330
C	1.85524970860265	-0.01536888497647	4.14583477895792
C	1.12062964340263	2.40719769855560	4.25787455964562
H	-0.50463309208562	0.48508487793548	5.56467636541621
H	-1.39203728249467	1.28800907368860	4.23518587431727
H	-0.90904675091583	-0.43152612085403	4.08281503710602
H	1.59496907680015	-1.01877420480660	3.77118588375308
H	2.79922257722715	0.30916152350248	3.67575546386125
H	2.01809156846153	-0.08674585184023	5.23530146771773
H	2.05472387512379	2.71781246434636	3.75967859932327
H	0.32338902060931	3.12309184284655	3.99457515420106
H	1.27682975428196	2.44627677180570	5.34942699902310

Table A3.5. Comparison EXAFS data fits within different *k* ranges for 10 mM MeCN solution of **1**.

k range	Mn-N/O			Mn-N			Mn-C			Goodness of fit[b]
	n	*r (Å)*	σ^2	*n*	*r (Å)*	σ^2	*n*	*r (Å)*	σ^2	
2-12	2	2.00	0.008	4	2.34	0.006	6	2.93	0.005	0.278
2-13	2	2.00	0.014	3	2.35	0.002	6	2.91	0.006	0.369
3-13	2	2.00	0.011	3	2.34	0.004	6	2.91	0.005	0.381